FERMILAB-THESIS-2003-29

A Measurement Of The Ratio $\mathrm{R} = \frac{\sigma_{\mathrm{W}^{\pm}} \cdot Br(\mathrm{W}^{\pm} \to \mathrm{e}^{\pm}\nu)}{\sigma_{\mathrm{Z}^{0}} \cdot Br(\mathrm{Z}^{0} \to \mathrm{e}^{+}\mathrm{e}^{-})}$ In $\mathrm{p}\bar{\mathrm{p}}$ Collisions At $\sqrt{s} = 1.96$ TeV.

Giulia Manca
St. John's College, Oxford

Thesis submitted in fulfilment of the requirements for the degree of Doctor of Philosophy at the University of Oxford

Trinity Term, 2003

A Measurement Of The Ratio R = $\frac{\sigma_{W^\pm} \cdot Br(W^\pm \to e^\pm \nu)}{\sigma_{Z^0} \cdot Br(Z^0 \to e^+e^-)}$ In $p\bar{p}$ Collisions At $\sqrt{s}$ = 1.96 TeV.

Giulia Manca, St. John's College, Oxford

Trinity Term, 2003

Abstract

The cross-sections of the Z boson decaying into electron-positron pairs and the W boson decaying into electron and neutrino are measured using high p_T electrons. The data were taken by the Collider Detector at Fermilab(CDF) from March 2002 through January 2003, with a total integrated luminosity of 72.0 pb^{-1}. These measurements yielded values of

$$\sigma_Z \cdot Br(Z^0 \to e^+e^-) = (267.0 \pm 23.0) \text{ pb}$$

and

$$\sigma_W \cdot Br(W^\pm \to e^\pm \nu) = (2.64 \pm 0.18) \text{ nb}$$

which agree well with both the theoretical prediction at $\sqrt{s}$ = 1.96 TeV and the Run Ia measurements when the correction due to the change in the centre-of-mass energy is made. From the ratio of these cross sections,

$$\begin{aligned} R &= \frac{\sigma_W \cdot Br(W^\pm \to e^\pm \nu)}{\sigma_Z \cdot Br(Z^0 \to e^+e^-)} \\ &= 9.88 \pm 0.53, \end{aligned}$$

the branching ratio of W in electron and neutrino and the total width of the W boson are extracted , giving

$$\begin{aligned} Br(W^\pm \to e^\pm \nu) &= \frac{\Gamma(W^\pm \to e^\pm \nu)}{\Gamma(W)} \\ &= (9.89 \pm 0.49)\%, \\ \text{and} & \\ \Gamma(W) &= (2.29 \pm 0.12) \text{ GeV}. \end{aligned}$$

The latter value agrees within 2σ of the Standard Model value. In addition, the CKM matrix element $|V_{cs}|$ has been extracted, giving

$$|V_{cs}| = 1.11 \pm 0.07.$$

This value is consistent with the other measurements in the literature.

Acknowledgements

This analysis would not exist without the presence of three persons. The first person I wish to thank is Greg Veramendi, for proposing this analysis to me when I was mostly depressed and hopeless, and helping me both practically and emotionally when I needed it most. But especially for being my best friend in these years at Fermilab, on whom I could always count.
I want to thank Prof. Young-Kee Kim for having adopted me and dedicated so much of her priceless time to me, teaching me a lot, both from the physics and the human point of view; for believing in me and giving me back that enthusiasm and energy that I had lost.
Thanks to Eva Halkiadakis, for working together with me every night until dawn for so many weeks, for providing and cross checking many parts of this analysis, for making with her friendship the laboratory a pleasant place to be (and people staying at Fermilab should know how difficult this is).

For my thesis work I wish to thank my supervisor Dr. Peter Renton for his essential suggestions and incommensurable help in writing my thesis, dedicating a lot of his time to this project.
Many thanks go to the all cross section group, in particular Willis Sakumoto who derived many of the numbers essential to this analysis.
I would like to thank the convenors of the Electroweak group Ashutosh Kotwal and Pasha Murat, for welcoming me in their group and managing to provide a friendly and relaxing atmosphere, in which working was a pleasure.
Kind thanks to W.J. Stirling, for being extremely helpful with all the theoretical calculations.
Many thanks to the CDF Oxford group, in particular to Todd Huffman because he gave me the possibility to stay at Fermilab for three years and always helped with any problem I had.
Thanks to Farrukh for being my family at Fermilab, and making sure that I didn't miss anything.

Thanks to Jonas, Thilo and Tracey for sharing part of this experience with me.
A special thank to Aidan Robson, my beloved office mate and my first fan, for bringing warmth to our office and making me feel always special.
Thank you to Paolo, for proofreading my thesis in a record time and have so many useful comments.
At the end I would like to thank my dinner club friends, for making my years at Fermilab so happy and eventful, for giving that spirit of companionship that I will never find again.
Finally thank you to Rolf, for answering to all my Physics questions even the most stupid ones, but especially for the emotional support he gave me, at any time; and thanks to my family, for always making clear that if I should fail in Physics I would always have a place to come back.

Contents

1 The Standard Model **1**

Chapter 1 **1**

1.1 The Standard Model 1

1.1.1 The Standard Model Elements 1

1.1.2 Quantum Electrodynamics: $U(1)_Q$ 4

1.1.3 Quantum Chromodynamics 6

1.1.4 Electroweak Theory 8

1.1.5 Electroweak Symmetry Breaking: The Higgs Mechanism 10

1.1.6 Renormalisability 12

1.1.7 Inputs to the Standard Model 13

1.1.8 Tests of the Standard Model 13

1.1.9 Beyond the Standard Model 14

2 Introduction **16**

Chapter 2 **16**

2.1 W/Z production and decay 16

2.1.1 Theory 19

2.2 Measurement of $\Gamma(W)$ from the W and Z cross-sections 23

2.3 Previous results 23

2.4 Strategy of this measurement 24

2.5 Outline of the thesis 25

3 The Experimental Apparatus **27**

Chapter 3 **27**

3.1 The Accelerator Chain 28

3.1.1 Production of Protons and the Booster 31

3.1.2 The Main Injector 32

3.1.3 The Tevatron 33
3.2 **The CDF detector** 33
3.2.1 Coordinate System 35
3.2.2 Magnetic Spectrometer 36
3.2.3 Tracking System 36
3.2.4 Calorimeters 40
3.2.5 Muon detectors 42
3.2.6 Trigger systems 43
3.3 Generation and Simulation 51
3.4 Object-oriented software 52

4 Electron and Neutrino identification **53**

Chapter 4 **53**
4.1 Electron clustering 54
4.2 Central Electron Identification 55
4.2.1 Creation of an electron object 55
4.2.2 Corrections 56
4.2.3 Central Electron Variables 60
4.3 Central Electron trigger 64
4.4 Neutrino Identification 64

5 Monte Carlo and Data Samples **71**

Chapter 5 **71**
5.1 Monte Carlo Samples 71
5.2 Data Sample 72
5.2.1 Good Run List 72
5.2.2 Luminosity Measurement 73
5.2.3 Inclusive Electron Sample 74
5.2.4 Tight Central Electron Sample 75
5.2.5 Z sample selection 76
5.2.6 W sample selection 78

6 Backgrounds **91**

Chapter 6 **91**
6.1 Backgrounds to the Z events 91
6.1.1 Background from Hadron Jets 91

6.1.2 Background from $Z^0/\gamma^* \to \tau^+\tau^-$ 97
6.1.3 Background from W+jets 100
6.1.4 Summary of Z Candidates and Backgrounds 100
6.2 Backgrounds to the W Boson 100
6.2.1 Background from Hadron Jets 101
6.2.2 Background from $Z^0/\gamma^* \to e^+e^-$ 102
6.2.3 Background from $W \to \tau\nu$ 103
6.2.4 Summary of W Candidates and Backgrounds 104

7 Central Electron Efficiencies 106

Chapter 7 106
7.1 Central Electron Trigger Efficiencies 106
7.2 Central Electron Tracking Efficiency 109
7.3 Central Electron ID Efficiencies 109
7.3.1 Selection of the events 110
7.3.2 Electron ID Efficiencies 111

8 Z and W Boson Geometric and Kinematic Acceptances 116

Chapter 8 116
8.1 Z Acceptance Calculation 116
8.1.1 Systematic Uncertainties on the Acceptance 118
8.1.2 Removing Drell-Yan Contributions from γ^* Exchange . 130
8.2 W Acceptance Calculation 130
8.2.1 Systematic Uncertainties on the Acceptance 131
8.3 Z Vertex Corrections 138

9 Results and Conclusions 139

Chapter 9 139
9.1 Z Cross Section Estimation 139
9.2 W Cross section estimation 142
9.3 Calculation of $R = \sigma_W/\sigma_Z$ 144
9.4 Extraction of $Br(W^\pm \to e^\pm\nu)$ 147
9.5 Extraction of $\Gamma(W)$ 147
9.6 Extraction of V_{cs} 148
9.7 Conclusions 149
9.8 Future Prospects 150

A Baseline Selection Criteria for Tight Central Isolated Electrons **154**
A.1 Method 154
A.2 Variables 155

B Electron Efficiencies using $Z^0 \to e^+e^-$ data **165**
B.1 Method 165

Bibliography **167**

List of Figures

1.1 *The Higgs potential V for a complex scalar field with $\mu^2 < 0$ and $\lambda > 0$.* 11

2.1 *Diagrams for production of a vector boson V = W,Z at Leading (upper left) and Next-To-Leading order(others).* 17

3.1 *Overview of the Tevatron accelerator chain at Fermilab.* . . . 27

3.2 *Total integrated luminosity delivered by the accelerator and recorded by CDF in the period from July 2001 until January 2003. The upper curve represents the luminosity delivered to the experiment by the Tevatron, while the lower one is the luminosity effectively recorded on tape by CDF.* 29

3.3 *The accelerators involved in the proton-antiproton collisions at the Tevatron. The Debuncher and the Accumulator are indicated with the label "ANTIPROTON SOURCE" in the figure.* 30

3.4 *Longitudinal view of half of the CDF Run II detector.* 34

3.5 *Coordinate system used at CDF.* 35

3.6 *Longitudinal view of the CDF tracking system, representing a quarter of the whole detector.* 37

3.7 *On the left, view of the three barrels of the SVX silicon detector. On the right, end view of one barrel showing the 12 wedges with the 5 layers.* 38

3.8 *On the left, the endplate slots are shown; in this figure the odd are stereo and the even are axial superlayers, according to the definition in the text. On the right, a single cell layout is shown.* 39

3.9 *View of one wedge of the central calorimeter. Each wedge covers 1 tower in the azimuthal direction ($\Delta\phi = 15^o$) and ten towers in the η direction (0< $|\eta|$ <1.1). The proportional chamber(CES), referred to as "Strip Chamber" in the figure, can be seen embedded at shower maximum. Both edges are uninstrumented in order to leave space for light guides that connect the scintillator to the photo-multipliers.* 45
3.10 *Three dimensional view of the CDF detector, where the muon chambers are indicated with their respective coverage in pseudorapidity.* 46
3.11 *The readout functional block diagram. The acronyms have been already introduced in the text, apart for the following: XFT = eXtremely Fast Tracker; XTRP = Track Extrapolation module; SVT = SVX track processor in Level2 trigger system; TSI = Trigger System Interface.* 47
3.12 *The trigger system block diagram* 48

4.1 *Distribution of the tower-to-tower gain variations for central electrons.The inverse of these values are used in the correction to the central electron energy.* 57
4.2 $\langle E/p \rangle$ *as a function of run number. Here E is the corrected E and p has the corrections described in section 4.2.2c). The average of E/p is calculated in the range between 0.9 and 1.1.* 58
4.3 *The CEM energy correction factor applied to the data (left) and $\langle E/p \rangle$ as a function of CES-x after the corrections (right). The average of E/p is calculated using values of E/p in the range between 0.9 and 1.1.* 59
4.4 *The E/p distributions for electrons and positrons (left) and $\langle E/p \rangle$ as a function of track ϕ (right) in the $Z^0 \rightarrow e^+e^-$ data before the curvature corrections are applied. The average of E/p is calculated in the range between 0.9 and 1.1.* 60
4.5 *The E/p distributions for electrons and positrons (top plots) and $\langle E/p \rangle$ as a function of CES-x (bottom left) and of track ϕ (bottom right) in the $Z^0 \rightarrow e^+e^-$ data after the curvature corrections are applied. In the upper section, the plot on the right is the blow-up of the plot on the left in the region 0.5 $< \langle E/p \rangle <$ 1.5.* 66

4.6 *The E/p distributions for electrons and positrons (top plots) and $\langle E/p \rangle$ as a function of CES-x (bottom left) and a function of track ϕ (bottom right) in the $Z^0 \to e^+e^-$ Monte Carlo sample. No corrections are applied to simulation.* 67
4.7 *The $Z^0 \to e^+e^-$ (CC) invariant mass distribution of data (dots) and* PYTHIA *Monte Carlo (solid histogram). The top plot shows the events with two electrons of opposite sign (OS), while the bottom plot shows the events where the electrons have the same sign (SS) electric charge. The number of events in the Monte Carlo sample has been normalized such that the number of OS events in the MC sample is equal to the number of OS events in the data. The arrows in the top plot indicate the invariant mass cut applied for this analysis.* 68
4.8 *The E/p distributions for the $Z^0 \to e^+e^-$ data (points) and Monte Carlo sample (histogram) in a linear scale (left) and a logarithmic scale (right).* 69
4.9 *$\langle E/p \rangle$ as a function of track η (top) and ϕ (bottom). The solid triangles are the $Z^0 \to e^+e^-$ data after the corrections and the open circles are the $Z^0 \to e^+e^-$ Monte Carlo simulation.* . . . 70

5.1 *Flow Chart of events in the R analysis. The labels next to the arrows refer to the selection criteria used to create each subsample.* 77
5.2 *Transverse energy distribution for all electrons in the Inclusive sample, in the tight sample and the tight isolated electrons.* . . 78
5.3 *The η and ϕ defined by the track associated with the tight and loose electrons for $Z^0 \to e^+e^-$ candidates (top and middle), and the distribution of the η tower index in the central region of the calorimeter for $Z^0 \to e^+e^-$ candidates. Points are data and histogram is the Monte Carlo simulation. It can be seen that the last tower, "tower 9", is excluded. The number of Monte Carlo events is normalised to the number of events in the data.* 81

5.4 *The electron variables used for the selection of the events. The tight electrons in the* $Z^0 \to e^+e^-$ *candidates events (dots) and in the signal Monte Carlo (solid histogram) are used; for each variable all the selection criteria, but the one including the variable itself, are applied. The number of Monte Carlo events is normalised to the number of events in the data. The disagreement in the central bin of the Lshr distribution is due to a problem in the simulation which is not currently understood. The arrows show the value at which it has been cut to obtain the sample. For Had/EM the cut is a sliding cut that depends on the energy of the cluster, and thus is not shown.* 82

5.5 *The electron variables used for the selection of the events. The tight electrons in the* $Z^0 \to e^+e^-$ *candidates events (dots) and in the signal Monte Carlo (solid histogram) are used; for each variable all the selection criteria, but the one including the variable itself, are applied. The number of Monte Carlo events is normalised to the number of events in the data. The arrows show the value at which it has been cut to obtain the sample. The variable* χ^2_{wires}*(as defined in section 4.2.3) has not been used in the selection of the sample.* 83

5.6 *Distribution of* E_T *and* p_T *for the tight electrons from* $Z^0 \to e^+e^-$ *candidate events.* 84

5.7 *The CES local Z and X distributions for* $Z^0 \to e^+e^-$ *candidates (dots) and signal Monte Carlo (solid histogram). The number of Monte Carlo events is normalised to the number of events in the data.* 85

5.8 *Distribution of* E_T *and* p_T *for the electrons from* $W^\pm \to e^\pm\nu$ *candidate events[4].* 86

5.9 *Distribution of electron* E_T *vs.* $\not{E}_T$ *for the* $W^\pm \to e^\pm\nu$ *candidate events[1].* 87

5.10 *Distribution of* $\not{E}_T$ *vs. the isolation fraction for the* $W^\pm \to e^\pm\nu$ *candidate events[1].* 87

5.11 *Distribution of* M_T *for* $W^\pm \to e^\pm\nu$ *candidate events[1].* 88

5.12 *Distribution of* E_T *for electrons in* $W^\pm \to e^\pm\nu$ *candidate events[1].* 89

5.13 *Distribution of* $\not{E}_T$ *for* $W^\pm \to e^\pm\nu$ *candidate events[1].* 90

5.14 *Distribution of* ϕ *versus* η *for electrons in* $W^\pm \to e^\pm\nu$ *candidate events[1].* 90

6.1 *The number of tracks pointing to electron clusters for the OS events (two left plots) and for the SS events (two right plots). The points are* $Z^0/\gamma^* \to e^+e^-$ *candidates and the histograms are* $Z^0/\gamma^* \to e^+e^-$ *Monte Carlo events; the number of events in the Monte Carlo is normalised to the number of opposite sign events in the data. The presence of clusters with two or three tracks associated with it in the SS sample is due to trident events, as described later in the text.* 92
6.2 Δz *between the two electron tracks for opposite-sign events (left) and same-sign events (right). The points are* $Z^0/\gamma^* \to e^+e^-$ *candidates and the histograms are* $Z^0/\gamma^* \to e^+e^-$ *Monte Carlo events.* 93
6.3 *Sketch of a "trident" event as described in the text. The green bands represent the layers of material in the detector.* 94
6.4 *The same sign invariant mass distribution in the data subtracted by the same sign invariant mass distribution obtained with the* $Z^0/\gamma^* \to e^+e^-$ *Monte Carlo sample with the default geometry (top) and with the added 5.5%* X_0 *extra material (bottom). As expected, in the Monte Carlo with the extra material the number of SS events (coming from tridents) is higher than in the default Monte Carlo, thus the difference with the data is smaller.* 95
6.5 *The* E/p *distributions for electrons in OS* $Z^0 \to e^+e^-$ *events (top) and invariant mass distributions of SS events (bottom) for data (points) and Monte Carlo (histograms). The shaded histograms represent simulation with the default geometry and the open histograms represent simulation with an extra 5.5%* X_0 *of the default material.* 96
6.6 *Left plot: comparison of the* $\tau^+\tau^-$ *and* e^+e^- *invariant mass distribution at generator level for the events from* $Z^0/\gamma^* \to e^+e^-$ *signal (yellow histogram) and* $Z^0/\gamma^* \to \tau^+\tau^- \to e^+\nu_e\bar{\nu}_\tau e^-\bar{\nu}_e\nu_\tau$ *background (dots) Monte Carlo as a consistency check before any cut is applied. The peak at low values of* $M_{\ell\ell}$ *is due to the presence of the* γ^**. In the right plot the invariant mass distribution (at generator level) from the electron pairs coming from the taus from the* $Z^0/\gamma^* \to \tau^+\tau^- \to e^+\nu_e\bar{\nu}_\tau e^-\bar{\nu}_e\nu_\tau$ *decay chain is reported for comparison.* 97

6.7 *Invariant mass distribution for the events from* $Z^0/\gamma^* \to e^+e^-$ *signal (yellow/light shaded histogram) and* $Z^0/\gamma^* \to \tau^+\tau^- \to e^+\nu_e\bar{\nu}_\tau e^-\bar{\nu}_e\nu_\tau$ *background Monte Carlo (red/dark shaded histogram).* 98
6.8 *Transverse energy distribution for the electrons from the Monte Carlo simulation for the* $Z^0/\gamma^* \to e^+e^-$ *signal (left) and* $Z^0/\gamma^* \to \tau^+\tau^- \to e^+\nu_e\bar{\nu}_\tau e^-\bar{\nu}_e\nu_\tau$ *background (right). The integrated luminosities of the two samples are the same.* 99
6.9 *Dependence of the number of QCD background events on the value of the isolation cut(top) and the* $\not{E}_T$ *cut (bottom)[1].* . . 105

7.1 *Level-1 (top) and Level-3 (bottom) tracking efficiencies as a function of* η *measured by CES[2]. Data from period III were used.* 110
7.2 E_T *distribution of electron candidates from data passing the L2 pre-scaled trigger used to measure L2 cluster trigger efficiency (top) and L2 cluster efficiency as a function of* E_T *(bottom)[2].* 111

8.1 *The Z coordinate as reconstructed from the CES for all the electrons in the event(upper plot), for the electrons in the events passing the fiducial cut (middle plot), and for the events that fail the fiducial cut (bottom plot). The regions* $|Z_{CES}| < 9$ cm *and* $|Z_{CES}| > 230$ cm *are excluded as expected (see section 4.2.3 and Table 8.1).* 118
8.2 *Left plot:* $\langle E/p \rangle$ *as a function of* η*, where the average has been calculated using values of* E/p *between 0.9 and 1.1. The dashed lines represent 1% variation in energy scale. In the right plots, the distribution observed in the data has been compared with that in the default Monte Carlo(top plot) and with the Monte Carlo with the extra material(bottom plot). The lines correspond to the fit with a second order polynomial function. The increase in the curve in the data is due to the presence of more material as the electrons pass through the detector at an angle (and thus bremsstrahlung more). The different shape in the Monte Carlo is probably due to missing material in the detector simulation and is currently under study.* 120

8.3 *On the left, the p_T distribution of the Z^0 boson as reconstructed from the momenta of the electrons in data (points) and Monte Carlo (solid histogram). The p_T distribution in the data is a bit broader than the one in the simulation. On the right, the Monte Carlo distribution has been reweighted toward larger and smaller values of p_T; the histograms are the ones described in Table 8.5, corresponding to the nominal(solid histogram), a "hard"(dashed) and a "soft"(dotted) distribution of p_T. The number of events in the Monte Carlo sample has been normalized to the number of events in the data.* 122
8.4 *The E_T(left plot) and p_T(right plot) distributions for the electrons from the $Z^0 \to e^+e^-$ default Monte Carlo(yellow solid histogram) and the Monte Carlo with extra material(blue line). The arrows indicate the E_T cut at 25 GeV and the p_T cut at 10 GeV/c applied in the acceptance calculation.* 123
8.5 *E/p distributions for default MC(top plot) and MC with extra material(bottom plot) compared with data for the region $0.5 < E/p < 1.5$.* 124
8.6 *E/p distribution for different regions of the track z_0 at the radius of 10.6 cm, for default Monte Carlo(yellow solid histogram), Monte Carlo with extra material (blue line) and data (red dots). The regions in z_0 are chosen to represent the different barrels of the Silicon Vertex Detector(SVX).* 125
8.7 *The ratio of the number of electrons in the region $1.5 < E/p < 2.5$ to the total for the default MC simulation(squares), extra material MC(triangles) and data(dots) as a function of $z_{0(R=10.6)}$. The values on the x axis have been slightly shifted to avoid overlapping.* 126
8.8 *Rapidity distribution of the Z for Run I $Z^0 \to e^+e^-$ data (squares) and Monte Carlo signal events (at generator level) generated with $\sqrt{s}$=1.96 TeV with default CTEQ5L PDFs (yellow solid histogram), and $\pm$ 1 σ variation (green solid line and dashed blue line).* 127
8.9 *Rapidity distribution of the Z for Run II $Z^0 \to e^+e^-$ data(dots) and Monte Carlo signal events (after simulation) generated with $\sqrt{s}$=1.96 TeV with default CTEQ5L PDFs (yellow solid histogram), and $\pm$ 1 σ variation (green solid line and dashed blue line).* 128

8.10 *Components of the vector $\vec{U}$ in the direction parallel to the electron ($\vec{U}_{\parallel}$, on the top left), and perpendicular to the electron ($\vec{U}_{\perp}$ on the top right) in the data (red dots) and Monte Carlo (solid histogram). In the bottom plot, the magnitude of $\vec{U}$ is shown in data and Monte Carlo with the same convention. All the plots are before any scale correction is applied[1].* 134
8.11 *Components of the vector $\vec{U}$ in the direction parallel to the electron ($\vec{U}_{\parallel}$, on the top left), and perpendicular to the electron ($\vec{U}_{\perp}$ on the top right) in the data (red dots) and Monte Carlo (solid histogram). In the bottom plot, the magnitude of $\vec{U}$ is shown in data and Monte Carlo with the same convention. All the plots are after the scale correction is applied[1].* 135
8.12 *The reconstructed W transverse momentum in the default Monte Carlo(solid histogram) and in the data(red dots). The top plot shows the nominal distribution, while the bottom plot shows the best reweighted distribution[1].* 136
8.13 *The $d\sigma/dy$ distribution with the default CTEQ5L PDFs at 1.96 TeV for $Z^0/\gamma^* \rightarrow e^+e^-$ ($Z^0 \rightarrow \mu^+\mu^-$) in red-solid(blue-dashed), and for $W^{\pm} \rightarrow e^{\pm}\nu$($W^{\pm} \rightarrow \mu^{\pm}\nu$) in pink-dotted(cyan,dot-dashed) are compared with the $Z^0 \rightarrow e^+e^-$ Run I data at $\sqrt{s}$ =1.8 TeV[1].* 137
8.14 *Distribution of the z_0 of the track associated to the electron for the $Z^0 \rightarrow e^+e^-$ candidate events selected without the cut at 60 cm.* 138

9.1 $Z \rightarrow \ell^+\ell^-$ *cross section measurements as a function of the centre of mass energy $\sqrt{s}$ for this measurement (indicated with the star) compared with other measurements in literature. The solid line corresponds to the standard model calculation from [5].* 143
9.2 $W^{\pm} \rightarrow \ell^{\pm}\nu$ *Cross section measurements as a function of the centre of mass energy $\sqrt{s}$ for this measurement (indicated with the star) compared with other measurements in literature. The solid line corresponds to the standard model calculation from [5].* 145

9.3 *Measurements of $R = \frac{\sigma_W}{\sigma_Z}$ performed in the years between 1991 and 2000 are compared with this measurement. The World Average is the value reported in the PDG [6], while the Standard Model prediction is taken from [6].* 152
9.4 *Measurements of $\Gamma(W)$ performed in the years between 1991 and 2000 are compared with this measurement. The World Average is the value reported in the PDG [6], while the Standard Model prediction is taken from [6].* 153

A.1 *In the upper plot, the distribution of the isolation variable in the sample of $Z^0/\gamma^* \to e^+e^-$ events is plotted. The events are selected applying all the cuts as in the text apart from the cut on the variable which is plotted ("N-1"). In the bottom plot, the efficiency of the chosen cut is shown as a function of the variable itself, when all the selection criteria except the one including the variable itself are applied ("N-1"). The background for this variable is not shown for two reasons; Firstly, the isolation is used to calculate the background and thus changing the cut will change the background itself; secondly, the background considered depends on the kind of physics processes analysed. The value of the efficiency for the chosen value is given[7].* . . 157
A.2 *In the upper plot, the distribution of the E/p variable in the sample of $Z^0/\gamma^* \to e^+e^-$ events, selected as in the text, is plotted. In the bottom plot, the efficiency of the chosen cut is shown as a function of the variable itself, together with the background contamination from the W sample, as explained in the text. Both plots are made when all the selection criteria,except the one including the variable itself, are applied("N-1"). The value of the efficiency for the chosen value is given[7].* 158
A.3 *Top Left: Had/Em vs. E_T for tight electrons with $E_T > 25$ GeV in events with $\not{E}_T > 25$ GeV. Top Right: the fraction of events that pass the running Had/EM cut that fail the fixed cut of Had/EM <0.05 as a function of the value of the cut on E_T . Bottom Left: the E_T spectrum of events with Had/EM <0.05. Bottom Right: the E_T spectrum of events with Had/EM >0.05[7].* 160

A.4 *In the upper plot, the distribution of the Lshr variable in the sample of* $Z^0/\gamma^* \rightarrow e^+e^-$ *events, selected as in the text, is plotted. In the bottom plot, the efficiency of the chosen cut (left-hand scale) is shown as a function of the variable itself, together with the background contamination from the W sample (right-hand scale), as explained in the text. Both plots are made when all the selection criteria, except the one including the variable itself, are applied ("N-1"). The value of the efficiency for the chosen value is given[7].* 161

A.5 *In the upper plot, the distribution of the* ΔZ *variable in the sample of* $Z^0/\gamma^* \rightarrow e^+e^-$ *events, selected as in the text, is plotted. In the bottom plot, the efficiency of the chosen cut (left-hand scale) is shown as a function of the variable itself, together with the background contamination from the W sample (right-hand scale), as explained in the text. Both plots are made when all the selection criteria, but the one including the variable itself, are applied ("N-1"). The value of the efficiency for the chosen value is given[7].* 162

A.6 *In the upper plot, the distribution of the* ΔX *variable in the sample of* $Z^0/\gamma^* \rightarrow e^+e^-$ *events, selected as in the text, is plotted. In the bottom plot, the efficiency of the chosen cut (left-hand scale) is shown as a function of the variable itself, together with the background contamination from the W sample (right-hand scale), as explained in the text. Both plots are made when all the selection criteria, but the one including the variable itself, are applied ("N-1"). The value of the efficiency for the chosen value is given[7].* 163

A.7 *In the upper plot, the distribution of the* χ^2 *variable in the sample of* $Z^0/\gamma^* \rightarrow e^+e^-$ *events, selected as in the text, is plotted. In the bottom plot, the efficiency of the chosen cut is shown as a function of the variable itself, together with the background contamination from the W sample, as explained in the text. Both plots are made when all the selection criteria but the one including the variable itself are applied. The value of the efficiency for the chosen value is given[7].* 164

List of Tables

1.1 *Experimentally measured masses of the fermions, as reported in the Review of Particle Physics(2002)[6]. In the Standard Model, neutrinos are defined to be massless.* 2

1.2 *Quantum numbers of the fermions in the Standard Model, where q is the charge, t and t_3 denote the weak isospin and its third component and y is the weak hypercharge. Members of a given weak isospin multiplet have a common hypercharge.* 3

1.3 *Quantum numbers of the bosons in the Standard Model, where q is the charge, t and t_3 denote the weak isospin and its third component. The masses are those reported in the Review of Particle Physics(2002)[6].* 4

2.1 *Known decay modes of the W^+, and decay rate relative to $e^{\pm}\nu$ to lowest order in the SM and $O(\alpha_s)$ in QCD[8]. All the quark decay channels except $\mathrm{u\bar{d}}$ and $\mathrm{c\bar{s}}$ are strongly Cabibbo suppressed, as can be seen from the $sin^2\theta_c \sim 0.05$ dependence. Decays to $\mathrm{u\bar{b}}$ and $\mathrm{c\bar{b}}$ are further suppressed and thus negligible.* 20

2.2 *Measured partial decay width and branching ratios for the W and Z bosons from the Review of Particle Physics(2002)[6].* . 21

2.3 *Measurements of the W and Z^0 production cross-sections times branching ratios from previous collider experiments, the corresponding value of R and the extracted value of* $\Gamma(\mathrm{W})$. 24

3.1 *Parameters characteristic of different Runs at the Tevatron. The leftmost column shows the operational performance of Run Ib, terminated in 1996; the middle column shows the current parameters of Run II, whilst the rightmost column is the performance that the Tevatron would have if there were 121 antiproton bunches in a 132 ns bunch spacing, instead of the 36 used at the moment. The scenario with 132 ns bunch spacing is still under development at the time of this writing.* 31
3.2 *Amount of data collected during the different periods of data-taking at CDF.* 35
3.3 *Design parameters of the Central Outer Tracker at CDF.* . . . 40
3.4 *Characteristics of the CDF RunII calorimeters. X_0 is the radiation length and λ is the hadronic interaction length.* 41
3.5 *Description of the Shower-Max (CES) and the Preshower (CPR) central detectors.* 42
3.6 *Design parameters of the CDF II Muon Detectors. Pion interaction lengths and multiple scattering are computed at a reference angle of $\theta = 55^o$ in CMX, and show a range of values for the BMU.* 43

5.1 *Systematic uncertainties in the luminosity calculation using the CLC and the CDF measurement of the inelastic cross-section.* 74
5.2 *Criteria used in the creation of the Inclusive Electron sample.* 75
5.3 *Criteria for electron candidates used in the selection of the "tight central" electron sample.* 75
5.4 *Criteria for electron candidates used in this analysis. The energy and momentum are corrected for data only. The central-central $Z^0 \to e^+e^-$ candidates require at least one tight electron and at least one loose electron in the invariant mass window between 66 and 116 GeV/c^2. (*) The E/p cut is released for electrons with E_T >50 GeV/c^2.* 79

6.1 *Sources and amounts of backgrounds to the $Z^0/\gamma^* \to e^+e^-$ signal.* 100
6.2 *QCD background estimates in the W sample. The last column shows the purity of the sample.* 102
6.3 *Sources and amounts of backgrounds to the $W^\pm \to e^\pm\nu$ signal.* 104

7.1 *Trigger requirements for the physics and back-up triggers. The* `Wnotrack_NoL2` *trigger has been pre-scaled of a factor 50 at Level-2 to maintain the desired trigger event rate with the higher luminosity.* 107
7.2 *Averages of total track trigger efficiencies for the three time periods.* 109
7.3 *Criteria for the selection of the initial sample to be used in the central electron efficiency calculation. The tight electron cuts are the same as listed on Table 5.4.* 112
7.4 *Number of events passing i-th variable cut (in addition to the CC selection) for both OS and SS events in data and for the expected number of SS events from* $Z^0 \to e^+e^-$ *Monte Carlo simulation.* 113
7.5 *Efficiency* (ϵ^i) *of each identification variable and total efficiency* ϵ_T *and* ϵ_L *for the tight and loose central identification cuts using* $Z^0 \to e^+e^-$ *events with SS event subtraction, QCD background subtraction, and no background subtraction.* . . . 114

8.1 *Effect of each geometric/kinematic cut on electrons and events. The numbers in the middle columns are originated from the default* $Z^0 \to e^+e^-$ *Monte Carlo simulation and the numbers in the right column are originated from the simulation when the extra material is added. The fractions are with respect to the number of events with* $66 < M_{ee}^{gen} < 116$ *GeV/c*^{2} *and* $|z_{vertex}^{gen}| < 60$ *cm, which is equal to 237652.* 119
8.2 *Effect on the acceptance due to the CEM energy scale variation.* 120
8.3 *Effect on the acceptance due to the energy resolution variation. The width of the invariant mass at Z peak,* $\sigma(M_{ee})$, *is extracted from the Gaussian fit in the range* $86 < M_{ee} < 98$ *GeV for the MC samples with the variation in resolution. They can be compared with the value measured from the data.* 120
8.4 *Effect on the acceptance due to the scale of the track* p_T. . . . 121
8.5 χ^2 *per degree of freedom between the data and Monte Carlo sample and acceptance values for various* p_T *distributions as shown in Figure 8.3.* 123
8.6 *Difference in acceptance due to the reweight of the rapidity distribution at generator level.* 128
8.7 *Summary of the systematic uncertainties on the Z acceptance.* 129

8.8 *Effect of each geometric/kinematic cut on the* $W^{\pm} \rightarrow e^{\pm}\nu$ *events using the default* $W^{\pm} \rightarrow e^{\pm}\nu$ *Monte Carlo simulation. The fractions are with respect to the number of events with* $|z^{gen}_{vertex}| < 60$ *cm, which is equal to 1443131.* 131
8.9 *Summary of the systematic uncertainties on the W acceptance.* 133

9.1 *Parameters involved in the* $Z^0 \rightarrow e^+e^-$ *cross-section calculation in Run Ia [9, 10] and Run IIa. Note that the kinematic cuts in Run Ia are looser than in the ones in Run IIa.* 141
9.2 *Improved calculation of* $Z^0 \rightarrow e^+e^-$ *cross-section by W.James Stirling et.al. for both* $\sqrt{s} = 1.8$ *and* $\sqrt{s} = 1.96$ *TeV [11]. The uncertainties reflect the 1.5% uncertainty on the calculation of the PDFs [12].* 141
9.3 *List of parameters used in the theoretical calculation of the NNLO* $Z^0 \rightarrow e^+e^-$ *and* $W^{\pm} \rightarrow e^{\pm}\nu$ *cross sections[11].* 142
9.4 *Improved calculation of* $W^{\pm} \rightarrow e^{\pm}\nu$ *cross-section by W.James Stirling et al. for both* $\sqrt{s} = 1.8$ *and* $\sqrt{s} = 1.96$ *TeV [11]. The uncertainties reflect the 1.5% uncertainty on the calculation of the PDFs [12].* 144
9.6 Systematic uncertainties in W, Z acceptances and on the ratio of acceptances. 146
9.5 *Summary of the results from the W and Z cross section results.* 151

A.1 *The parameters in the linear fit to the cut in Had/EM to maintain the efficiency in column 1[7].* 158

Chapter 1

The Standard Model

In this chapter the Standard Model(SM) of Particle Physics is outlined; Quantum Electrodynamics, Electroweak theory and Quantum Chromodynamics are considered, as is the generation of masses via the Higgs mechanism. The experimental status of the Standard Model is briefly reviewed, and possible extensions to it are discussed.

1.1 The Standard Model

The Standard Model is a quantum field theory that describes the fundamental particles and their interactions. It has his roots in *gauge* theory and exploits some of the symmetries that are inherent in many physical theories. The following sections describe some of the different parts of the Standard Model. For a more comprehensive description of it see for instance [13].

1.1.1 The Standard Model Elements

The matter fields that constitute the Standard Model can be classified into two groups according to their spins. These are the *fermions*, which are spin - $\frac{1}{2}$ particles and the *bosons*, which are spin-0 or spin-1. They are described in the following sections.

leptons	mass	**quarks**	mass
$\begin{pmatrix} \nu_e \\ e \end{pmatrix}$	$< 3\,\mathrm{eV/c^2}$ $0.511\,\mathrm{MeV}/c^2$	$\begin{pmatrix} u \\ d \end{pmatrix}$	$1.5 - 4.5\,\mathrm{MeV/c^2}$ $5 - 8.5\,\mathrm{MeV}/c^2$
$\begin{pmatrix} \nu_\mu \\ \mu \end{pmatrix}$	$< 0.19\,\mathrm{MeV/c^2}$ $105.66\,\mathrm{MeV}/c^2$	$\begin{pmatrix} c \\ s \end{pmatrix}$	$1.0 - 1.4\,\mathrm{GeV/c^2}$ $80 - 155\,\mathrm{MeV}/c^2$
$\begin{pmatrix} \nu_\tau \\ \tau \end{pmatrix}$	$< 18.2\,\mathrm{MeV/c^2}$ $1.777\,\mathrm{GeV}/c^2$	$\begin{pmatrix} t \\ b \end{pmatrix}$	$174.3\,\mathrm{GeV/c^2}$ $4.0 - 4.5\,\mathrm{GeV}/c^2$

Table 1.1: *Experimentally measured masses of the fermions, as reported in the Review of Particle Physics(2002)[6]. In the Standard Model, neutrinos are defined to be massless.*

The Fermions

These particles are characterised by their spin-$\frac{1}{2}$ nature and are thus governed by Fermi-Dirac statistics. They can be split into two groups, *quarks* and *leptons*, which are distinguished by the charges associated with them. They are the six quarks: up (u), down(d), charm(c), strange(s), top(t) and bottom(b), and the six leptons: electron (e), muon(μ) and tau(τ) with their corresponding neutrinos. Quarks carry the colour charge of the strong interactions of Quantum Chromodynamics (QCD) and fractional electric charge[1], whereas leptons are colourless and have integer electric charge. In addition, the fermions can be split into *generations* which correspond to doublets of left-handed and singlets of right-handed quarks and leptons of increasing mass. This separation is based on the empirical evidence of the chirality of the weak interactions and corresponds to massless neutrinos[2]. Table 1.1 and 1.2 show the fermions and their properties.

The Bosons

There are four known forces which act on matter. Three have a basis within the SM, *electromagnetic, weak*, combined in the *electroweak* interaction, and *strong*. The fourth, *gravity*, is negligibly small at the energy scales at which the SM is thought to be relevant, and it is not included. The forces are

[1] In units of e, the charge of the electron.

[2] There is recent evidence from the Super-Kamiokande neutrino oscillation experiment[14] and the Sudbury Neutrino Observatory(SNO)[15, 16], showing that neutrinos may in fact have mass. This is not accounted for within the SM.

generation number 1	2	3	q	t	t_3	y
	leptons					
$\begin{pmatrix} \nu_e \\ \mathrm{e} \end{pmatrix}_L$	$\begin{pmatrix} \nu_\mu \\ \mu \end{pmatrix}_L$	$\begin{pmatrix} \nu_\tau \\ \tau \end{pmatrix}_L$	0 -1	$\frac{1}{2}$	$+\frac{1}{2}$ $-\frac{1}{2}$	-1
e_R	μ_R	τ_R	-1	0	0	-2
	quarks					
$\begin{pmatrix} \mathrm{u} \\ \mathrm{d} \end{pmatrix}_L$	$\begin{pmatrix} \mathrm{c} \\ \mathrm{s} \end{pmatrix}_L$	$\begin{pmatrix} \mathrm{t} \\ \mathrm{b} \end{pmatrix}_L$	$+\frac{2}{3}$ $-\frac{1}{3}$	$\frac{1}{2}$	$+\frac{1}{2}$ $-\frac{1}{2}$	$\frac{1}{3}$
u_R	c_R	t_R	$+\frac{2}{3}$	0	0	$+\frac{4}{3}$
d_R	s_R	b_R	$-\frac{1}{3}$	0	0	$-\frac{2}{3}$

Table 1.2: *Quantum numbers of the fermions in the Standard Model, where q is the charge, t and t_3 denote the weak isospin and its third component and y is the weak hypercharge. Members of a given weak isospin multiplet have a common hypercharge.*

mediated by the spin-1 gauge bosons, which are shown in Table 1.3 along with their masses.

Although the gravitational interaction is not featured in the SM, it is thought to be mediated by a spin-2 gauge boson, known as the graviton. For a possible realisation of Quantum Gravity and the graviton, which constitutes physics beyond the Standard Model, see for instance [17].

The Standard Model Structure

The Standard Model is based on the local gauge symmetry of the fundamental $\mathrm{SU}(2)_L \otimes \mathrm{U}(1)_Y$ electroweak and the $\mathrm{SU}(3)_C$ strong interactions in particle physics,

$$\mathrm{SU}(3)_\mathrm{C} \otimes \mathrm{SU}(2)_\mathrm{L} \otimes \mathrm{U}(1)_\mathrm{Y}. \tag{1.1}$$

Here C stands for the colour charge carried by the strong interactions, L refers to the fact that there are only left-handed doublets, *i.e.* no right-handed neutrinos are allowed, and Y represents the weak hypercharge carried by the electroweak interactions, defined as

$$Y = 2(\frac{Q}{e} - t_3). \tag{1.2}$$

By demanding local gauge invariance of the Standard Model Lagrangian,

boson	interaction	mass	q	t	t_3
Vector Bosons					
W^+	weak	80.423 ± 0.0039 GeV/c^2	+1	+1	+1
Z^0	electroweak	91.1876 ± 0.0021 GeV/c^2	0	+1	0
W^-	weak	80.423 ± 0.0039 GeV/c^2	−1	+1	−1
γ	QED	0	0	0	0
g	QCD	0	0	0	0
Scalar Boson					
H	Yukawa	> 114.4 GeV/c^2 CL=95%	0	0	0

Table 1.3: *Quantum numbers of the bosons in the Standard Model, where q is the charge, t and t_3 denote the weak isospin and its third component. The masses are those reported in the Review of Particle Physics(2002)[6].*

massless spin-1 fields, mediating the interactions, are required. However, this makes the theory inconsistent with experimental observation of the massive electroweak bosons $W^{\pm}$ and Z^0. The mechanism that generates masses in the SM is based on *spontaneous symmetry breaking* (SSB) of the electroweak $SU(2)_L \otimes U(1)_Y$ symmetry. This causes the decoupling of the weak and electromagnetic forces while preserving the local gauge invariance of the whole theory. A consequence of SSB is the prediction of there being a massive scalar (spin-0) particle known as the Higgs boson (see Table 1.3), as yet undiscovered experimentally[3]. The following sections explain the above in more detail. The electromagnetic interaction, based on the symmetry group $U(1)_Q$, is used as an example of how local gauge invariance requires the existence of an extra massless vector field, in this case identified with the photon.

1.1.2 Quantum Electrodynamics: $U(1)_Q$

Quantum Electrodynamics (QED) is the gauge theory of electromagnetic interactions. For a free Dirac field Ψ with spin $s = \frac{1}{2}$, mass m and electric charge eQ, the corresponding Lagrangian[4] is:

$$\mathcal{L}_{free} = \bar{\Psi}(x)(i\gamma_\mu \partial^\mu - m)\Psi(x) \tag{1.3}$$

[3]Recent data from LEP taken in 2000 at energies up to 209 GeV show a 2σ excess for a SM Higgs with mass $M_H \simeq 115$ GeV[18].

[4]The Lagrangian, or more correctly the Lagrangian density, is defined as $\mathcal{L} = \mathcal{T} - \mathcal{V}$, where $\mathcal{T}$ and $\mathcal{V}$ are the kinetic and potential energy densities respectively.

and the corresponding equation of motion is the Dirac equation

$$(i\gamma_\mu\partial^\mu - m)\Psi(x) = 0. \tag{1.4}$$

The Lagrangian can be seen to be invariant under the global U(1) transformations as follows:

$$\Psi \to e^{iQ\theta}\Psi; \quad \bar{\Psi} \to \bar{\Psi}e^{iQ\theta}; \quad \partial_\mu\Psi \to e^{iQ\theta}\partial_\mu\Psi, \tag{1.5}$$

where $Q\theta$ is the global phase and θ is the continuous parameter. *Noether's Theorem* states that if a system is invariant under a global transformation, then there is a conserved current and associated charge. Therefore, the global U(1) invariance of $\mathcal{L}_{free}$ implies the conservation of electromagnetic charge, eQ, and current,J_μ,

$$J_\mu = \bar{\Psi}\gamma_\mu eQ\Psi; \quad \partial_\mu J^\mu = 0; \quad eQ = \int d^3x J_0(x). \tag{1.6}$$

Now, if we make the global transformation into a local one, *i.e.*, the continuous parameter θ is allowed to depend on the space-time point x, then the Lagrangian is now only invariant if a vector field A_μ is introduced. This transforms under the local gauge transformations as

$$A_\mu \to A_\mu - \frac{1}{e}\partial_\mu\theta(x), \tag{1.7}$$

and it is identified with the propagator of the electromagnetic force, the photon.

In order to complete the expression for the Lagrangian a term has to be introduced to account for the propagation of the vector field, which must also be gauge invariant. The so called kinetic term is given in terms of the field strength tensor,

$$F_{\mu\nu} = \partial_\mu A_\nu - \partial_\nu A_\mu. \tag{1.8}$$

Thus, the Lagrangian of the Quantum Electrodynamics theory is

$$\mathcal{L}_{QED} = -\bar{\Psi}(x)\gamma_\mu(\partial_\mu + ieQA_\mu) - m\bar{\Psi}(x)\Psi(x) - \frac{1}{4}F_{\mu\nu}(x)F^{\mu\nu}(x). \tag{1.9}$$

The addition of a mass term $\frac{1}{2}m^2A_\mu A^\mu$ would cause the QED Lagrangian to change under a local gauge transformation and is therefore not allowed. Thus the gauge field, the photon, is massless, which is consistent with experimental observation and ensures that the electromagnetic force has infinite range.

1.1.3 Quantum Chromodynamics

Quantum Chromodynamics is the gauge theory for strong interactions. It is based on the symmetry group $SU(3)_C$ of phase transformations on the quark colour fields. The quark colour charge, conventionally taken to be red, blue or green, was originally postulated to preserve the Pauli exclusion principle for states such as Ω^- and Δ^{++} which would otherwise be described by symmetric wave-functions. The colour quantum number has since been shown to accurately describe many other aspects of the strong interaction. Local gauge invariance of the non-Abelian $SU(3)_C$ results in the addition of eight massless vector fields[5], the *gluons*, which themselves carry the colour charge. The QCD Lagrangian is written in terms of the quark fields $q(x)$ and contains in addition the kinetic term for the gluon fields,

$$\mathcal{L}_{QCD} = -\sum_q \bar{q}(x)\gamma_\mu(\partial_\mu - igA^\alpha_\mu t_\alpha)q(x) - \sum_q m_q\bar{q}(x)q(x) - \frac{1}{4}F^\alpha_{\mu\nu}(x)F^{\mu\nu}_\alpha(x). \tag{1.10}$$

The new element with respect to the QED Lagrangian defined in equation 1.9 is the set of eight SU(3) 3×3 matrices t_α, numbered by the gluon index α = 1,...,8. They fulfill the SU(3) commutation relations

$$[t_\beta, t_\alpha] = iC^\alpha_{\beta\gamma}t_\alpha, \tag{1.11}$$

where $C^\alpha_{\beta\gamma}$ are the SU(3) algebra structure constants.

The gluon field tensors $F^\alpha_{\mu\nu}$ are defined as

$$F^\alpha_{\mu\nu} = \partial_\mu A_n u^\alpha - \partial_\nu A^\alpha_\mu + C^\alpha_{\beta\gamma}A^\beta_\mu A^\gamma_\nu. \tag{1.12}$$

The last term in equation 1.12 is responsible for gluon self-interactions, which accounts for both the asymptotic freedom of quarks and their confinement within colour singlet states. Gluon anti-screening of the quark colour charge causes the strong coupling constant α_S to decrease with decreasing distance, such that quarks behave as free particles at high momentum transfers. As a $q\bar{q}$ pair is separated α_S increases. Field lines stretch into a tube until the field gains sufficient energy to create a new $q\bar{q}$ pair; no finite amount of energy can liberate a single quark. This behaviour is in contrast to the running coupling constant of QED, the fine-structure constant α, which increases with

[5]The number of gauge bosons is equal to the number of generators, n, for the group, *i.e.* for the group SU(N), n=N^2 - 1.

increasing q^2 (the transferred momentum) due to the lack of self-interactions between photons.
By means of Deep Inelastic Scattering (DIS) experiments, it has been shown that the point-like quarks are the constituents of the nucleons, proton and neutron. Indeed it is possible to reconstruct and explain the properties of the nucleons from the quantum numbers of these constituents. For this purpose, two different types of quarks are needed, u and d. As the quarks and the nucleons both have spin $\frac{1}{2}$, the nucleons have to be made of at least three quarks: the proton has two u-quarks and one d-quark, while the neutron has two d-quarks and one u-quark. These three quarks determine the quantum numbers of the nucleons and are called "*valence quarks*". A "*sea*" of virtual quark-antiquark pairs, formed by u-d as well as the other quark flavours, is also present in the nucleon, but the contribution from charm and more massive quarks is heavily suppressed. Their effective quantum numbers average to zero such that they don't alter the quantum numbers of the nucleon. They are also visible in DIS interactions because of their electric charge, but they carry a smaller fraction of the nucleon momentum. Quarks inside the nucleon produce gluons by the process q→q+g. The sea quarks are produced by gluon splitting into $q\bar{q}$ pairs through the process $g \rightarrow q\bar{q}$. The fractional momentum of the nucleon carried by the valence quarks, sea quarks and gluons changes as the momentum transfer squared (q^2) of the probe is increased. As q^2 increases the fractional momenta carried by the sea quarks and gluons increase at the expense of the valence quarks. The distribution of the quarks and gluons in the nucleons is described by functions called Structure Functions or Parton Distribution Functions (PDFs). For a more complete treatment of this subject see [19].
The lepton doublets participating in the weak interaction are the doublets listed in Table 1.1. In the quark sector, the weak interaction quark doublets are a linear combination of the strong interaction mass eigenstates. This idea was first postulated by Cabibbo for *uds* quarks to accommodate both quark-lepton universality and the different decay rates of fully leptonic muon decay and strangeness changing and conserving hadronic decays. The principle has been extended to a second generation including charm using the GIM (Glashow, Iliopoulos and Maiani) mechanism in order to explain the absence of flavour-changing neutral currents and to a third generation incorporating $\begin{pmatrix} t \\ b' \end{pmatrix}$ to account for small CP-violating effects (where C refers to charge conjugation and P to parity). The 3×3 Cabibbo-Kobayashi-Maskawa (CKM)

matrix incorporates the mixing terms of this mechanism. It is expressed as

$$V_{CKM} = \begin{pmatrix} V_{ud} & V_{us} & V_{ub} \\ V_{cd} & V_{cs} & V_{cb} \\ V_{td} & V_{ts} & V_{tb} \end{pmatrix}. \tag{1.13}$$

Being unitary, it can be parametrised in terms of three angles and a single phase. Off-diagonal terms ($V_{i,j}, i \neq j$) describe flavour-changing charged currents. V_{ud} is the most accurately measured, whereas V_{cb} and V_{ub}, small but yet non-zero, are the most difficult to measure. The most accurate measurement of $|V_{cs}|$ to date has been made by LEP[6].

1.1.4 Electroweak Theory

The SM electroweak theory is based upon the symmetry group $\mathrm{SU(2)}_L \otimes \mathrm{U(1)}_Y$, which is a local symmetry of the electroweak Lagrangian. $\mathrm{SU(2)}_L$ is the isospin group which acts only on the left-handed fermions and $\mathrm{U(1)}_Y$ is the weak hypercharge group. Within the electroweak formalism the electromagnetic and weak interactions are unified, and the $\mathrm{U(1)}_Q$ symmetry group of section 1.1.2 appears as a subgroup of the total electroweak group

$$\mathrm{U(1)_Q} \subset \mathrm{SU(2)_L} \otimes \mathrm{U(1)_Y}. \tag{1.14}$$

The local gauge transformations of the electroweak theory are obtained by combining the local transformations for the U(1) and SU(2) groups, thus:

$$U = exp\{-i[\frac{g}{2}\sigma_i\theta_i(x) + \frac{g'}{2}Y\theta'(x)]\} \tag{1.15}$$

under which the doublet Ψ_L and the singlet Ψ_R transform,

$$\begin{aligned} \Psi'_L &= U\Psi_L \\ \Psi'_R &= U\Psi_R; \end{aligned} \tag{1.16}$$

here σ_i are the Pauli spin matrices and Y is the diagonal matrix of the weak hypercharges, y, of the particles being transformed. These are different for left- and right-handed components. Performing these local transformations and demanding gauge invariance generates interactions between the particles in the form of four vector fields. There are three fields identified with the $\mathrm{SU(2)}_L$ transformations—(W^1_μ,W^2_μ,W^3_μ)— and one field belonging to the

$U(1)_Y$ transformations-B_μ. The electroweak Lagrangian is as follows:

$$\begin{aligned}\mathcal{L}_{EW} &= i\bar{\Psi}\gamma_\mu\partial^\mu\Psi \\ &- \bar{\Psi}_L\gamma_\mu(\tfrac{g}{2}\sigma\cdot\mathbf{W}^\mu + \tfrac{g'}{2}Y_L\mathbf{I}B^\mu)\Psi_L \\ &- \bar{\Psi}_R\gamma_\mu\tfrac{g'}{2}Y_R B^\mu\Psi_R \\ &- -\tfrac{1}{4}\hat{\mathbf{W}}^{\mu\nu}\hat{\mathbf{W}}_{\mu\nu} - \tfrac{1}{4}\mathbf{B}^{\mu\nu}\mathbf{B}_{\mu\nu}.\end{aligned} \tag{1.17}$$

The U(1) gauge field, B_μ, couples to weak hypercharge with coupling g'. The triplet of gauge fields W^a_μ couple to weak isospin with coupling g. As in the case of QED in section 1.1.2, gauge invariance is preserved by ensuring that the fields are massless. The massless fields in the above Lagrangian can be combined to form the physical fields of the electroweak theory. The charged W bosons are formed from the $\mathbf{W}^\mu$ and couple to left-handed chirality states,

$$W^\pm_\mu = \frac{1}{\sqrt{2}}\left(W^1_\mu \mp W^2_\mu\right). \tag{1.18}$$

The Z^0 and photon couple to both left- and right-handed fermions and are formed from orthogonal linear combinations of the $\mathbf{W}$ and B fields,

$$\begin{aligned}Z_\mu &= \cos\theta_W W^3_\mu - \sin\theta_W B_\mu \\ A_\mu &= \sin\theta_W W^3_\mu + \cos\theta_W B_\mu,\end{aligned} \tag{1.19}$$

where θ_W is the Weinberg or weak mixing angle. It relates the couplings of the electromagnetic and weak interactions according to

$$g\sin\theta_W = g'\cos\theta_W = e. \tag{1.20}$$

As with QED the addition of a mass term of the form $\frac{1}{2}m^2V_\mu V^\mu$ for the bosonic field $V = W$ or B would break gauge invariance. It is also possible to express the coupling of the Z^0 boson to the fermions in terms of the two coupling constants g_V and g_A, which can be related to the coupling to left- and right-handed fermions:

$$\frac{g}{\cos\theta_W}\sum_{h=L,R}\bar{\Psi}_h\gamma_\mu\left(t_3 - Q\sin^2\theta_W\right)Z^\mu\Psi_h = \frac{g}{2\cos\theta_W}\sum_{h=L,R}\bar{\Psi}\gamma_\mu\left(g_V - g_A\gamma_5\right)Z^\mu\Psi. \tag{1.21}$$

Thus,

$$\begin{aligned}g_V &= t_3 - 2Q\sin^2\theta_W \\ g_A &= t_3,\end{aligned} \tag{1.22}$$

where t_3 is the third component of weak isospin for the left-handed field.

1.1.5 Electroweak Symmetry Breaking: The Higgs Mechanism

Electroweak theory predicts the existence of four gauge bosons γ, $W^{\pm}$ and Z^0. These are necessarily massless in order to preserve the local gauge invariance of the theory. However, it is known that the $W^{\pm}$ and Z^0 bosons of the weak interaction have mass.

The Higgs mechanism [20, 21, 22] provides a possible explanation of the origin of the masses through gauge invariant spontaneous symmetry breaking of the electroweak sector. It is an extension of the *Goldstone Theorem* which states that if a Lagrangian has a global symmetry which is not a symmetry of the vacuum (*i.e.* the ground state) then there must exist one massless boson, scalar or pseudoscalar, associated to each generator which does not annihilate the vacuum. These modes are known as the *Goldstone Bosons*.In the Higgs mechanism a weak isospin doublet of complex scalar fields $\phi^0(x)$ and $\phi^+(x)$ is introduced which must belong to the $SU(2)_L \otimes U(1)_Y$ multiplets:

$$\phi(x) = \begin{pmatrix} \phi^0(x) \\ \phi^+(x) \end{pmatrix} = \frac{1}{\sqrt{2}} \begin{pmatrix} \phi_1(x) + i\phi_2(x) \\ \phi_3(x) + i\phi_4(x) \end{pmatrix} \tag{1.23}$$

along with the scalar potential $V(\phi)$:

$$V(\phi) = \mu^2 \phi^\dagger \phi + \lambda(\phi^\dagger \phi)^2, \quad \lambda > 0. \tag{1.24}$$

This gives a contribution to the electroweak Lagrangian:

$$\mathcal{L}_{Higgs} = (\mathcal{D}_\mu \phi)^\dagger (\mathcal{D}^\mu \phi) - V(\phi) \tag{1.25}$$

where the covariant derivative $\mathcal{D}_\mu$ is defined as:

$$\mathcal{D}_\mu = \partial_\mu - ig\frac{\sigma}{2}W_\mu - ig'B_\mu. \tag{1.26}$$

The minimum of V corresponds to the ground state of the system or *vacuum* which is at $|\phi|$=0 for $\mu^2 > 0$, but for the choice $\mu^2 < 0$ the minimum shifts to

$$|\phi|^2 = -\frac{\mu^2}{2\lambda} = \frac{v^2}{2}, \tag{1.27}$$

where v is the vacuum expectation value. The solutions are now degenerate and any point satisfying the equation of a circle

$$|\phi|^2 = \phi^\dagger \phi = \frac{1}{2}(\phi_1^2 + \phi_2^2 + \phi_3^2 + \phi_4^2) = \frac{v^2}{2} \tag{1.28}$$

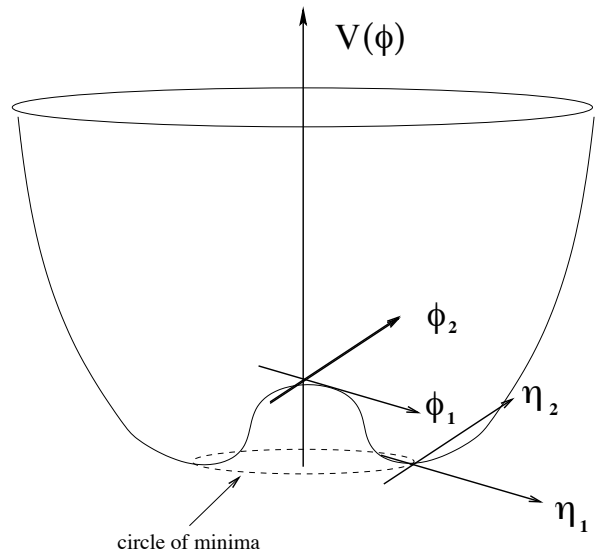

Figure 1.1: *The Higgs potential V for a complex scalar field with $\mu^2 < 0$ and $\lambda > 0$.*

is a ground state.
The perturbation procedure of Feynman calculus starts with fields which are fluctuations from the vacuum ground state. This leads to the definition of two new field variables η_1 and η_2, so that the potential is of the form in Figure 1.1. They have their origin at an arbitrarily chosen minimum

$$\begin{array}{ccc} |\langle 0|\phi|0\rangle| = \frac{1}{\sqrt{2}}\begin{pmatrix} 0 \\ v \end{pmatrix}, & \text{where} & \phi_2 = \phi_3 = \phi_4 = 0,\ \phi_1^2 = v^2, \\ \eta_1 = \phi_1 - v & \text{and} & \eta_2 = \phi_2. \end{array} \tag{1.29}$$

The symmetry of the Lagrangian becomes *hidden* by the choice of a particular minimum. The Lagrangian expressed in terms of the new fields reveals a massive scalar particle η_1 of mass $M_{\mathrm{H}} = \sqrt{2\lambda v^2}$, the Higgs boson H, and three massless Goldstone bosons ϕ_3, ϕ_4 and η_2. These unwanted Goldstone bosons can be removed by applying a unitary gauge transformation to $\phi(x)$ such that only the real Higgs field remains,

$$\phi(x) \to U\phi(x) = \frac{1}{\sqrt{2}}\begin{pmatrix} 0 \\ v + H(x) \end{pmatrix}. \tag{1.30}$$

In doing so, the three Goldstone bosons *disappear* from the theory: their corresponding degrees of freedom are *eaten* by the $\mathrm{W}^{\pm}$ and Z^0 fields which acquire mass and a third, longitudinal, polarisation state. By invoking the

Higgs mechanism, expanding the fields about the chosen vacuum ϕ_0 and *gauging away* the Goldstone bosons, the gauge boson masses are generated:

$$M_{\mathrm{W}} = \frac{gv}{2}; \qquad M_{\mathrm{Z}} = \frac{gv}{2\cos\theta_W}; \qquad M_\gamma = 0. \tag{1.31}$$

Eliminating gv gives a relation between $\mathrm{M_W}$ and $\mathrm{M_Z}$:

$$M_{\mathrm{W}} = M_{\mathrm{Z}}\cos\theta_W. \tag{1.32}$$

These equations are valid at the Born level and are modified by the inclusion of radiative corrections, such that

$$\rho = \frac{M_{\mathrm{W}}^2}{M_{\mathrm{Z}}^2\cos^2\theta_W} \neq 1. \tag{1.33}$$

The Fermion Masses

As well as coupling to the gauge fields $\mathbf{W}_\mu$ and B_μ the Higgs field couples to the fermion matter fields to generate their masses. The coupling of the Higgs field to a fermion pair is parametrised by an arbitrary Yukawa coupling constant $\lambda_f = m_f\sqrt{2}/v$, different for each fermion and proportional to its mass m_f. Lepton number conservation is assumed within the SM, giving a diagonal lepton mass matrix. The lack of quark generation number conservation in electroweak interactions means that the observed physical mass eigenstates of quarks are not eigenstates of weak isospin. The level of quark mixing is parametrised in terms of the Cabibbo-Kobayashi-Maskawa mixing matrix, introduced in section 1.1.3.

1.1.6 Renormalisability

Calculations within the SM have to be performed using perturbative expansions in terms of the strengths of the couplings. This is because loops of particles can be added to the process without altering the final state. These series are infinite and as such the individual terms of the loop can diverge making calculations impossible. The calculations can be made non-divergent in a theory which is renormalisable. The process of renormalisation relates the physical masses and charges of the calculable theory to experimentally unobservable "bare" masses and charges which absorb the divergences. It was shown by t'Hooft and Veltman[23, 24, 25] that any gauge theory, such as the SM, is renormalisable.

1.1.7 Inputs to the Standard Model

The Standard Model theory was developed over a period of years from both theoretical and empirical discoveries. The theory has predictive power, yet it still requires 18 empirically determined parameters. These are:

- α_S the strength of the coupling of strong interaction.
- g and g', the strength of the electromagnetic and weak couplings respectively.
- $\mathrm{M_H}$ the mass of the Higgs boson and v the vacuum expectation value of the Higgs potential.
- The Yukawa couplings, λ_f, of the nine massive fermions.
- The four parameters of the CKM matrix describing the quark mixing.

This large number of free parameters and their arbitrary values is one reason why it is thought that the Standard Model is not a final theory.

1.1.8 Tests of the Standard Model

The Standard Model as described is in very good agreement with current experimental observations. It has been verified by the discovery of particles that it has predicted, and by the comparison of direct measurements with indirect measurements obtained from fits to the SM. As an example, measurements of the weak mixing angle $\sin^2\theta_W$ have provided important tests of the SM. Initial measurements used $e\nu_\mu$ scattering, and more recently forward-backward and left-right scattering asymmetries A_{FB} and A_{LR} at e^+e^- colliders have improved the precision. The Z^0 boson parameters, namely its mass and width, have been very accurately measured by the LEP experiments[26] by determining the Z^0 resonance line-shape by scanning beam energies across the Z peak. The mass and width are then extracted by fitting a Breit-Wigner resonance to the line-shape accounting for radiative corrections. The error on the Z^0 mass is 2.1 MeV/c^2 and that on the width is 2.3 MeV, while the weak mixing angle has been measured to a precision of 1.7×10^{-4}[26].
Partial widths, defined as $\frac{\Gamma_{decay}}{\Gamma_{total}}$, are also interesting as they are sensitive to physics beyond the SM.

The top quark discovery at the Tevatron[27, 28] is a more recent example of a systematic search for, and discovery of, a particle predicted by the Standard Model. The measurement of its mass allows constraints on other SM parameters to be determined. No significant deviations from the SM predictions have yet been observed[6].

1.1.9 Beyond the Standard Model

The Standard Model depends on experimental input; there are no predictions for the 18 free parameters in the SM. Other unanswered questions include the presence of *three* generations of particles, the different treatment of left- and right-handed states in the electroweak model, the differences in energy dependence of the three coupling constants, the quantisation of charge and the conservation of lepton and baryon quantum numbers. Although only small deviations from the SM are allowed due to its impressive experimental verification, it is nevertheless still possible that the SM gauge group $SU(3)_C \otimes SU(2)_L \otimes U(1)_Y$ may be a subgroup of a larger grand unified gauge group. This would go some way towards answering the remaining questions and would predict the values of these parameters. In this case the SM becomes an *effective* field theory valid up to some physical cut-off scale Λ.
At very high energies the coupling constants may converge to a common value and a single unified field may be sufficient to explain elementary particle interactions. Predictions of these Grand Unified Theories (GUTs) involve transitions between quarks and leptons and lead to the possibility of proton decay, neutrino masses and oscillation, a baryon-antibaryon asymmetry in the early universe, and of course new particles. The difference between the scales at which the different symmetry breaking stages of the unified gauge group occur leads to divergences known as the *hierarchy problem.* This can be resolved in three types of model[13]: *compositeness,* where fundamental particle interactions are no longer point-like and the Higgs scalars are replaced by a fermion condensate; *Supersymmetry*(SUSY), where the divergences are cancelled with the introduction of additional particles, and *extra-dimensions.* An example of the first solution is *Technicolour*, which is an extension of QCD. However, it presents several generic problems not least

[6]There is a recent result from the NuTeV experiment which measured $\sin^2\theta_W$ from the Neutral Current to Charged Currents ratio in deep inelastic $\nu(\bar{\nu})$-nucleon scattering to be[29] $\sin^2\theta_W = 0.2277$, which is 3σ's apart from the SM value.

the reproduction of fermion masses and mixing, and deviations from the SM that are much larger than the present experimental accuracy. The SUSY model is favoured theoretically. Here, transformations between bosons and fermions can occur. Each SM particle has a supersymmetric partner with the same quantum numbers, but SUSY quarks and leptons have zero spin and gauginos (the SUSY partners of the gauge bosons) have half integer spin. The SM survives as a subset of supersymmetry. SUSY must be a broken symmetry, as no supersymmetric particles degenerate in mass with the SM partners have been observed in nature. The mass spectrum of SUSY particles depends on the nature of the symmetry breaking. Experimental searches for SUSY at hadron colliders are based primarily on missing energy signals from the lightest supersymmetric particle (LSP), which is weakly interacting and assumed stable in the majority of the models. As well as solving the hierarchy problem, local gauge invariance of the SUSY Lagrangian plays an important role in the unification with gravity.

A very different approach to solving the hierarchy problem is the existence of *extra spatial dimensions*; in this scenario, gravitational field lines would spread throughout the full higher dimensional space modifying the behaviour of gravity. The geometry of these extra spatial dimensions would be responsible for the hierarchy[30, 31].

Active searches for New Physics beyond the SM are currently underway at the Tevatron and have been presented at the most recent conferences[32, 33, 34, 35].

Chapter 2

Introduction

A measurement of $\sigma_{\mathrm{W}}^{\pm} \cdot Br(\mathrm{W}^{\pm} \to \mathrm{e}^{\pm}\nu)$, $\sigma_{\mathrm{Z}}^{0} \cdot Br(\mathrm{Z}^{0} \to \mathrm{e}^{+}\mathrm{e}^{-})$ and the ratio,

$$\mathrm{R} = \frac{\sigma_{\mathrm{W}^{\pm}} \cdot Br(\mathrm{W}^{\pm} \to \mathrm{e}^{\pm}\nu)}{\sigma_{\mathrm{Z}^{0}} \cdot Br(\mathrm{Z}^{0} \to \mathrm{e}^{+}\mathrm{e}^{-})}$$

precisely tests the W and Z^0 boson production cross-sections $\sigma_{\mathrm{Z}^0}, \sigma_{\mathrm{W}}$ as well as the total decay width of the W boson, $\Gamma(\mathrm{W})$, within the framework of the Standard Model of Particle Physics(SM). This analysis is sensitive to deviations of the branching ratio of $\Gamma(\mathrm{W})$ at the level of 7% using 72.0 pb^{-1} of data taken in 2002-2003 (Run IIA) by the Collider Detector at Fermilab (CDF).

2.1 W/Z production and decay

The production of vector bosons W and Z at hadron colliders, of the form $\mathrm{f_1 f_2} \to \mathrm{f_3 f_4}$, are shown at leading and higher orders in Figure 2.1. The matrix element for this process has the form[36]

$$\mathcal{M}_{fi} \propto j_{12}^{\mu}(P_{\mathrm{V}})_{\mu\nu} j_{34}^{\nu}, \tag{2.1}$$

with $j_{12}^{\mu} = \bar{\mathrm{f}}_2 \gamma^{\mu}(g_V - g_A\gamma^5) f_1$ and so on. Here g_A and g_V, are the vector- and axial-vector couplings defined in section 1.1.4. The vector-boson propagator P_{V} has the relativistic Breit-Wigner resonance form

$$P_{\mathrm{V}} \propto \frac{1}{\hat{s} - M_{\mathrm{V}}^2 + i\hat{s}\Gamma_{\mathrm{V}}/M_{\mathrm{V}}} \tag{2.2}$$

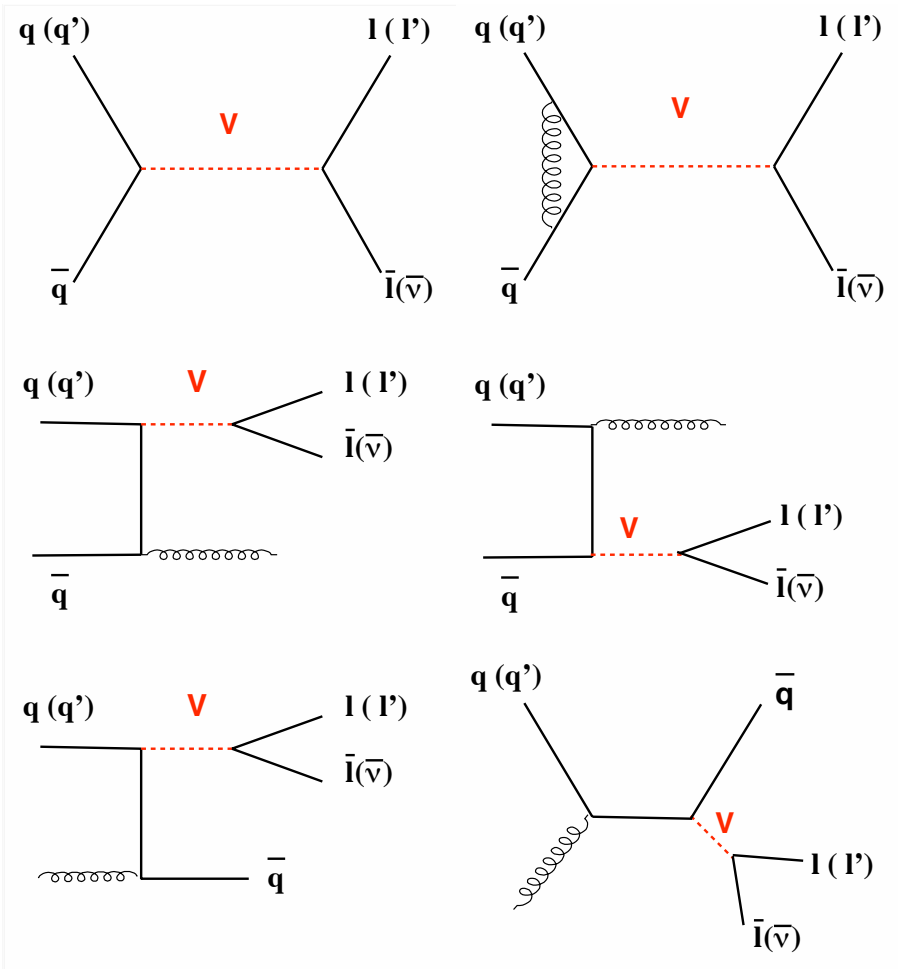

Figure 2.1: *Diagrams for production of a vector boson V = W,Z at Leading (upper left) and Next-To-Leading order(others).*

for V = W or Z, where $\hat{s}$ is the invariant mass squared of the incident q and $\bar{q}$. For the case of a neutral current interaction involving charged particles, both γ and Z exchange are possible, so there is a γ-Z interference term. This latter term has an energy dependence proportional to the difference $(\hat{s}-\mathrm{M}_\mathrm{Z}^2)$, and so changes sign in going from below to above the Z pole. In the case of hadron colliders, the cross section $\sigma(\mathrm{q}_1 + \bar{\mathrm{q}}_2 \to \mathrm{V} + \mathrm{X})$ for a vector boson V = W,Z is given by

$$\sigma_\mathrm{V}(\hat{s}) = \frac{\pi|\mathcal{M}_{12}|^2}{4M_\mathrm{V}^2}\delta(\hat{s} - M_\mathrm{V}^2), \tag{2.3}$$

where the zero-width approximation has been used. In the above formula $\hat{s} = x_1 x_2 s$, where $x_{1,2}$ are the momentum fractions of the proton and antiproton carried by the quarks and s is the centre-of-mass energy squared. Substituting the value of the matrix element $|\mathcal{M}_{12}|^2 = g^2 M_{\mathrm{V}}^2$, eq. 2.3 becomes

$$\hat{\sigma}_{\mathrm{V}}(x_1, x_2) = \frac{\pi g^2}{4}\delta(x_1 x_2 s - M_{\mathrm{V}}^2) = \sqrt{2}\pi G_F M_{\mathrm{V}}^2 \delta(x_1 x_2 s - M_{\mathrm{V}}^2), \qquad (2.4)$$

where the expression $\frac{G_F}{\sqrt{2}} = \frac{g^2}{8M_{\mathrm{W}}^2}$ valid at low energies ($q^2 \ll M_{\mathrm{W}}^2$) has been used. The total cross section involves the convolution of the parton cross sections integrated over the q and $\bar{\mathrm{q}}$ density functions. This formula only describes the momentum spectra in the longitudinal direction (*i.e.* the direction of the incident beams); gluon radiation also produces significant momenta in the transverse direction, much greater than the intrinsic transverse momenta of the quarks. A further complication in the estimate of the W and Z cross-sections is caused by higher order QCD effects; for a discussion see [13].
The decay vertex involving a vector boson and a fermion-antifermion pair can be classified as *charged* or *neutral* currents, depending on the nature of the boson.
Charged current interactions involve the $\mathrm{W}^{\pm}$ bosons, and the interaction Lagrangian for the $\mathrm{W}\mathrm{f}\bar{\mathrm{f}}'$ vertex has the form

$$\mathcal{L}_{CC} = -\frac{g}{2\sqrt{2}} W_{\mu}^{-} j_{CC}^{\mu}, \qquad (2.5)$$

with

$$j_{CC}^{\mu} = V_{ij}\bar{\mathrm{f}}'\gamma^{\mu}(1-\gamma^5)\mathrm{f}, \qquad (2.6)$$

where V_{ij}=1 for $(\mathrm{f},\bar{\mathrm{f}}') = (\ell^-, \bar{\nu}_\ell)$ for leptons and $V_{ij} = V_{\mathrm{q}\bar{\mathrm{q}}}$ for quarks $(\mathrm{q}_{\frac{1}{3}}, \bar{\mathrm{q}}_{\frac{2}{3}})$. Here $V_{\mathrm{q}\bar{\mathrm{q}}}$ are the CKM matrix elements described in section 1.1.3, $\mathrm{q}_{\frac{1}{3}} = (\mathrm{d,s,b})$ and $\mathrm{q}_{\frac{2}{3}} = (\mathrm{u,c,t})$. This form corresponds to the pure left-handed coupling of the W to fermions.
The *neutral current* Lagrangian for the $\mathrm{Z}\mathrm{f}\bar{\mathrm{f}}$ vertex can be written as

$$\mathcal{L}_{NC}^{Z} = -\frac{g}{2\cos\theta_W} Z_{\mu} j_{NC}^{\mu}, \qquad (2.7)$$

with

$$j_{NC}^{\mu} = \bar{\mathrm{f}}\gamma^{\mu}(g_V - g_A\gamma^5)\mathrm{f}. \qquad (2.8)$$

The photon-fermion coupling for a fermion of charge q_f has the form

$$\mathcal{L}_{NC}^{\gamma} = -e q_f A_{\mu} j_{\gamma}^{\mu}, \qquad (2.9)$$

with

$$j_\gamma^\mu = \bar{\mathrm{f}}\gamma^\mu \mathrm{f}, \tag{2.10}$$

that is, the left- and right-handed couplings are equal, and there is only a vector term. For the case of polarised fermions, the left and right-handed fermion components, *i.e.* $(1-\gamma^5)$ and $(1+\gamma^5)$, are used.
More details and specific Born-level calculations in the SM can be found in [13].

2.1.1 Theory

In 1933 Fermi[37, 38] proposed a new ("weak") force to explain nuclear β-decay, and in 1938 Klein[39] proposed the existence of a massive force carrier, the W, to explain the weak force's short range. The massive $W^\pm$ and Z^0 particles are the intermediate vector bosons which carry this weak force. Together with the massless photon (γ), they compose the bosonic fields of the unified electroweak theory proposed by Weinberg[40], Salam[41], and Glashow[42] as discussed in the previous chapter.
The $W^\pm$ and Z^0 bosons were discovered in 1983 in the UA1 and UA2 detectors which were designed and built for this very purpose. The use of the transverse momentum (p_T) distribution in the leptonic ($\ell\bar{\nu}_\ell$) decay channel was used to determine the W mass, while the Z^0 boson mass was determined using again the leptonic channel ($\ell^+\ell^-$), but by directly reconstructing the invariant mass distribution of the lepton pair decay products.
Present experimental measurements of electroweak parameters such as the masses and decay widths of the vector bosons are precise enough to provide tests of Quantum Chromodynamics and of the Electroweak part of the Standard Model beyond just the leading order. These precise measurements not only test the electroweak theory, but also provide possible windows to sectors of the theory at mass scales higher than those directly observable at current accelerator energies. These sectors enter into the electroweak observables through radiative corrections. While the parameters of the Z^0 boson have been well-studied, the properties of the charged current carrier, the W, are known with less precision. In hadron-hadron collisions the W and Z^0 are predominantly produced via the processes illustrated in Figure 2.1[1]: that is, a quark in one hadron annihilates with an antiquark in the other hadron to

[1] In the case of Z/γ^* this process is called Drell-Yan[43].

Decay mode of W^+	Partial decay width in units of $\Gamma(\mathrm{W}^\pm \to \mathrm{e}^\pm\nu)$
$\mathrm{e}^+ + \nu_e$	1
$\mu^+ + \nu_\mu$	1
$\tau^+ + \nu_\tau$	1
$\mathrm{u\bar{d}}$	$3(1+\alpha_s/\pi)\cos^2\theta_c$
$\mathrm{u\bar{s}}$	$3(1+\alpha_s/\pi)\sin^2\theta_c$
$\mathrm{c\bar{s}}$	$3(1+\alpha_s/\pi)\cos^2\theta_c$
$\mathrm{c\bar{d}}$	$3(1+\alpha_s/\pi)\sin^2\theta_c$

Table 2.1: *Known decay modes of the W^+, and decay rate relative to $e^\pm\nu$ to lowest order in the SM and $O(\alpha_s)$ in QCD[8]. All the quark decay channels except* $\mathrm{u\bar{d}}$ *and* $\mathrm{c\bar{s}}$ *are strongly Cabibbo suppressed, as can be seen from the $sin^2\theta_c$ ~0.05 dependence. Decays to* $\mathrm{u\bar{b}}$ *and* $\mathrm{c\bar{b}}$ *are further suppressed and thus negligible.*

produce a vector boson. Measurements of the W boson mass, for example, by the CDF[44] and D0[45] collaborations have yielded[2]

$$\begin{aligned} M_\mathrm{W} &= 80.456 \pm 0.059\,\mathrm{GeV} \\ \Gamma(\mathrm{W}) &= 2.115 \pm 0.105\,\mathrm{GeV}. \end{aligned} \tag{2.11}$$

The most recently reported combined measurements from LEP are[26]:

$$\begin{aligned} M_\mathrm{W} &= 80.412 \pm 0.042\,\mathrm{GeV} \\ \Gamma(\mathrm{W}) &= 2.150 \pm 0.091\,\mathrm{GeV}. \end{aligned} \tag{2.12}$$

This thesis presents both the measurement of the ratio of the cross-sections, as defined in the introduction of this chapter, and the extraction of the decay width of the W boson, $\Gamma(\mathrm{W})$. The W decays with universal coupling to pairs of fermions within weak isodoublets. The decay modes of the W^+ are listed in Table 2.1 (the W^- decays to charged conjugate pairs), along with the decay rates to lowest order in the electroweak theory and to order $\mathrm{O}(\alpha_s)$ in QCD[8]. The experimental values are listed in Table 2.2 for both W and Z. The partial width into fermion pairs is calculated to be[8]

$$\Gamma_0(\mathrm{W} \to \mathrm{f\bar{f}'}) = |V_{\mathrm{ff'}}|^2 N_C g^2 M_\mathrm{W}/48\pi, \tag{2.13}$$

where

[2]This is the combined measurement from the two papers, which has recently been submitted to the PRD[46].

Decay mode	Partial decay width (GeV)		Branching ratio	
W				
$e^+\nu_e$	$0.227 = 0.006$	0.678 ± 0.011	$(10.72 \pm 0.16)\%$	32.3 ± 0.4 %
$\mu^+\nu_\mu$	$0.224 = 0.006$		$(10.57 \pm 0.22)\%$	
$\tau^-\nu_\tau$	$0.227 = 0.007$		$(10.74 \pm 0.27)\%$	
hadrons	1.439 ± 0.007		$(67.96 \pm 0.35)\%$	
$\pi^+\gamma$	0		$< 8 \times 10^{-5}$ 95% CL	
Total	2.118 ± 0.042			
Z^0				
e^+e^-	0.0839 ± 0.0001	0.2520 ± 0.0003	$(3.363 \pm 0.004)\%$	$10.09 \pm 0.11\%$
$\mu^-\mu^-$	0.0839 ± 0.0002		$(3.366 \pm 0.007)\%$	
$\tau^-\tau^-$	0.0841 ± 0.0002		$(3.370 \pm 0.008)\%$	
invisible	0.499 ± 0.002		$(20.00 \pm 0.06)\%$	
hadrons	1.744 ± 0.002		$(69.91 \pm 0.06)\%$	
Total	2.4952 ± 0.0023			

Table 2.2: *Measured partial decay width and branching ratios for the W and Z bosons from the Review of Particle Physics(2002)[6].*

- $V_{ff'}$ is the Cabibbo-Kobayashi-Maskawa (CKM) matrix element for two quarks and is 1.0 for leptons;
- M_W is the W boson mass;
- g is the W's coupling to fermions; in the SM it is given by $g^2 = \frac{8}{\sqrt{2}} G_F M_W^2$, where G_F is the Fermi coupling constant derived from the muon lifetime;
- N_C is the colour factor, which is 3 for quarks and 1 for leptons.

The partial widths for decays into quarks receive an additional QCD correction due to vertex graphs involving gluon exchange; implementing these corrections N_C can be expressed as

$$N_C = 3\left\{1 + \alpha_s(M_V)/\pi + 1.409(\alpha_s(M_V)/\pi)^2 - 12.77(\alpha_s(M_V)/\pi)^3\right\}, \quad (2.14)$$

where $\alpha_s(M_V)$ is the strong coupling constant evaluated at the vector boson mass. Using this expression the width to leading order in QCD has been calculated to be[6]:

$$\begin{aligned} \Gamma_0(W) &= \{3 + 6(1 + \alpha_s(M_W)/\pi + 1.409(\alpha_s(M_W)/\pi)^2 \\ &\quad -12.77(\alpha_s(M_W)/\pi)^3)\}^{-1} \cdot \Gamma_0(W^\pm \to e^\pm\nu\ ) \\ &= 2.0921 \pm 0.0025\,\text{GeV} \end{aligned} \quad (2.15)$$

and

$$\Gamma_0(\mathrm{W}^{\pm} \to \mathrm{e}^{\pm}\nu\ ) = \frac{G_F M_{\mathrm{W}}^3}{6\sqrt{2}\pi} \approx 226.4 \pm 0.3\,\mathrm{MeV}. \tag{2.16}$$

The W width also receives electroweak corrections due to next-to-leading order graphs which alter the effective coupling g at the W-fermion vertex for all fermions. Within the context of the Standard Model the W width receives vertex and bremsstrahlung corrections[8] that depend upon the top quark and Higgs boson masses. The corrections can be summarised in the equation

$$\Gamma(\mathrm{W} \to \mathrm{f}\bar{\mathrm{f}'})_{SM} = \Gamma_0(\mathrm{W} \to \mathrm{f}\bar{\mathrm{f}'})[1 + \delta_V + \delta_W(0) + \delta_\mu], \tag{2.17}$$

where

- $\delta_W(0)$ is the correction to the width from loops at the W-fermion vertex involving Z^0's or a Standard Model Higgs boson;
- δ_V describes the boson self-energies, and
- δ_μ is a correction made necessary when g is parametrized using the W mass and the value of G_F from muon decay[47, 48].

Since all the corrections are small ($\sim$ -0.35%), the measurement of Γ(W) is not very sensitive to higher order electroweak corrections.

A measurement of the ratio is sensitive to all the corrections listed above and to any new physics process that either changes the W and/or the Z^0 production cross-sections or the $\mathrm{W}^{\pm} \to \mathrm{e}^{\pm}\nu$ branching ratio. The $\mathrm{W}^{\pm} \to \mathrm{e}^{\pm}\nu$ branching ratio could be directly affected by new decay modes of the W boson, such as Supersymmetric decays that do not similarly couple to the Z^0 boson. Any new resonance at a higher mass scale that decays to W or Z^0 bosons would directly change the production cross-sections. One example of a higher mass particle that has been observed is the top quark at $\mathrm{m_t}$ = 174.3±5.1 GeV/c^2, which decays to a W boson and a bottom quark[6]. In $\mathrm{p\bar{p}}$ collisions at $\sqrt{s} = 1.8$ TeV the production cross-section for $\mathrm{t\bar{t}}$ pairs is $6.5^{+1.7}_{-1.4}$ pb[27], about 3000 times smaller than the direct W boson production[49]. The decay of top quarks (where there are two W bosons per event because a $\mathrm{t\bar{t}}$ pair is produced) should change the measured value of R by about 0.07%, which is well below our sensitivity.

2.2 Measurement of $\Gamma(\mathrm{W})$ from the W and Z cross-sections

The width of the W boson may be extracted from the measurement of the ratio, R, of the cross-sections times branching ratios into electrons of the W and the Z^0, $\sigma_{\mathrm{W}} \cdot Br(\mathrm{W} \to \mathrm{e}\nu)$ and $\sigma_{\mathrm{Z}} \cdot Br(\mathrm{Z}^0 \to \mathrm{ee})$, in proton-antiproton collisions. This method was first proposed by Cabibbo in 1983 as a method to determine the number of light neutrino families[50] and has grown into a method to indirectly measure the branching ratio of $\mathrm{W}^{\pm} \to \mathrm{e}^{\pm}\nu$. Theoretically, R may be expressed as:

$$\mathrm{R} = \frac{\sigma_{\mathrm{W}} \cdot Br(\mathrm{W} \to \mathrm{e}\nu)}{\sigma_{\mathrm{Z}} \cdot Br(\mathrm{Z}^0 \to \mathrm{ee})} = \frac{\sigma_{\mathrm{W}}}{\sigma_{\mathrm{Z}}} \frac{\Gamma(\mathrm{W} \to \mathrm{e}\nu)}{\Gamma(\mathrm{Z}^0 \to \mathrm{ee})} \frac{\Gamma(\mathrm{Z}^0)}{\Gamma(\mathrm{W})}. \tag{2.18}$$

On the right hand side, the ratio of the W and Z^0 production cross-sections may be calculated from the boson couplings and knowledge of the proton structure. The Z^0 total width, $\Gamma(\mathrm{Z}^0)$, and the leptonic partial width, $\Gamma(\mathrm{Z}^0 \to \mathrm{ee})$, are well measured by the LEP experiments[26].
Thus, from eq. 2.18 using the measured value of R it is possible to measure the branching ratio $\mathrm{Br}(\mathrm{W}^{\pm} \to \mathrm{e}^{\pm}\nu) = \frac{\Gamma(\mathrm{W}^{\pm} \to \mathrm{e}^{\pm}\nu)}{\Gamma(\mathrm{W})}$. Substituting the Standard Model prediction of the partial width $\mathrm{W} \to \mathrm{e}\nu$, it is possible to extract the total width, $\Gamma(\mathrm{W})$, of the W boson. By using the same identification criteria for an electron in $\mathrm{W}^{\pm} \to \mathrm{e}^{\pm}\nu$ and $\mathrm{Z}^0 \to \mathrm{e}^+\mathrm{e}^-$ events, many of the systematic uncertainties associated with the cross-section can be either reduced or eliminated. The uncertainties due to the luminosity delivered to CDF and the overall event acceptance due to the location of the $\mathrm{p}\bar{\mathrm{p}}$ interaction point cancel in R because it is the ratio of the cross-sections. Systematic uncertainties due to the efficiency for identifying an electron, for triggering an event with an electron and uncertainties in the acceptance are reduced or eliminated because the same selection criteria are placed on one electron for both $\mathrm{W}^{\pm} \to \mathrm{e}^{\pm}\nu$ and $\mathrm{Z}^0 \to \mathrm{e}^+\mathrm{e}^-$ boson events.

2.3 Previous results

Direct evidence for $\mathrm{W}^{\pm}$ and Z^0 production have been first obtained by the UA1 and UA2 experiments in $\mathrm{p}\bar{\mathrm{p}}$ collisions at the CERN $\mathrm{Sp}\bar{\mathrm{p}}\mathrm{S}$ collider with a centre-of-mass energy of 0.56 TeV. Later, at $\sqrt{s} = 0.63$ TeV, these collab-

orations performed the first estimate of the production cross-sections times branching ratios in the electron[51] and muon[52] channels. These results were used in the measurement of R and the extraction of the total W width. A summary of the values of the cross-sections, R and the W width is given in Table 2.3, together with the more recent measurement from the Tevatron (CDF[9, 10] and D0[53, 54] Run I results) at $\sqrt{s} = 1.8$ TeV. The most recent

Experiment	mode	σ_W**Br**($W^+ \to e^-\nu$) (nb)	σ_Z**Br**($Z^0 \to e^+e^-$) (pb)	R	Γ(W)
UA1[51]	e	0.609±103	58.6±11.5	10.4±2.0	
UA1[51]	e+μ			$9.5^{+1.1}_{1.0}$	2.18±0.26
UA2[52]	e	0.660±40	70.4±6.8	9.38±0.86	2.30±0.20
CDF[9, 10]	e	2.49±0.12	231±12	10.94±0.45	2.064±0.084
D0(Run 1A)[53]	e	2.36±0.15	218±16		
D0(Run 1A)[53]	e+μ			10.9±0.49	2.044±0.093
D0(Run 1B)[54]	e	2.31±0.11	221±11	10.43±0.27	2.17±0.07

Table 2.3: *Measurements of the W and Z^0 production cross-sections times branching ratios from previous collider experiments, the corresponding value of R and the extracted value of* Γ(W).

direct measurement of Γ(W) obtained by LEP is 2.150 ± 0.091 GeV[55].

2.4 Strategy of this measurement

The signature of high p_T electrons from $W^\pm$ and Z^0 decay is a quite distinctive signature in the environment of hadron collisions. As such, the decay of $W^\pm$ and Z^0 bosons into electrons provides a clean experimental measurement of their production. Experimentally, the cross-sections times branching ratios are extracted from:

$$\sigma_W \cdot Br(W^\pm \to e^\pm\nu) = \frac{N_W^{candidates} - N_W^{background}}{A_W \cdot \epsilon^e_{trig} \cdot \epsilon_{zvertex} \cdot \epsilon_W \cdot \int Ldt}$$

$$\sigma_Z \cdot Br(Z^0 \to e^+e^-) = \frac{N_Z^{candidates} - N_Z^{background}}{A_Z \cdot \epsilon^{ee}_{trig} \cdot \epsilon_{zvertex} \cdot \epsilon_Z \cdot \int Ldt}$$

where

- $N_W^{candidates}, N_Z^{candidates}$ are the numbers of $W^\pm$ and Z^0 candidates observed in the data;
- $N_W^{background}, N_Z^{background}$ are the numbers of expected background events in the $W^\pm$ and Z^0 candidate sample;

- A_W, A_Z are the acceptances for the $W^{\pm}$ and Z^0 decays, which include the efficiency for the kinematic cuts on the leptons and the geometric acceptance of the detector;
- $\epsilon^{e}_{trig}, \epsilon^{ee}_{trig}$ are the efficiencies of the trigger selecting one or two electrons;
- $\epsilon_{zvertex}$ is the efficiency of the cut on the primary vertex of the event;
- ϵ_W, ϵ_Z are the efficiencies for the $W^{\pm}$ and Z^0 to pass the lepton identification criteria, and
- $\int Ldt$ is the integrated luminosity of the experiment.

In measuring the ratio of the cross-sections some of the quantities above, together with their errors, will cancel. The strategy of this measurement will be to select $W^{\pm}$ and Z^0 decay events with one or both electrons falling into the central region of the CDF detector. Since CDF is a cylindrical detector with calorimetry and tracking system in the central region, and only calorimetry in the forward, electron identification is more difficult in the latter region. Choosing the same selection criteria (which appear in the factors ϵ_W and ϵ_Z) for the electron common to $W^{\pm}$ and Z^0 events has the great advantage of decreasing the systematic uncertainties in the measurement of the ratio, as they almost completely cancel in its computation. These smaller errors offset the expected increase in statistical error from requiring the presence of a common central electron.

2.5 Outline of the thesis

This thesis is organized as follows: in Chapter 3 the accelerator and CDF detector are described, with particular attention to the CDF subdetectors essential in the identification of electrons and neutrinos; Chapter 4 describes the Monte Carlo and data samples used in this analysis and the creation of the $W^{\pm}$ and Z^0 candidates samples, which are discussed in more detail in Chapter 5 and Chapter 6 (respectively); here studies of the background from QCD and processes such as $W^{\pm} \to \tau^{\pm}\nu$ and $Z^0/\gamma^* \to \tau^+\tau^-$ are also presented. The efficiency for the triggers used and the efficiency of the electron selection are reported in Chapter 7. In Chapter 8 the calculation of the acceptances is presented, together with the estimate of the systematic

uncertainty associated with it. Finally, the extraction of the cross-sections and the ratio is performed in Chapter 9.

Chapter 3

The Experimental Apparatus

The detector used in this analysis is the Collider Detector at Fermilab (CDF) located at the Fermi National Accelerator Laboratory (Fermilab), in Batavia, Illinois (USA). CDF uses the proton-antiproton collisions generated at the Tevatron Accelerator complex, whose schematic view is shown in Figure 3.1. Until the Large Hadron Collider is completed at CERN, the Tevatron is

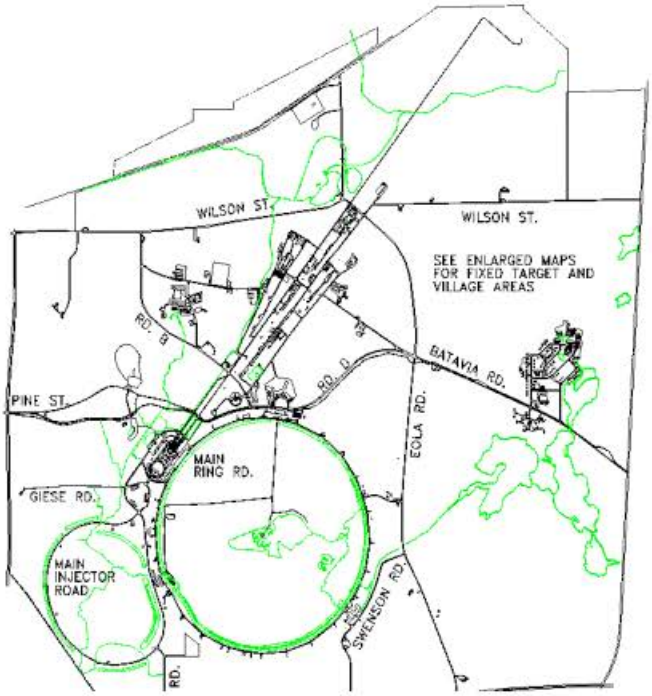

Figure 3.1: *Overview of the Tevatron accelerator chain at Fermilab.*

the highest energy collider in the world. In this chapter the Tevatron and CDF are described in their components and functions, and their recent and previous performances are illustrated[1].

3.1 The Accelerator Chain

The Tevatron is a circular accelerator of about 1 km of radius which collides bunches of protons and antiprotons accelerated in opposite directions with a total *centre-of-mass energy* of 1.96 TeV. This quantity, commonly represented with the symbol $\sqrt{s}$ in the literature, represents the total energy available in the centre of mass of the two colliding particles. For a collider such as the Tevatron the total centre of mass energy, and thus the energy available for the production of new particles, is $\sqrt{s} = E_1 + E_2$, where E_1 and E_2 are the energies of the two colliding particles[2]. By contrast, for a fixed target experiment, the available centre of mass energy is $\sqrt{s} \simeq \sqrt{2E_1 m_2}$ for a projectile of energy E_1 incident upon a target at rest of mass m_2. The centre of mass energy $\sqrt{s}$ is a key parameter in collider experiments, as the cross-sections of the different processes, as well as the masses of known and possibly unknown particles which can be created, depend upon its value. The other essential parameter in collider experiments is the *luminosity* which determines the maximum size of the sample which can be collected during a defined functioning period of the machine (commonly called a "Run"). The number of events N collected for a process of cross-section σ and generated in a time interval ΔT is given by the relation

$$N = \sigma \int_{\Delta T} L dt = \sigma \mathcal{L}. \tag{3.1}$$

The quantity $\mathcal{L}$ is called the "integrated luminosity" and is usually defined for all the period of data collection of the experiment, as opposed to the "instantaneous luminosity" L, which is the luminosity at a specific time. In practice, in proton-antiproton collisions L is determined by measuring the number of inelastic proton-antiproton interactions per second. The units are[3]

[1] Most of the information in this chapter is taken from [56] and [57].

[2] This expression is valid only if $E_1 = E_2$; otherwise the formula $\sqrt{s} = 2\sqrt{E_1 + E_2}$ holds.

[3] As in the following most of the cross-sections and luminosities will be given in sub-multiples of barns (b), where 1 b = 10^{-28} m^2 = 10^{-24} cm^2.

$[L] = [\text{cm}^{-2}\text{s}^{-1}]$ and $[\mathcal{L}] = [\text{cm}^{-2}]$. The goal of colliding beam experiments is to keep the luminosity as high as possible, compatible with the technical capabilities of the analysing experiments. As the luminosity increases, the events become more complicated due to the production of multiple events at the same bunch crossing, and thus more difficult to analyse. The total integrated luminosity included the period used in this analysis is shown in Figure 3.2; here the luminosity is given in units of pb^{-1} from the definition

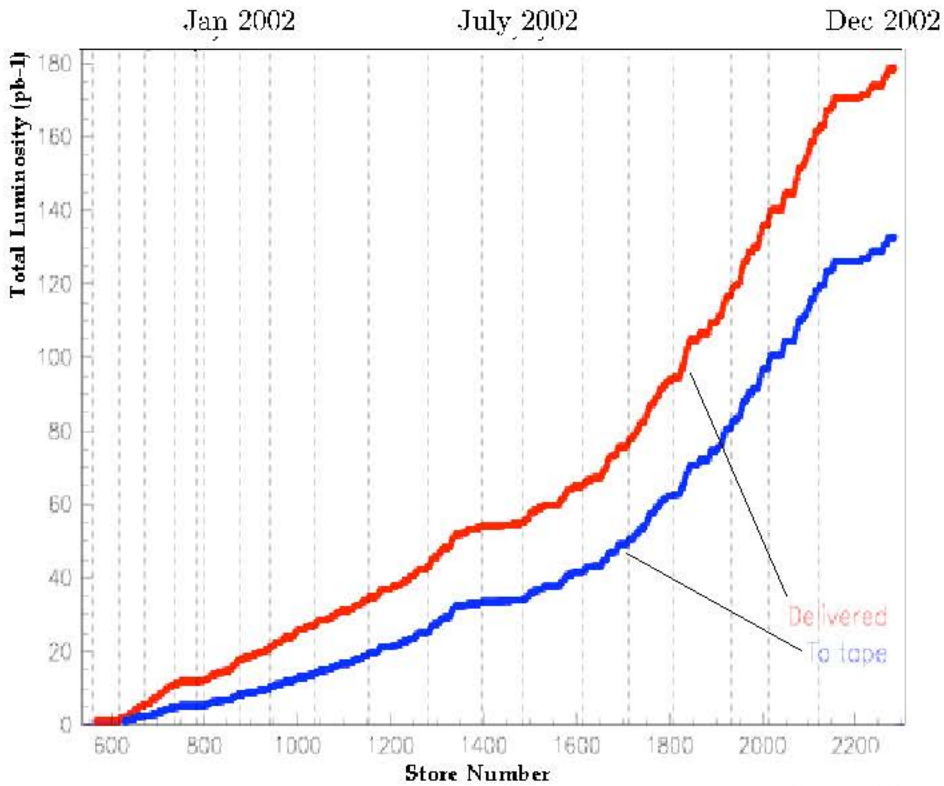

Figure 3.2: *Total integrated luminosity delivered by the accelerator and recorded by CDF in the period from July 2001 until January 2003. The upper curve represents the luminosity delivered to the experiment by the Tevatron, while the lower one is the luminosity effectively recorded on tape by CDF.*

in the formula 3.1, where σ is in pb.

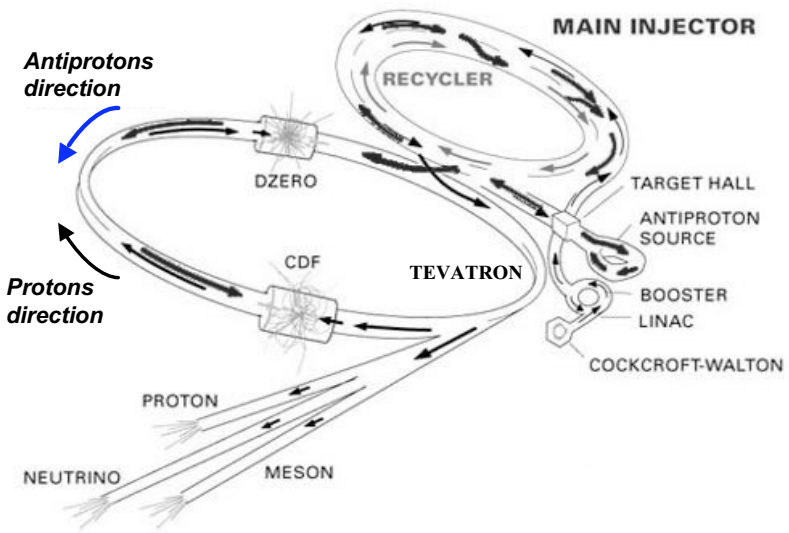

Figure 3.3: *The accelerators involved in the proton-antiproton collisions at the Tevatron. The Debuncher and the Accumulator are indicated with the label "ANTIPROTON SOURCE" in the figure.*

In 1996, after a ten year period of data taking (called "Run I", divided in Run Ia and Ib), the Tevatron was closed to undergo technical upgrades to improve both the centre of mass energy, which has been increased from 1.8 to 1.96 TeV, and the delivered luminosity for the new period of data taking called "Run II". Some parameters in Run I and Run II are compared in Table 3.1. The values in the rightmost column indicate the performance ex-

Run	**Run Ib**	**RunII (present*)**	**Run II (future)**
bunches of p × bunches of $\bar{p}$	6×6	36×36	140×121
p/bunch	$2.3{\cdot}10^{11}$	$2.1{\cdot}10^{11}$	$2.7{\cdot}10^{11}$
$\bar{p}$/bunch	$5.5{\cdot}10^{10}$	$2.5{\cdot}10^{10}$	$3.0{\cdot}10^{10}$
total number of $\bar{p}$	$3.3{\cdot}10^{11}$	$9.0{\cdot}10^{11}$	$3.6{\cdot}10^{12}$
Energy (p+$\bar{p}$) (GeV)	900+900	980+980	980+980
L (cm^{-2}s^{-1})	$1.6{\cdot}10^{30}$	$4.1{\cdot}10^{31}$	$1.6{\cdot}10^{32}$
Bunch spacing(ns)	~3500	396	132
Number of interactions per collision	2.5	2.3	1.3

*The values refer to the second best simultaneous performance. The best individual parameters are higher[58].

Table 3.1: *Parameters characteristic of different Runs at the Tevatron. The leftmost column shows the operational performance of Run Ib, terminated in 1996; the middle column shows the current parameters of Run II, whilst the rightmost column is the performance that the Tevatron would have if there were 121 antiproton bunches in a 132 ns bunch spacing, instead of the 36 used at the moment. The scenario with 132 ns bunch spacing is still under development at the time of this writing.*

pected for a scenario where the parameters of the bunches remain the same, but filling 121 antiproton bunches at a 132 ns bunch spacing instead of the 36 (in 396 ns) that are used at the moment. During the period of data used for this analysis the accelerator was operating in a 396 ns mode, as the 132 ns mode is currently under development[4].
The achievement of such results has been possible thanks to the combined improvements of several accelerator systems, which are described in the following sections. A diagram of the Tevatron components is shown in Figure 3.3.

3.1.1 Production of Protons and the Booster

The first stage of the accelerator is the **Cockroft-Walton preaccelerator** which produces the protons. Hydrogen gas is ionised to generate negative

[4]According to the latest news at the time of this writing, there is a serious chance that the 132 ns scenario will never be implemented.

ions, consisting of two electrons and one proton, which are subsequently accelerated through a positive voltage to reach an energy of 750 keV, from the initial 25 keV. In the second step these ions enter a linear accelerator (the **LINAC**, in Figure 3.3) about 150 m long, where they are accelerated by oscillating electric fields to 400 MeV. At the end of the LINAC tunnel the ions are passed through a carbon foil and through interactions they lose the two electrons, giving a pure beam of protons. In the third stage the proton beam is injected into the **BOOSTER**, a proton synchrotron of 75 m radius located about 6 m below ground. Here the protons are circulated until they acquire 8 GeV, before being collected in bunches of $6 \cdot 10^{10}$ particles each for use in the Tevatron, (or $5 \cdot 10^{12}$ for protons used for the production of antiprotons).

3.1.2 The Main Injector

Finally protons are sent to the **Main Injector**, where a further acceleration takes place, increasing the energy of the protons from 8 to 150 GeV, before they are sent into the adjacent Tevatron. The main injector, which is a synchrotron of 3 km in circumference, has been built with the main purpose of reducing the inefficiency of the antiproton production and use, found in Run I. In Run II the antiprotons are produced by randomly selecting protons from the Main Injector which have reached 120 GeV in energy, and sending them towards a target of nickel. Among the wide range of collision products the antiprotons (which are diffused with an average momentum of about 8 GeV) are selected and focused through lithium lenses and a dedicated magnetic field. Subsequently they enter the **Debuncher**, an accumulator ring that decreases the momentum distribution of the bunches through the "stochastic cooling" technique. At the same time this increases their spatial distribution, producing a continuous beam. At this point the antiprotons are sent to the **Accumulator** where they are further cooled and stacked in bunches. They are then accelerated to 150 GeV, together with the protons, and sent to the Tevatron for the final acceleration and collision. With the use of the Main Injector the number of available antiprotons at the beginning of a new "store"[5] has increased by a factor of ten with respect to Run I. Thanks to the construction of the **Recycler Ring**, which shares the same tunnel as

[5] The period from which the beams enter in the Main Injector ring until they collide in the Tevatron.

the Main Injector, the antiprotons which are not utilized in the Tevatron at the end of the store (which correspond to about 75% of the original quantity) will not be dumped but collected and undergo the same procedures as before until they will be stacked in bunches of appropriate density and they will be ready to be sent to the Main Injector and to the Tevatron again. This recycling procedure will essentially double the luminosity obtainable by the machine.

3.1.3 The Tevatron

The Tevatron receives the protons and antiprotons at 150 GeV (the "shot") and accelerates them to 0.98 TeV in opposite directions. Once 36 bunches of protons and 36 of antiprotons (a "store") are obtained and they are circulating in the accelerator, the two beams are focused using quadrupole magnets in two regions around the ring, where they collide on average every 396 ns. These two regions are denominated D0, where the experiment of the same name is located, and B0, the centre of the CDF experiment. The luminous region at CDF has a dispersion of about 30 cm in the direction of the beams ($\sigma_z \simeq 30$ cm) due to the geometric configuration of the bunches. The profile of the beam in the transverse plane is approximately circular and has a gaussian dispersion $\sigma_l^{beam} \simeq 30$ μm. At present, the Tevatron is functioning with an instantaneous luminosity close to $4{\cdot}10^{31}$ cm^{-2}s^{-1}. The goal of Run II is to reach an instantaneous luminosity of $3{\cdot}10^{32}$ cm^{-2}s^{-1} and an integrated luminosity of 5-10 fb^{-1}, by 2008[58].

3.2 The CDF detector

CDF is a general purpose detector designed to detect the secondary particles produced in the proton-antiproton collisions and to measure the physics observables associated with them. As illustrated in Figure 3.4, CDF is a cylindrical detector with a central barrel region, two end-cap (plug) regions closing the barrel, and two far-forward detector regions. It features electromagnetic (EM) and hadronic (HAD) shower counters arranged in projective tower geometry, as well as charged particle tracking chambers. The tracking chambers are immersed in a 1.4 T uniform magnetic field oriented along the proton beam direction provided by a 3 m diameter, 5 m long super-

conducting solenoidal magnet coil. Although not used in this analysis, drift chambers outside the hadron calorimeters for muon detection cover the region $|\eta| < 1.5$. A detailed description of the detector is published in the CDF Technical Design Report[59]. In coincidence with the Tevatron operation his-

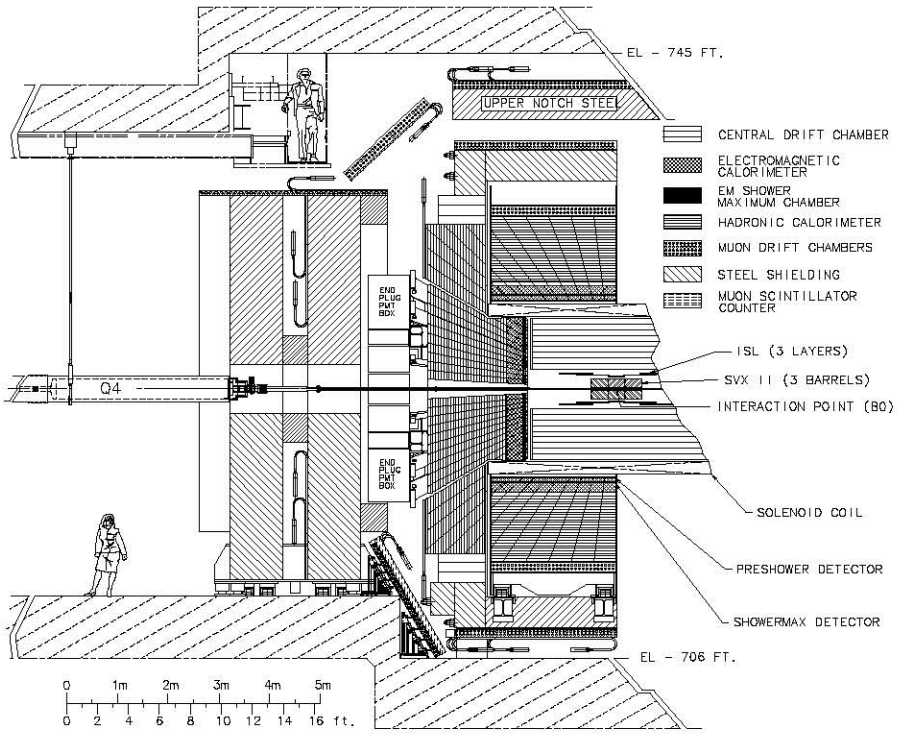

Figure 3.4: *Longitudinal view of half of the CDF Run II detector.*

tory, the CDF experiment had also a first period of data taking called "Run I" (Ia+Ib), which officially started at the end of 1985 and lasted for about ten years. The amount of data collected in this first stage is summarised in Table 3.2. During the shutdown between 1996 and 2001 CDF has been upgraded and several subdetectors have been replaced with more advanced ones, in order to better handle the increase in luminosity. They are described in the following.

Run	Year	Integrated Luminosity (pb^{-1})
	1987	0.025
Run 0	1988-89	4.5
Run Ia	1992-93	19.4
Run Ib	1994-96	90.4
Run IIa	2001-02	72.0

Table 3.2: *Amount of data collected during the different periods of data-taking at CDF.*

3.2.1 Coordinate System

In order to understand the terminology used in the description of the detector, it is useful to first define the quantities mentioned hereafter. CDF uses a cylindrical system of coordinates, with the z-axis oriented along the nominal direction of the beams, in the same direction as the incoming protons and with the origin at the centre of the detector. The coordinates r and the azimuthal angle ϕ are measured in the plane orthogonal to this direction (transverse plane) passing by the vertex of the interaction[6].
A cartesian system of coordinates is also defined (shown in Figure 3.5), where

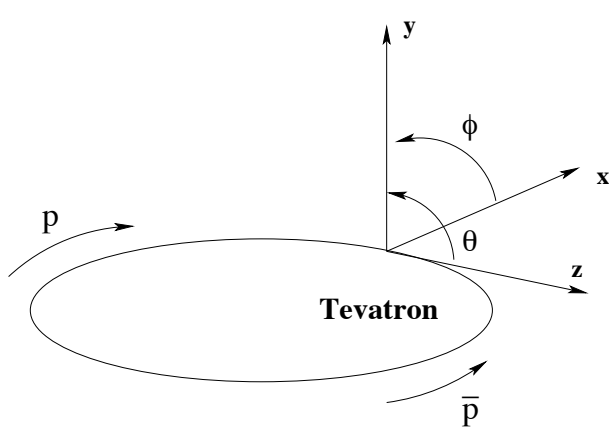

Figure 3.5: *Coordinate system used at CDF.*

the x and y axes, which also lie in the transverse plane, are oriented horizontally away from the detector and vertically upwards, respectively, to form a right-handed system with the z-axis as previously introduced. The polar

[6] ϕ is measured in an anti-clockwise direction from the x-axis viewed in the proton direction.

angle θ is measured upwards from the positive z-axis, and is related to z and r by the expression

$$z = r \times cos\theta. \tag{3.2}$$

The pseudorapidity η, indicated in Figure 3.6 is defined as

$$\eta = -log(tan(\frac{\theta}{2})), \tag{3.3}$$

and depends uniquely on the angle θ.

3.2.2 Magnetic Spectrometer

A 5 meters superconducting solenoidal coil produces a magnetic field with a central value of 1.412 Tesla to enable the measurement of the momenta of the charged particles. The field is uniform to 0.1% in the region $|z| <$ 150 cm and $|r| <$ 150 cm. The solenoid and cryogenic equipment represent 0.85 radiation lengths (X_0) of material for a particle at 90° incidence.

3.2.3 Tracking System

The "integrated tracking system" at CDF, shown in Figure 3.6, involves a new open cell drift chamber, the Central Outer Tracker (COT), which covers the region $|\eta|$ <1 (central region), and the "silicon inner tracker" system, which provides full coverage up to $|\eta|$ <2 (forward region).

Silicon detectors

The silicon inner tracker consists of three concentric silicon detectors located at the very centre of CDF.
The innermost one, **Layer 00** (L00), is a single-sided, radiation-hard silicon layer located at 1.35 cm radius, just outside the beampipe (which is located between the radii of 0.83 and 1.25 cm).
The **Silicon Vertex Detector** (SVX), placed immediately outside L00 at the radius of 1.6 cm, is composed of three barrels, each 29 cm long, as shown in Figure 3.7; all together they extend about 45 cm in the z direction on each side of the interaction point. Each barrel is divided into 12 wedges in ϕ (Figure 3.7), and each wedge supports five layers of double-sided silicon micro-strip detectors between the radii of 2.4 and 10.7 cm from the beam line,

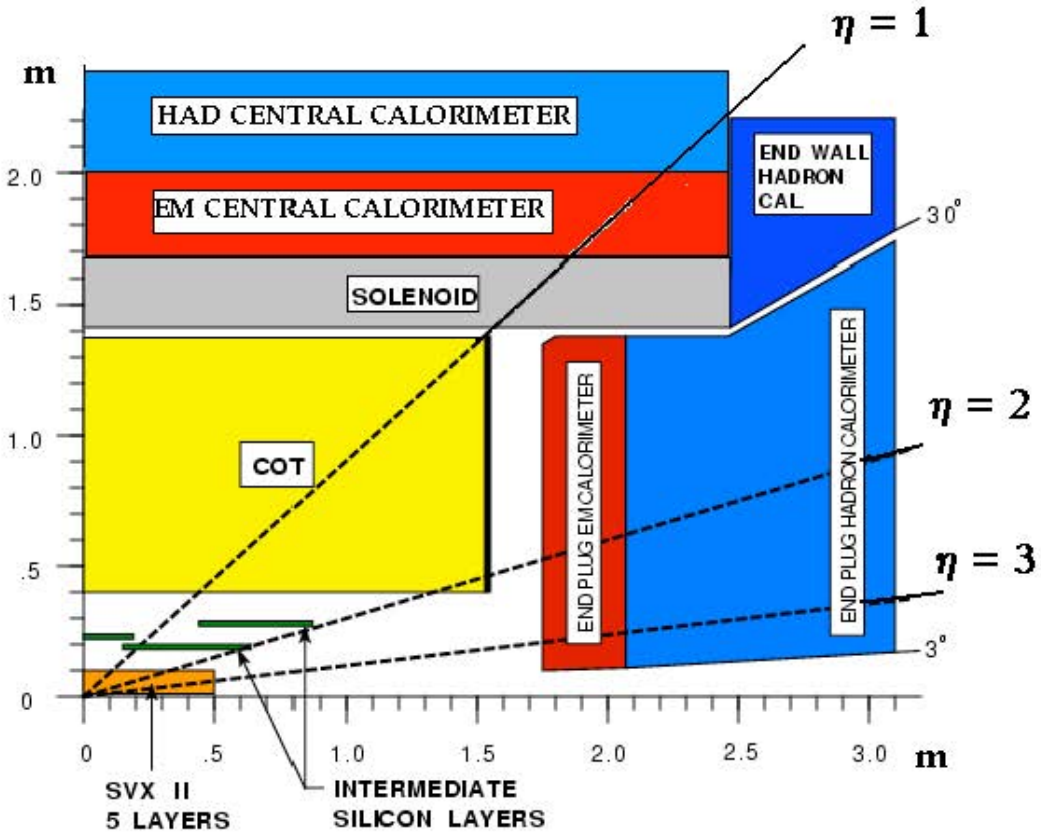

Figure 3.6: *Longitudinal view of the CDF tracking system, representing a quarter of the whole detector.*

to cover the while region $-2 < \eta < 2$. Three of the layers combine the r-ϕ measurement on one side with a 90° stereo measurement on the other. The remaining two layers combine the r-ϕ measurements on one side, with a small stereo angle of 1.2° on the other. The stereo angle information from all the layers is combined to form a three dimensional track. A highly parallel fiber-based data acquisition system reads out the entire detector in approximately 10 μs.

The **Intermediate Silicon Layer** (ISL) consists of three silicon layers placed at radii 20, 22 and 28 cm respectively from the proton-antiproton beams. The central layer covers the central region $|\eta| < 1$, while the two outer layers cover the forward region corresponding to $1 < |\eta| < 2$, where

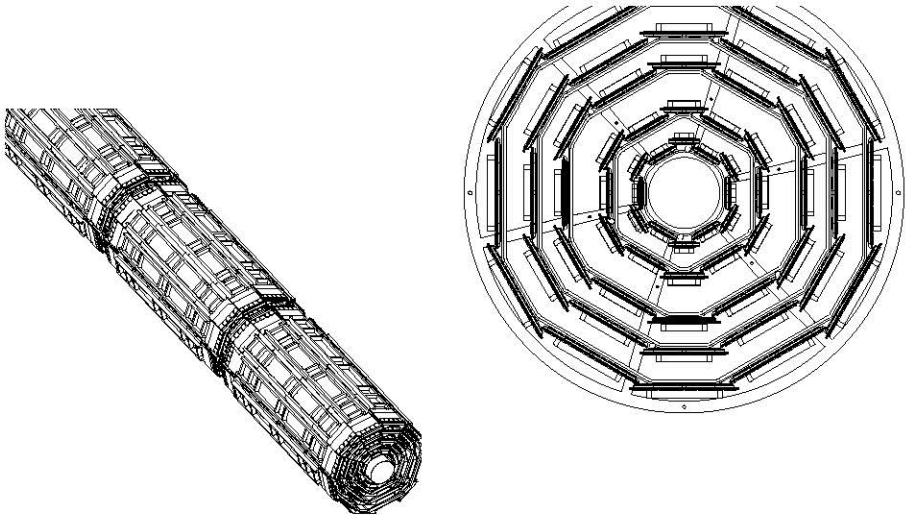

Figure 3.7: *On the left, view of the three barrels of the SVX silicon detector. On the right, end view of one barrel showing the 12 wedges with the 5 layers.*

the coverage from the COT is incomplete. Each layer is double sided as in the SVX, and assembled in a similar way.
The combined information of the SVX and ISL allows the reconstruction of three dimensional tracks independently of the COT (stand-alone mode), thus providing a tool to measure the efficiency of the latter. However, in this analysis only central electrons are used and no information from the silicon systems is used anywhere. Since the silicon was still being commissioned for a long part of the period of the data used here, requiring the presence of the silicon would have reduced the amount of data available by a factor 2. The resolution of the SVX+ISL systems has been estimated by simulations to be[7]

$$\sigma_{p_T}/p_T^2 \sim 0.4\%[\mathrm{GeV}/c]^{-1}; \quad \sigma_{d_0} = 15\,\mu\mathrm{m}; \quad \sigma_{\phi_0} = 0.3\,\mathrm{mrad},$$

where d_0 is the impact parameter of the track and ϕ_0 is the angle that the track forms with the x-axis.

Central Outer Tracker

Tracking in the central region is provided by the Central Outer Tracker, an open cell drift chamber which consists of eight superlayers (Figure 3.8) of

[7]The resolutions refer to tracks with transverse momentum $p_T > 10$ GeV/c (with negligible multiple scattering) and $1< |\eta| <2$. For more details see [59], section 7.5.3.

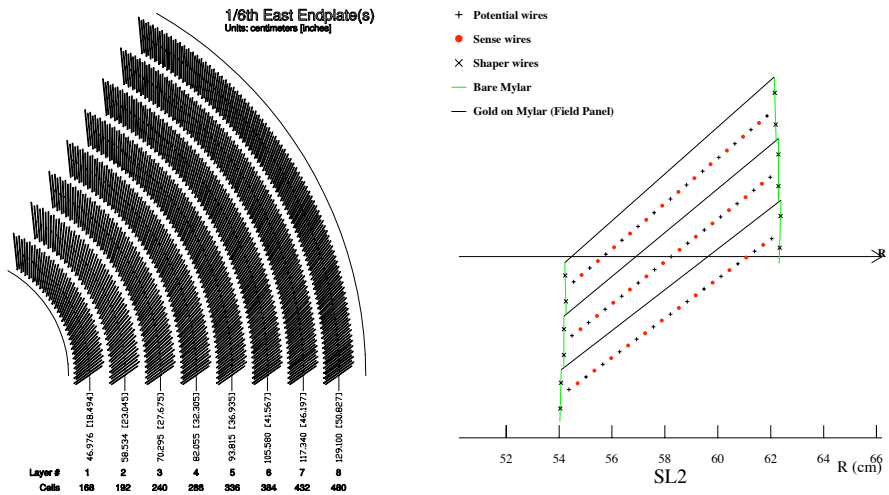

Figure 3.8: *On the left, the endplate slots are shown; in this figure the odd are stereo and the even are axial superlayers, according to the definition in the text. On the right, a single cell layout is shown.*

cells placed between the radii of 40 and 132 cm from the beam pipe. Each superlayer is composed of 12 layers of sense wires alternated with potential wires in a plane, as shown in Figure 3.8. The space between the cells is filled with a gas mixture of Argon and Ethane in the proportions 50:50, chosen to ensure a fast drift velocity ($\sim 100\,\mu m/\text{ns}$) in order to deal with the expected high luminosity[8]. Four of the superlayers are axial (for the measurements in the transverse plane) and the other four are stereo (for the z measurements), with stereo angles of $\pm 2^o$[60]; the superlayers are alternated starting with a stereo superlayer. A summary of the COT characteristics is given in Table 3.3. The ions produced by a charged particle passing through the COT are collected at the sense wires giving the $r-\phi$ information on the position of the hits. The hits from the stereo and axial wires are combined to obtain the z position. The three-dimensional sequence of hits is fitted to form a track. The track momentum and charge are determined from the curvature in the magnetic field. If B is the strength of the magnetic field, the transverse momentum p_T of the track can be obtained by the relationship

$$p_T = Bqr, \tag{3.4}$$

[8]This choice has been made to ensure full efficiency of the chamber with 132 ns bunch spacing, as expected in a later stage of Run II.

COT	
radial coverage	44 to 132 cm
number of superlayers	8
stereo angle (^{o})	+3, 0, -3, 0, +3, 0, -3, 0
layers per superlayer	12
drift field	2.5 kV/cm
maximum drift distance	0.88 cm
maximum drift time	100 ns
resolution per measurement	180 μm
rapidity coverage	$\|\eta\|$ <1
number of channels	30,240
material thickness	1.6%X_0

Table 3.3: *Design parameters of the Central Outer Tracker at CDF.*

where q is the charge of the particle and r is the radius of curvature of the track. The resolution on the curvature has been studied using detailed simulation[59] and cosmic ray data and has been found to be 3.6×10^{-6} cm^{-1} which corresponds to a momentum resolution of $\sigma_{p_T}/p_T^2 \simeq 1.7 \times 10^{-3}$ [GeV/c]$^{-1}$. As more energetic tracks bend less, the curvature, and thus the momentum resolution of the COT, decreases for higher momentum tracks. The resolution on the impact parameter d_0 is about 600 μm, the resolution on $cot\,\theta$ is $\sim 6 \times 10^{-3}$. The COT is a crucial element in the identification of the electrons in the central region, as electron candidates are formed by clusters in the electro-magnetic calorimeter matched to a track in the COT, as will be explained in more detail in section 4.1. In this analysis the momenta of the tracks associated with the electrons are measured using the COT alone.

3.2.4 Calorimeters

Located immediately outside the solenoid, the calorimetry system at CDF is used to measure the energy of charged and neutral particles produced in the p$\bar{\text{p}}$ collisions. The calorimeter is divided into two physical sections: the Central ($|\eta|$ <1), which is the same detector as in Run I, and the brand new Plug (1.1< $|\eta|$ <3.64) detector. Each section is subdivided into an electromagnetic (CEM,PEM) and hadronic portion (CHA,PHA). The end-wall hadronic calorimeter(WHA) covers a gap between the central and plug hadronic sections, as shown in Figure 3.6. The properties of each calorimeter are summarised in Table 3.4. The central calorimeter is divided at η=0 into two halves; each half consists of 24 wedges in ϕ, giving a total of 48 wedges. A wedge, as shown in Figure 3.9, is segmented into ten towers,

	CEM	CHA,WHA	PEM		PHA	
Energy Resolution	$14\%/\sqrt{E}$	$75\%/\sqrt{E}$	$16\%/\sqrt{E}$		$80\%/\sqrt{E}$	
Angular Coverage (in $\|\eta\|$)	<1.1	<1.3	$1.1 < \|\eta\| < 3.6$		$1.2 < \|\eta\| < 3.6$	
Segmentation ($\|\eta\|$ range, $\Delta\eta \times \Delta\phi$)						
	< 1.1		1.1-1.8	1.8-2.1	2.1-3.6	
	0.1×15°		0.1×7.5^o	0.16×7.5^o	$0.2\text{-}0.6\times15^o$	
Absorber, Active Medium	lead, scintil-lator	iron, scintil-lator	lead, scintil-lator		iron, scintil-lator	
Position Resolution $(r-\phi\times z)^{(a)}$	$0.2\,\text{cm} \times 0.2\,\text{cm}^{(b)}$	$10\,\text{cm} \times 5\,\text{cm}$				
Longitudinal Depth	$19\ X_0, 1\lambda$	4.5λ	$21\ X_0, 1\lambda$		7λ	

$^{(a)}$ At 50 GeV incident energy $^{(b)}$ Using the CES chambers

Table 3.4: *Characteristics of the CDF RunII calorimeters. X_0 is the radiation length and λ is the hadronic interaction length.*

labeled 0-9, subtending 0.1 in η and 15° in ϕ. The CEM is a sampling calorimeter made of lead sheets interspersed with polystyrene scintillator. While passing through the calorimeter, particles interact with the material producing "showers" of photons, electrons and positrons depending on their nature. Electrons and photons will start showering earlier and their showers will be almost completely contained in the EM sections, while hadrons (such as pions) in the form of hadronic jets will start later releasing a significant fraction of their energy in the hadronic portions. The photons produced by scintillation during this process are funnelled to light guides at the edges of the scintillator, where photo-multiplier tubes (PMT) (two per EM tower) are used to measure the number of scintillation photons produced in a shower. The CHA and WHA use acrylic scintillator sandwiched between sheets of iron with a similar readout scheme to that of the CEM. Proportional chambers (CES and PES) are embedded near the shower maximum in the range $0< |\eta| <0.613$ and $0.623< |\eta| <1.1$, about six radiation lengths (X_0) deep into the EM calorimeters. These chambers, two per calorimeter wedge, have wires in the r-ϕ view and cathode strips in the z view to record the three dimensional position of the shower. This information determines the location of the incident particle within a tower and allows shower-track matching to be performed. A second set of proportional chambers, the Central or Plug

Preradiator (CPR or PPR) is placed in between the front face of the EM calorimeters and the magnet coil. Acting as shower presampler, this chamber can be very useful in the pion-photon separation and in the identification of the electrons. The characteristics of the CES and the CPR are summarized in Table 3.5. In this analysis only the central calorimeter is used.

	CES (2 per 15° wedge) wires (r-ϕ view)	strips (z view)	**CPR** (2 per 15° wedge) wires (r-ϕ view)
number of channels	64	64	32
spacing (cm)	0.63	1.8	1.0
spatial resolution (cm)	0.2	0.2	0.5
chamber length in z(cm)	115		103
chamber width in $\phi(^o)$	12.4		10.2

Table 3.5: *Description of the Shower-Max (CES) and the Preshower (CPR) central detectors.*

3.2.5 Muon detectors

If electrons lose most of their energy in the EM calorimeters and hadrons in the hadron calorimeters, muons are known to penetrate the tracking systems and the calorimeters leaving very little energy[9]. For this reason a muon candidate is created from minimum energy deposited in the calorimeters matched with a minimum ionising track in the COT and with hits in the "muon chambers", placed outside the CDF detector, which will be described in the following. For muon detection CDF uses four systems of absorbers, scintillators and proportional chambers in the detection of muons over the region $|\eta| \leq 2.0$. They are the Central Muon detector(CMU), the Central Muon Upgrade detector(CMP), the Central Muon Extension(CMX) detector and the Barrel Muon Detector(BMU). All four detectors are composed of layers of single wire drift chambers, of which alternating layers are staggered, in order to eliminate hits position ambiguities. The creation of a muon object involves the process of forming a "stub" from hits in the muon chambers, and matching it to a COT track. An overview of their η and ϕ coverages at CDF is shown in Figure 3.10[61], and their characteristics are briefly summarized

[9]Muons from Z decays, for instance, deposit on average about 0.4 GeV in the electromagnetic portion of the calorimeter and 2 GeV in the hadronic one.

in Table 3.6. None of these detectors are used in this analysis.

	CMU	CMP	CMX	BMU
pseudorapidity coverage	$\|\eta\| < 0.6$	$\|\eta\| < 0.6$	$0.6 \leq \|\eta\| \leq 1.0$	$1.0 \leq \|\eta\| \leq 1.5$
drift tube length	226 cm	640 cm	180 cm	363 cm
drift tube width	6.35cm	15 cm	15 cm	8.4 cm
max drift time	800 ns	1.4μs	1.4μs	800 ns
total drift tubes	2304	1076	2208	1728
scintillation counter thickness		2.5 cm	1.5 cm	2.5 cm
scintillation counter width		30 cm	30-40 cm	17 cm
scintillation counter lengths		320 cm	180 cm	180 cm
total counters	–	269	324	864
pion interaction length	5.5	7.8	6.2	6.2-20
minimum detectable muon p_T	1.4 GeV/c	2.2 GeV/c	1.4 GeV/c	1.4-2.0 GeV/c
multiple scattering resolution	12 cm/p	15 cm/p	13 cm/p	13-25 cm/p

Table 3.6: *Design parameters of the CDF II Muon Detectors. Pion interaction lengths and multiple scattering are computed at a reference angle of $\theta = 55^o$ in CMX, and show a range of values for the BMU.*

3.2.6 Trigger systems

The trigger plays a crucial role in hadron-hadron collider experiments. Since they usually have a high rate of collisions, much higher than the speed with which these events can be written to tape, it is essential that the trigger system be able to provide as much event throughput as possible in the shortest time. In Run II the collision rate is, at nominal luminosity, essentially equal to the crossing-rate, 7.6 MHz, while the tape recording rate is less than 75 Hz. The role of the trigger is to efficiently select the most interesting events among the large amount of "minimum bias"[10]. Due to the improvements in the accelerator configuration discussed in section 3.1, all of the trigger system needed to be replaced in Run II to have a higher rejection factor with respect to Run I and still ensure the maximum event recording efficiency. The CDF trigger system has a three level architecture, with each level providing a rate of reduction sufficient to allow for processing in the next level with the minimum deadtime. The three levels will be described separately in the following paragraphs. Figure 3.11 shows a functional block diagram of

[10]We refer to minimum bias as those events which satisfy the minimal trigger conditions, *i.e.* some activity at small angle with respect to the beamline.

the data acquisition system, while the block diagram of the trigger system is shown in Figure 3.12.

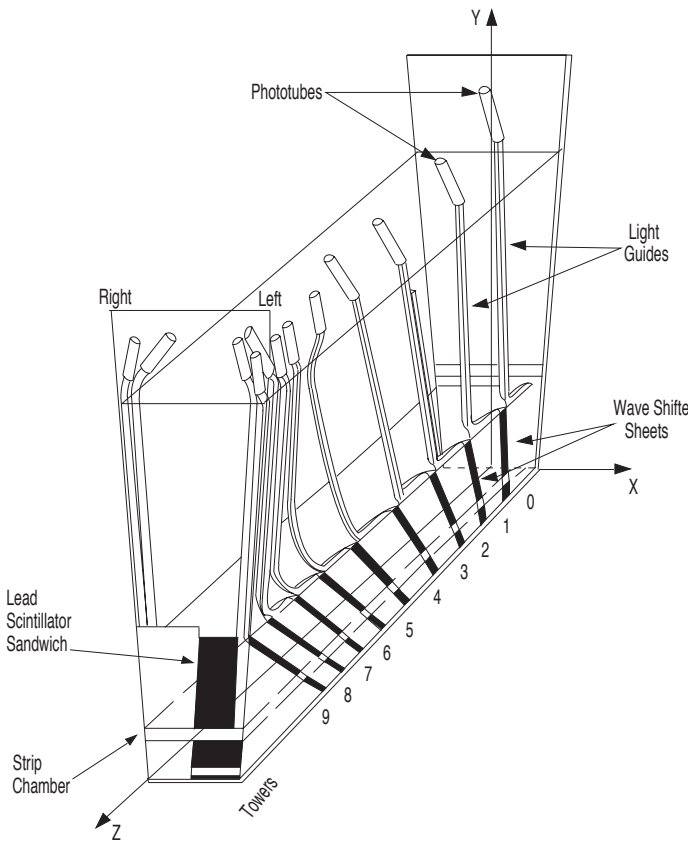

Figure 3.9: *View of one wedge of the central calorimeter. Each wedge covers 1 tower in the azimuthal direction ($\Delta\phi = 15^o$) and ten towers in the η direction (0< $|\eta|$ <1.1). The proportional chamber(CES), referred to as "Strip Chamber" in the figure, can be seen embedded at shower maximum. Both edges are uninstrumented in order to leave space for light guides that connect the scintillator to the photo-multipliers.*

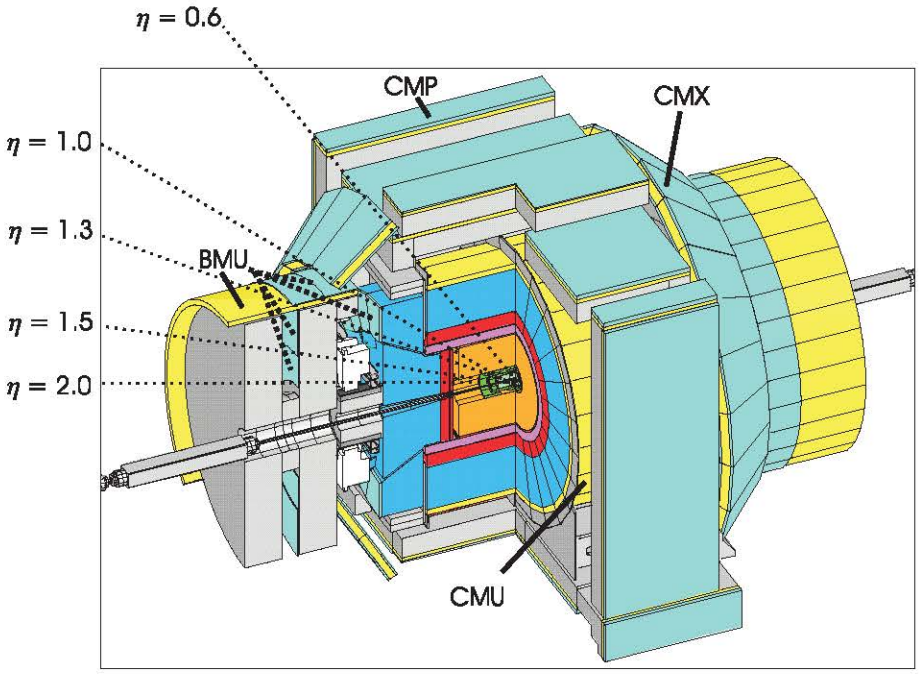

Figure 3.10: *Three dimensional view of the CDF detector, where the muon chambers are indicated with their respective coverage in pseudorapidity.*

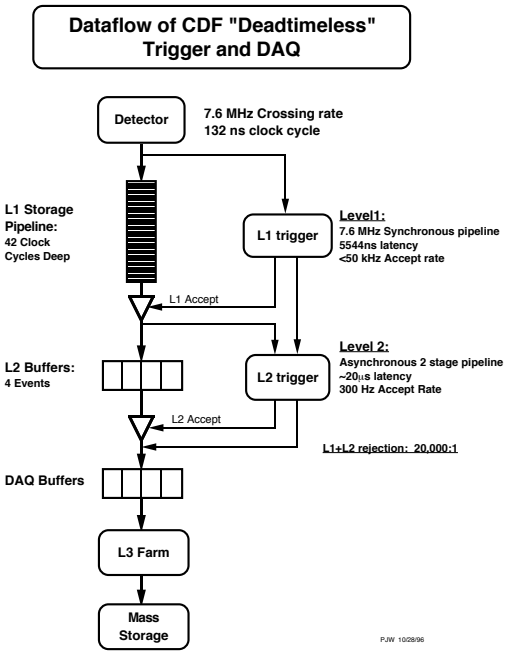

Figure 3.11: *The readout functional block diagram. The acronyms have been already introduced in the text, apart for the following: XFT = eXtremely Fast Tracker; XTRP = Track Extrapolation module; SVT = SVX track processor in Level2 trigger system; TSI = Trigger System Interface.*

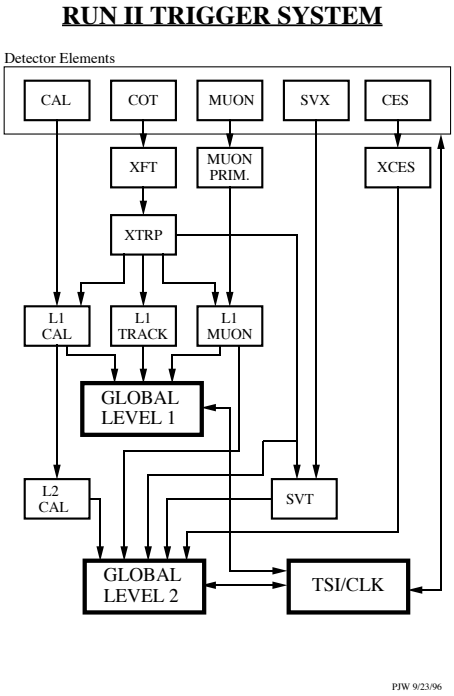

Figure 3.12: *The trigger system block diagram*

Level-1

The first level of trigger selection **Level-1(L1)** uses custom designed hardware to find physics objects based on a subset of the detector information and then makes a decision based on simple counting of these objects. The input to the L1 hardware comes from the calorimeters, tracking chambers and muon detectors. The decision to retain an event for further processing is based on the number and energies of the electron, jet and muon candidates as well as the missing energy in the event, or on the kinematic properties of few of these objects. The Level-1 hardware consists of three parallel synchronous processing streams which feed inputs of the single Global Level-1 decision unit. One stream finds calorimeter objects (e.g. electrons and jets), another finds muons and the third finds tracks in the central region. Triggers can be formed using these streams singularly as well as AND or OR combinations of them. All elements of the Level-1 trigger are synchronised to the same 132 ns clock, with a decision made every 132 ns by Global Level-1. In the period of data taking considered in this analysis the accelerator was operating in 36 bunches mode (396 ns) and the trigger was clocked every 132 ns with the two intermediate clock cycles automatically rejected. The maximum L1 accept rate is $\sim$ 20 kHz, while the typical one is about 12 kHz.

Level-2

Events accepted by L1 are processed by the second level of trigger **Level-2(L2)**, which is composed of several asynchronous subsystems. These provide input data to programmable L2 processors in the Global Level-2 crate, which determine if any of the Level-2 triggers are satisfied. Processing for a Level-2 trigger decision starts after the event is written into one of the four L2 buffers by a Level-1 accept. When L2 is analysing the event in one of the buffers, that buffer cannot be used for additional L1 accepts. If all the four buffers are full the experiment incurs deadtime. It follows that the time required for a Level-2 decision needs to be less than about 80% of the average time between L1 accepts in order to keep the deadtime as low as possible. For this purpose L2 has been pipelined into two stages each taking approximately 10 μs, which is sufficient to keep the deadtime at a minimum, even if L1 had an accept-rate of 50 kHz. The Level-2 buffers perform a limited event reconstruction using essentially all the information used in L1, but with higher precision. In addition, at L2 data from the central shower-max detector and the SVX are available, which improve respectively the iden-

tification of electrons and photons and the reconstruction of the secondary vertices. Furthermore, a jet reconstruction algorithm is provided by the L2 cluster finder. After all of the data are stored in the processors, the event is examined to check if the criteria of any of the L2 triggers have been satisfied. This operation can be performed while the new events are being loaded into memory, thus not affecting the dead time. The typical L2 accept rate, as of this writing, is between 100 and 300 Hz, depending on the initial luminosity.

Level-3

The **Level-3 (L3)** trigger subsystem is composed of two main components, the **Event Builder (EVB)** and the Level-3 Farm. Level-1 and Level-2 systems need to make their decisions at a very high rate which makes it impossible to fully reconstruct each event. While Level-1 and Level-2 algorithms use small predefined pieces of event data to make their decision, the event pieces are stored in the buffers of the 140 Front End crates which constitute the EVB. After a Level-2 decision is made, the Event Builder assembles all event fragments from the Front End crates into one data block.

The 16 subfarms which compose the **Level-3 farm** receive event fragments from the EVB and build complete events into the appropriate data structure for analysis. As it takes about one second for one computer unit to make a trigger decision on one event, it takes a large farm of 250 Dual Pentium Linux Personal Computers (called "processors") to ensure the required input rate. Each subfarm contains between 14 and 18 processor nodes and one "convertor" node, which acts as "farm input" distributing the data flow coming from the EVB.

The events are then passed to a trigger algorithm (a different one for each processor) that categorizes the event and makes the decision as to whether or not to permanently store it. The selected events are passed to the Data-Logger subsystem. During the building processing, the event integrity is checked. The L3 algorithms take advantage of the full detector information and improved resolution unavailable to the lower trigger levels. This includes full three-dimensional track reconstruction and tight matching of tracks to calorimeter and muon-system information. Results from the lower levels are used to drive the algorithms, which are based on the off-line analysis packages. This is a modular system consisting of a number of general reconstruction modules and separate filter modules for specific triggers. L3 accepts events with a rate of approximately 75 Hz. More details about the

Level-3 software used to identify electrons will be given in section 4.3.

3.3 Generation and Simulation

Based on the known physics of the processes under study, physicists have developed computer programs which

a) reproduce the kinematics of the physics processes, which in the case of the physics of elementary particles involves the production and decay of the examined particles;

b) simulate the effect of the passage through matter (represented by the detector) of these particles, simulating the amount of energy they will lose, the direction they will take and so on.

The first step is called *"generation"* and it is usually performed by sophisticated computer programs called "*Monte Carlos*". They assemble the known physics of several processes and reproduce their kinematic characteristics, such as Z production from proton-antiproton interactions. That is, knowing the energy of the incoming proton and antiproton, they will assign a certain energy to the Z (according to the the $p\bar{p}$ Parton Distribution Functions), a certain boost, and so on.

After the generation is performed, these data are passed through the "simulation" program. This reproduces the physics of the interaction of the generated particles through the matter of the detector, their consequent decay and the amount of energy they deposit in each subdetector. In CDF a GEANT[62] parameterization of the detector is used, which contains all the information regarding the amount of material in the detector and the geometry of its components. The output of the simulation program has exactly the same structure as the actual data taken from real interactions, consisting of a series of hits in the COT or energy depositions in the calorimeters or in the muon chambers. To reproduce the real event coming from a $p\bar{p}$ interaction, many different physics concepts have to be introduced and coded into the simulation program, such as bremsstrahlung, to realistically reproduce the behaviour of the particles passing through the detector. Once the simulated data have been processed, they are analysed by the same analysis code used to analyse the collision data; the agreement of the two gives confidence that

both the physics and the detector response are well understood and under control. Any inconsistencies between the data and the simulation is indicative of lack of knowledge or deficiencies in the code, and thus needs to be investigated.

Details on the generation and simulation of the samples used as reference for this analysis are described in section 5.1.

3.4 Object-oriented software

All the reconstruction and data acquisition system at CDF is built upon a C++ infrastructure. C++ is an object-oriented software language which makes use of "*objects*", intended as separate self-existing structures of a general nature identifying all entities of the same kind. An object defining a certain category will contain by definition all the properties and links to the quantities common to that particular category. In CDF these objects are the most basic physics quantities such as a track, or the more sophisticated ones such as electrons and muons and jets. According to this philosophy, a separate piece of software exists to identify each separate physics object. Once the basic requirements to form a physics object are fulfilled, the latter can be filled with links to all the physics properties or quantities which can help to better identify it. As an example, a "jet object" will contain a certain value for the energy measured in the hadronic calorimeter, one for the EM energy, the coordinates of its position in the detector, and so on. In general, for each object only one quantity of a kind is chosen to be associated with it. In this way the user who has access to the object will obtain the energy or the pseudorapidity value which has been uniquely associated to it by selection criteria defined "a priori". More information on the creation of the "electron object", essential for this analysis, will be given in section 4.2.1.

Chapter 4

Electron and Neutrino identification

This analysis searches for Z^0 bosons decaying to electrons and positrons ($Z^0 \rightarrow e^+e^-$) and W bosons decaying to electrons and neutrinos ($W^\pm \rightarrow e^\pm\nu$). In this chapter the detection of electrons and the presence of a neutrino through missing transverse energy is described. This includes the procedure to create electron and neutrino candidates in the CDF detector (described in section 3.2), and the variables used to identify high transverse momentum(p_T) electrons and neutrinos in this analysis. Electrons are identified by means of the calorimeters and the magnetic spectrometer, while neutrinos are found by looking for missing transverse energy ($\not{E}_T$) using only the calorimeters.

The starting point in the creation of an electron candidate is a cluster in the EM calorimeter, through a procedure described in section 4.1. The creation of an electron candidate, after making further requirements on the cluster, is described in section 4.2. Here the corrections applied are also discussed, together with the definition of the variables used in the electron identification. In section 4.3 how these variables are used in the trigger selecting high p_T electrons is described. Finally, the procedure of identifying neutrinos through the missing E_T variable is described in section 4.4.

4.1 Electron clustering

The creation of an electron object[63] begins in the calorimeter. The search for an electromagnetic (EM) shower in the calorimeter begins with all the towers which have more than 3 GeV of EM transverse energy. These are defined as seed towers[1]. The list of seed towers is ordered in transverse energy from the highest to the lowest. The towers adjacent in η to the highest E_T seed tower ("shoulder towers") form a cluster in the Central Electromagnetic calorimeter together with the seed tower itself if they have at least 100 MeV of EM or hadronic energy. The shoulder towers have to be within the same wedge in η as the seed tower; this means that the cluster has to be contained in a single wedge and can consist of, at most, the seed tower and its nearest neighbours in η on either side of it. The maximum cluster size is 3 towers in η and 15° in ϕ. If the seed tower is either in the outer or in the innermost region of the CEM (called "tower 0" and "tower 9", corresponding to the annular region including all towers[2] with the same value of η), then only "tower 1" or "tower 8" is added to the cluster, and no towers of a cluster are allowed to cross a region boundary or the centre of the detector. Only electromagnetic energy is used to determine the centroid and the total energy of the cluster.

Any tower chosen to be in a cluster is removed from the seed tower list, eliminating the possibility of overlapping clusters. For this analysis it is required that electron or photon candidates have greater than 5 GeV of energy in the cluster. Also, the energy in the hadronic towers corresponding to the towers of the electromagnetic cluster must be less than 1/8 of the total electromagnetic energy, to reduce the background coming from hadronic events(jets). If these two criteria are satisfied the cluster is considered to be an electron or photon candidate (a "CdfEmObject")[3]. More information is required to define the cluster as an electron.

[1]The standard calorimeter corrections discussed in the following sections are applied at this point.

[2]On this occasion the CDF nomenclature can be misleading; the terms "seed tower" and "shoulder tower" refer to a specific region in the calorimeter corresponding to 0.11 units in η and 15°; the term "tower i", with i any number between 0 and 9, refer to a region of 0.11 units in η and 360^0 in ϕ, meaning the all annular region including all the towers with the same value of η. Below, every time the term tower is used it indicates the single tower of 0.11 η times 15° in ϕ, unless a number is specified after it. In this latter case it will indicate the annular region as just described.

[3]If the total electromagnetic energy of the cluster is greater than 100 GeV, the cluster is accepted independently of any other selection criteria.

4.2 Central Electron Identification

4.2.1 Creation of an electron object

If a valid EM cluster is found, a series of other objects, if they are defined to match, are added to the CdfEmObject to form an electron. These include a track, a shower-max(CES) cluster and a pre-radiator(CPR) cluster.
For each CdfEmObject, each **track** is in turn iteratively extrapolated to the plane of the CES for the wedge containing the associated EM cluster[4]. The final extrapolated track is required to be within 25 cm in x-ϕ (where x is the local x from the CES) and 38 cm in z from the centre of the EM tower seeding the cluster. This provides a region in the CEM that covers slightly more than three physical towers. Among the tracks which fulfill these requirements, the "best matching" one is chosen to be the highest p_T track located within the seed tower or not more than 5 cm beyond the seed tower boundary in the z direction, which passes some "Quality Cuts" requiring a minimum number of COT axial and stereo hits.
The next objects checked for association with the CdfEmObject are **shower-max clusters**. In the central calorimeter there are two CES cluster collections; an "unbiased" collection which is created from a list of wires or strip seeds over a threshold energy, typically used in the creation of photon objects, and a "track based" collection that uses the wire or strip nearest an extrapolated track as a seed; the latter is used in electron analyses. Among the CES clusters belonging to the unbiased collection, a subset is created, requiring the clusters to be in the same wedge as the EM cluster previously found, and to which they are potentially being associated. The best matching one is taken to be the one with the highest energy. For the "track-based" CES clusters, the track seeding each CES cluster is required to belong to the collection of tracks which have been found to match the CdfEmObject. Among these CES clusters, the "best matching" one is chosen to be the one seeded by the best track previously determined. This is the CES cluster which will be used in this analysis. The association of the **pre-shower** clusters is performed in a similar way to the CES clusters, although this information is not used in this analysis.

[4]Extrapolation is performed assuming the particle follows a helical path in a solenoidal field oriented parallel to the negative z-axis in the global CDF coordinate system (as described in section 3.2.1).

In this analysis, the presence of a track and a CES cluster, seeded by the same track, is required for the electron to be created.

4.2.2 Corrections

In this section, the corrections applied to the central electron variables in the data are introduced. Plots shown in this section are from $Z^0 \rightarrow e^+e^-$ data and Monte Carlo samples, described in chapter 5. The selection criteria applied to the electrons are described in section 6.1.

a) Vertex Correction

The electron transverse energy in EM Objects is calculated assuming the interaction point is located at $z = 0$. We recalculate the transverse energy E_{T} using z_0 of the track [64] associated to the electron as the event interaction point, and the angle of the track as the direction of the electron.

b) CEM Energy Corrections

In order to tune the central electromagnetic calorimeter, the CEM response needs to be determined and corrected. This procedure includes individual tower gains, local x and z position dependent mapping corrections, time dependent corrections, and attenuation of the light passing through the scintillator. They are discussed in the following text.

- The corrections for the tower-to-tower gain variations have been determined using a calibration electron sample collected during the first stage of Run II data-taking[65]. The gains are defined as the average E/p for each tower in the window 0.8-1.25; their distribution can be observed in Fig. 4.1[5]. Correcting CEM energies for this effect results in approximately 5% improvement in the energy resolution.

- CEM gain changes with time. These time-dependent corrections, ex-

[5]Here E is the energy measured in the CEM and p is the momentum measured in the COT (beam constrained). For more information see section 4.2.3.

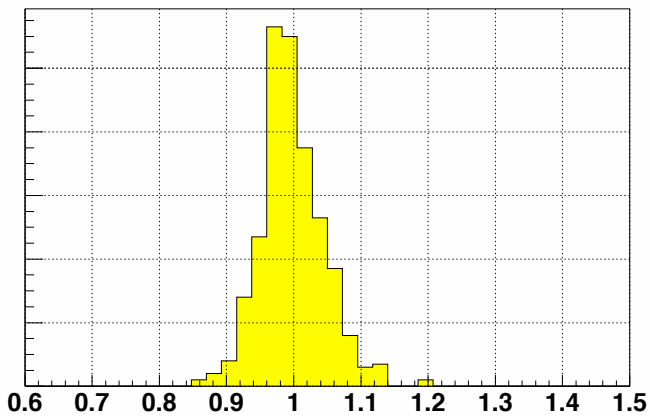

Figure 4.1: *Distribution of the tower-to-tower gain variations for central electrons.The inverse of these values are used in the correction to the central electron energy.*

tracted by plotting[6] $\langle E/p \rangle$ as a function of time[7], have been implemented in the data. This includes the overall scale correction to make the peak of the di-electron invariant mass be at 91 GeV. Figure 4.2 demonstrates that the corrections are made properly.

- The CEM response is dependent on local x and z coordinates within a tower. These corrections, called "face corrections", are extracted from the test-beam data taken in 1994 and are applied [67] to both data and simulation. Corrections for the attenuation of light passing through the scintillator towards wavelength shifters and other corrections are also applied at this stage.

Despite these corrections, about 7% variation was observed when $\langle E/p \rangle$ was plotted as a function of the local x position (CES-x). In order to make a flat distribution of $\langle E/p \rangle$ versus CES-x, the following correction factor is applied to the CEM energy:

$$f_x = \frac{1.015}{(1 + 0.000157 \times x^2)},$$

[6]Here and in all the following the average of E/p, written as $\langle E/p \rangle$, is calculated using values of E/p in the range between $\langle E/p \rangle = 0.9$ and $\langle E/p \rangle = 1.1$.

[7]Work done by Larry Nodulman[66].

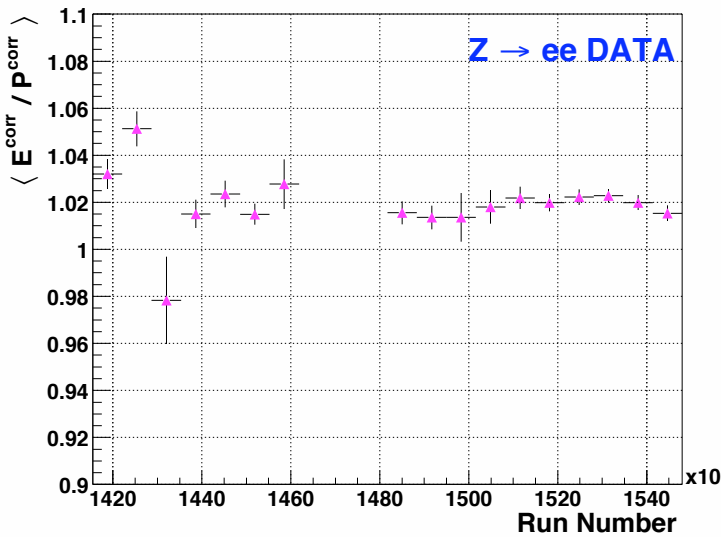

Figure 4.2: $\langle E/p \rangle$ *as a function of run number. Here E is the corrected E and p has the corrections described in section 4.2.2c). The average of* E/p *is calculated in the range between 0.9 and 1.1.*

where x is measured by the CES. The corrected CEM energy is then

$$E_{corr} = f_x \times E.$$

The correction factor and $\langle E/p \rangle$ as a function of CES-x after that the corrections are applied are shown in Figure 4.3.

After the corrections the response is flat. The scale is then set by comparing the peak of the $Z^0 \rightarrow e^+e^-$ invariant mass distribution to a Monte Carlo simulation. The ratio of the central values from each fit is used to scale all electron energies.

The isolation variable in the calorimeter, as defined in section 6.1, has been corrected for leakages to the neighbour calorimeter towers. The corrections are described in [68].

c) Beam Constrained COT Tracking

Tracking resolution tends to dominate the E/p resolution once the energy has been tuned. The raw COT resolution can be substantially improved by imposing a beam constraint[69], that is forcing the track fit to go through the beam-spot. All the tracks used in this document are beam constrained

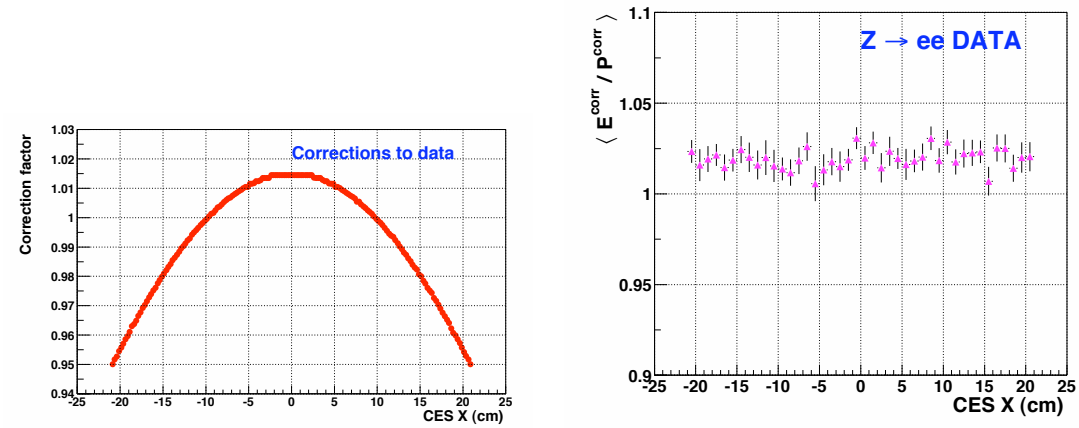

Figure 4.3: *The CEM energy correction factor applied to the data (left) and $\langle E/p \rangle$ as a function of CES-x after the corrections (right). The average of E/p is calculated using values of E/p in the range between 0.9 and 1.1.*

"COT-only" tracks.
As shown in Figure 4.4 (E/p distributions for electrons and positrons), there is a systematic bias in momentum measurements in the data as a function of the azimuthal angle ϕ. No bias is observed in the Monte Carlo simulation and none is expected. The bias is removed by recalculating the signed curvature [66], Q/p_T, where Q is the charge of the track and p_T is the COT beam-constrained transverse momentum:

$$\frac{Q}{p_T^{corr}} = \frac{Q}{p_T} - 0.00042 - 0.00116 \times sin(\phi + 0.3).$$

No corrections are needed to the polar angle, θ, of tracks. Figure 4.5 demonstrates that most of the bias is removed by these corrections. The corresponding plots from the $Z^0 \rightarrow e^+e^-$ Monte Carlo sample without the corrections are shown in Figure 4.6. A dip of about 2%, near |CES-x| $\sim$ 20 cm (Figure 4.6 bottom left), is not yet understood.

d) Summary on corrections

The corrections applied to the energy measured in the calorimeter and to the momentum measured in the COT have been described. Note that the CEM energy corrections are the standard ones applied automatically in the processing of the data, and thus common to all analyses using high p_T electrons at CDF. On the other hand, the momentum corrections have to be applied

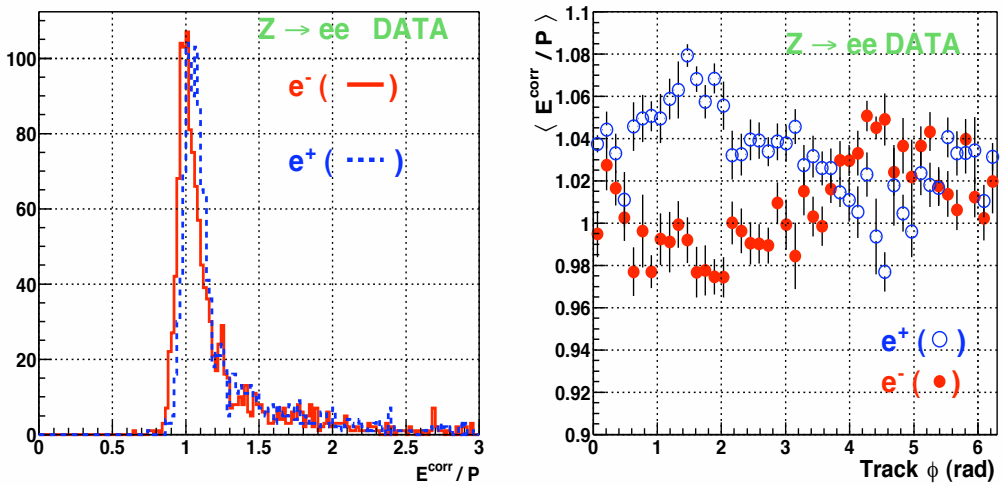

Figure 4.4: *The E/p distributions for electrons and positrons (left) and $\langle E/p \rangle$ as a function of track ϕ (right) in the $Z^0 \to e^+e^-$ data before the curvature corrections are applied. The average of E/p is calculated in the range between 0.9 and 1.1.*

separately as there is no automatic procedure at present.
Figure 4.7 compares the invariant mass distributions between the $Z^0 \to e^+e^-$ data (after the corrections) and the $Z^0 \to e^+e^-$ Monte Carlo sample[8]. The good agreements in the mass peak location and width demonstrate that the CEM energy scale and resolution are in good shape for this analysis. Reasonable agreements between the data and Monte Carlo are also observed for the E/p distribution (see Figure 4.8) and $\langle E/p \rangle$ as a function of the η and ϕ of the electron tracks (see Figure 4.9).

4.2.3 Central Electron Variables

The variables used in the selection of the central electrons are summarized in the following paragraphs.

- *Electromagnetic(EM) cluster and E_T*
  An electron cluster is formed from a seed EM tower and a number of shoulder EM towers, which are added to the seed tower until the

[8]The distributions will be analysed in more detail in chapter 5 and 6, where the presence of same sign events will be discussed.

maximum cluster size is reached as explained in section 4.1. This is defined by two towers in pseudo-rapidity ($\Delta\eta \simeq 0.3$) and one tower in azimuth ($\Delta\phi \simeq 15^o$). The transverse electromagnetic energy E_T is calculated as the EM cluster energy times $sin\,\theta$, where θ is measured using the COT track associated with the electron.

- *Had/EM*
  This variable is the ratio of the total energy in the hadron calorimeter to the total energy in the EM calorimeter for the towers included in the EM cluster. In this analysis the value of Had/EM will be scaled by a factor (0.0045) multiplied by the total energy of the cluster[9]. This is done to compensate for the logarithmic dependence of the hadronic energy deposition by an electron. This cut has a flat efficiency up to 175 GeV as observed in test-beam data[70].

- *Isolation*
  This variable is defined as the ratio $E_T^{iso}/E_T^{cluster}$; here

$$E_T^{iso} = E_T^{0.4} - E_T^{cluster},$$

  where $E_T^{0.4}$ is the energy in a cone of radius $\Delta R = \sqrt{\Delta\eta^2 + \Delta\phi^2} \leqslant 0.4$ around the electron cluster excluding the electron cluster, and $E_T^{cluster}$ is the energy in the electron cluster. ΔR is defined between the cluster centroid and the centre of a candidate tower.

- χ^2_{strip}, χ^2_{wire}
  The pulse height shape in the Central Electromagnetic Shower-Max (CES) detector is compared to the one obtained with test-beam data using a χ^2 test. The variable χ^2_{strip} is the χ^2 of the fit between the energy deposited on each of the 11 strips in z in the CES shower and the shape obtained using test beam data. An energy dependent correction is used in the calculation of the χ^2, where the total energy of the cluster is the scale factor. A similar variable χ^2_{wire} tests the energy deposition on the wires in the r-ϕ view. The latter is not used in the selection of the events as it is largely affected by bremmstrahlung emission.

- L_{shr}
  The purpose of this quantity is to provide some discrimination of electrons and photons from hadronic showers faking these particles in the

[9]For a chosen cut value, the equation of the sliding cut is Had/EM < Had/EM(cut value) + 0.0045×E.

central electromagnetic calorimeter. This is done by comparing the observed sharing of energy deposition between towers in the CEM to that expected for a "true" electromagnetic shower, taken with test-beam data and recorded in the database. The Lshr (Lateral Shower Sharing variable) represents the amount of lateral sharing and it is defined as

$$L_{shr} = 0.14\Sigma_i \frac{E_i^{adj} - E_i^{expected}}{\sqrt{(0.14\sqrt{E})^2 + (\Delta E_i^{expected})^2}},$$

where the sum is only over towers in the electron cluster, not extending across region boundaries or $\eta = 0$, and

- E_i^{adj} is the measured energy (in GeV) in a tower adjacent to the seed tower,
- $E_i^{expected}$ is the expected energy (in GeV) in the adjacent tower, calculated using a parametrisation from test beam data,
- $0.14\sqrt{E}$ (E in GeV) is the error on the energy measurement, and
- $\Delta E_i^{expected}$ is the error on the energy estimate.

- *E/p and p_T*
  These quantities involve the momentum of the track associated with the electron. The track is selected as the beam-constrained COT track with the highest momentum pointing to the electron cluster. During the passage through the material up to the COT active volume the electron might radiate a photon (external bremsstrahlung), which is collinear with the electron and generally deposits energy in the same calorimeter cell as the electron, thus not much affecting the value of E_T (which is still the original energy of the electron). However, the momentum measured in the COT after the bremsstrahlung radiation will be smaller. This causes a long tail in the distribution of E/p above the value of one.

- *Z_{vertex}*
  This variable is the z_0 coordinate of the interaction vertex where the electron has originated. The z of the electron track is used in this context.

- ΔX and ΔZ
  These variables are the differences between the x and z coordinates of

the track extrapolated to the CES and the value of x and z as measured by the CES itself. ΔX is the separation in the $r-\phi$ view , while ΔZ is the separation in the z view. The cut on ΔX has been multiplied by the sign of the charge of the electron and it is asymmetric in $r-\phi$, to account for photons emitted in bremsstrahlung radiation, which distort the CES cluster towards one direction depending on the charge. Both quantities are corrected for the CES and COT alignments wedge-by-wedge.

- *Track quality cuts*
  To ensure that the track associated with the electron is a good quality reconstructed track, we ask that the track has been reconstructed in the COT in 3 axial and 3 stereo super-layers with at least 7 hits in each.

- *Fiduciality*
  This variable ensures that the electron is reconstructed in a region of the detector which is well instrumented. The electron position in the CEM is determined using either the value determined by the CES shower ("CES-based") or by the extrapolated track ("track-based"), and it must satisfy the following requirements:

  - the electron must lie within 21 cm of the tower centre in the $r-\phi$ view in order for the shower to be fully contained in the active region; this corresponds to the cut $|X_{CES}| < 21$ cm, where X_{CES} is the local coordinate of the calorimeter tower;
  - the electron should not be in the regions $|Z_{CES}| < 9$ cm, where the two halves of the central calorimeter meet, and $|Z_{CES}| > 230$ cm, which corresponds to the outer half of the last CEM tower (tower 9), prone to leakage into the hadronic part of the calorimeter;
  - the electron should not be in the region immediately closest to the point of penetration of the cryogenic connections to the solenoidal magnet (the "chimney"), which is un-instrumented. This corresponds to $0.77 < \eta < 1.0$, $75^o < \phi < 90^o$ and $|Z_{CES}| > 193$ cm.

  In addition, the region $1.05 < |\eta| < 1.10$ is excluded because of the smaller depth of the electromagnetic calorimeter.

4.3 Central Electron trigger

The data used in this analysis are selected with a trigger path which requires the three levels of the trigger, as described in section 3.2.6, to have fired. The requirements for each level are listed in the following.

- At **Level-1** a COT track has to be found by the eXtremely Fast Tracker(XFT)[71], with transverse momentum above 8 GeV. In addition, a tower in the central calorimeter with transverse energy above 8 GeV and Had/EM less than 0.125 (for E_T <14 GeV) has to be matched to this track.

- At **Level-2** shoulder towers are added to the central seed tower found at Level 1 if they have $E_T > 7.5$ GeV. An XFT track has again to be found, matched to the seed tower of the central cluster. The total energy of the cluster has to be above 16 GeV, and the ratio Had/EM has to be less than 0.125.

- There is no threshold on the minimum energy of the shoulder towers at **Level-3**, where the cluster has to be found with transverse energy of 18 GeV and Had/EM less than 0.125. The track has to be found by the 3-D COT reconstruction algorithm, with $p_T > 9$ GeV.

4.4 Neutrino Identification

The calorimeter response to the total activity in the event determines the resolution on the measurement of the neutrino p_T, which is inferred by invoking momentum conservation. A noninteracting neutrino in the CDF detector is detected by the presence of a large transverse momentum imbalance ("missing E_T" or $\not\!\!E_{\mathrm{T}}$). The missing E_T is calculated from

$$\vec{\not\!\!E}_{\mathrm{T}} \equiv \left| -\sum_i \vec{E}_t^i \right| \tag{4.1}$$

where $\vec{E}_t^i$is a vector whose magnitude is the transverse energy energy in a calorimeter tower and whose direction points from the event vertex to the center of the calorimeter tower. The sum involves all towers with total

energy (hadronic and electromagnetic) above 0.1 GeV within the region $\eta < 3.6$, corresponding to the all central and plug calorimeter. The direction is corrected for the vertex of the electron track; no other correction factor is applied. Events with perfect momentum balance and no resolution effects would have $\not\!\!E_{\mathrm{T}} = 0$. The smearing about 0 on each component (x and y) of $\not\!\!E_{\mathrm{T}}$ is Gaussian and grows with the $\sum \vec{E}_t$ in the calorimeter. The $\sum \vec{E}_t$ is the scalar sum of E_T over all towers in the calorimeter, corresponding to the region of $\eta < 3.6$. At the $\sum \vec{E}_t$ typical of W events, the resolution on $\not\!\!E_{\mathrm{T}}$ is of the order of 3 GeV, while the neutrino p_T is of the order 20-40 GeV.

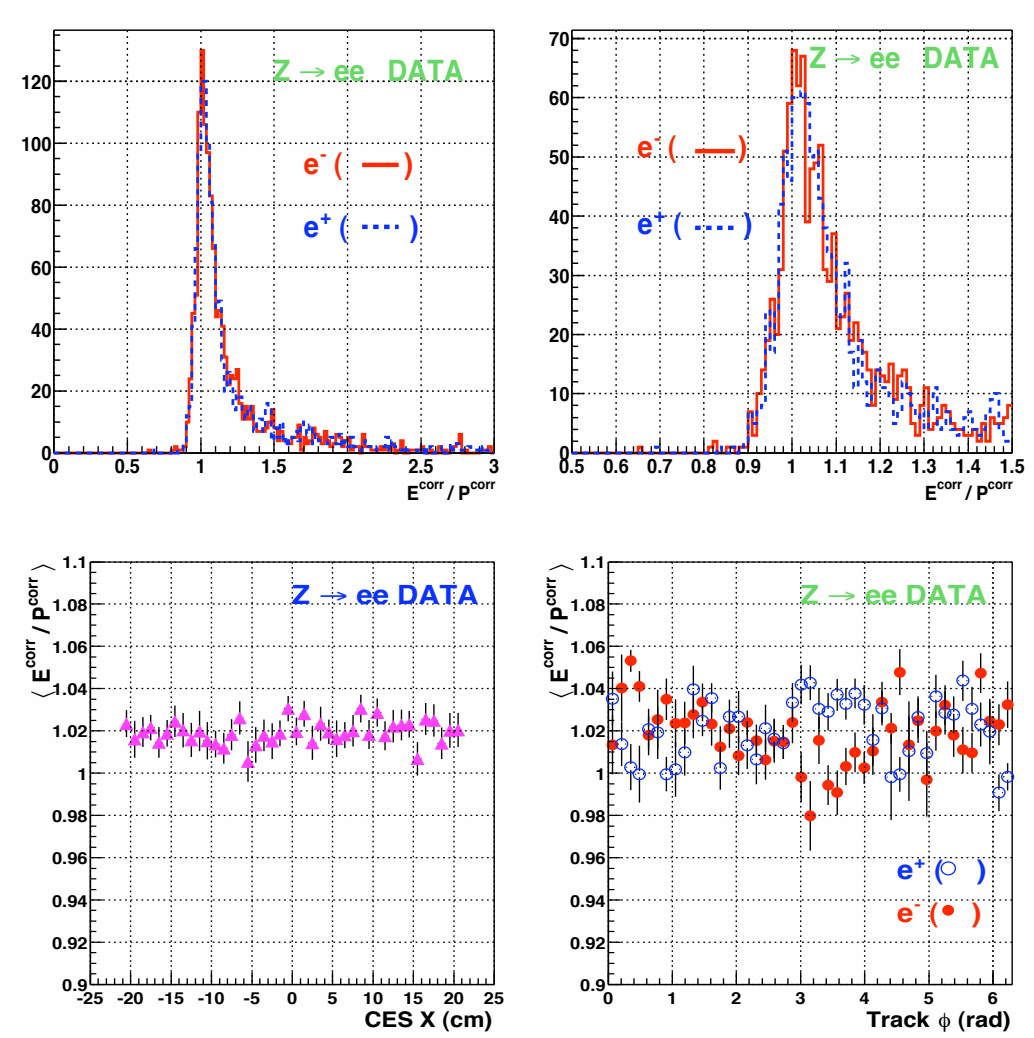

Figure 4.5: *The E/p distributions for electrons and positrons (top plots) and $\langle E/p \rangle$ as a function of CES-x (bottom left) and of track ϕ (bottom right) in the $Z^0 \to e^+e^-$ data after the curvature corrections are applied. In the upper section, the plot on the right is the blow-up of the plot on the left in the region $0.5 < \langle E/p \rangle < 1.5$.*

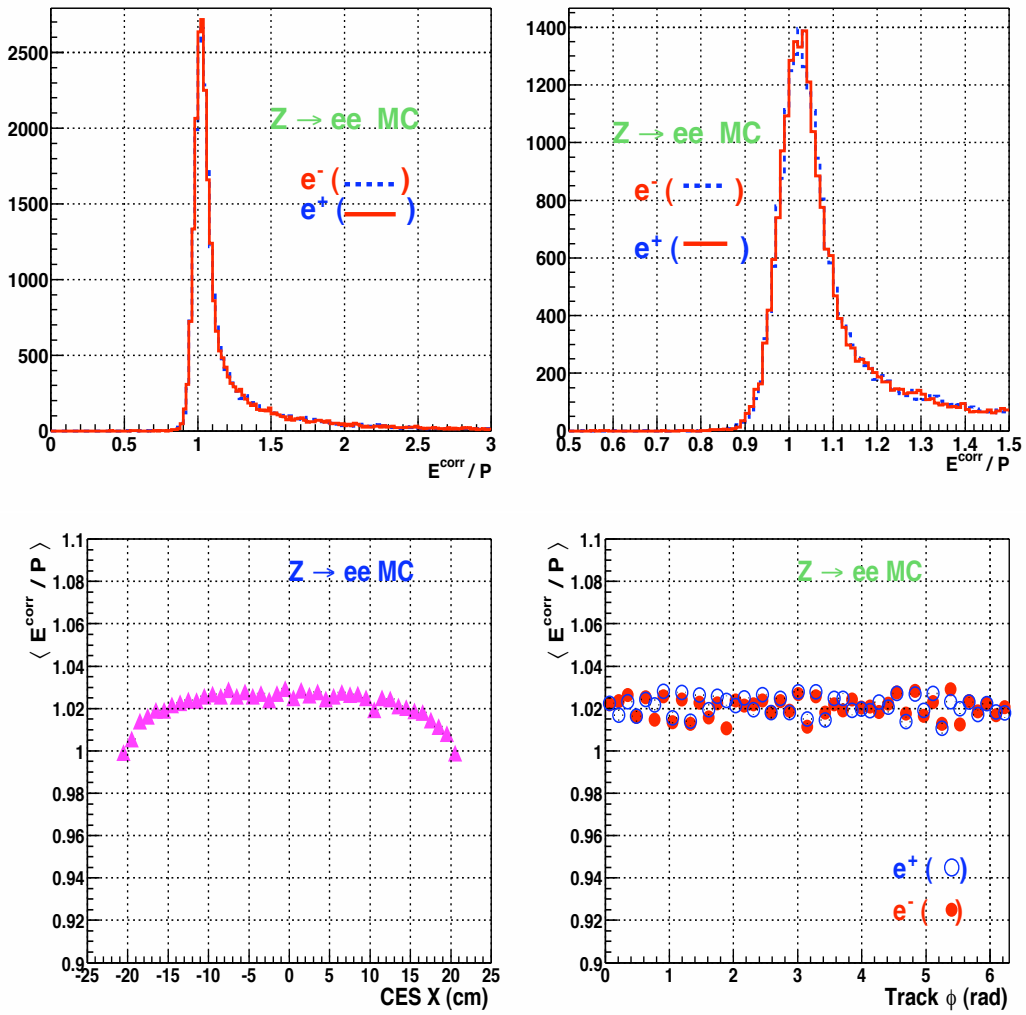

Figure 4.6: *The E/p distributions for electrons and positrons (top plots) and $\langle E/p \rangle$ as a function of CES-x (bottom left) and a function of track ϕ (bottom right) in the $Z^0 \rightarrow e^+e^-$ Monte Carlo sample. No corrections are applied to simulation.*

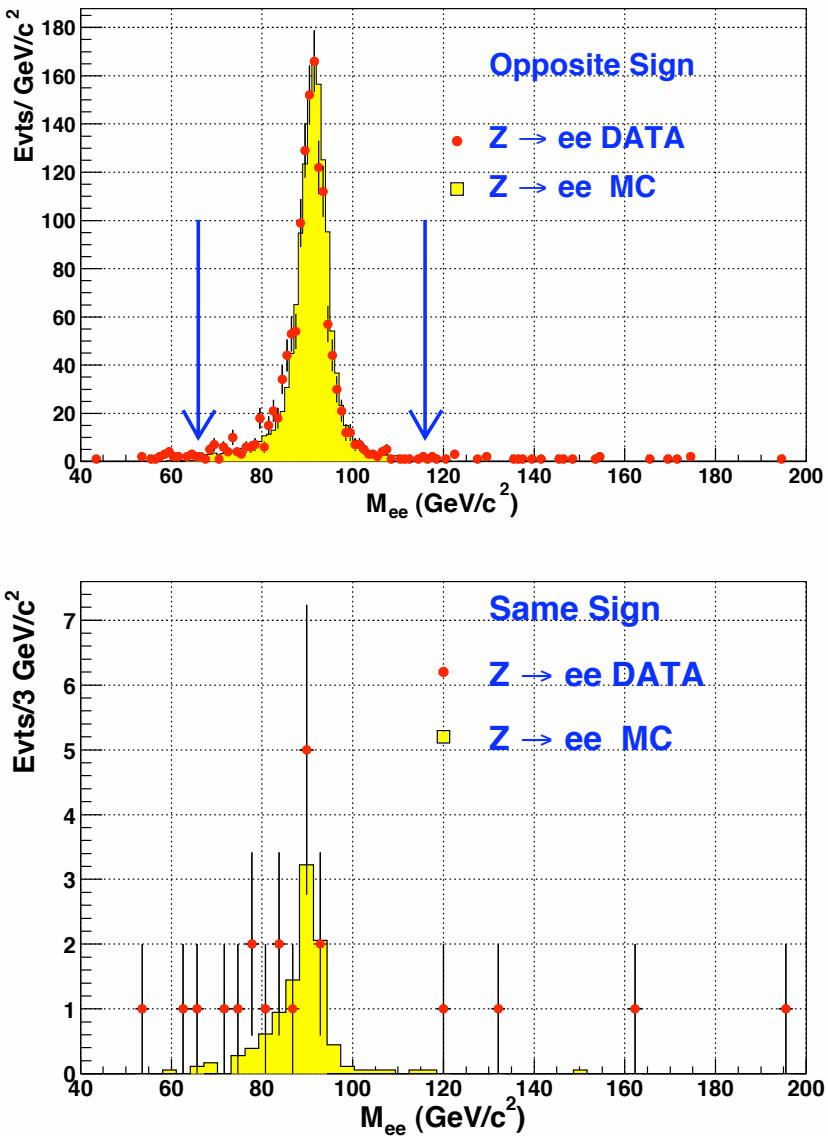

Figure 4.7: *The* $Z^0 \rightarrow e^+e^-$ *(CC) invariant mass distribution of data (dots) and* PYTHIA *Monte Carlo (solid histogram). The top plot shows the events with two electrons of opposite sign (OS), while the bottom plot shows the events where the electrons have the same sign (SS) electric charge. The number of events in the Monte Carlo sample has been normalized such that the number of OS events in the MC sample is equal to the number of OS events in the data. The arrows in the top plot indicate the invariant mass cut applied for this analysis.*

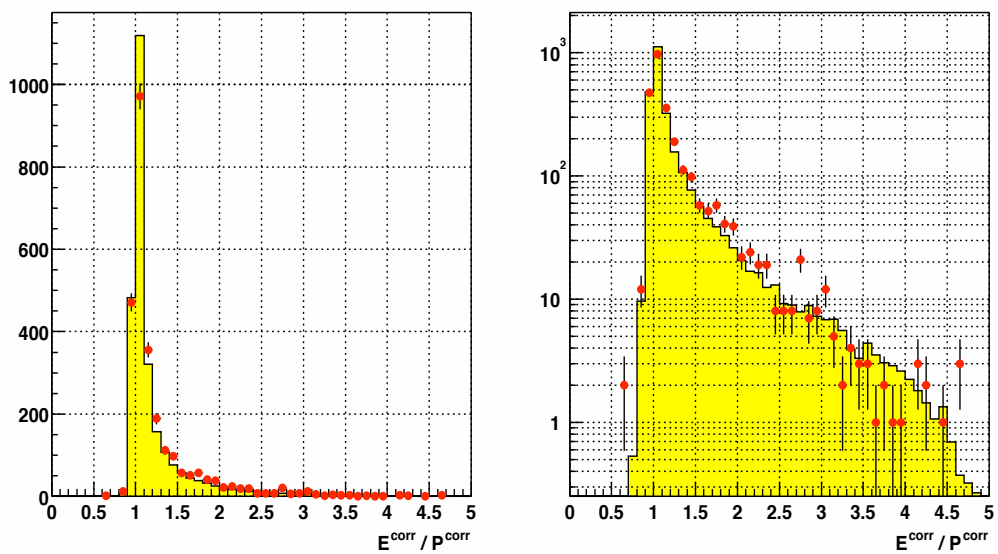

Figure 4.8: *The E/p distributions for the $Z^0 \rightarrow e^+e^-$ data (points) and Monte Carlo sample (histogram) in a linear scale (left) and a logarithmic scale (right).*

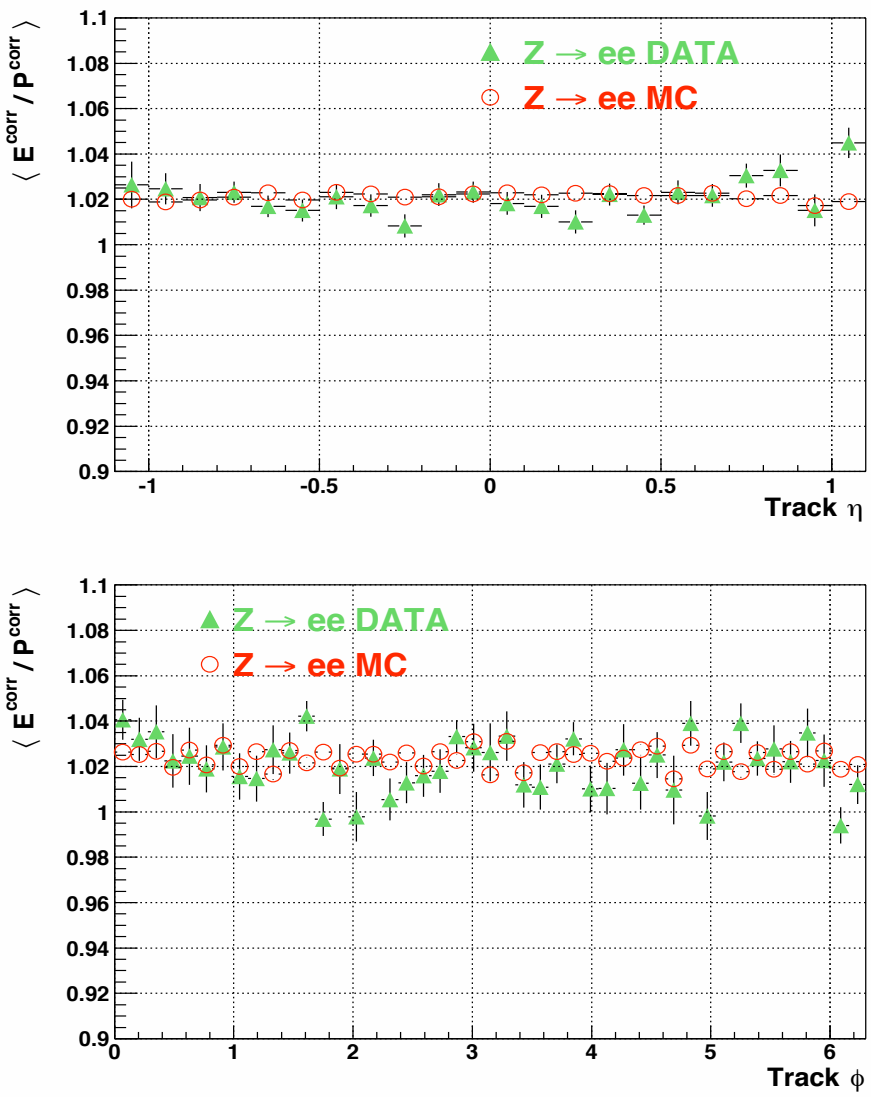

Figure 4.9: $\langle E/p \rangle$ *as a function of track* η *(top) and* ϕ *(bottom). The solid triangles are the* $Z^0 \to e^+e^-$ *data after the corrections and the open circles are the* $Z^0 \to e^+e^-$ *Monte Carlo simulation.*

Chapter 5

Monte Carlo and Data Samples

In this section the samples used in this analysis are described. They include the Monte Carlo samples, signal and background, and the sample of data collected with the CDF detector.

5.1 Monte Carlo Samples

Monte Carlo[1] was used to estimate the detector acceptance and background contributions to both $W^{\pm}$ and Z^0 production. The Monte Carlo samples were generated with PYTHIA 6.203[72], using Parton Distribution Functions CTEQ 5L[73]. The PYTHIA Monte Carlo generates Z^0 and W bosons at leading order(LO) with the p_T parametrised to closely match the next-to-leading order(NLO) calculation[72]. A full detector simulation is used to model the behaviour of the CDF detector. The Monte Carlo samples used for this analysis are:

1.) A sample of 320,000 $Z^0/\gamma^* \rightarrow e^+e^-$ events, with minimum invariant mass of the dielectrons of 30 GeV. This sample is used for the detector acceptance and background studies;

2.) A sample of 1.4M $W^{\pm} \rightarrow e^{\pm}\nu$ events, used for the detector acceptance and background studies;

[1]Details of the Monte Carlo simulation of data from the CDF detector are given in section 3.3.

3.) A sample of 196,000 $Z^0/\gamma^* \to e^+e^-$ and $W^\pm \to e^\pm\nu$ events, generated and simulated with exactly the same procedure as in **1.)** and **2.)**, but with an additional extra material, consisting of 0.515 cm thick silicon cylinder (corresponding to 5.5% X_0) placed between the beamline and the COT inner radius. This sample will be used for studying the systematic uncertainties on the acceptance;

4.) A sample of 238,000 $Z^0/\gamma^* \to \tau^+\tau^-$, generated with minimum $\tau^+\tau^-$ invariant mass of 30 GeV, and 500,000 $W^\pm \to \tau^\pm\nu$ events, used for the background studies.

No restrictions were placed at generation level on the transverse momentum of the final state leptons or on their pseudorapidity. Initial and final state radiation were turned on, so were multiple interactions and fragmentation and decay. In order to generate Monte Carlo which modelled the data, the beam energy used was set to 980 GeV/c^2 and the vertex parameters were adjusted to match the data. This means that the vertex parameter mean was set to 3 cm in z, and the gaussian spread to 25 cm.

5.2 Data Sample

For the measurement of R we use a dataset that contains events with high energy electrons from two sources, $W^\pm \to e^\pm\nu$ and $Z^0 \to e^+e^-$ decays. The global data sample requires that events have one electron in the central region that passes electron identification cuts. Additional criteria are used to form two datasets, one with missing transverse energy $\not\!\!E_T$, containing decays of W bosons, and the other with a second electron, containing decays of Z^0 bosons.

5.2.1 Good Run List

A "Good Run List" database is maintained by the CDF experiment, which contains the amount of luminosity written to tape and the status of all detector components for the period of data taking from March 2002 until January 2003. All periods of continuous data taking with more than 10 nb^{-1} of data written to tape are included, and the parts of the run when any detector component other than the silicon vertex detector were not properly

functioning are excluded. As stated above, the subset of data used in this analysis corresponds to an integrated luminosity of 72.0 pb^{-1}.

5.2.2 Luminosity Measurement

The total integrated luminosity is derived from the rate of the inelastic $\mathrm{p\bar{p}}$ events measured with the luminosity monitor Cerenkov Luminosity Counters (CLC)[74], $R_{\mathrm{p\bar{p}}}$, the CLC acceptance, ϵ_{CLC}, and the inelastic cross section, σ_{in}, at 1.96 TeV, according to the expression:

$$L = \frac{R_{\mathrm{p\bar{p}}}}{\epsilon_{CLC} \cdot \sigma_{in}}.$$

The CLC acceptance was estimated using data and simulation through the formula

$$\epsilon_{CLC} = \frac{\mathrm{N(CLC\,East - West\,coincidence)}}{\mathrm{N(CLC + Plug\,tagged\,inelastic)}} \cdot \frac{\mathrm{N(CLC + Plug\,tagged\,inelastic)}}{\mathrm{N(inelastic)}} \tag{5.1}$$

where N(CLC + Plug tagged inelastic) is the number of inelastic events tagged by the CLC and the plug calorimeter, N(CLC East − West coincidence) is a subset of those including the events which pass the online selection criteria. The fraction $\frac{\mathrm{N(CLC+Plug\,tagged\,inelastic)}}{\mathrm{N(inelastic)}}$ is extracted from simulation while the ratio $\frac{\mathrm{N(CLCEast-West\,coincidence)}}{\mathrm{N(CLC+Plug\,tagged\,inelastic)}}$ is measured from data. The acceptance calculated in this way is estimated to be $(60.2 \pm 2.4)\%$[75].
The inelastic cross section 61.7 mb is obtained by scaling the CDF measurement $\sigma_{in} = 60.4 \pm 2.3$ mb at $\sqrt{s} = 1.8$ TeV to 1.96 TeV[76]. Using these numbers, and requiring the run to belong to the "Good Run List" described in section 5.2.1, the total luminosity is estimated to be

$$(72.0 \pm 4.3)\ \mathrm{pb}^{-1}.$$

The 6% quoted uncertainty is dominated by the uncertainty in the absolute normalization of the CLC acceptance for a single $\mathrm{p\bar{p}}$ inelastic collision. The complete list of systematic uncertainties, including uncertainties from the inelastic cross-section and from the luminosity monitor, can be found in Table 5.1.

Effect	Uncertainty Estimate
inelastic cross-section (CDF measurement)	2.5%
CLC acceptance	4.4%
Detector instability	< 2%
Detector calibration	< 1.5%
On-line to off-line transfer	< 1.0%
non-linearity at high-luminosity($> 10^{32}$)	n.a.
Total Uncertainty	~5.7%

Table 5.1: *Systematic uncertainties in the luminosity calculation using the CLC and the CDF measurement of the inelastic cross-section.*

5.2.3 Inclusive Electron Sample

Inclusive high p_T electrons are produced in hadron collisions in decays of the electroweak bosons, such as $W^{\pm} \to e^{\pm}\nu$, $Z^0 \to e^+e^-$, or $Z^0/\gamma^* \to \tau^+\tau^-$ and $W^{\pm} \to \tau^{\pm}\nu$, where one of the taus decays to an electron. High p_T electron clusters are also produced in QCD processes, where the electron is embedded in a high p_T jet of hadrons. The processes in which hadronic jets can produce an electron cluster are:

1) electrons which come in e^+e^- pairs, either from photon conversions or Dalitz decays[2];

2) semileptonic decays of heavy quarks, e.g. $b \to ce\nu$ or $c \to se\nu$,

3) fake electron clusters which are really hadron showers that pass our electron identification cuts.

The types of hadrons which would pass our electron identification cuts are overlaps of $\pi^{\pm}$ and π^0 showers, which thus produce a charged track and an electromagnetic cluster, and pion "charge exchange", $\pi^{\pm} + N \to \pi^0 + N'$ which can occur in the calorimeters.

Among the 72.0 pb^{-1} of data described in section 5.2.1, we select events satisfying the trigger described in section 4.3. The "Inclusive Electron Sample" subset is then created by requiring each event to fulfill the requirements listed on Table 5.2, where the variables have the same meaning as defined in section 4.2.3. After this selection we have 2,027,335 events in the Inclusive Electron Sample.

[2]For more information about Dalitz decays see [77].

Cut	value
EM E_T	$\geq$ 18 GeV
Had/Em	$\leq$ 0.125
Lshr	$\leq$ 0.3
p_T	$\geq$ 9.0 GeV/c
E/p	$\leq$ 4.0
ΔX	$\leq$ 5.0 cm
ΔZ	$\leq$ 3.0 cm

Table 5.2: *Criteria used in the creation of the Inclusive Electron sample.*

5.2.4 Tight Central Electron Sample

From the inclusive electron data sample, additional selection criteria are applied to obtain a sample of events with electrons which is referred to as a "tight" central electron sample. Requiring tight cuts on a central electron

Variable	Tight Central Cut
E_T	> 25 GeV
Fiduciality	(CES based)
Had/EM	$< 0.055 + 0.0045 \times E$
p_T	p_T >10 GeV/c
E/p	E/p <2.0(*)
Track Quality Cuts	at least 3 Axial and 3 Stereo SL with at least 7 hits each
Z_{vertex}	$\lvert z_0^{electron} \rvert$ <60.0 cm
L_{shr}	<0.2
χ^2_{strip}	<10.0
$Q \cdot \Delta X$	$-3.0 < Q \cdot \Delta X < 1.5$ cm
$\lvert \Delta Z \rvert$	<3.0 cm

Table 5.3: *Criteria for electron candidates used in the selection of the "tight central" electron sample.*
(*) *The E/p cut is released for electrons with E_T >50 GeV/c^2.*

serves three purposes. First, this well-understood central region has added information from the tracking and the strip chambers that can be used to suppress background from other physics processes. Second, the tight cuts on the central electron allow loose, highly efficient cuts to be placed on the second lepton (the neutrino in the case of W decays and the second electron in the case of Z^0 decays). Third, and perhaps most importantly, selecting both W and Z^0 candidate events from such a common sample of inclusive electrons cancels several systematic uncertainties in the ratio of the W and

Z^0 cross sections. The criteria[3] used in this process are listed in Table 5.3. Electrons from $W^{\pm} \rightarrow e^{\pm}\nu$ and $Z^0 \rightarrow e^+e^-$ decays are produced without other particles nearby, characteristic of an electron with low isolation. Electrons produced by QCD processes are not expected to have low isolation e.g. from QCD jets faking an electron and semi-leptonic decays of heavy quarks. All electrons which satisfy the selection criteria in Table 5.3 are also required to have isolation (as defined in section 4.2.3) less than 0.1. A total of 139,293 events pass the tight central electron event selection criteria in an exposure of 72.0 pb^{-1}. A total of 95277 of these events also pass the isolation requirement[4]. Figure 5.1 summarises the division of the inclusive electrons and gives details about the relative sizes and selection cuts used to create each subsample. The E_T spectra of the electrons in the inclusive, tight and isolated samples are shown in Figure 5.2. A peak from the Jacobians of the W and Z^0 is already apparent.

5.2.5 Z sample selection

$Z^0 \rightarrow e^+e^-$ events are selected starting from the tight central isolated electron sample, with a "tight" electron selection as described in the first column of Table 5.4, and also requiring the presence of another electron, the "loose" electron, satisfying the selection criteria listed in the rightmost column of Table 5.4. The tight cuts on the first electron are sufficient to ensure the selection of Z events. Consequently, the criteria on the selection of the loose electron have been on purpose relaxed to accept more signal. For more details about the efficiency of the tight and loose set of cuts see chapter 7.
The electron variables are the same described in section 4.2.3. In this analysis only electrons falling in the central region of the detector have been used. Using these selection criteria we find 1830 $Z^0 \rightarrow e^+e^-$ candidates with opposite sign (OS) charge requirement and 22 with same sign (SS) (as shown in Figure 4.7). Estimation of the background in this sample is discussed in chapter 6. The η and ϕ distributions for the candidate events are shown in Figure 5.3 (top), while in Figure 5.3 (bottom) the value of the seed tower ("iEta") is shown. Also shown is the signal Monte Carlo, which is normalised to the number events in the data. In Figure 5.4, Figure 5.5 and Figure 5.6

[3]These are the standard criteria at CDF for the high p_T electrons analyses; for more information and motivation of each of these see Appendix A and [7].

[4]Plot of the isolation variable for the tight central electrons can be found in Figure 5.4.

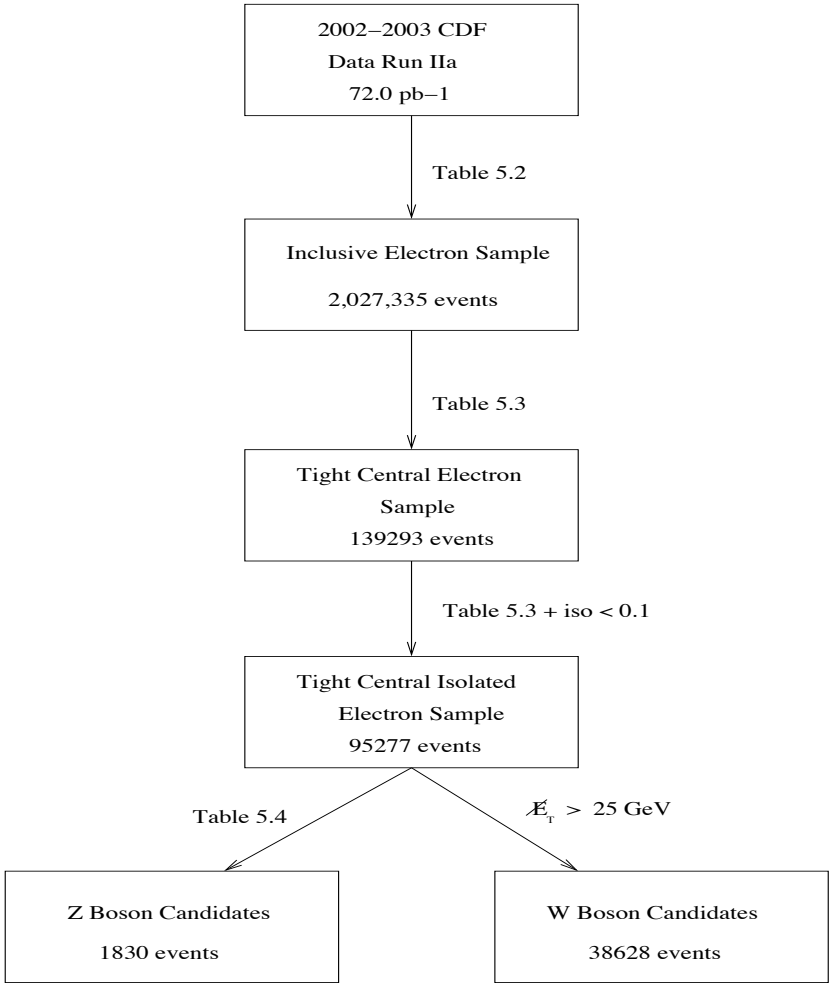

Figure 5.1: *Flow Chart of events in the R analysis. The labels next to the arrows refer to the selection criteria used to create each subsample.*

the electron variables used for selecting the $Z^0 \rightarrow e^+e^-$ candidate events are compared with the signal Monte Carlo. The agreement is overall very good[5]. In Figure 5.7 the CES local Z and X distributions are shown for Monte Carlo and data.

[5]The disagreement for the bin at zero in the Lshr distribution is due to a problem in the simulation and it is currently under study.

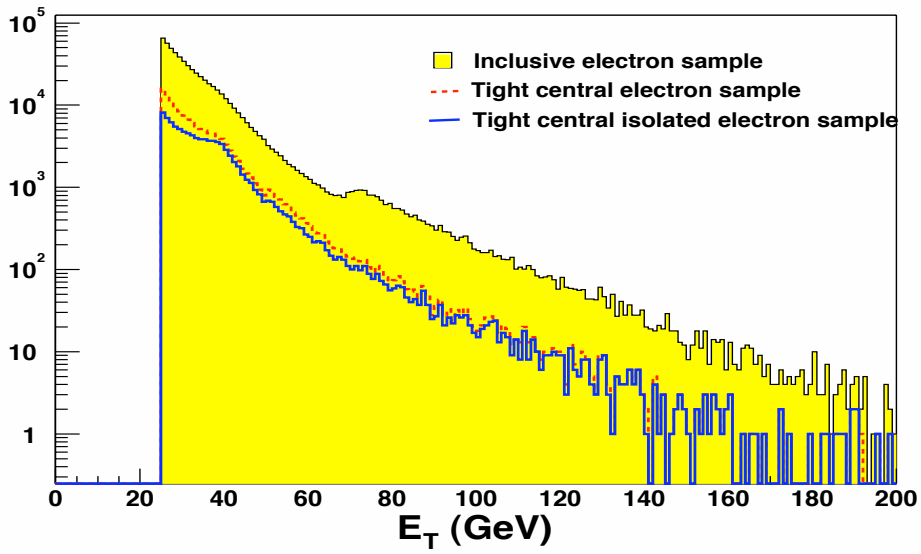

Figure 5.2: *Transverse energy distribution for all electrons in the Inclusive sample, in the tight sample and the tight isolated electrons.*

5.2.6 W sample selection

The $W^{\pm} \rightarrow e^{\pm}\nu$ events are selected requiring a tight central isolated electron, as described in Table 5.3 and missing energy, $\not{E}_T > 25$ GeV. Using these selection criteria 38628 $W^{\pm} \rightarrow e^{\pm}\nu$ candidate events are found[1]; an estimation of the background in this sample can be found in chapter 6. Figure 5.8 shows the E_T and p_T distributions for the electrons from the W, while Figure 5.9 shows the distribution of E_T versus $\not{E}_T$ for these events; the $W^{\pm} \rightarrow e^{\pm}\nu$ signal events are distributed along the diagonal. In Figure 5.10 the distribution of the Isolation fraction as defined in section 4.2.3 is plotted versus the missing energy; the $W^{\pm} \rightarrow e^{\pm}\nu$ signal events are visible in the region of an isolated electron with large missing energy. For the W events it is not possible to construct the $e^{\pm}\nu$ invariant mass because the neutrino is not directly detected. Hence another variable is chosen, the Transverse Mass M_T, which is defined as

$$M_T = \sqrt{p_T^e p_T^\nu (1 - cos\phi^{e\nu})}. \tag{5.2}$$

Here p_T^e and p_T^ν are the transverse momenta of the electron and neutrino respectively, while $\phi^{e\nu}$ is the separation angle between the two. Figure 5.11

Variable	Tight Central	Loose Central
E_T	> 25 GeV	> 25 GeV
Fiduciality	CES based	CES based
Had/EM	$< 0.055 + 0.0045 \times E$	$< 0.055 + 0.0045 \times E$
E_T^{iso}/E_T	< 0.1	< 0.1
p_T	p_T >10 GeV/c	p_T >10 GeV/c
E/p	E/p <2.0(*)	
Track Quality Cuts	at least 3 Axial and 3 Stereo SL with at least 7 hits each	at least 3 Axial and 3 Stereo SL with at least 7 hits each
Z_{vertex}	$\lvert z_0^{electron} \rvert$ <60.0 cm	$\lvert z_0^{electron} \rvert$ <60.0 cm
L_{shr}	<0.2	
χ^2_{strip}	<10.0	
$Q \cdot \Delta X$	$-3.0 < Q \cdot \Delta X < 1.5$ cm	
$\lvert \Delta Z$	<3.0 cm	
$66 < M_{ee} < 116$ GeV/c^2		

Table 5.4: *Criteria for electron candidates used in this analysis. The energy and momentum are corrected for data only. The central-central* $Z^0 \rightarrow e^+e^-$ *candidates require at least one tight electron and at least one loose electron in the invariant mass window between 66 and 116 GeV/c^2. (*) The E/p cut is released for electrons with E_T >50 GeV/c^2.*

shows the transverse mass for these data, while Figure 5.12 and Figure 5.13 show the transverse energy of the electron from the W boson and the missing E_T respectively[6]. The disagreement between the data and the Monte Carlo in these plots can be due to the calorimeter calibration (which would affect the missing E_T calculation), and to a poor understanding of the missing E_T resolution and of the hadronic recoil energy. There is work in progress at the moment on all these issues. The signal MC histograms have been normalised to the number of background subtracted candidate events observed in the data, and the background histograms were normalized to the estimated background events (see chapter 6). The shape[7] of the QCD background was taken from non-isolated events in the data. In making the $\not\!\!E_T$ plot the $\not\!\!E_T$ cut has been removed and the isolation cut has been replaced with an anti-isolation cut $E_T^{iso} > 0.3$ to obtain the shape of the QCD background. As the E_T and M_T plots were made after applying the $\not\!\!E_T$ cut the number of QCD-type events is very small after applying the anti-isolation cut. Hence, for these plots some of the electron ID cuts have been removed

[6]In all the plots the blue dots are the data, the red histogram is PYTHIA signal Monte Carlo, the magenta is the QCD background, the green is $Z^0 \rightarrow e^+e^-$ background Monte Carlo and the cyan is PYTHIA $W^\pm \rightarrow \tau^\pm\nu$ background Monte Carlo.

[7]The estimate for the number of QCD background events is given in chapter 6.

(Lshr, ΔX,ΔZ,χ^2_{strip}), the anti-isolation cut has been loosened to $E_T^{iso} > 0.1$, and an anti Had/Em cut has been applied, in order to obtain the shape of the QCD background for these distributions. The agreement between the data, the Monte Carlos and the QCD background is reasonable. In addition, Figure 5.14 shows the ϕ and η distributions for the $W^{\pm} \rightarrow e^{\pm}\nu$ candidate events in the data. For the distributions of the electron ID variables see Figure 5.4 and 5.5.

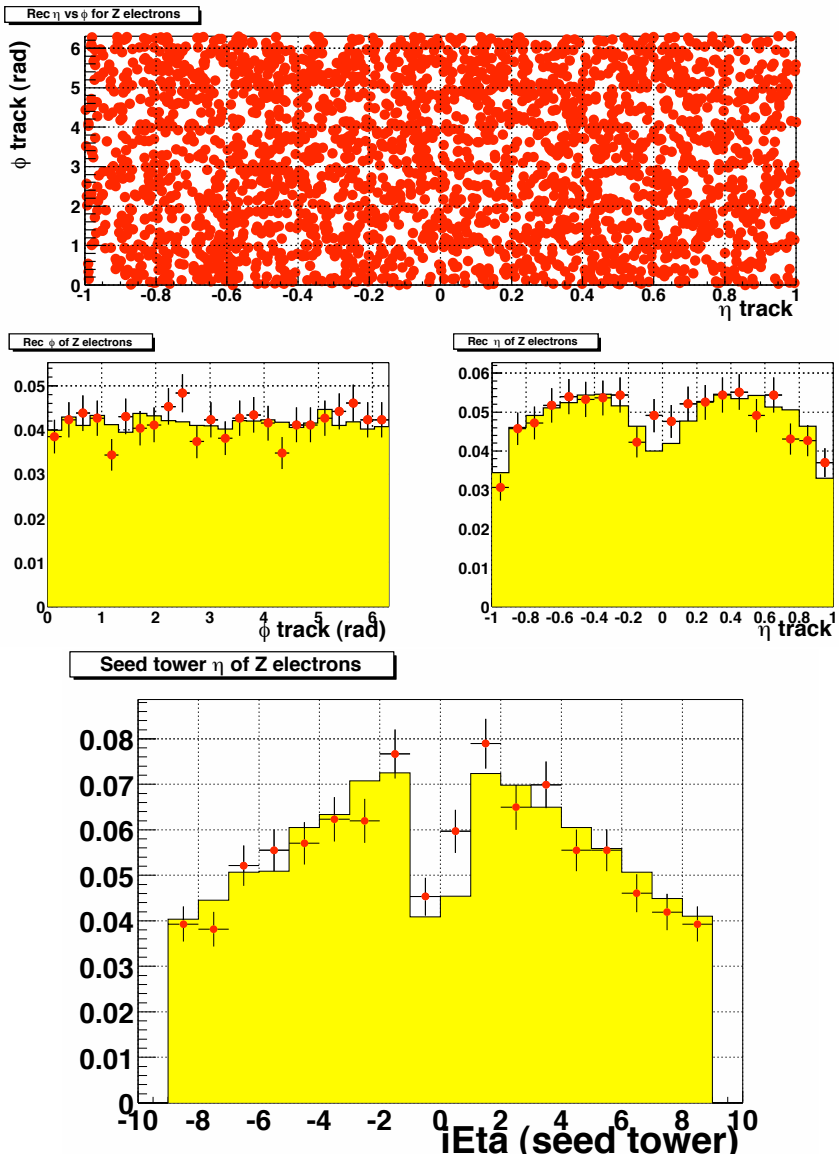

Figure 5.3: *The η and ϕ defined by the track associated with the tight and loose electrons for $Z^0 \rightarrow e^+e^-$ candidates (top and middle), and the distribution of the η tower index in the central region of the calorimeter for $Z^0 \rightarrow e^+e^-$ candidates. Points are data and histogram is the Monte Carlo simulation. It can be seen that the last tower, "tower 9", is excluded. The number of Monte Carlo events is normalised to the number of events in the data.*

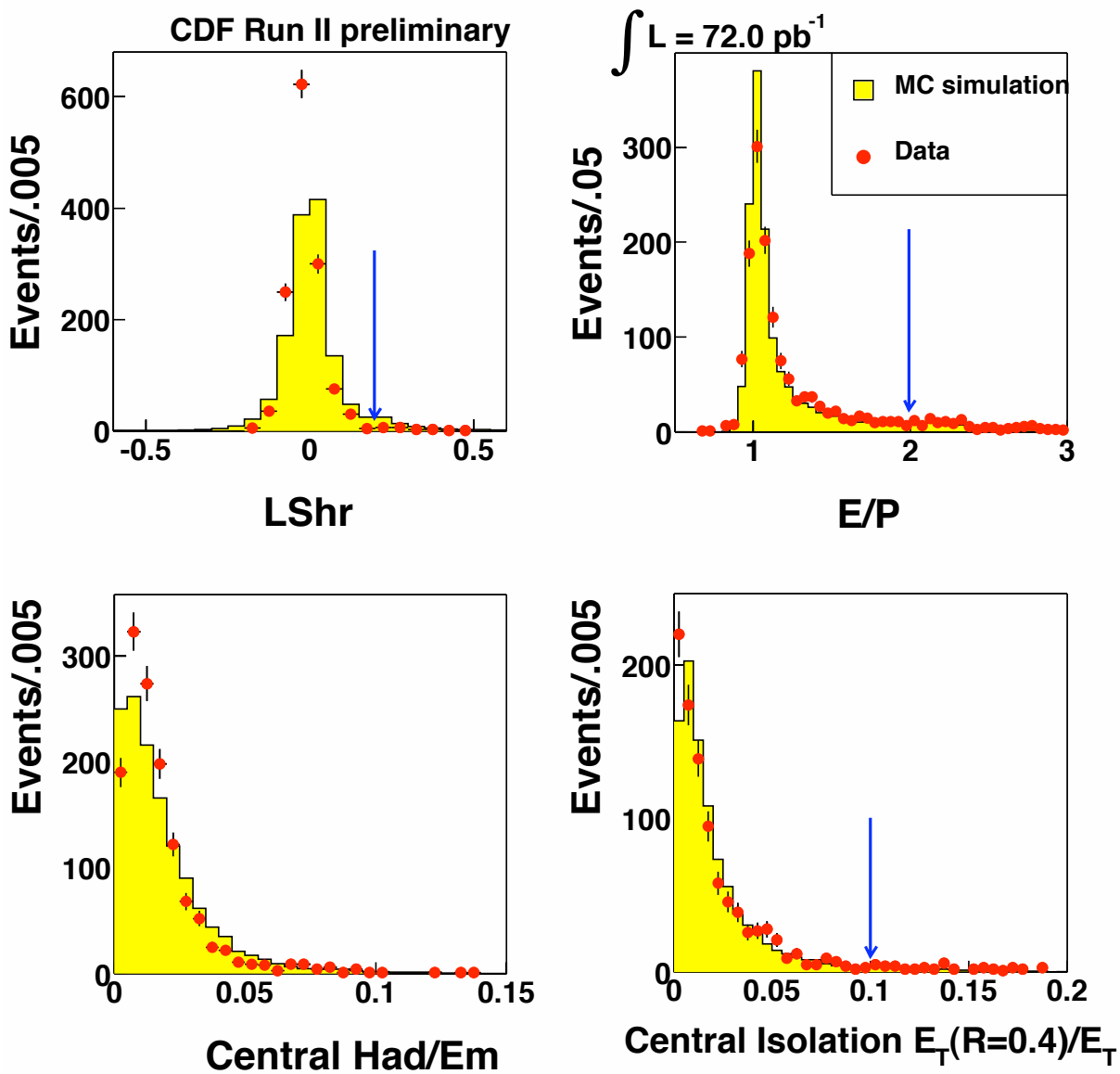

Figure 5.4: *The electron variables used for the selection of the events. The tight electrons in the* $Z^0 \rightarrow e^+e^-$ *candidates events (dots) and in the signal Monte Carlo (solid histogram) are used; for each variable all the selection criteria, but the one including the variable itself, are applied. The number of Monte Carlo events is normalised to the number of events in the data. The disagreement in the central bin of the Lshr distribution is due to a problem in the simulation which is not currently understood. The arrows show the value at which it has been cut to obtain the sample. For Had/EM the cut is a sliding cut that depends on the energy of the cluster, and thus is not shown.*

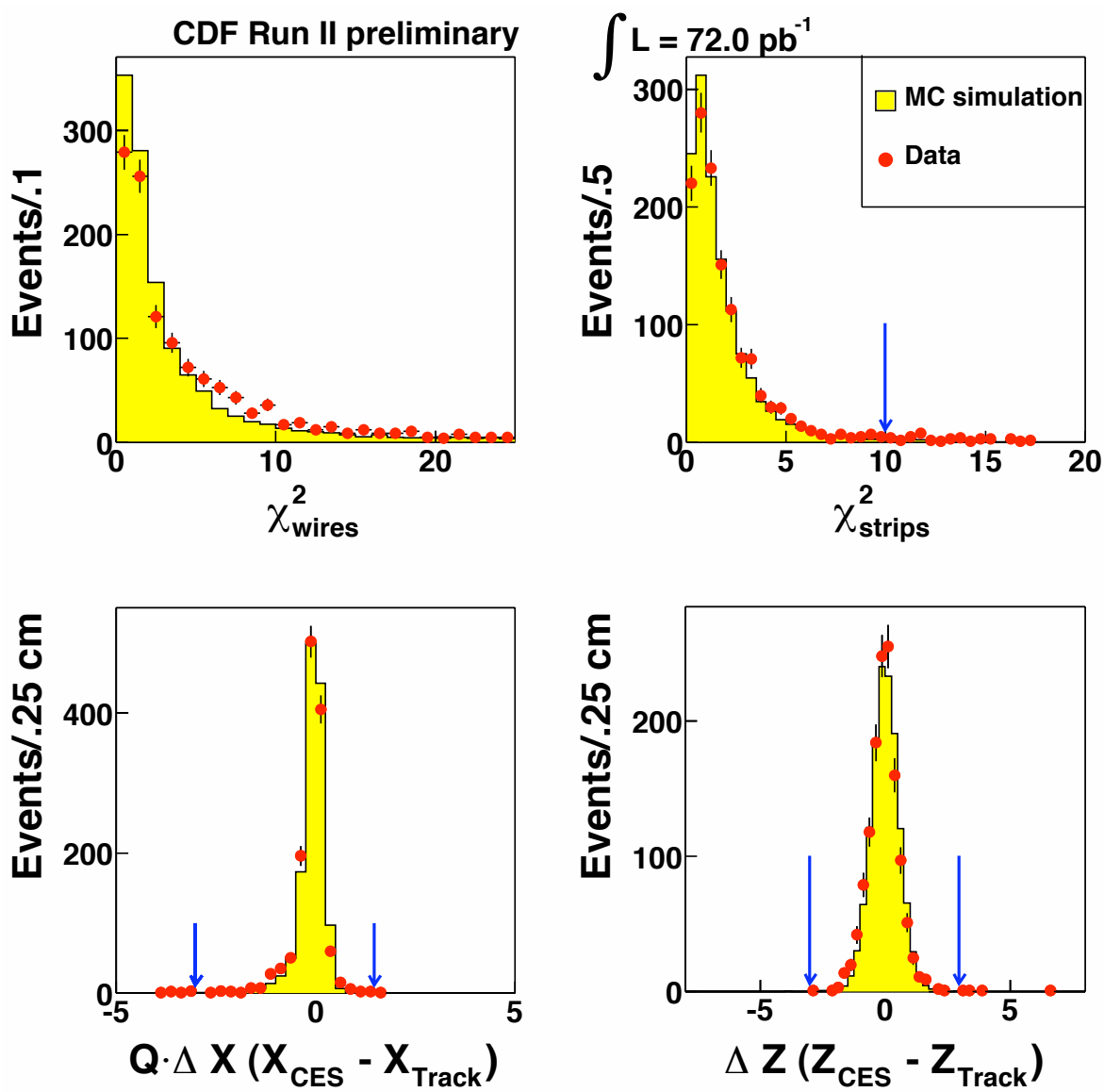

Figure 5.5: *The electron variables used for the selection of the events. The tight electrons in the* $Z^0 \to e^+e^-$ *candidates events (dots) and in the signal Monte Carlo (solid histogram) are used; for each variable all the selection criteria, but the one including the variable itself, are applied. The number of Monte Carlo events is normalised to the number of events in the data. The arrows show the value at which it has been cut to obtain the sample. The variable* χ^2_{wires}*(as defined in section 4.2.3) has not been used in the selection of the sample.*

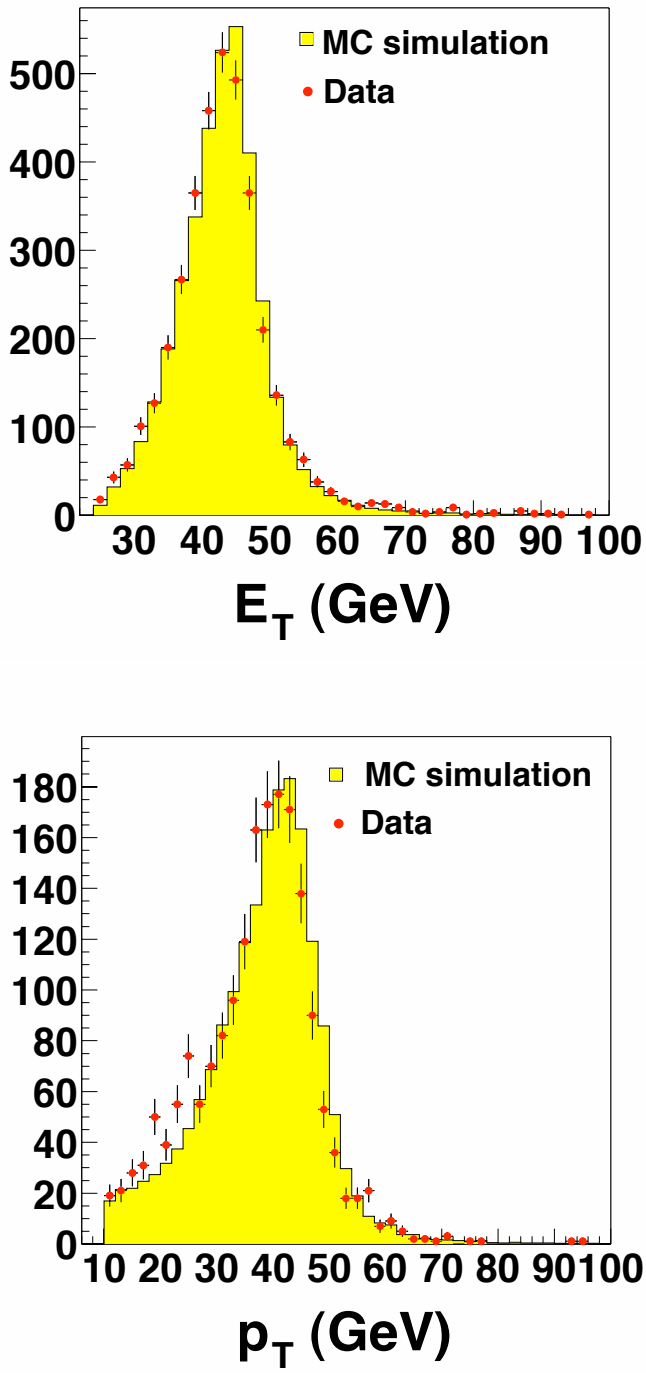

Figure 5.6: *Distribution of E_T and p_T for the tight electrons from* $Z^0 \to e^+e^-$ *candidate events.*

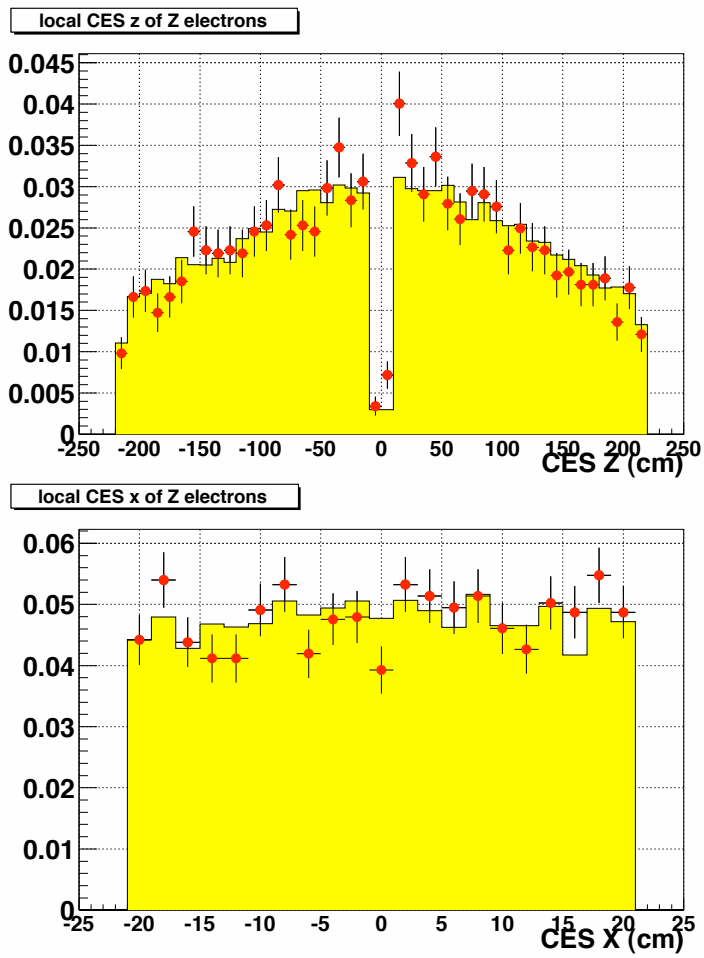

Figure 5.7: *The CES local Z and X distributions for* $Z^0 \to e^+e^-$ *candidates (dots) and signal Monte Carlo (solid histogram). The number of Monte Carlo events is normalised to the number of events in the data.*

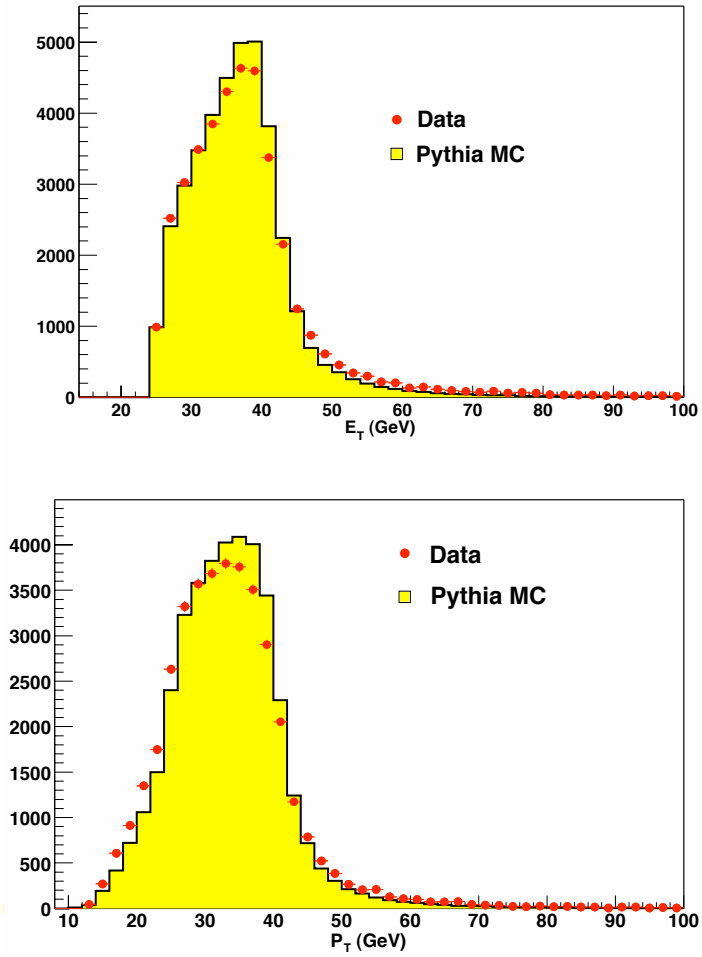

Figure 5.8: *Distribution of E_T and p_T for the electrons from* $W^{\pm} \rightarrow e^{\pm}\nu$ *candidate events[4].*

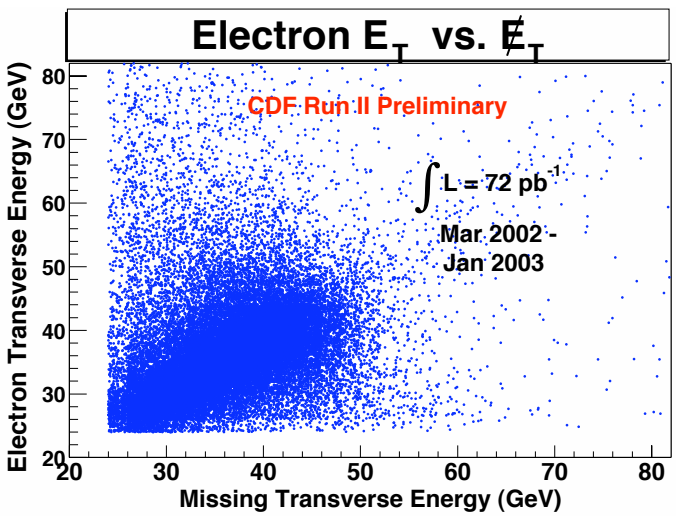

Figure 5.9: *Distribution of electron E_T vs. $\not{E}_T$ for the* $W^{\pm} \rightarrow e^{\pm}\nu$ *candidate events[1].*

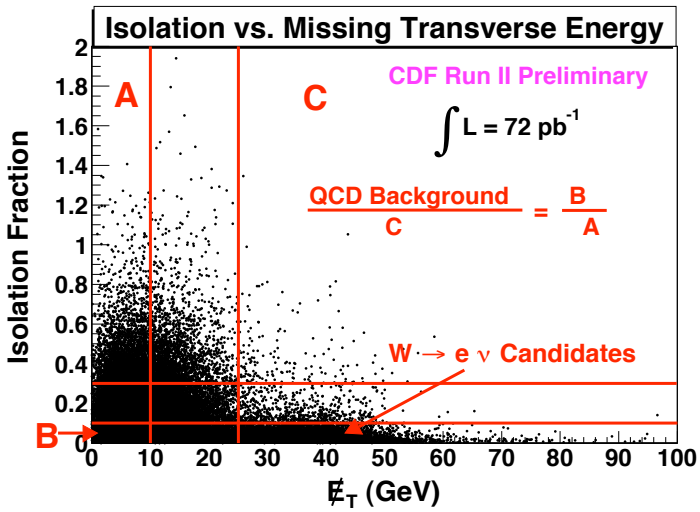

Figure 5.10: *Distribution of $\not{E}_T$ vs. the isolation fraction for the* $W^{\pm} \rightarrow e^{\pm}\nu$ *candidate events[1].*

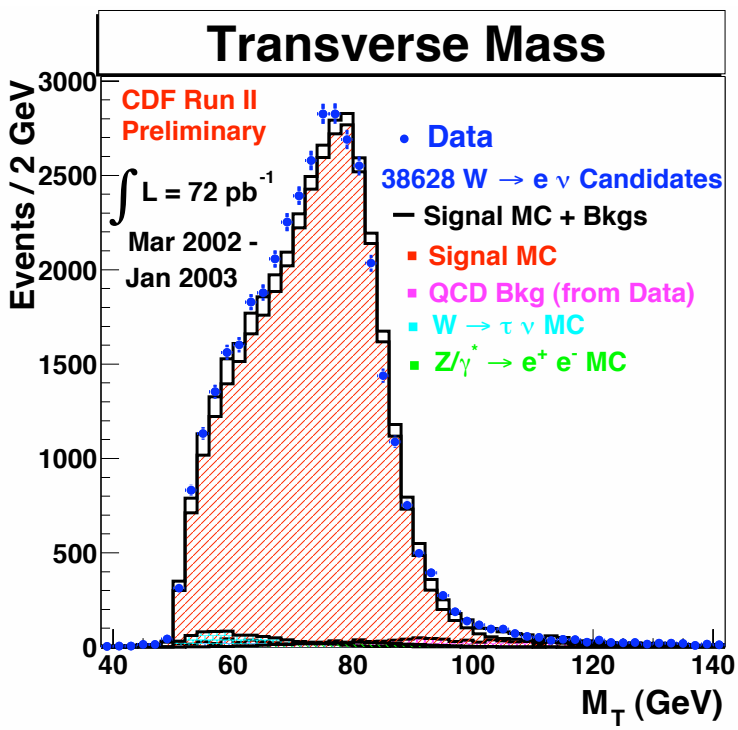

Figure 5.11: *Distribution of M_T for* $W^{\pm} \rightarrow e^{\pm}\nu$ *candidate events[1].*

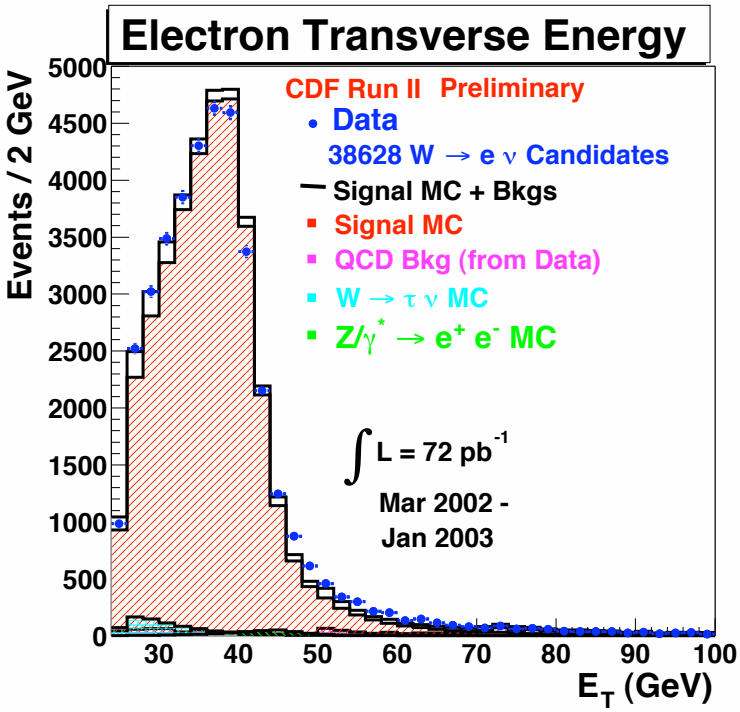

Figure 5.12: *Distribution of E_T for electrons in* $W^{\pm} \rightarrow e^{\pm}\nu$ *candidate events[1].*

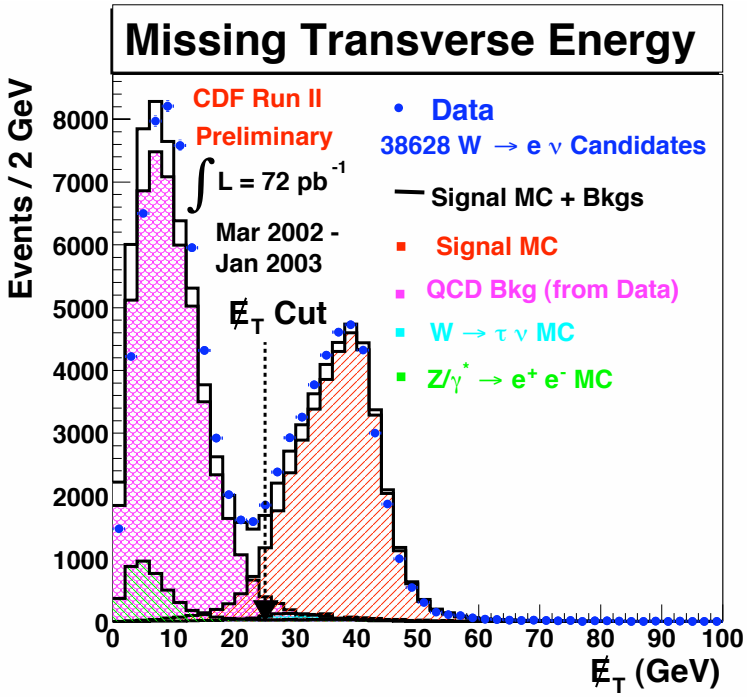

Figure 5.13: *Distribution of* $\not\!\!E_T$ *for* $W^{\pm} \rightarrow e^{\pm}\nu$ *candidate events[1].*

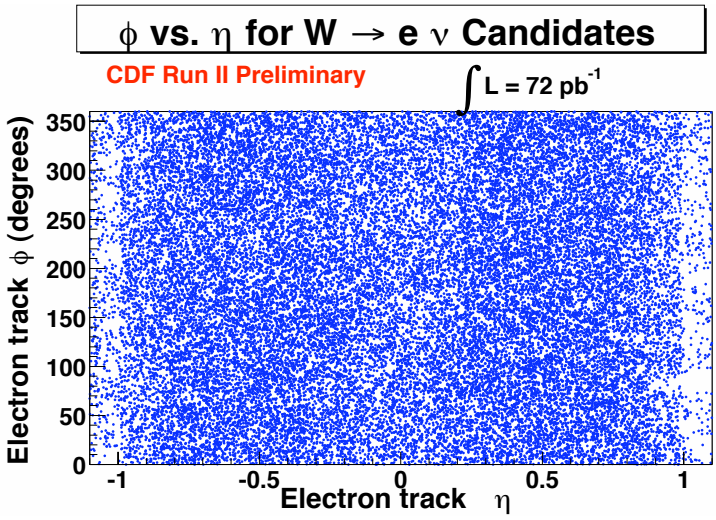

Figure 5.14: *Distribution of* ϕ *versus* η *for electrons in* $W^{\pm} \rightarrow e^{\pm}\nu$ *candidate events[1].*

Chapter 6

Backgrounds

Many physics processes can mimic the signature of Z and W events in the CDF detector, either because other objects are misidentified and mistakenly reconstructed as electrons, or because the event presents a similar topology. In this chapter the sources of backgrounds to real Z and W events are analysed, and the estimates for these backgrounds are given.

6.1 Backgrounds to the Z events

$Z^0 \rightarrow e^+e^-$ candidates present the very distinctive signature of an isolated, tight central electron and a second isolated electron, selected according to the criteria described in section 5.2.5 and Table 5.4. Very few physics processes can mimic this signature, with the QCD quark-antiquark production being the dominant one. Smaller contributions come from the $Z^0/\gamma^* \rightarrow \tau^+\tau^-$ and W+jets processes. All of these constitute background to $Z^0 \rightarrow e^+e^-$ events and as such will be analysed in the following sections.

6.1.1 Background from Hadron Jets

Processes which contain a real electron (such as a semi-leptonic decay of a quark or conversion of photons) or which can fake one (such as QCD jets or di-jets events) are included in the QCD background analysed in this section. As there is no reason for these kind of events to be preferentially positively

or negatively charged, they are expected to be charge symmetric; that is, the number of opposite sign(OS) and same sign(SS) QCD background events should be the same. Thus, it is possible to use the number of SS sign events to estimate the number of QCD background events in the OS sample.
In this analysis the number of events in the data that pass all the event selection criteria, but fail the opposite sign requirement, is first corrected for the number of real $Z^0 \to e^+e^-$ events (which can mimic SS events as discussed below) using the Monte Carlo predictions. The remaining number is then used as an estimate of the QCD background in the OS sample. The number of OS events in the data is 1830, and the number of SS sign events is 22; their invariant mass distributions are shown in Figure 4.7. The number of tracks pointing to the EM cluster and the difference in z_0 between the two electron tracks for the OS and SS samples are compared between the data and the simulation in Figure 6.1 and Figure 6.2.
As can be observed from the invariant mass distributions, both the Monte

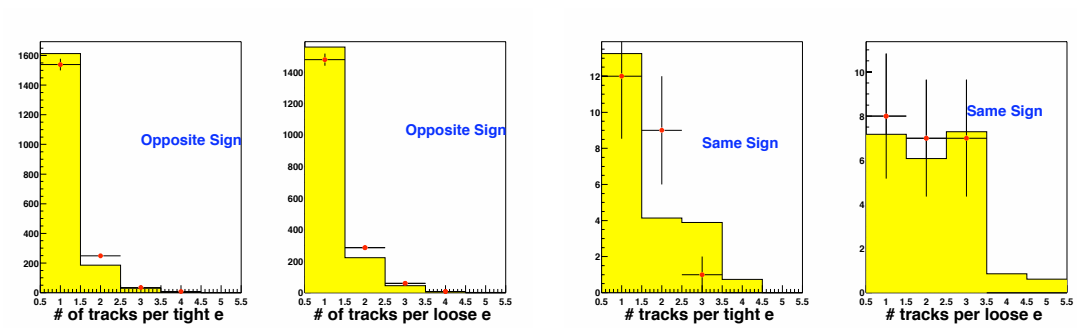

Figure 6.1: *The number of tracks pointing to electron clusters for the OS events (two left plots) and for the SS events (two right plots). The points are* $Z^0/\gamma^* \to e^+e^-$ *candidates and the histograms are* $Z^0/\gamma^* \to e^+e^-$ *Monte Carlo events; the number of events in the Monte Carlo is normalised to the number of opposite sign events in the data. The presence of clusters with two or three tracks associated with it in the SS sample is due to trident events, as described later in the text.*

Carlo and the data same sign distributions show a peak around 91 GeV, the mass of the Z boson. The events in the peak are the so called "trident" events (an example of a trident event is given in Figure 6.3). They are $Z^0/\gamma^* \to e^+e^-$ events where one electron from the Z radiates a high E_T photon while passing through the material; the photon then converts into an electron and a positron in the material.

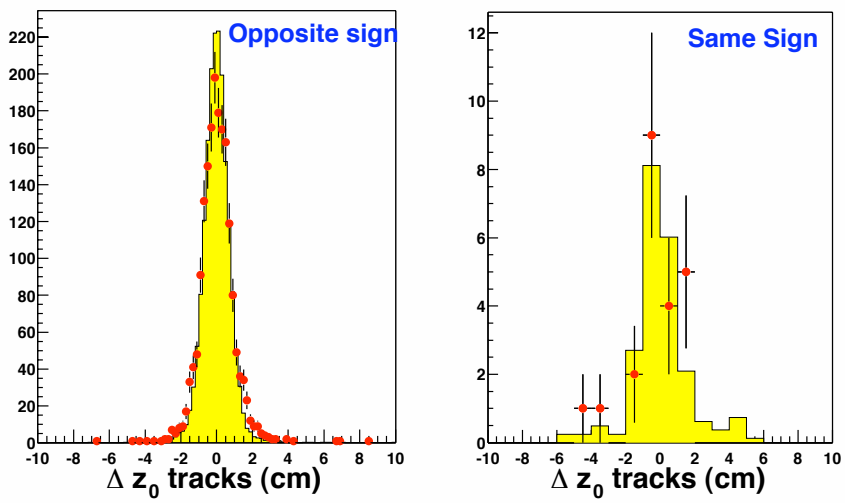

Figure 6.2: *Δz between the two electron tracks for opposite-sign events (left) and same-sign events (right). The points are $Z^0/\gamma^* \to e^+e^-$ candidates and the histograms are $Z^0/\gamma^* \to e^+e^-$ Monte Carlo events.*

If the positron from the photon conversion is chosen as the track associated to the electron cluster, the two tracks will have the same sign charge. As these are real $Z^0/\gamma^* \to e^+e^-$ events, they should not be removed from the sample. In order to account for this effect, the number of SS events in the data is corrected subtracting the number of same sign events in the Monte Carlo (which gives an estimate of the number of tridents in the data), normalised to the number of OS events in the data. As already stated, there are 22 SS events in the di-electron data sample with invariant mass between 66 GeV and 116 GeV, and 13.3 SS events are found in the $Z^0/\gamma^* \to e^+e^-$ Monte Carlo sample (see Figure 4.7 bottom). Thus, the QCD background is estimated to be $8.7 \pm 4.7(stat.)$, where the statistical uncertainty is on the number of SS events in the data. The invariant mass distribution of SS events, after the 13.3 Monte Carlo SS events are subtracted, is shown in Figure 6.4 (top).
The dominant source of systematic uncertainty on the QCD background is expected to come from the uncertainty on the amount of material between the beam-line and the COT inner cylinder, as this affects the probability that an electron emits a photon by bremsstrahlung. This effect has been studied using an *ad-hoc* sample with an extra 5.5% X_0 of the material added to the default geometry database, as described in section 5.1. Figure 6.5 shows the

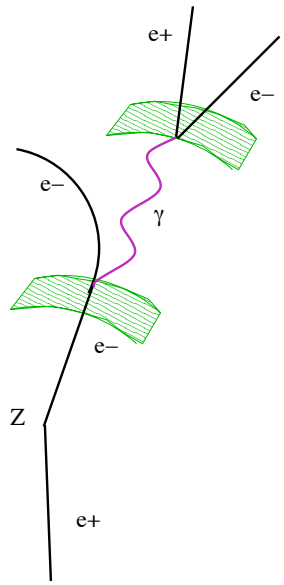

Figure 6.3: *Sketch of a "trident" event as described in the text. The green bands represent the layers of material in the detector.*

E/p distribution of electrons in the $Z^0/\gamma^* \to e^+e^-$ data compared with the default simulation (shaded histogram) and the simulation with the extra material (open histogram). The number of SS events in the mass region between 66 GeV/c^2 and 116 GeV/c^2 changes from 13.3 to 15.7 when the extra material is added (Figure 6.4 bottom). The difference between these two values is taken as a systematic uncertainty on the number of QCD background events in the OS $Z^0/\gamma^* \to e^+e^-$ sample. The QCD background is thus estimated to be $8.7 \pm 4.7(stat.) \pm 2.4(syst.) = 8.7 \pm 5.3$, where the total uncertainty is calculated by adding the statistical and systematic uncertainties in quadrature. More studies on the material are discussed in chapter 8.

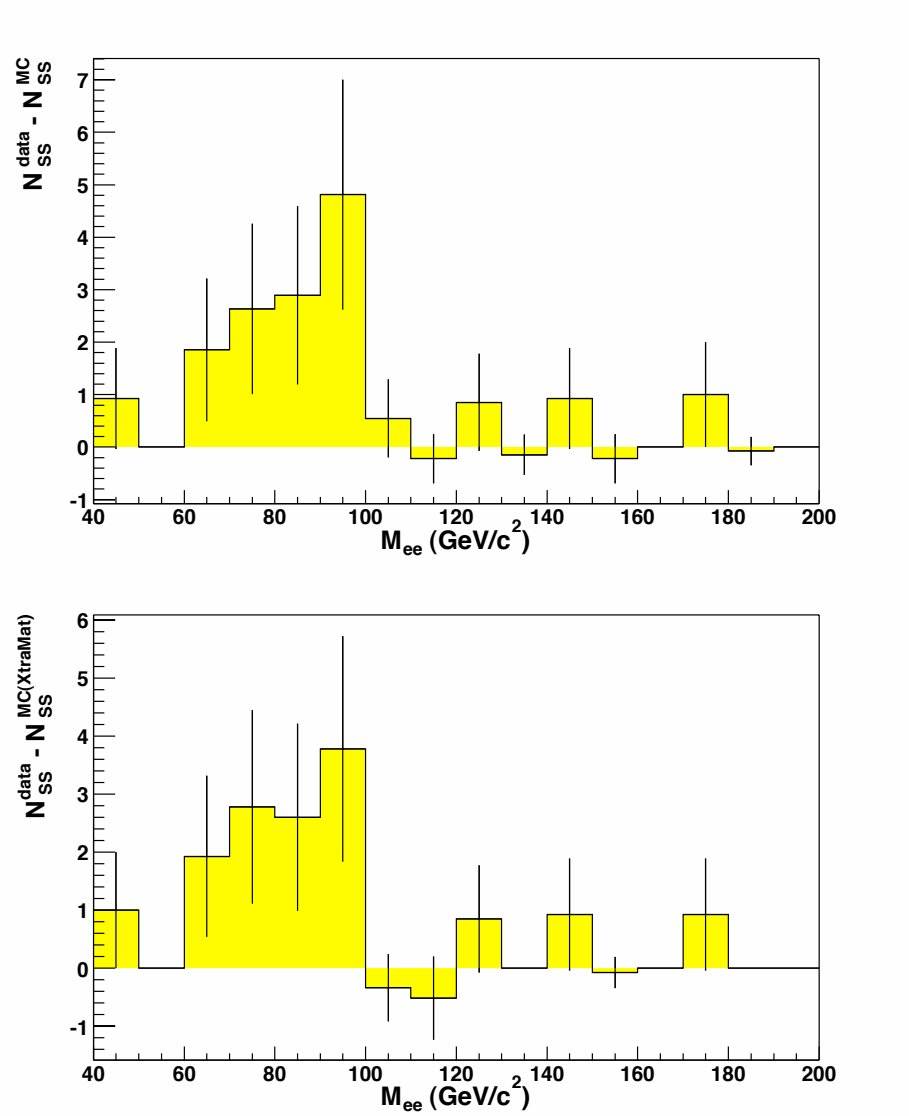

Figure 6.4: *The same sign invariant mass distribution in the data subtracted by the same sign invariant mass distribution obtained with the* $Z^0/\gamma^* \rightarrow e^+e^-$ *Monte Carlo sample with the default geometry (top) and with the added 5.5%* X_0 *extra material (bottom). As expected, in the Monte Carlo with the extra material the number of SS events (coming from tridents) is higher than in the default Monte Carlo, thus the difference with the data is smaller.*

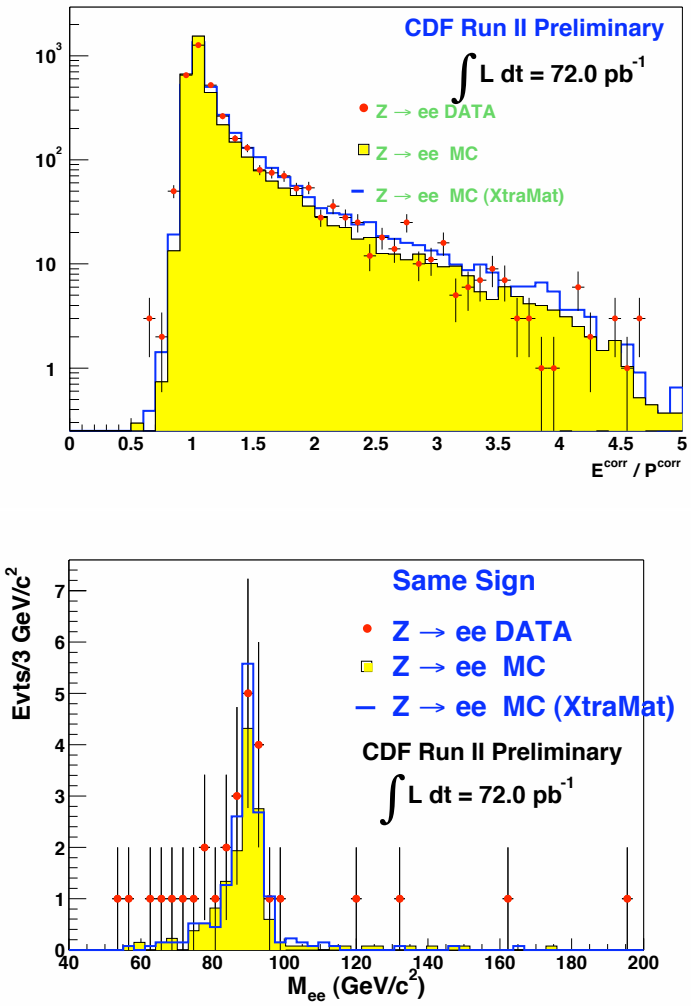

Figure 6.5: *The E/p distributions for electrons in OS $Z^0 \to e^+e^-$ events (top) and invariant mass distributions of SS events (bottom) for data (points) and Monte Carlo (histograms). The shaded histograms represent simulation with the default geometry and the open histograms represent simulation with an extra 5.5% X_0 of the default material.*

6.1.2 Background from $Z^0/\gamma^* \to \tau^+\tau^-$

The production of $Z^0/\gamma^* \to \tau^+\tau^-$ can sometimes be background to $Z^0/\gamma^* \to e^+e^-$ events when both taus decay via $\tau \to e\nu_e\nu_\tau$, and if the electrons form an invariant mass between 66 and 116 GeV/c^2. The Monte Carlo sample described in section 5.1 has been used for this study. In the left plot of Figure 6.6 the invariant mass distribution of the di-electron pairs in the MC $Z^0/\gamma^* \to e^+e^-$ signal sample is compared with the invariant mass from the di-tau pairs at the generator level . The right plot of Figure 6.6 shows the invariant mass

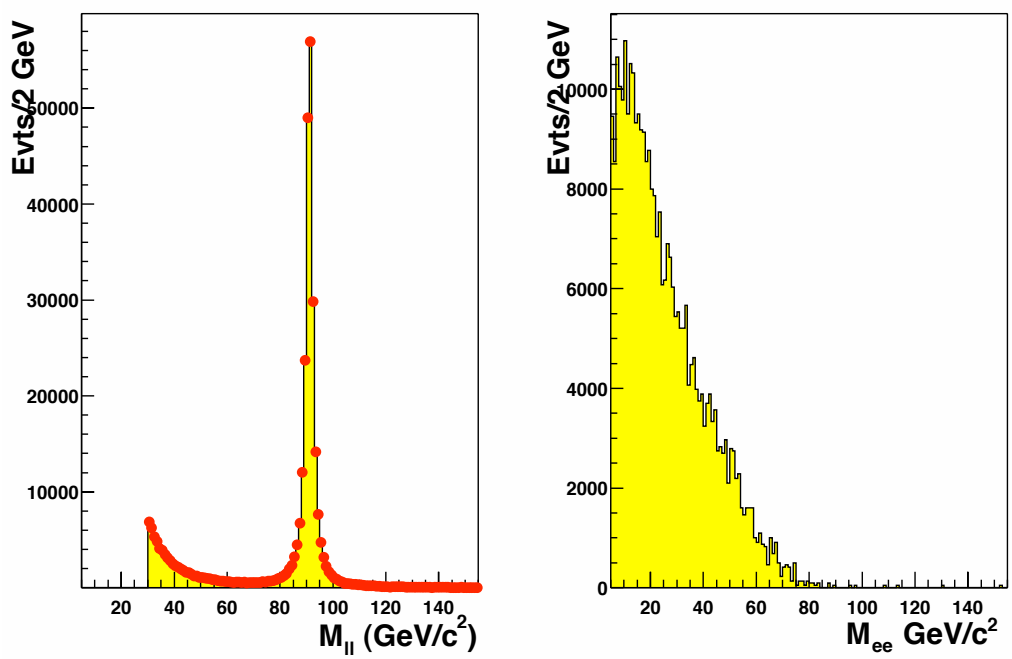

Figure 6.6: *Left plot: comparison of the $\tau^+\tau^-$ and e^+e^- invariant mass distribution at generator level for the events from $Z^0/\gamma^* \to e^+e^-$ signal (yellow histogram) and $Z^0/\gamma^* \to \tau^+\tau^- \to e^+\nu_e\bar{\nu}_\tau e^-\bar{\nu}_e\nu_\tau$ background (dots) Monte Carlo as a consistency check before any cut is applied. The peak at low values of $M_{\ell\ell}$ is due to the presence of the γ^*. In the right plot the invariant mass distribution (at generator level) from the electron pairs coming from the taus from the $Z^0/\gamma^* \to \tau^+\tau^- \to e^+\nu_e\bar{\nu}_\tau e^-\bar{\nu}_e\nu_\tau$ decay chain is reported for comparison.*

distribution from di-electron pairs in $Z^0/\gamma^* \to \tau^+\tau^- \to e^+\nu_e\bar{\nu}_\tau e^-\bar{\nu}_e\nu_\tau$ events at the generator level. The reconstructed invariant mass distribution of the

electrons from the $Z^0/\gamma^* \to e^+e^-$ and $Z^0/\gamma^* \to \tau^+\tau^- \to e^+\nu_e\bar{\nu}_\tau e^-\bar{\nu}_e\nu_\tau$ samples is shown in Fig. 6.7 for the whole range of invariant masses. It can be seen that the majority of the electrons from the tau decays have low invariant masses and would be already rejected by the invariant mass window cut at 66-116 GeV/c^2. In Fig. 6.8 the reconstructed E_T distributions for the electrons from the two samples are shown. After normalising to the luminosity

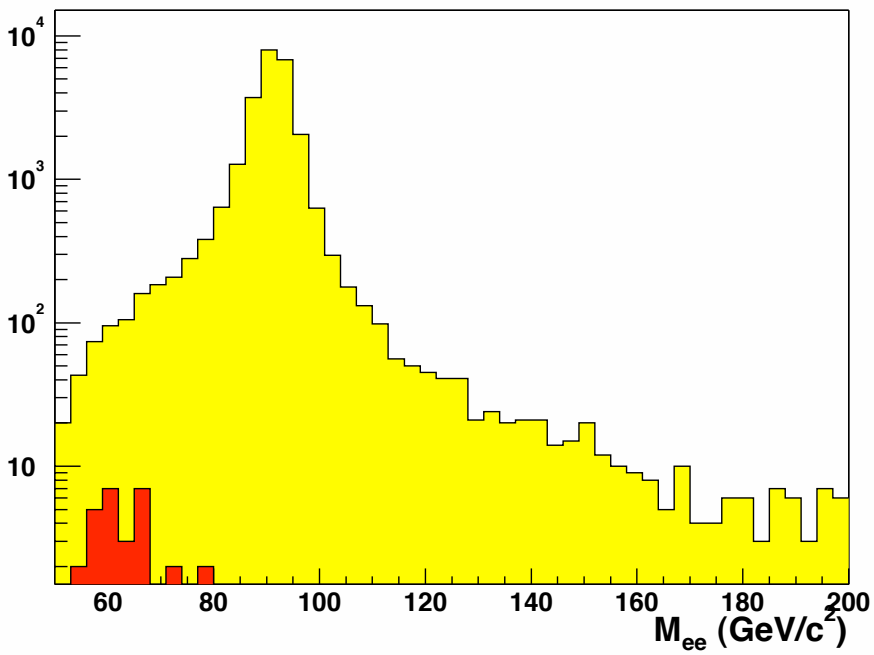

Figure 6.7: *Invariant mass distribution for the events from* $Z^0/\gamma^* \to e^+e^-$ *signal (yellow/light shaded histogram) and* $Z^0/\gamma^* \to \tau^+\tau^- \to e^+\nu_e\bar{\nu}_\tau e^-\bar{\nu}_e\nu_\tau$ *background Monte Carlo (red/dark shaded histogram).*

of the signal Monte Carlo sample, ten events pass the selection criteria. Assuming lepton universality, the number of $Z^0/\gamma^* \to \tau^+\tau^-$ background events can be written as

$$N_{\tau^+\tau^-} = N_{e^+e^-}^{signal} \cdot \frac{r_{\tau\tau}}{r_{ee}}$$

where :

- $N_{e^+e^-}^{signal}$ is the number of $Z^0/\gamma^* \to e^+e^-$ events in the data, thus

$$N_{e^+e^-}^{signal} = N_{e^+e^-}^{candidates} - N_{\tau^+\tau^-} - N_{QCD} - N_O,$$

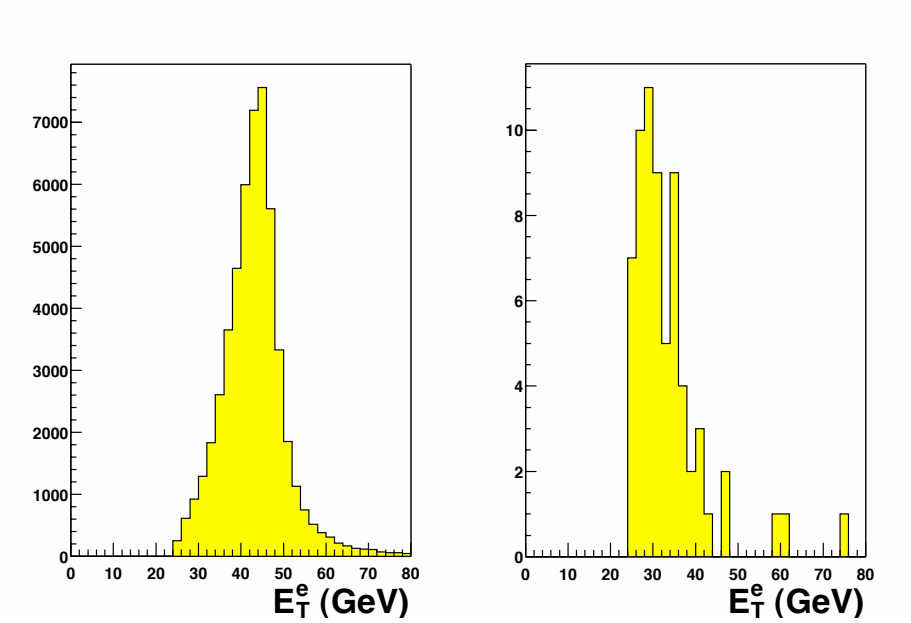

Figure 6.8: *Transverse energy distribution for the electrons from the Monte Carlo simulation for the* $Z^0/\gamma^* \to e^+e^-$ *signal (left) and* $Z^0/\gamma^* \to \tau^+\tau^- \to e^+\nu_e\bar{\nu}_\tau e^-\bar{\nu}_e\nu_\tau$ *background (right). The integrated luminosities of the two samples are the same.*

where $N_{\tau\tau}$ is the number of $Z^0/\gamma^* \to \tau^+\tau^-$ background, N_{QCD} is the number of QCD background[1] and N_O is the sum of all other backgrounds. The last is found to be negligible (see section 6.1.4 for details);

- r_{ee} is the number of the $Z^0/\gamma^* \to e^+e^-$ Monte Carlo events passing the selection criteria, normalised to the luminosity of the signal Monte Carlo sample, and

- $r_{\tau\tau}$ is the number of the $Z^0/\gamma^* \to \tau^+\tau^-$ Monte Carlo events passing the selection criteria, normalised as before.

The number of $Z^0/\gamma^* \to \tau^+\tau^-$ background events found is 1.0 ± 0.2, corresponding to $r_{\tau\tau}/r_{ee} = (0.05 \pm 0.01)\%$ contribution to the $Z^0 \to e^+e^-$ events.

[1]See section 6.1.1 for the calculation of the QCD background in the $Z^0/\gamma^* \to e^+e^-$ sample.

source of background	fraction of the sample	number of events
QCD	$(0.5 \pm 0.3)\%$	8.7 ± 5.3
$Z^0/\gamma^* \to \tau\ \tau\ \to e\ \nu_e\nu_\tau e\ \nu_e\nu_\tau$	$(0.05 \pm 0.01)\%$	1.0 ± 0.2
total	$(0.6 \pm 0.3)\%$	9.7 ± 5.3

Table 6.1: *Sources and amounts of backgrounds to the* $Z^0/\gamma^* \to e^+e^-$ *signal.*

6.1.3 Background from W+jets

The process of W production, where the W decays into an electron and neutrino, can mimic $Z^0/\gamma^* \to e^+e^-$ decays if the W is produced in association with a hadron jet that showers in the EM calorimeters and the W electron and the jet together fall in the 66-116 GeV/c^2 invariant mass window. This background is accounted for in the hadron jet background, since many of the second, misidentified electrons would be non-isolated. Using the Run I prediction[10] for the estimation of this background, it is found to be negligible(*i.e.* $<< 1$ event) for the value of luminosity considered in this analysis.

6.1.4 Summary of Z Candidates and Backgrounds

The total number of background events in the $Z^0 \to e^+e^-$ sample in the invariant mass range of 66 GeV/c^2 and 116 GeV/c^2 is estimated to be 9.7$\pm$5.3 events. The main source of background and the number of background events for each source are summarised in Table 6.1.

6.2 Backgrounds to the W Boson

The signature for W boson events used in this analysis is a single isolated central electron with missing transverse energy, as described in section 5.2.6. This signature can be mimicked by the same type of events which are backgrounds to the $Z^0/\gamma^* \to e^+e^-$ events, with the missing energy signature reproduced by QCD jets mismeasurements or by particles falling into uninstrumented regions of the detector. For instance, the decay of a W boson to a τ lepton or the loss of an electron in a $Z^0/\gamma^* \to e^+e^-$ event produce indistinguishable backgrounds. This section discusses the determination of the sizes of all backgrounds to the W boson.

6.2.1 Background from Hadron Jets

The high energy electrons produced through decays of heavy quarks and processes that fake electrons are grouped into the QCD background sample. Real electrons are produced by heavy quarks which decay semileptonically, pair production by photons and Dalitz decays. QCD hadronic jets can lead to background to the W signal if the hadron jet containing the electron fluctuates so that the electron is isolated in the calorimeters, and if the other jet falls into an uninstrumented region of the detector, creating $\not\!\!E_{\mathrm{T}}$.
The sum of these backgrounds is estimated by extrapolating[2] the isolation variable for the electron from a region away from the W signal, into the W signal region. This method does not identify the individual background contributions, but the sum of all the processes.
The motivation of the method is that electrons from hadron jets are generally produced embedded in a jet of other particles which will cause them to have a higher value of the isolation variable. If the fluctuation that caused the electron to be isolated is independent of the fluctuation that caused the other jet to be mismeasured, then the isolation and $\not\!\!E_{\mathrm{T}}$ variables are non-correlated in QCD events. This lack of correlation would imply that the shape of the isolation variable at low $\not\!\!E_{\mathrm{T}}$ may be extrapolated upward in $\not\!\!E_{\mathrm{T}}$ towards the W signal region. Figure 5.10 shows the manner in which the hadron backgrounds contaminate the signal region. The isolation fraction of the central electron in a high p_T electron event versus the $\not\!\!E_{\mathrm{T}}$ in the event is plotted. Four regions are identified within the plot:

Region A, defined by having isolation > 0.3 and $\not\!\!E_{\mathrm{T}} < 10$ GeV;

Region B, defined by having isolation < 0.1 and $\not\!\!E_{\mathrm{T}} < 10$ GeV;

Region C, defined by having isolation > 0.3 and $\not\!\!E_{\mathrm{T}} > 25$ GeV;

Region D, the signal region, defined by having isolation < 0.1 and $\not\!\!E_{\mathrm{T}} > 25$ GeV;

The background in the signal region is estimated from the equation:

$$\frac{W\ background}{\#Events\ in\ Region\ C} = \frac{\#Events\ in\ Region\ B}{\#Events\ in\ Region\ A}. \tag{6.1}$$

[2]This method was first used in [78].

Region A	Region B	Region C	Background	Purity (%)
6041	28379	286	$1344 \perp 82(stat.) \perp 672(syst.)$	$96.5 \perp 0.2(stat.)$

Table 6.2: *QCD background estimates in the W sample. The last column shows the purity of the sample.*

Using the 38,628 candidate events in the $W^{\pm} \rightarrow e^{\pm}\nu$ sample (as stated in section 5.2.6), and the events in regions A,B and C as reported in Table 6.2, the amount of QCD background events is estimated to be 1344±82, where the uncertainty is the statistical uncertainty on the number of events. The last column of Table 6.2 shows the purity of the sample, estimated ignoring the other backgrounds. In order to estimate the systematic uncertainty associated with this technique, the location of the upper isolation value and of the lower $\not{E}_T$ value used to identify the regions A and B have been varied and the background has been recalculated for each value. Figure 6.9 shows the number of QCD background events as a function of the isolation (top) and $\not{E}_T$ (bottom) values chosen to define the control regions. The background estimate seems to be independent of the value of the $\not{E}_T$ cut, but highly dependent on the location of the isolation cut. Using the difference between the highest and the lowest values in the upper plot of Figure 6.9, the systematic uncertainty was estimated to be 50%, corresponding to 672 events[1].

6.2.2 Background from $Z^0/\gamma^* \rightarrow e^+e^-$

$Z^0/\gamma^* \rightarrow e^+e^-$ events can also mimic the $W^{\pm} \rightarrow e^{\pm}\nu$ signal when one of the electrons falls into an uninstrumented region of the detector, creating missing energy. The estimate of this background has been performed using the $Z^0/\gamma^* \rightarrow e^+e^-$ MC sample described in section 5.1. 7716 survived the selection criteria described in section 5.2.6. Following the same procedure as in section 6.1.2, the number of $Z^0/\gamma^* \rightarrow e^+e^-$ background events can be written as

$$N_{Z^0/\gamma^* \rightarrow e^+e^-} = N^{signal}_{W^{\pm} \rightarrow e^{\pm}\nu} \cdot \frac{r_{Z^0/\gamma^* \rightarrow e^+e^-}}{r_{W^{\pm} \rightarrow e^{\pm}\nu}}$$

where:

- $N^{signal}_{W^{\pm} \rightarrow e^{\pm}\nu}$ is the number of $W^{\pm} \rightarrow e^{\pm}\nu$ events in the data, thus

$$N^{signal}_{W^{\pm} \rightarrow e^{\pm}\nu} = N^{candidates}_{W^{\pm} \rightarrow e^{\pm}\nu} - N_{Z^0/\gamma^* \rightarrow e^+e^-} - N_{W^{\pm} \rightarrow \tau^{\pm}\nu} - N_{QCD},$$

with $N_{W^{\pm}\to\tau^{\pm}\nu}$ and N_{QCD} being the number of $W^{\pm} \to \tau^{\pm}\nu$ and QCD background events respectively. The estimates for these events can be found in sections 6.2.1 and 6.2.3;

- $r_{W^{\pm}\to e^{\pm}\nu}$ is the number of the $W^{\pm} \to e^{\pm}\nu$ Monte Carlo events passing the selection criteria, normalised to the luminosity of the signal Monte Carlo sample,

- $r_{Z^0/\gamma^*\to e^+e^-}$ is the number of the $Z^0/\gamma^* \to e^+e^-$ Monte Carlo events passing the $W^{\pm} \to e^{\pm}\nu$ selection criteria, normalised as before.

344±17 background events are found, corresponding to $r_{Z^0/\gamma^*\to e^+e^-}/r_{W^{\pm}\to e^{\pm}\nu} = (0.95 \pm 0.05)\%$ contribution to the signal events[1].

6.2.3 Background from $W \to \tau\nu$

$W^{\pm} \to \tau^{\pm}\nu$ is a source of background events to the $W^{\pm} \to e^{\pm}\nu$ signal when the τ decays leptonically to an electron and neutrinos, creating a high p_T electron and missing energy. The $W^{\pm} \to \tau^{\pm}\nu$ MC sample described in section 5.1 has been used in this study. 2166 events survive the selection criteria described in section 5.2.6. Following the same procedure of sections 6.1.2 and 6.2.2, the number of $W^{\pm} \to \tau^{\pm}\nu$ background events can be expressed as

$$N_{W^{\pm}\to\tau^{\pm}\nu} = N^{signal}_{W^{\pm}\to e^{\pm}\nu} \cdot \frac{r_{W^{\pm}\to\tau^{\pm}\nu}}{r_{W^{\pm}\to e^{\pm}\nu}}$$

where:

- $N^{signal}_{W^{\pm}\to e^{\pm}\nu}$ is the number of $W^{\pm} \to e^{\pm}\nu$ events in the data, thus

  $$N^{signal}_{W^{\pm}\to e^{\pm}\nu} = N^{candidates}_{W^{\pm}\to e^{\pm}\nu} - N_{W^{\pm}\to\tau^{\pm}\nu} - N_{Z^0/\gamma^*\to e^+e^-} - N_{QCD}$$

  (see sections 6.2.1 and 6.2.2 for the estimates of N_{QCD} and $N_{Z^0/\gamma^*\to e^+e^-}$);

- $r_{W^{\pm}\to e^{\pm}\nu}$ is the number of the $W^{\pm} \to e^{\pm}\nu$ Monte Carlo events passing the selection criteria, normalised to the luminosity of the signal Monte Carlo sample,

- $r_{W^{\pm}\to\tau^{\pm}\nu}$ is the number of the $W^{\pm} \to \tau^{\pm}\nu$ Monte Carlo events passing the $W^{\pm} \to e^{\pm}\nu$ selection criteria, normalised as in section 6.2.2.

This procedure leads to 768 ± 22 background events, corresponding to $r_{W^{\pm}\to\tau^{\pm}\nu}/r_{W^{\pm}\to e^{\pm}\nu} = (2.12 \pm 0.06)\%$ contribution to the signal events[1].

source of background	fraction of the sample	number of events
QCD	$(3.7 \pm 1.9)\%$	1344 ± 677
$Z^0/\gamma^* \to e^-e^-$	$(0.95 \pm 0.05)\%$	344 ± 17
$W^+ \to \tau^+\nu$	$(2.12 \pm 0.06)\%$	768 ± 22
total	$(6.8 \pm 1.9)\%$	2456 ± 678

Table 6.3: *Sources and amounts of backgrounds to the* $W^\pm \to e^\pm\nu$ *signal.*

6.2.4 Summary of W Candidates and Backgrounds

The total number of background events to the $W^\pm \to e^\pm\nu$ signal is $2456 \pm 82(stat.) \pm 673(syst.)$. The main sources and the relative contributions are reported in Table 6.3. A separate evaluation of the systematic errors on the $Z^0/\gamma^* \to e^+e^-$ and the $W^\pm \to \tau^\pm\nu$ backgrounds has not been made as these are covered by that on the QCD background, which is conservative.

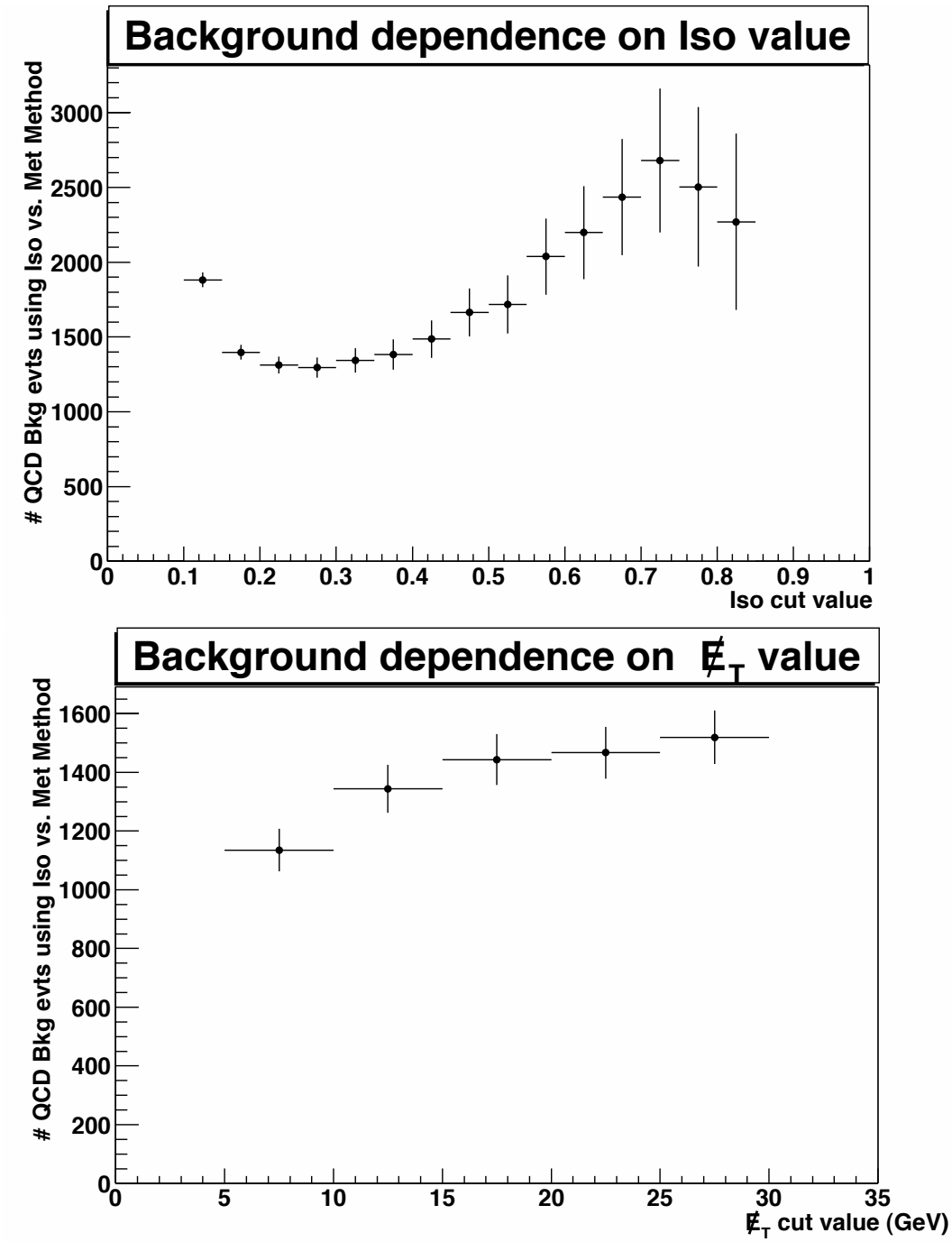

Figure 6.9: *Dependence of the number of QCD background events on the value of the isolation cut(top) and the $\not\!\!E_T$ cut (bottom)[1].*

Chapter 7

Central Electron Efficiencies

The cross section estimation has to be corrected for the efficiency of finding an electron. This includes the efficiency of the trigger finding the electron, the COT tracking efficiency and the efficiency of the criteria used to select the events, as listed in Table 5.4. The calculation of these efficiencies is discussed in the following sections.

7.1 Central Electron Trigger Efficiencies

This analysis uses samples triggered by the high p_T electron trigger described in section 4.3. The efficiency of the triggers has been studied in detail in [2], and the results are briefly summarized in this section. As explained in section 4.3, the high p_T electron trigger consists of track triggers, involving the XFT at Level-1 and Level-2 and the COT at Level-3, and calorimeter triggers at Level-2 and Level-3. In order to estimate the efficiency of this trigger, each component has been tested separately and the correspondent efficiency calculated at each step.
To find the efficiency of a single part of the high p_T electron trigger, a "back-up" trigger has been used, where no requirement has been made about the quantity which will be tested. The same criteria applied in the trigger are then applied on the variable which is being tested, finding the efficiency of the criteria. The "back-up" triggers used in this procedure are listed hereafter.

- The XFT and COT tracking efficiencies have been calculated using the

	high p_T electrons	W no track	W notr. No L2	inclusive muons
L1 Req.	Central EM cluster E_T >8 GeV *and* XFT track p_T >8 GeV	EM cluster E_T >8 GeV *and* $\not\!\!E_T$ > 15 GeV	EM cluster E_T >8 GeV *and* $\not\!\!E_T$ >15 GeV	XFT track p_T >8 GeV *and* Muon stub
L1 Pre-Scale	1	1	1	1
L2 Req.	Central EM cluster E_T >16 GeV *and* XFT track p_T >8 GeV	Central EM cluster E_T >20	Auto Accept	Auto Accept
L2 Pre-Scale	1	1	50	1
L3 Req.	Central EM cluster E_T >18 GeV *and* COT track p_T >9 GeV	EM cluster E_T >25 *and* $\not\!\!E_T$ > 25 GeV	EM cluster E_T >25 GeV *and* $\not\!\!E_T$ > 25 GeV	COT track p_T >12 GeV *and* Muon stub
L3 Pre-Scale	1	1	1	1

Table 7.1: *Trigger requirements for the physics and back-up triggers. The* `Wnotrack_NoL2` *trigger has been pre-scaled of a factor 50 at Level-2 to maintain the desired trigger event rate with the higher luminosity.*

"`Wnotrack`" trigger, which demands the same calorimeter requirements used for the high p_T electron trigger, but does not require tracks associated with the EM clusters. Since the Level-1 track trigger definitions have been changed[79] twice over the period of data taking considered for this analysis[1], the track efficiencies have been calculated separately for these three periods, I, II and III, corresponding to: before July 2002, between July and September 2002, and between September 2002 and January 2003 respectively.

- The calorimeter trigger efficiency at Level-1 has been calculated using the `inclusive muon triggers`, which select a sample with hits in the muon chambers but have no requirements on the calorimeter quantities.

- Finally, the L2 calorimeter cluster trigger efficiency has been tested using the "`Wnotrack_NoL2`" trigger, which is the same as the "`Wnotrack`" trigger, but without any requirement at Level-2 ("Level-2 Auto Accept"). The efficiency has been calculated applying these requirements off-line.

The requirements for the high p_T electron trigger and the back-up triggers are listed in Table 7.1. The **track triggers' efficiencies** are found to be independent of p_T for tracks with $p_T > 10$ GeV/c, but dependent on η for both the Level-1 and Level-3 triggers, as shown in Figure 7.1. The efficiencies measured in the three periods are:

[1]This has been done in order to optimize trigger rates and efficiencies and minimize fake rates with the increase in instantaneous luminosity.

L1 : the average efficiencies at Level-1 are $(96.76 \pm 0.25)\%$ in period I, $(98.99 \pm 0.14)\%$ in period II, and $(96.6 \pm 0.1)\%$ in period III.

L3 : the average efficiencies at Level-3 are $(99.59 \pm 0.09)\%$, $(98.94 \pm 0.14)\%$, and $(99.24 \pm 0.10)\%$, respectively.

The η dependence of track trigger efficiencies can be written as

$$\epsilon_{tracking}(\mathrm{L1}) = 1 - \frac{\mathrm{p}_0}{2\pi\sigma} \cdot \exp(-\frac{\eta^2}{2\sigma^2}),$$

where $p_0 = 0.0541 \pm 0.0038$ and $\sigma = 0.297 \pm 0.023$, and

$$\epsilon_{tracking}(\mathrm{L3}) = \mathrm{p}_0 + \mathrm{p}_1 \cdot |\eta| + \mathrm{p}_2 \cdot |\eta|^2,$$

where $p_0 = -3.83 \pm 0.12$, $p_1 = 11.24 \pm 0.14$, and $p_2 = -6.53 \pm 0.13$. The Level-2 track triggers are 100% efficient.

The Level-1 **calorimeter trigger** has been studied using a sample of inclusive muons and removing any activity in the plug. The probability for electrons with $20 < E_T < 25$ GeV to fail the L1 trigger is found to be less than $1\% \times 0.46\% = 0.005\%$; thus, the L1 calorimeter trigger efficiency for electrons with $E_T > 20$ GeV is estimated to be 100%.
The E_T dependent Level-2 calorimeter trigger efficiency as shown in Figure 7.2 is measured to be

$$\epsilon_{calorimeter}(\mathrm{L2}) = 1 - \mathrm{p}_0 \cdot \exp(-\mathrm{p}_1 \cdot \mathrm{E_T}),$$

where $p_0 = 134.2 \pm 186.6$ and $p_1 = 0.412 \pm 0.071$. As the Level-3 clustering algorithm is identical to the one used offline, the calorimeter trigger efficiency is estimated to be 100%. Possible inefficiencies due to different scale factors and the tower-to-tower gain corrections (which are not applied at L3) are currently under study.

As the L1 and L3 calorimeter triggers are fully efficient, the electron trigger efficiency is just the tracking trigger efficiency, averaged over the three periods. The average tracking-trigger efficiency for triggering a single electron in the event is calculated by multiplying the values described in the previous paragraphs in each period (see Table 7.2 for the average tracking trigger efficiencies), and weighting them by the integrated luminosities in the three periods. Its value is measured to be $\langle \epsilon^e_{trig} \rangle = 96.6 \pm 0.1\%$. In the selection of the $Z^0 \to e^+e^-$ events, because there are two chances to fire

Period	I	II	III
Int. Luminosity	9.9 pb^{-1}	18.5 pb^{-1}	43.6 pb^{-1}
$\epsilon_{\text{track}}^{\text{trigger}}$	$(96.4 \pm 0.3)\%$	$(97.9 \pm 0.2)\%$	$(96.1 \pm 0.2)\%$

Table 7.2: *Averages of total track trigger efficiencies for the three time periods.*

the trigger, the average tracking trigger efficiency for at least one of the Z^0 electrons to fire the trigger is estimated to be

$$\langle \epsilon_{trig}^{ee} \rangle = \epsilon_{trig}^{e} + (1 - \epsilon_{trig}^{e})\epsilon_{trig}^{e} = \epsilon_{trig}^{e}(2 - \epsilon_{trig}^{e}) = (99.9^{+0.1}_{-0.7})\%.$$

7.2 Central Electron Tracking Efficiency

The tracking efficiency in the central region is mainly the efficiency of the COT algorithms used to reconstruct the track. This efficiency has been studied[80] both in Monte Carlo, using the true information, and data, using events selected with the "`Wnotrack`" trigger, described in section 7.1, and the silicon information. In the calculation of the cross sections for the ratio the tracking efficiency enters either in the selection of the events (data) or in the calculation of the acceptance (Monte Carlo). As the tracking efficiency in the data ϵ_{COT}^{data} appears in the numerator and the tracking efficiency in the Monte Carlo ϵ_{COT}^{MC} is in the denominator in the cross sections formulae, the number used in this analysis is the ratio of these two[80]

$$\begin{aligned} R_{COT} &= \frac{\epsilon_{COT}^{data}}{\epsilon_{COT}^{MC}} \\ &= 1.000^{+0.000}_{-0.004} \end{aligned}$$

The COT tracking algorithm can thus be considered 100% efficient.

7.3 Central Electron ID Efficiencies

In this section the efficiencies of the cuts used to select the Z and W events are estimated using the tight central electron data sample described in sec-

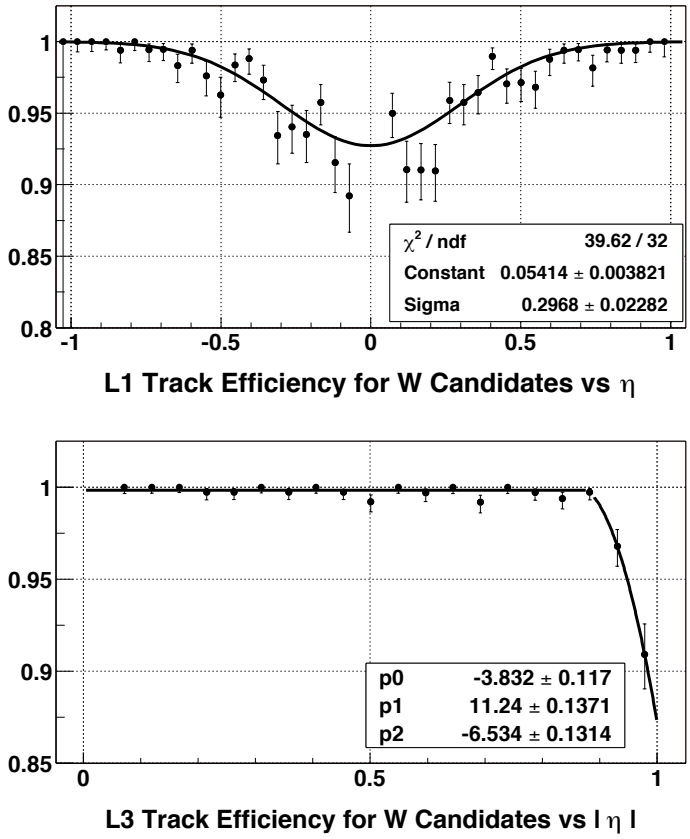

Figure 7.1: *Level-1 (top) and Level-3 (bottom) tracking efficiencies as a function of η measured by CES[2]. Data from period III were used.*

tion 5.2.4. As there are two selection criteria for the tight and loose electron, a tight and a loose efficiency will be calculated.

7.3.1 Selection of the events

To calculate the efficiencies of the cuts listed in Table 5.4, events are selected from the tight central electron data sample requiring a tight electron and a second cluster in the central region. The criteria for this selection are described in Table 7.3; the invariant mass window $75 < \mathrm{M}_{ee} < 105$ GeV/c^2 has been used, to reduce the number of background events in the sample. The distributions of the electron variables can be found in Figure 5.4 and Figure 5.5. The sample consists of 1933 events with one tight electron and

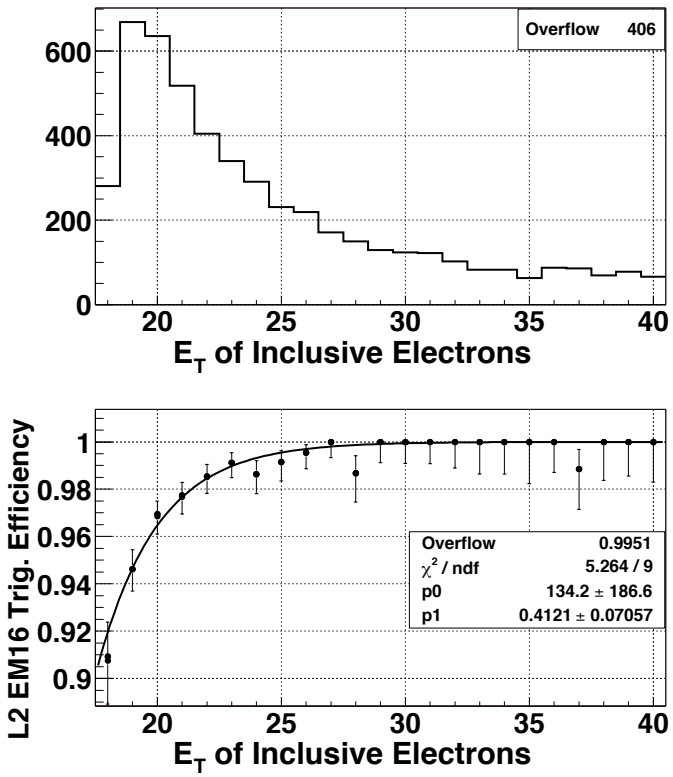

Figure 7.2: *E_T distribution of electron candidates from data passing the L2 pre-scaled trigger used to measure L2 cluster trigger efficiency (top) and L2 cluster efficiency as a function of E_T (bottom)[2].*

one second central cluster. These events are used to calculate the electron ID efficiencies.

7.3.2 Electron ID Efficiencies

For the case of the W events selection, the efficiency ϵ_W appearing in the formula of the cross-section on page 24 is just the efficiency of the tight electron selection, ϵ_T, as it is the only electron in the event. In the case of the Z events, the efficiency ϵ_Z in the formula on page 24 is a function of the two efficiencies, one for the tight electron selection, ϵ_T, the same as for the W, and the other for the loose electron selection, ϵ_L, as listed in Table 5.4;

Variable	Tight Central	2nd central cluster
E_T	> 25 GeV	> 25 GeV
$\|\eta\|$	<1.1 (CEM)	<1.1 (CEM)
Fiduciality	CES based	Track based
p_T	$p_T > 10$ GeV/c	$p_T > 10$ GeV/c
Track Quality Cuts	at least 3 Axial and 3 Stereo SL with at least 7 hits each	at least 3 Axial and 3 Stereo SL with at least 7 hits each
Z_{vertex}	$\|z_0^{track}\|$ <60 cm	$\|z_0^{track}\|$ <60 cm
Had/EM	$< 0.05 + 0.0045 \times E$	
E_T^{iso}/E_T	< 0.1	
E/p	$E/p < 2.0$ (*)	
L_{shr}	<0.2	
χ^2_{strip}	<10.0	
$Q \cdot \Delta X$	$-3.0 < Q \cdot \Delta X < 1.5$ cm	
$\|\Delta Z$	<3.0 cm	
$75 < M_{ee} < 105$ GeV/c^2		

Table 7.3: *Criteria for the selection of the initial sample to be used in the central electron efficiency calculation. The tight electron cuts are the same as listed on Table 5.4.*
(*) *The E/p cut is released for electrons with E_T >50 GeV/c^2.*

that is[2],

$$\epsilon_Z = \epsilon_T(2\epsilon_L - \epsilon_T).$$

Starting with the $N_{CC} = 1933$ OS events with one tight electron and one central cluster, selected as described in the previous section 7.3.1, all the cuts are applied in turn to the second cluster. The efficiency is measured for each of them according to the expression:

$$\epsilon^i = \frac{N_{TT} + N_{Ti}}{N_{CC} + N_{TT}},$$

where N_{TT} is the total number of tight-tight events and N_{Ti} is the number of events satisfying the tight cuts on one leg and the i-th ID cut on the second leg. These numbers are corrected for the QCD background coming from the SS events (see section 6.1.1), as explained in the next paragraph. For the total efficiency, when both legs pass the tight cuts, this formula becomes

$$\epsilon_T = \frac{2N_{TT}}{N_{CC} + N_{TT}}$$

[2]See appendix B for a derivation of all the following formulae.

for the tight electron efficiency and

$$\epsilon_L = \frac{N_{TT} + N_{TL}}{N_{CC} + N_{TT}}$$

for the loose efficiency, where N_{TL} is the total number of tight-loose events. The number of OS and SS events together with the number of expected SS events from the $Z^0 \to e^+e^-$ Monte Carlo sample are reported in Table 7.4.

The electron identification efficiencies are corrected for the QCD background

i-th Variable	# of OS events (data)	# of SS events (data)	# of SS events (MC)
Starting sample (N_{CC})	1933	66	16.4
Had/EM< $0.05 + 0.0045 \times E$	1877	29	15.5
$E/p < 2.0$	1688	38	11.4
$E_T^{iso}/E_T < 0.1$	1813	25	13.3
L_{shr} <0.2	1879	37	15.2
$-3.0 < Q \cdot \Delta X < 1.5$ cm	1886	55	15.7
$\lvert\Delta Z\rvert$ <3.0 cm	1901	55	15.0
χ^2_{strip} <10.0	1816	39	14.9
Track Quality Cuts	1918	64	15.5
Total (tight central electron)	1373	11	7.0
Total (loose central electron)	1691	18	11.7

Table 7.4: *Number of events passing i-th variable cut (in addition to the CC selection) for both OS and SS events in data and for the expected number of SS events from* $Z^0 \to e^+e^-$ *Monte Carlo simulation.*

in three different ways; one by subtracting SS events observed in data, one by subtracting the "real" QCD background (which is the number of SS events in data minus the number of SS events in MC, scaled to the number of OS events in the data), and one without SS event subtraction (see Table 7.5). The "real" QCD subtraction method is taken as default method and the efficiency difference between the SS subtraction and the QCD subtraction method is taken as a systematic uncertainty. The total efficiencies for the tight and loose central electron identification cuts are found to be

$$\epsilon_T = 84.2 \pm 0.7(stat.) \pm 0.2(syst.)\% = (84.2 \pm 0.7)\%$$

and

$$\epsilon_L = 93.9 \pm 0.5(stat.) \pm 0.1(syst.)\% = (93.9 \pm 0.5)\%.$$

The efficiency for the selection of the loose electron, ϵ_L, needs to be corrected for the efficiency $\epsilon_{CESfidele}$ of the CES fiducial cut, which is applied

i-th Variable	efficiency, ϵ^i		
	(All SS sub)	(QCD sub)	(no SS sub)
Track Quality Cuts	$97.6 \pm 0.3\%$	$97.5 \pm 0.3\%$	$97.3 \pm 0.3\%$
Had/EM$< 0.05 + 0.00045\times E$	$99.4 \pm 0.3\%$	$99.4 \pm 0.3\%$	$98.3 \pm 0.2\%$
$E_T^{iso}/E_T < 0.1$	$97.6 \pm 0.4\%$	$97.5 \pm 0.4\%$	$96.4 \pm 0.3\%$
$E/p < 2.0$	$93.3 \pm 0.5\%$	$93.2 \pm 0.5\%$	$92.6 \pm 0.5\%$
L_{shr} <0.2	$99.2 \pm 0.3\%$	$99.2 \pm 0.3\%$	$98.4 \pm 0.2\%$
χ^2_{strip} <10.0	$97.2 \pm 0.4\%$	$97.2 \pm 0.4\%$	$96.5 \pm 0.3\%$
$Q * \Delta X$ >-3.0 cm, <1.5 cm	$98.9 \pm 0.2\%$	$98.9 \pm 0.2\%$	$98.6 \pm 0.2\%$
$\lvert\Delta Z\rvert$ <3.0 cm	$99.3 \pm 0.2\%$	$99.3 \pm 0.2\%$	$99.0 \pm 0.2\%$
$\epsilon_{\mathbf{T}}$	$\mathbf{84.4 \pm 0.7\%}$	$\mathbf{84.2 \pm 0.7\%}$	$\mathbf{83.1 \pm 0.7\%}$
$\epsilon_{\mathbf{L}}$	$\mathbf{94.0 \pm 0.5\%}$	$\mathbf{93.9 \pm 0.5\%}$	$\mathbf{92.7 \pm 0.5\%}$

Table 7.5: *Efficiency (ϵ^i) of each identification variable and total efficiency ϵ_T and ϵ_L for the tight and loose central identification cuts using* $Z^0 \to e^+e^-$ *events with SS event subtraction, QCD background subtraction, and no background subtraction.*

in the selection of the events (see Table 5.4) but not in the selection of the second leg used for the calculation of the efficiency (Table 7.3). To calculate $\epsilon_{CESfidele}$, events are selected with one tight electron and a second cluster which satisfies the cuts in Table 7.3[3], plus the loose identification cuts:

- Had/EM$< 0.05 + 0.00045\times E$
- $E_T^{iso}/E_T < 0.1$.

Among these events, indicated with $N_{TRKfidele}$, a subset is created with those which are also fiducial in the CES, $N_{CESfidele}$. The efficiency of the CES fiducial cut will then be

$$\epsilon_{CES} = \frac{N_{CESfidele}}{N_{TRKfidele}} = (99.92 \pm 0.01)\%.$$

Based on these results, the total selection efficiency of $Z^0 \to e^+e^-$ events, consisting of one tight electron and one loose electron, is

$$\epsilon_Z = \epsilon_T(2\epsilon_{CESfidele} \cdot \epsilon_L - \epsilon_T) = (87.1 \pm 0.9)\%.$$

[3]The cuts on the local coordinates for the track `fidele` requirement have been tightened to be $|X| < \pm 18$ cm and $18 < |Z| < 190$ cm (see section 4.2.3), to avoid the inclusion of events on the borders of the wedges which are mistakenly considered fiducial for the smearing due to COT tracking resolution.

The efficiency for the selection of $W^{\pm} \rightarrow e^{\pm}\nu$ events is

$$\epsilon_W = \epsilon_T = (84.2 \pm 0.7)\%.$$

Chapter 8

Z and W Boson Geometric and Kinematic Acceptances

In this chapter the kinematic and geometric acceptances A_Z and A_W are calculated using the $Z^0/\gamma^* \to e^+e^-$ and $W^\pm \to e^\pm\nu$ Monte Carlo samples described in section 5.1. The kinematic component includes the transverse energy threshold for the electrons and the missing transverse energy threshold used to select events with a W boson. The geometric component is the probability that an electron falls within the fiducial volume of the detector. The estimates of the acceptances and their uncertainties are discussed in this chapter.

8.1 Z Acceptance Calculation

The acceptance for the geometric and kinematic cuts in Table 5.4 was determined using the MC sample of $Z^0/\gamma^* \to e^+e^-$ events described in section 5.1. As stated there, the generated events have been simulated and have gone through the same reconstruction algorithms as the data. Events in this sample were selected by requiring:

1. The z position of the primary vertex at generator level to lie within ± 60 cm of the proton-antiproton interaction point at $z = 0$; and the

presence of at least 2 electrons[1] with the following characteristics[2]:

2. The cluster contained no towers in the Plug calorimeter.

3. The region "tower 9"[3] was excluded.

4. The cluster was in the fiducial region (according to the CES variables) as shown in Figure 8.1 (see section 4.2.3 for the definition of the fiducial volume).

5. The p_T as measured by the beam-constrained COT tracking was greater than 10 GeV/c.

6. E_T was greater than 25 GeV.

7. The reconstructed invariant mass of the electrons was within 66 and 116 GeV/c^2.

The acceptance is

$$A_Z = \frac{\text{number of events passing cuts 1. to 7.}}{\text{number of events with } 66 < M_{\text{ee}}^{gen} < 116 \text{ GeV}/c^2 \text{ and } |z_{vertex}^{gen}| < 60 \text{ cm}}.$$

The effect of each cut is summarized in Table 8.1. The effect of reweighting the z primary vertex distribution has been studied at an earlier stage of the analysis[81] and found to be negligible. The effect of the reweighting of the p_T distribution will be discussed in section 8.1.1.

The acceptance is found to be

$$A_Z = 11.49 \pm 0.07(stat.)\%,$$

where the uncertainty is the statistical error of the Monte Carlo simulation sample. As a cross check, a calculation of the acceptance has been performed with the same cuts as defined in the Run I analyses [10, 82] and the details can be found in [81].

[1]Events with no reconstructed electron were discarded.

[2]The selection criteria are applied to the quantities obtained after passing through the entire reconstruction chain.

[3]See section 4.1 for the definition of the "tower 9" region.

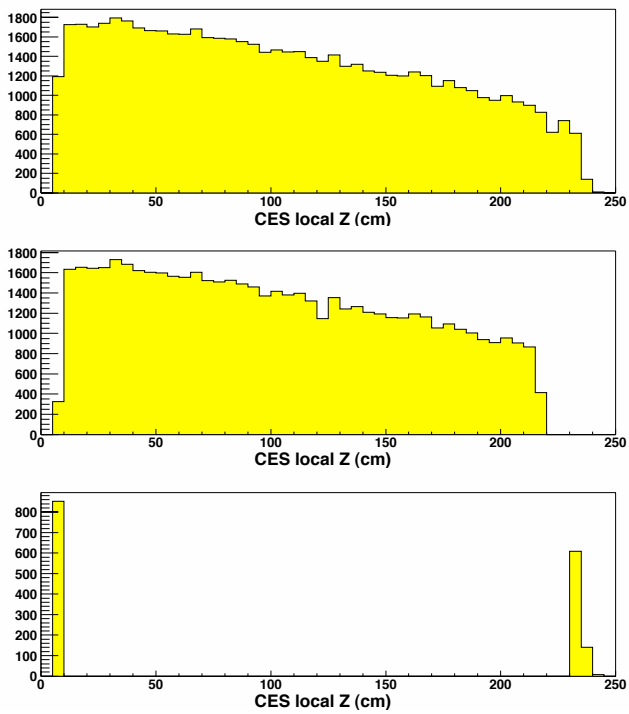

Figure 8.1: *The Z coordinate as reconstructed from the CES for all the electrons in the event(upper plot), for the electrons in the events passing the fiducial cut (middle plot), and for the events that fail the fiducial cut (bottom plot). The regions* $|Z_{CES}| < 9$ cm *and* $|Z_{CES}| > 230$ cm *are excluded as expected (see section 4.2.3 and Table 8.1).*

8.1.1 Systematic Uncertainties on the Acceptance

The systematic uncertainties on the calculation of the acceptance include several elements. Their single contributions are analysed in the following sections. In each case the input parameters of the Monte Carlo responsible of the effect (corresponding to the variable) under investigation are varied and the change in acceptance is examined.

Systematics from the E_T scale and resolution

The cut on the E_T of the electrons can be affected by the E_T scale and resolution correction factors applied in the data, as explained in section 4.2.2. The systematic uncertainties on these cuts was evaluated by varying the CEM energy scale and resolution separately and evaluating the change in

Selection	Default		+5.5 % X_0 Material
	# of events	Acceptance	Acceptance
generated $\lvert z^{gen}_{vertex}\rvert$ <60 cm	309445		
$\geqslant$ 1 `CdfEmObject`	307657		
first electron			
no plug towers	227543	95.75%	95.75%
no seed in tower 9	219306	92.28%	92.14%
fiducial: $\lvert x\rvert$ < 21 cm; 9< $\lvert z\rvert$ <230 cm no "chimney"; no "tower 9":	187393	78.85%	78.98%
p_T >10 GeV/c	162427	68.35%	66.59%
E_T >25 GeV	118742	49.96%	48.82%
second electron			
no plug towers	59086	24.86%	24.34%
no seed in tower 9	55188	23.35%	22.77%
fiducial: $\lvert x\rvert$ < 21 cm; 9< $\lvert z\rvert$ <230 cm no "chimney"; no "tower 9":	38010	15.99%	15.87%
p_T >10 GeV/c	31006	13.05%	12.51%
E_T >25 GeV	28336	11.92%	11.38%
66 < M_{ee} < 116 GeV/c^2	27298	11.49%	10.95%
Total Acceptance A_Z		(11.49±0.07)%	10.95%

Table 8.1: *Effect of each geometric/kinematic cut on electrons and events. The numbers in the middle columns are originated from the default* $Z^0 \rightarrow e^+e^-$ *Monte Carlo simulation and the numbers in the right column are originated from the simulation when the extra material is added. The fractions are with respect to the number of events with* $66 < M^{gen}_{ee} < 116$ *GeV/*c^2 *and* $\lvert z^{gen}_{vertex}\rvert < 60$ *cm, which is equal to 237652.*

acceptance. The CEM energy scale was varied by 1%; in Figure 8.2, where the E/p variable is plotted as a function of η, it is shown that a variation of 1% contains most of the data and Monte Carlo points and thus it is suitable for this purpose. This variation corresponds to a change of $\delta A_Z = 0.03\%$ in acceptance. In Table 8.2 the energy scale variation up to 2% and the corresponding acceptances are given. A variation of ±1% is used in the final calculation of the uncertainty.

The energy resolution has been moved up to 2%, resulting in a change of $\delta A_Z = 0.02\%$ in acceptance. In Table 8.3 the variations in resolution with the corresponding acceptances are summarised. The different values of the width of the gaussian from the fit to the dielectron's invariant mass are also reported for the different resolution values, in the default Monte Carlo and in the data. The value of +2% is used in the estimation of the uncertainty.

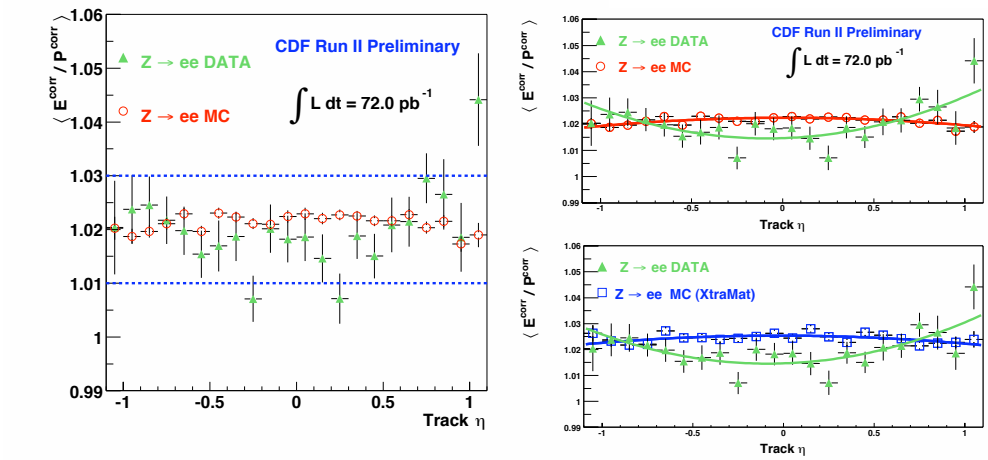

Figure 8.2: *Left plot: $\langle E/p \rangle$ as a function of η, where the average has been calculated using values of E/p between 0.9 and 1.1. The dashed lines represent 1% variation in energy scale. In the right plots, the distribution observed in the data has been compared with that in the default Monte Carlo(top plot) and with the Monte Carlo with the extra material(bottom plot). The lines correspond to the fit with a second order polynomial function. The increase in the curve in the data is due to the presence of more material as the electrons pass through the detector at an angle (and thus bremsstrahlung more). The different shape in the Monte Carlo is probably due to missing material in the detector simulation and is currently under study.*

Energy scale change	$\mathbf{A}_Z$	$\delta\mathbf{A_Z}$
+2%	11.54%	+0.05%
+1%	11.51%	+0.02%
Default	11.49%	–
-1%	11.46%	-0.03%
-2%	11.42%	-0.07%

Table 8.2: *Effect on the acceptance due to the CEM energy scale variation.*

Extra smearing of energy in MC	$\sigma(M_{ee})$	$\mathbf{A}_Z$	$\delta\mathbf{A_Z}$
+4%	4.426 GeV	11.45%	+0.04%
+2%	3.441 GeV	11.47%	+0.02%
Default	2.965 GeV	11.49%	–
DATA	(2.873 ± 0.109) GeV	–	–

Table 8.3: *Effect on the acceptance due to the energy resolution variation. The width of the invariant mass at Z peak, $\sigma(M_{ee})$, is extracted from the Gaussian fit in the range $86 < M_{ee} < 98$ GeV for the MC samples with the variation in resolution. They can be compared with the value measured from the data.*

Systematics from the track p_T scale

In the same way as in the previous section, the correction for the track p_T scale can affect the selection of the electrons through the p_T variable. This effect has been studied by scaling the track momentum by $\pm 1\%$, corresponding to $\delta A_Z = 0.01\%$, as reported in Table 8.4.

p_T scale change	A_Z	δA_Z
+1%	11.48%	+0.01%
Default	11.49%	
-1%	11.50%	-0.01%

Table 8.4: *Effect on the acceptance due to the scale of the track p_T.*

Systematics from the p_T of the Z boson

The distribution of the p_T of the Z^0 boson in the Monte Carlo directly affects the acceptance as it changes the momenta and angular distributions of the electrons. In the Monte Carlo the p_T of the Z boson is modelled according to a particular choice of input parameters; the systematic uncertainty associated with this choice is studied by reweighting the default distribution ("nominal", shown in Figure 8.3, compared with the data) towards higher ("harder") and lower ("softer") values of p_T using simple linear functions. The acceptances recalculated for each of these distributions are listed in Table 8.5, where the χ^2 between each reweighted distribution, and the one observed in the data, is also shown. The difference between the acceptance of the reweighted distribution which fits better the data and the nominal value is taken as a systematic uncertainty. This results in a $\delta A_Z = 0.01\%$ variation in acceptance.

Systematics from the detector material

An important source of systematic uncertainty is the amount of material in the detector simulation. As this amount is not known with precision at present, different studies are in progress to determine the amount of material between the ISL and the COT inner cylinder and to correct the simulation accordingly. In this analysis the $Z^0/\gamma^* \rightarrow e^+e^-$ Monte Carlo sample with an extra 5.5% X_0 of material (a 0.515 cm thick silicon cylinder) described

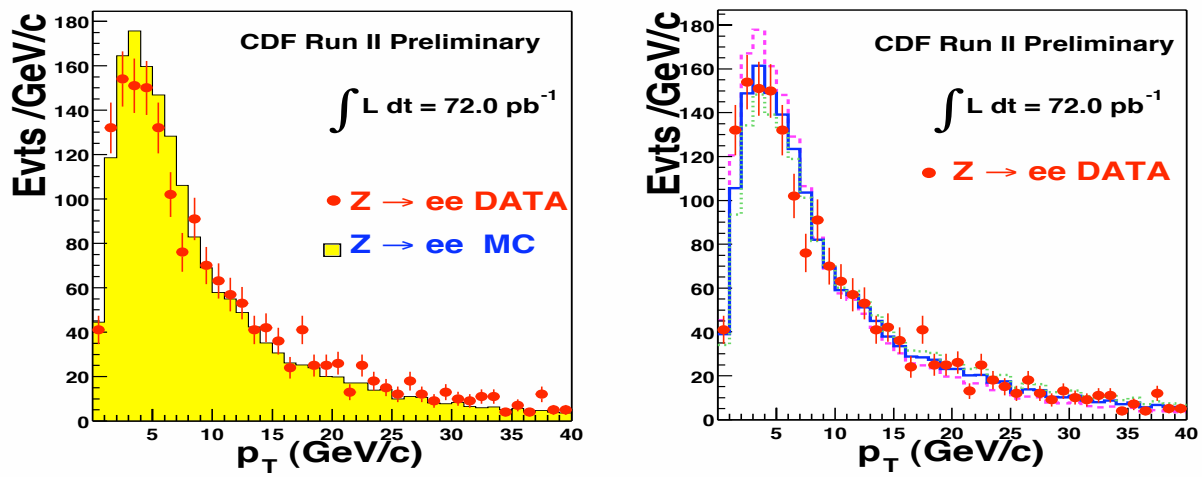

Figure 8.3: *On the left, the p_T distribution of the Z^0 boson as reconstructed from the momenta of the electrons in data (points) and Monte Carlo (solid histogram). The p_T distribution in the data is a bit broader than the one in the simulation. On the right, the Monte Carlo distribution has been reweighted toward larger and smaller values of p_T; the histograms are the ones described in Table 8.5, corresponding to the nominal(solid histogram), a "hard"(dashed) and a "soft"(dotted) distribution of p_T. The number of events in the Monte Carlo sample has been normalized to the number of events in the data.*

in section 5.1 is used to determine the effect of the extra material on the acceptance.

Acceptance decreases quite significantly when the extra material is added, as shown in Table 8.1, where the acceptance is calculated after each cut for both Monte Carlo samples. This decrease in acceptance is mainly due to the increase of external bremsstrahlung resulting in a lower p_T of the electrons (see Figure 8.4). Figure 6.5(top) and Figure 8.5 show the E/p distributions of the data, the default simulation, and the simulation with the extra material, as this quantity is directly affected by electron bremsstrahlung especially in the tail at higher E/p. Figure 8.6 compares the E/p distributions in various regions of $z_{0(R=10.6)}$, where $z_{0(R=10.6)}$ is the z position of the track at the radius of 10.6 cm[4], corresponding to the silicon outermost radius of

[4]Calculated as

$$z_{0(R=10.6)} = z_0^{track} + 10.6 \times (cos(\theta^{track})/sin(\theta^{track})).$$

p_T distribution	χ^2/dof	A_Z	δA_Z
Dotted histogram	62.6/41	11.505%	+0.019%
Solid histogram	38.8/41	11.496%	+0.010%
Default	62.3/41	11.486%	–
Dashed histogram	80.3/41	11.484%	-0.002%

Table 8.5: χ^2 *per degree of freedom between the data and Monte Carlo sample and acceptance values for various* p_T *distributions as shown in Figure 8.3.*

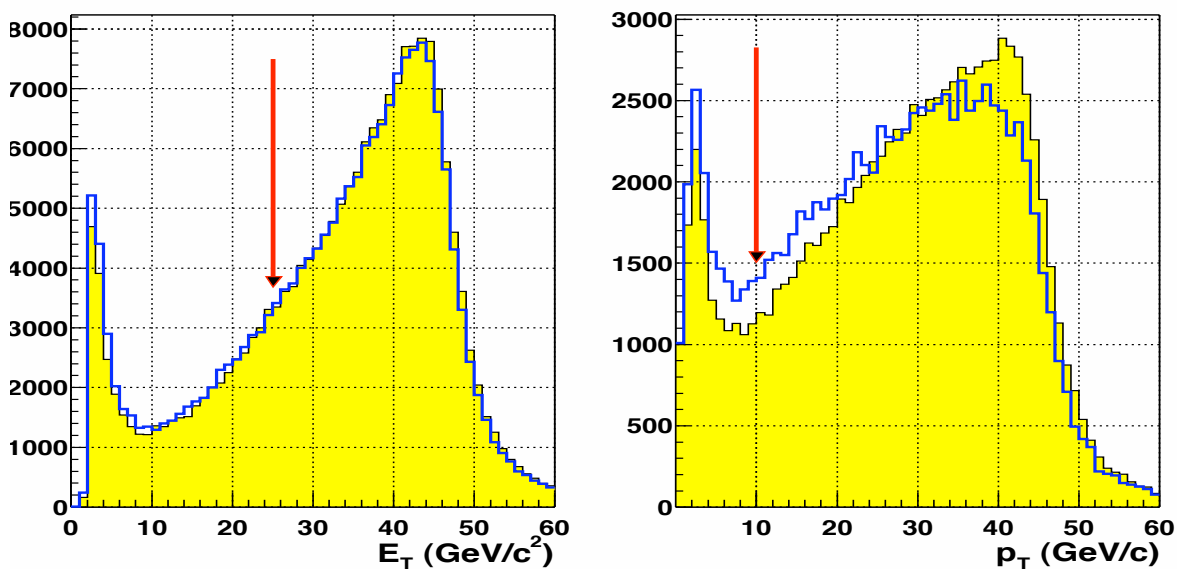

Figure 8.4: *The* E_T *(left plot) and* p_T *(right plot) distributions for the electrons from the* $Z^0 \rightarrow e^+e^-$ *default Monte Carlo(yellow solid histogram) and the Monte Carlo with extra material(blue line). The arrows indicate the* E_T *cut at 25 GeV and the* p_T *cut at 10 GeV/c applied in the acceptance calculation.*

the silicon. The regions correspond to the different barrels of the silicon vertex detector SVX. The difference in behaviour of the three distributions in the region $1.5 < E/p < 2.5$ is indicative of the amount of material in the detector, as E/p in the tail is sensitive to the radiation length.
In Figure 8.7 the ratios of the number of electrons with $1.5 < E/p < 2.5$ to the total (taken from the histograms in Fig. 8.6) are shown as a function of the four regions in $z_{0(R=10.6)}$, while Figure 8.2 (right) shows the effects of the extra material in $\langle E/p \rangle$ between 0.9 and 1.1 as a function of η.
In Figure 8.2 the rise in the data at high η is due to the electron passing through the material at an angle, thus losing more energy. The different shape in the Monte Carlo is probably due to missing material in the detector

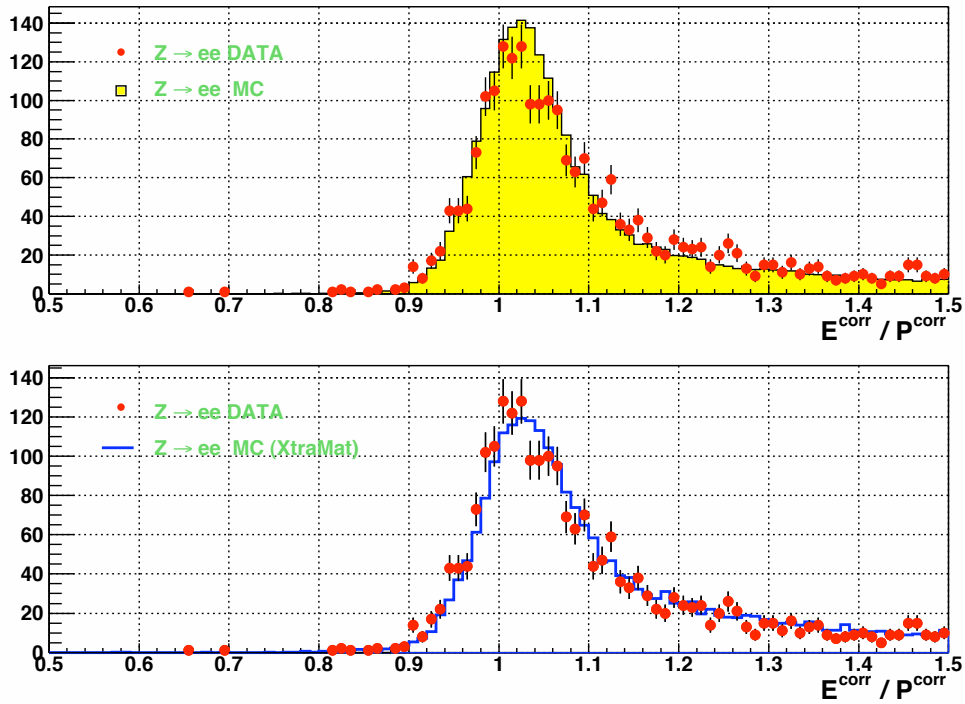

Figure 8.5: *E/p distributions for default MC(top plot) and MC with extra material(bottom plot) compared with data for the region* $0.5 < E/p < 1.5$.

simulation and is currently under study (as explained in the caption). All of these studies indicate that the data points lie somewhere between the default simulation points and the points with the extra 5.5% X_0 material, closer to the extra material points. Further studies are in progress to extract the exact radiation length. For the purposes of this analysis, the difference in acceptance between these two materials is taken as a systematic uncertainty.

Systematics from the PDFs

The choice of Parton Distribution Functions in the Monte Carlo has an effect on the acceptance as it changes the angular distribution of the electrons, and the detector had limited angular coverage. As described in section 5.1, the PYTHIA Monte Carlo used in this analysis uses Leading Order(LO) cross sections and Leading Log (LL) PDFs (CTEQ5L) and parton showering. The estimate of the uncertainty on the acceptance using the standard prescription involves a NLL calculation and is therefore impossible with this Monte Carlo.

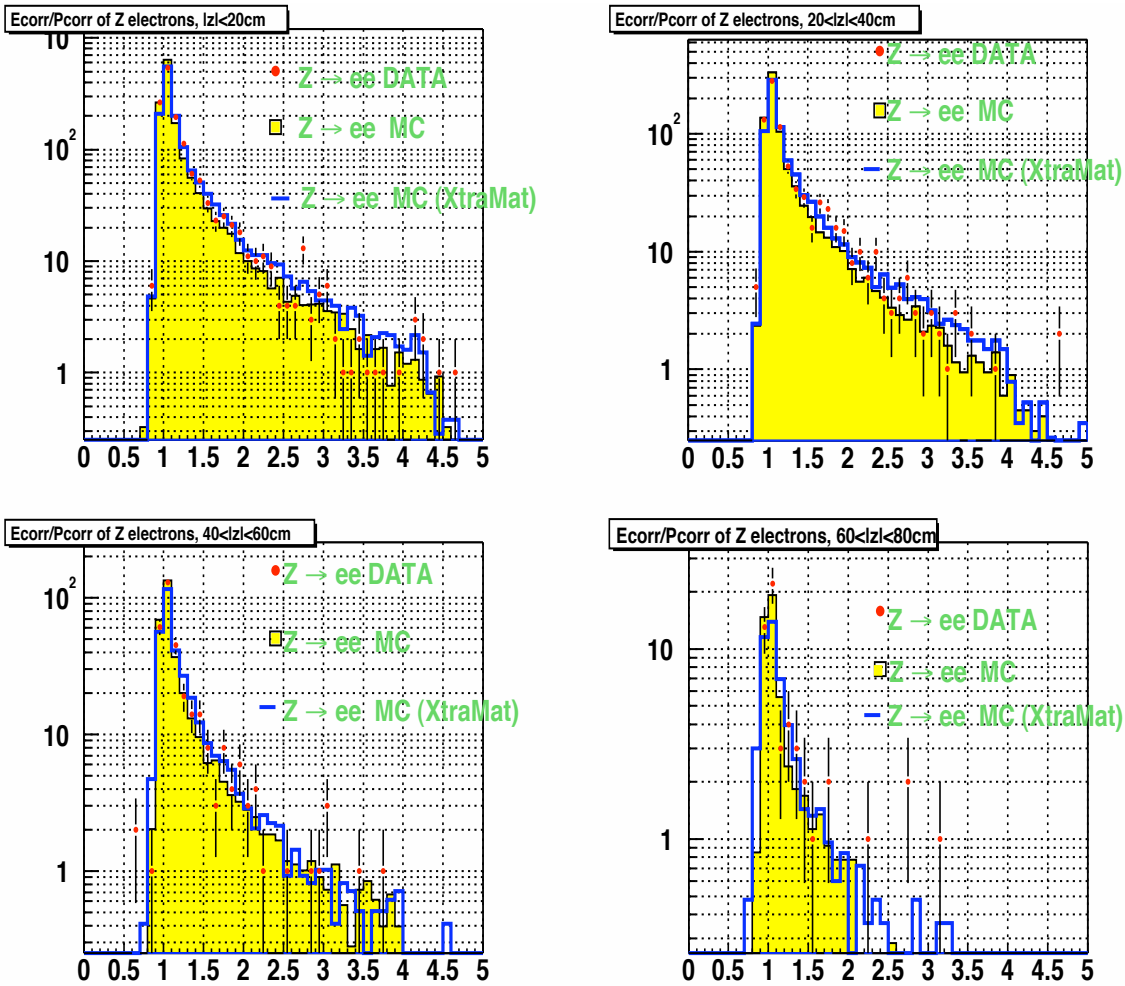

Figure 8.6: *E/p distribution for different regions of the track z_0 at the radius of 10.6 cm, for default Monte Carlo(yellow solid histogram), Monte Carlo with extra material (blue line) and data (red dots). The regions in z_0 are chosen to represent the different barrels of the Silicon Vertex Detector(SVX).*

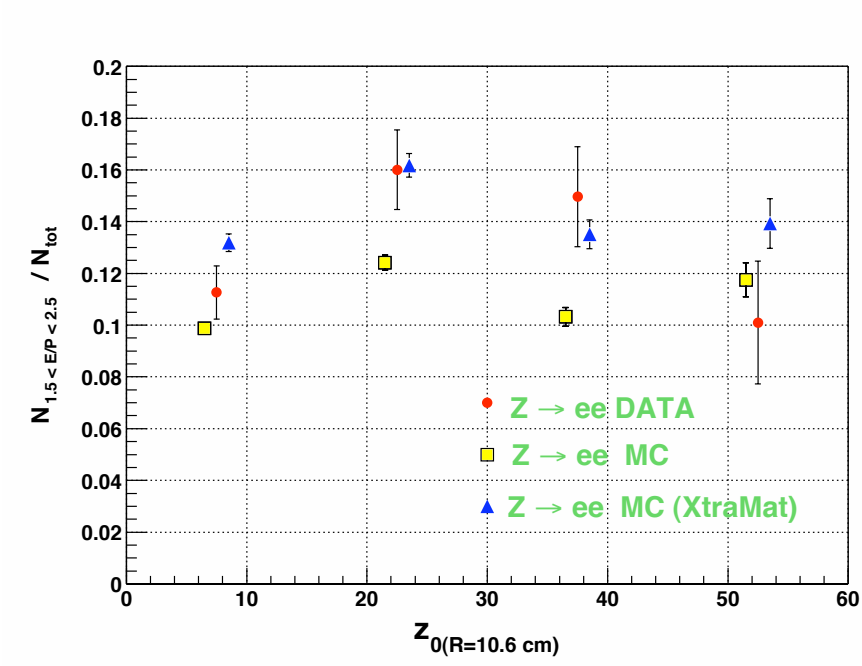

Figure 8.7: *The ratio of the number of electrons in the region* $1.5 < E/p < 2.5$ *to the total for the default MC simulation(squares), extra material MC(triangles) and data(dots) as a function of* $z_{0(R=10.6)}$. *The values on the* x *axis have been slightly shifted to avoid overlapping.*

As the boson rapidity distribution $d\sigma/dy$ is a measure of the underlying parton flux, changes in the PDFs will have an effect on $d\sigma/dy$ and thus on the acceptance. Following the procedure described in [83], the systematics related to the choice of the Parton Distribution Functions (PDFs) have been studied using the standard PDFs error sets to find the corresponding variation in $d\sigma/dy$. A $\pm 1\sigma$ variation, estimated using the Run I rapidity measurement[84], has been applied as generator level cross section reweighting factors to the default MC sample, generated with CTEQ5L, and the acceptance recalculated. The reweighting factors have been arbitrarily normalized by setting $d\sigma/dy = 1$ for $|y| = 0$, as only the shape of the distribution is relevant to the acceptance calculation. Figure 8.8 shows the rapidity distributions at the generator level, corresponding to the default PDFs and $\pm 1\sigma$ variations, compared to Run I data corrected for acceptance and resolution, and Figure 8.9 shows the reconstructed rapidity distributions with Run II events passing the selection criteria. The acceptance values in the three cases are listed in Table 8.6. This method leads to a net acceptance variation

δA_Z=0.34%, corresponding to the difference between the default value and the value with the $\pm 1\sigma$ variation.

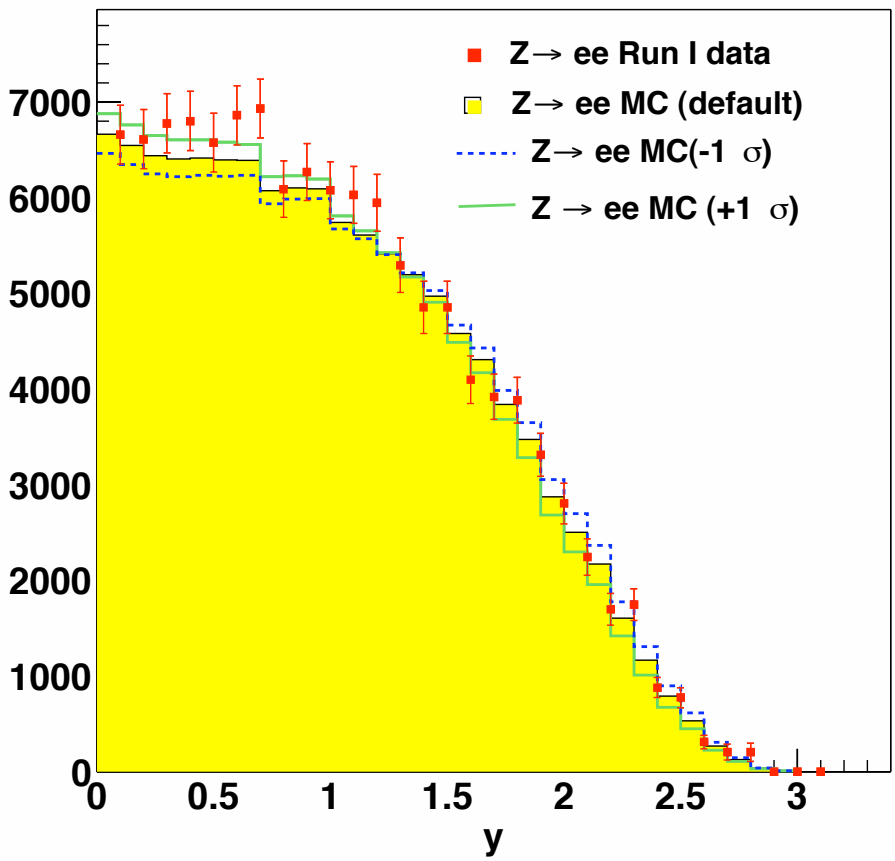

Figure 8.8: *Rapidity distribution of the Z for Run I* $Z^0 \to e^+e^-$ *data (squares) and Monte Carlo signal events (at generator level) generated with* $\sqrt{s}$*=1.96 TeV with default CTEQ5L PDFs (yellow solid histogram), and* $\pm$ *1* σ *variation (green solid line and dashed blue line).*

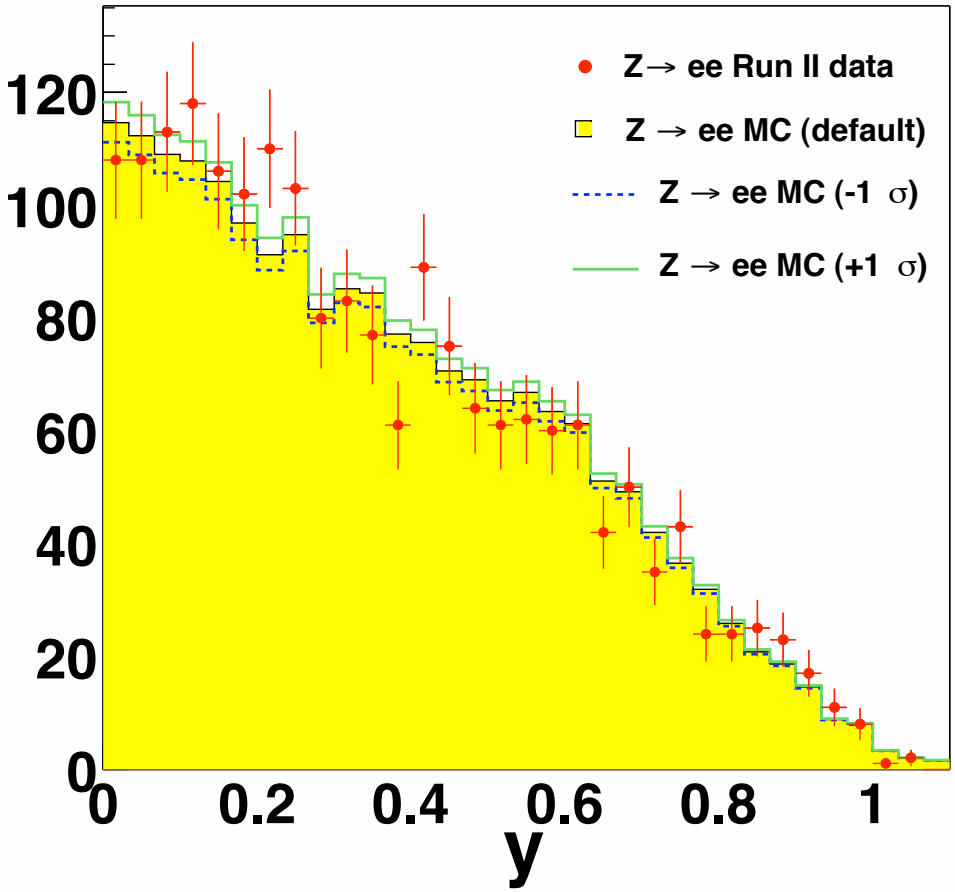

Figure 8.9: *Rapidity distribution of the Z for Run II* $Z^0 \rightarrow e^+e^-$ *data(dots) and Monte Carlo signal events (after simulation) generated with* $\sqrt{s}$*=1.96 TeV with default CTEQ5L PDFs (yellow solid histogram), and* $\pm$ *1* σ *variation (green solid line and dashed blue line).*

variation in rapidity	A_Z	δA_Z
minus 1 σ	11.824%	+0.338%
Default	11.486%	–
plus 1 σ	11.170%	-0.316%

Table 8.6: *Difference in acceptance due to the reweight of the rapidity distribution at generator level.*

Summary on systematic uncertainties

The systematic uncertainties are summarized in Table 8.7. The total sys-

source	**variation**	$\Delta \mathbf{A}_Z$	$\Delta \mathbf{A}_Z / \mathbf{A}_Z$
E_T^e scale	1% variation	0.03%	0.3%
E_T^e resolution	2% extra smearing	0.02%	0.2%
p_T^e scale	1% variation	0.01%	0.1%
p_T modelling		0.01%	0.1%
Material	5.5 % X_0	0.54%	4.7%
PDFs	reweighting of y	0.34%	2.9%
overall		0.64%	5.5%

Table 8.7: *Summary of the systematic uncertainties on the Z acceptance.*

tematic uncertainty on A_Z is 5.5%, with the main contributions coming from the modelling of the material and the PDFs.

8.1.2 Removing Drell-Yan Contributions from γ^* Exchange

A correction needs to be applied to the number of $Z^0 \rightarrow e^+e^-$ candidates to account for the fact that some of the e^+e^- pairs in the considered invariant mass window come from the continuum $p\bar{p} \rightarrow \gamma^* \rightarrow e^+e^-$ or the interference term between γ^* and Z^0, and not from Z^0 resonant production. The correction factor is obtained by the computation of the integrals $I_1 \equiv \int_{66}^{116} |Z^0 + \gamma|^2 dM$ and $I_2 \equiv \int_0^{\infty} |Z^0|^2 dM$ at $\sqrt{s}$=1.96 TeV using the PYTHIA generator; the number $\frac{I_2}{I_1} = 1.003$ is obtained, which is consistent with the most recent theoretical calculation at NNLO[83]

$$\frac{I_2}{I_1} = 1.004 \pm 0.001.$$

The ratio $\frac{I_2}{I_1}$= 1.004 ± 0.001 will be multiplied by the total number of Z^0/γ^* signal events.

8.2 W Acceptance Calculation

The acceptance for the geometric and kinematic cuts was determined using the $W^{\pm} \rightarrow e^{\pm}\nu$ Monte Carlo sample described in section 5.1. The same selection criteria as in the calculation of the Z boson acceptance (section 8.1.2) have been used on the highest energy electron in the event[5]; in addition, the missing transverse energy in the event, calculated using the z_0 of the electron track, is required to be greater than 25 GeV. The energy recoil of the W, $\vec{U} = -\vec{\not{E}}_T - \vec{E}^e_T$, was compared for data and Monte Carlo in Figure 8.10. To improve the matching of $\vec{U}$ in Monte Carlo with the data, the MC $|\vec{U}|$ was scaled up by 5%. Consequently, the missing transverse energy was recalculated as $|-\vec{U}_{(corr)} - \vec{E}^e_{T(corr)}|$, where $\vec{E}^e_{T(corr)}$ is the electron transverse energy corrected for the z_0 of the electron track as described beforehand.
The comparison between data and the corrected Monte Carlo $\vec{U}$ is shown in Figure 8.11. All the cuts applied to the sample are summarised in Table 8.8. The acceptance is found to be 24.62±0.04%, where 0.04% is the statistical error on the number of events in the Monte Carlo sample.

[5]Events with no reconstructed electron were discarded.

Selection	Default	
	# of events	Acceptance
electron		
generated $\lvert z^{gen}_{vertex}\rvert$ <60 cm	1443131	
$\geqslant$ 1 `CdfEmObject`	1381540	95.73%
no plug towers	708633	49.10%
fiducial: $\lvert x\rvert$ < 21 cm; 9< $\lvert z\rvert$ <230 cm no "chimney"; no "tower 9":	560009	38.81%
p_T >10 GeV/c	507158	35.14%
E_T >25 GeV	381719	26.45%
missing energy		
$\not\!\!E_T$ > 25 GeV	355320	24.62%
Total Acceptance A_W		(24.62±0.04)%

Table 8.8: *Effect of each geometric/kinematic cut on the* $W^{\pm} \rightarrow e^{\pm}\nu$ *events using the default* $W^{\pm} \rightarrow e^{\pm}\nu$ *Monte Carlo simulation. The fractions are with respect to the number of events with* $\lvert z^{gen}_{vertex}\rvert$ *<60 cm, which is equal to 1443131.*

8.2.1 Systematic Uncertainties on the Acceptance

The determination of the systematic uncertainties on the acceptance of the W boson events has been calculated[1] in the same way as for the Z, analysing the same source of uncertainties and following the same method, in order to reduce the systematics on the calculation of the ratio. The procedure and the results are briefly reported in the following sections.

Systematics from the Energy Scale and Resolution and Momentum Scale

The energy scale and resolution in the cut of the energy of the electron in the event are studied as sources of systematic uncertainty by varying these quantities by 1% and 2% (as done in section 8.1.1). The variations in the results are $\delta A_W = 0.15\%$ and $\delta A_W = 0.01\%$ respectively. In addition, the p_T of the track associated with the electron has been varied by $\pm 1\%$ to study the systematic uncertainty from the track p_T scale. This results in an uncertainty δA_W=0.02%.

Systematics from the p_T of the W boson

The systematic uncertainty from the choice of the Monte Carlo input parameters which determine the p_T of the W boson has been studied as in section 8.1.1, reweighting the p_T distribution using linear functions built in the same way. Figure 8.12 shows the reconstructed p_T spectrum in the Monte Carlo overlaid on the p_T spectrum observed in the data. A different method is currently under study to improve the agreement between data and MC, giving a more precise estimate of the systematic uncertainty. Using this method results in a systematic uncertainty on the acceptance δA_W=0.04%.

Systematics from the $\vec{U}$ scale

The effect of the 5% scaling factor applied to $|\vec{U}|$ was studied by varying $|\vec{U}_{corr}|$ by ±10%, corresponding to twice the applied correction. The resulting change in acceptance, δA_W=0.17%, has been taken as the systematic uncertainty on this procedure. Figure 8.10 and 8.10 show the distribution of $|\vec{U}|$ before and after the corrections are applied. The level of agreement between the plots is still poor and makes a sensible estimate of the systematic error very difficult. Work is in progress to use a χ^2 fit between the data and the MC, including the signal and the other backgrounds. The preliminary results are more satisfactory than the method used here.

Systematics from the detector material

The systematic uncertainty from the amount of material in the detector has been studied with the same procedure as used for the Z (section 8.1.1). The $W^{\pm} \rightarrow e^{\pm}\nu$ Monte Carlo sample with an extra 5.5% X_0 of material, as described in section 5.1, has been used in this study. The difference δA_W=0.29% between the value of the acceptance obtained with the default simulation and the simulation with the extra material is taken as a systematic uncertainty.

Systematics from the PDFs

The effect of the choice of the PDFs on the acceptance of W events has been studied using the same method described in section 8.1.1 and [83]. In

Figure 8.13 the rapidity distributions for Z and W in the electron and muon channels are compared with the Run I $Z^0 \rightarrow e^+e^-$ measurement[84]. The systematic uncertainty determined is $\delta A_W = 0.58\%$.

Summary on systematics uncertainties

The systematic uncertainties on the W boson acceptance are summarized in Table 8.9. The total systematic uncertainty on A_W is 2.8%, with the main

source	**variation**	$\delta \mathbf{A}_W$	$\Delta \mathbf{A}_W / \mathbf{A}_W$
E_T^e scale	1% variation	0.15%	0.6%
E_T^e resolution	2% extra smearing	0.01%	0.04%
p_T^e scale	1% variation	0.02%	0.08%
$\vec{U}$ scale	10% variation	0.17%	0.7%
p_T modelling		0.04%	0.16%
Material	5.5 % X_0	0.29%	1.2%
PDFs	reweighting of y	0.58%	2.4%
overall		0.69%	2.8%

Table 8.9: *Summary of the systematic uncertainties on the W acceptance.*

contributions coming from the PDFs and from the modelling of the material.

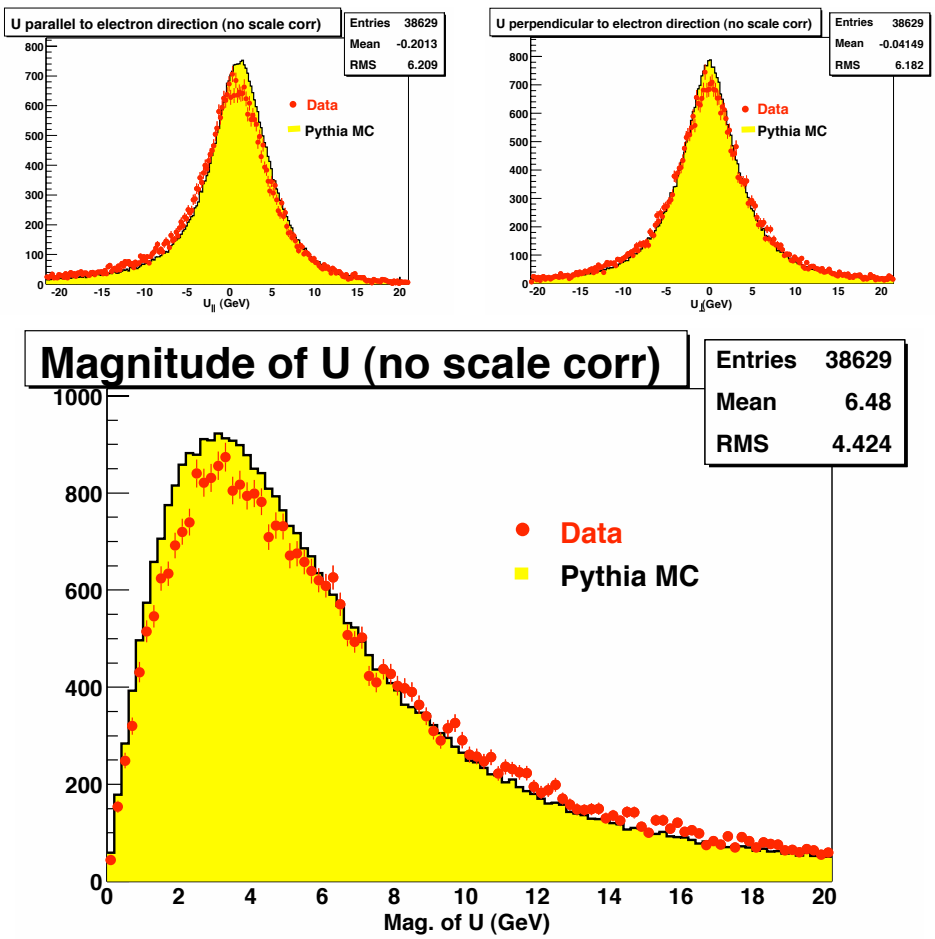

Figure 8.10: *Components of the vector $\vec{U}$ in the direction parallel to the electron ($\vec{U}_{||}$, on the top left), and perpendicular to the electron ($\vec{U}_{\perp}$ on the top right) in the data (red dots) and Monte Carlo (solid histogram). In the bottom plot, the magnitude of $\vec{U}$ is shown in data and Monte Carlo with the same convention. All the plots are before any scale correction is applied[1].*

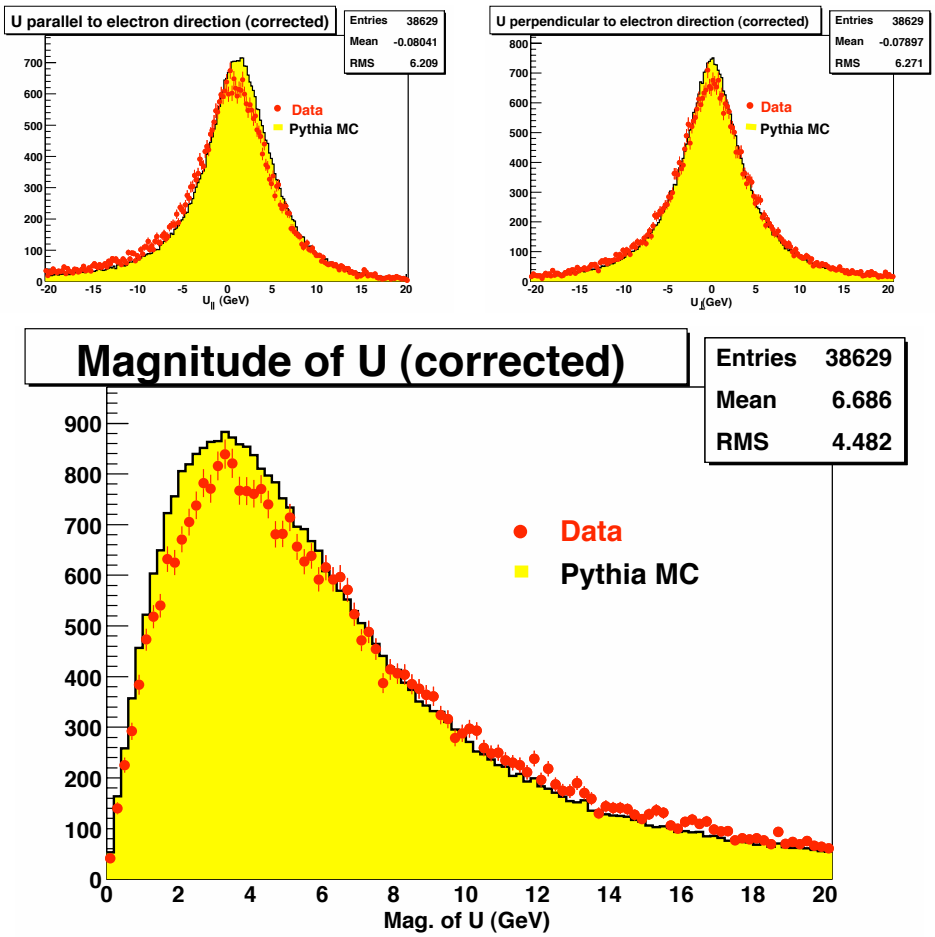

Figure 8.11: *Components of the vector $\vec{U}$ in the direction parallel to the electron ($\vec{U}_{||}$, on the top left), and perpendicular to the electron ($\vec{U}_{\perp}$ on the top right) in the data (red dots) and Monte Carlo (solid histogram). In the bottom plot, the magnitude of $\vec{U}$ is shown in data and Monte Carlo with the same convention. All the plots are after the scale correction is applied[1].*

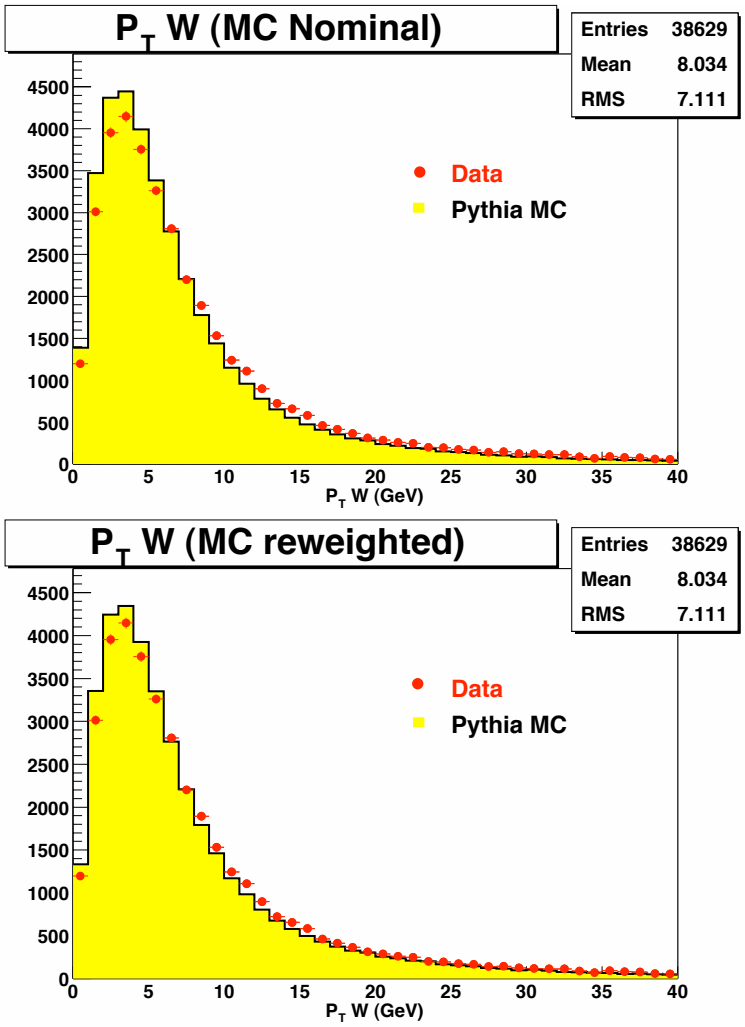

Figure 8.12: *The reconstructed W transverse momentum in the default Monte Carlo(solid histogram) and in the data(red dots). The top plot shows the nominal distribution, while the bottom plot shows the best reweighted distribution[1].*

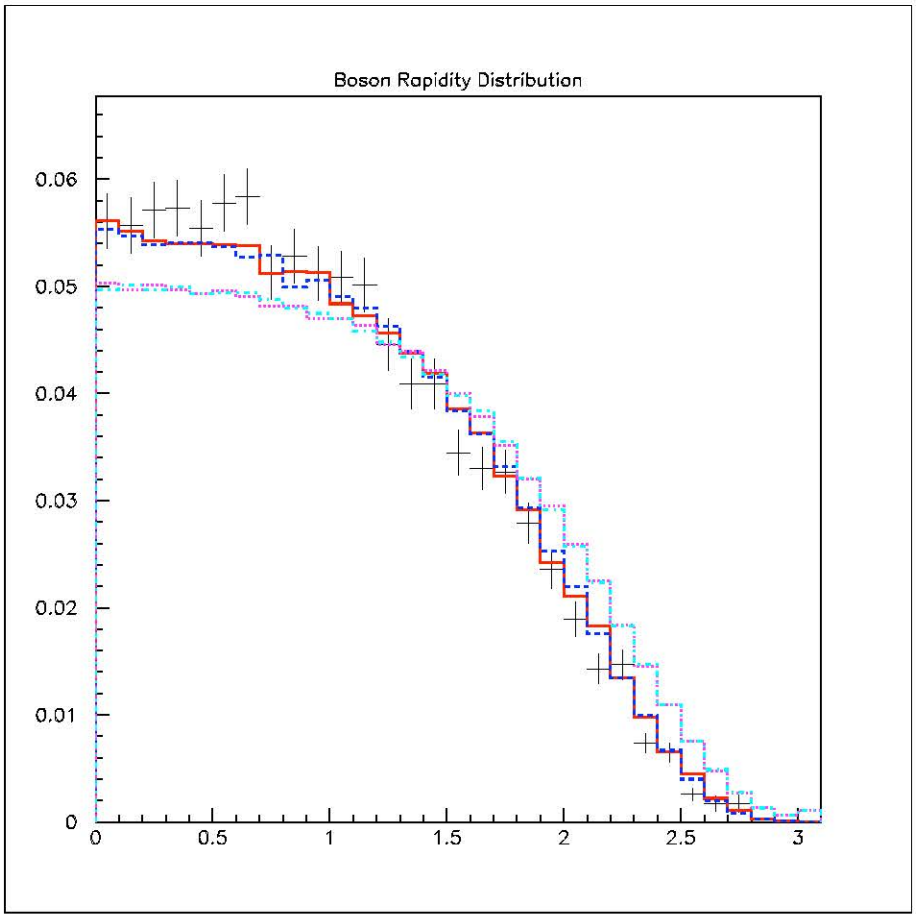

Figure 8.13: *The $d\sigma/dy$ distribution with the default CTEQ5L PDFs at 1.96 TeV for $Z^0/\gamma^* \to e^+e^-$ ($Z^0 \to \mu^+\mu^-$) in red-solid(blue-dashed), and for $W^\pm \to e^\pm\nu$($W^\pm \to \mu^\pm\nu$) in pink-dotted(cyan,dot-dashed) are compared with the $Z^0 \to e^+e^-$ Run I data at $\sqrt{s}$ =1.8 TeV[1].*

8.3 Z Vertex Corrections

The luminosity correction for the $|z_{vertex}| \leqslant 60$ cm for both the Z and the W acceptances is estimated via the $p\bar{p}$ beam luminosity function [85]

$$\frac{d\mathcal{L}}{dz} = N_0 \frac{\exp(-z^2/2\sigma_z^2)}{1 + (\frac{z - z_{min}}{\beta^*})^2},$$

where z is the z_{vertex}, N_0 is a normalization factor and the rest are the beam parameters. The details of this measurement are described in [1]; using this procedure the result for $\epsilon_{zvertex}$ (as introduced in chapter 2, page 25)

$$\epsilon_{zvertex} = 95.1 \pm 0.1(stat.) \pm 0.5(syst.)\%$$

is obtained [3], which is to be compared with the Run I result of $(95.5 \pm 1.0)\%$ [85]. The agreement between the z_{vertex} distribution in data and simulation is shown in Figure 8.14.

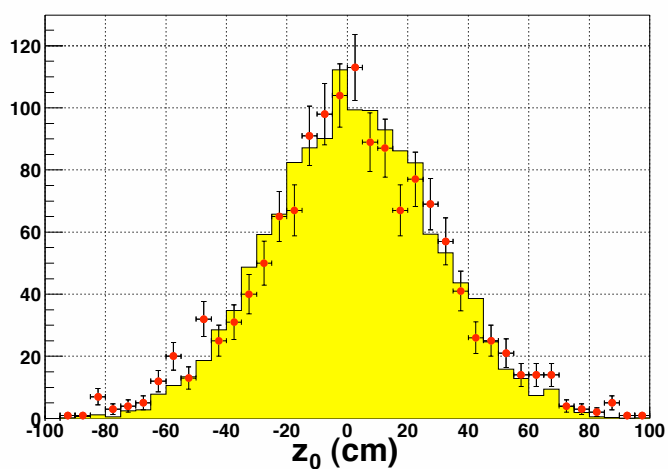

Figure 8.14: *Distribution of the z_0 of the track associated to the electron for the $Z^0 \to e^+e^-$ candidate events selected without the cut at 60 cm.*

Chapter 9

Results and Conclusions

In this chapter all the elements estimated in the previous sections are combined in the calculation of the Z and W cross sections, in sections 9.1 and 9.2. In section 9.3 the components of the calculation of the ratio are determined and its value is calculated; and from it the value of the width of the W is extracted in section 9.4. Finally, comments and future prospects are discussed in section 9.5.

9.1 Z Cross Section Estimation

The cross section $\sigma(\bar{\mathrm{p}}\mathrm{p} \to \mathrm{Z}^0)$ times the branching ratio $\mathrm{Br}(\mathrm{Z}^0 \to \mathrm{e}^+\mathrm{e}^-)$ is calculated using the expression given in section 2.4

$$\sigma_Z \cdot B(\mathrm{Z}^0 \to \mathrm{e}^+\mathrm{e}^-) = \frac{I_2}{I_1} \cdot \frac{\mathrm{N}_{Z/\gamma^*}^{candidates} - \mathrm{N}_{\mathrm{Z}}^{background}}{\mathrm{A}_Z \cdot \langle \epsilon_{trig}^{ee} \rangle \cdot \epsilon_{zvertex} \cdot \epsilon_Z \cdot \int \mathcal{L} dt}$$

where

- $\mathrm{N}_{Z/\gamma^*}^{candidates} = 1830 \pm 43(stat.)$;
- $\mathrm{N}_{\mathrm{Z}}^{background} = 9.7 \pm 5.3$;
- $\mathrm{A}_Z = (11.49 \pm 0.64)\%$;
- $\langle \epsilon_{trig}^{ee} \rangle = (99.9^{+0.1}_{-0.7})\%$;

- $\epsilon_{zvertex} = (95.1 \pm 0.5)\%$;
- $\epsilon_Z = (87.1 \pm 0.9)\%$;
- $\int \mathcal{L} dt = (72.0 \pm 4.3)\ \mathrm{pb}^{-1}$;
- $\frac{I_2}{I_1} = 1.004 \pm 0.001$.

Substituting these values

$$\begin{aligned} \sigma_Z \cdot Br(\mathrm{Z}^0 \to \mathrm{e}^+\mathrm{e}^-) &= 267.0 \pm 6.3(stat.) \pm 15.2(syst.) \pm 16.0(lum.)\,\mathrm{pb} \\ &= (267.0 \pm 23.0)\ \mathrm{pb}. \end{aligned}$$

In Table 9.1 these values are compared with those obtained in Run Ia, where the luminosity is taken from [9] and the other quantities are taken from [10]. The uncertainty on the luminosity measurement is dependent on the uncertainty on the $\mathrm{p\bar{p}}$ inelastic cross section. The two measurements of this cross section differ from each other of about 6%; to be conservative, in Run II the uncertainty on the luminosity has been increased to cover this number; in Run I the CDF measurement was used[86], which results in a smaller uncertainty. An update from Run Ia and Run Ib, but without a detailed breakdown of the systematic errors, is given in [84]. The measured Run Ia+Ib value is

$$\begin{aligned} \sigma_Z \cdot Br(\mathrm{Z}^0 \to \mathrm{e}^+\mathrm{e}^-) &= (253 \pm 4(stat. + syst.) \pm 10(lum.))\,\mathrm{pb} \\ &= (253 \pm 11)\,\mathrm{pb}; \end{aligned}$$

scaling this value up by 9% for the $\sqrt{s}$ dependence, it becomes

$$\sigma_Z \cdot Br(\mathrm{Z}^0 \to \mathrm{e}^+\mathrm{e}^-) = (276 \pm 12)\,\mathrm{pb},$$

which is consistent with the measurement reported here.

W. James Stirling *et al.*[11] have worked on an improved calculation of the $\mathrm{W} \to \mathrm{e}\nu$ and $\mathrm{Z}^0 \to \mathrm{e}^+\mathrm{e}^-$ cross-sections, including the higher colliding energy at the Tevatron. The predicted value at $\sqrt{s} = 1.96$ TeV with NNLO corrections is (250.5 ± 3.8) pb for $\mathrm{Z}^0 \to \mathrm{e}^+\mathrm{e}^-$ (where the uncertainty comes primarily from the uncertainty on the PDF calculation) which agrees well with the measurement reported here and with the more recent theoretical calculation [83] of (252 ± 9) pb. The calculation of the cross sections in this paper is based on the zero-width approximation approach described in [87,

Variable	**Run Ia**	**Run IIa**
$\mathcal{L}(\mathrm{pb}^{-1})$	19.7 ± 0.7	72.0 ± 4.3
$\mathrm{N}_{Z}^{candidates}$ (CC) in $66 < M_{ee} < 116$ GeV/c^2	529	1830
$\mathrm{N}_{Z}^{background}$ (CC) in $66 < M_{ee} < 116$ GeV/c^2	1 ± 1	9.7 ± 5.3
A_Z^{CC}	$(15.2 \pm 1.2)\%$	$(11.49 \pm 0.64)\%$
ϵ_T	$(84.5 \pm 1.2)\%$	$(84.2 \pm 0.7)\%$
ϵ_L	$(91.7 \pm 0.8)\%$	$(93.9 \pm 0.5)\%$
ϵ_{trig}	$(89.2 \pm 0.3)\%$	$(99.9^{+0.1}_{-0.7})\%$
$\epsilon_{Z_{vtx}}$	$(95.5 \pm 1.1)\%$	$(95.1 \pm 0.5)\%$
$\sqrt{s}(p\bar{p})$	1.8 TeV	1.96 TeV
$\sigma_Z \cdot Br(\mathrm{Z}^0 \to \mathrm{e}^+\mathrm{e}^-)$ (pb)	248 ± 25	267 ± 23

Table 9.1: *Parameters involved in the* $\mathrm{Z}^0 \to \mathrm{e}^+\mathrm{e}^-$ *cross-section calculation in Run Ia [9, 10] and Run IIa. Note that the kinematic cuts in Run Ia are looser than in the ones in Run IIa.*

88]. The estimation of the uncertainty from the PDFs on these total cross sections has been performed with the NLL CTEQ6 and MRST2001E error PDFs sets according to the prescriptions in [89, 90], obtaining the relative uncertainties of 3.5% and 1.1% respectively. To be conservative, the CTEQ6 errors are used. Table 9.2 shows the recent calculations of Stirling *et al.* [11]

Corrections	$\sqrt{s}$ (TeV)	$\sigma_Z \cdot Br(\mathrm{Z}^0 \to \mathrm{e}^+\mathrm{e}^-)$(nb)
LO	1.80	0.1609 ± 0.0024
NLO	1.80	0.2202 ± 0.0033
NNLO	1.80	0.2298 ± 0.0034
LO	1.96	0.1765 ± 0.0026
NLO	1.96	0.2406 ± 0.0036
NNLO	1.96	0.2505 ± 0.0038

Table 9.2: *Improved calculation of* $\mathrm{Z}^0 \to \mathrm{e}^+\mathrm{e}^-$ *cross-section by W.James Stirling et.al. for both* $\sqrt{s} = 1.8$ *and* $\sqrt{s} = 1.96$ *TeV [11]. The uncertainties reflect the 1.5% uncertainty on the calculation of the PDFs [12].*

for $\sqrt{s} = 1.8$ TeV compared to $\sqrt{s} = 1.96$ TeV. The higher energy increases the Z^0 cross section by $\sim 9\%$. The uncertainties reflect the 1.5% uncertainty on the calculation of the PDFs [12]. The other parameters have been updated

since the previous calculation [5] to incorporate the latest results from LEP. For a complete list of the parameters used in this calculation see Table 9.3. Figure 9.1 shows this measurement compared with the other measurements

Parameter	**value**
$Br(\mathrm{Z}^0 \to \mathrm{e}^+\mathrm{e}^-)$	0.033658
$Br(\mathrm{W}^0 \to \mathrm{e}\nu^-)$	0.0168
M_W	80.4230
M_Z	91.1876
$\sin^2_{\theta_W}$	0.23143
G_F	1.16639
W coupling: $\sqrt{2} \cdot G_F \cdot M_W^2$	yes
W coupling: $\pi \cdot \frac{\alpha}{sin^2_{\theta_W}}$	no
Z coupling: $\sqrt{2} \cdot G_F \cdot \frac{M_Z^2}{4}$	yes
Z coupling: $\pi \cdot \frac{\alpha}{4sin^2_{\theta_W}} \cdot cos^2_{\theta_W}$	no
CKM elements:	
V_{ud}	0.9734
V_{us}	0.2196
V_{ub}	0.0036
V_{cd}	0.224
V_{cs}	0.996
V_{cb}	0.0412

Table 9.3: *List of parameters used in the theoretical calculation of the NNLO* $\mathrm{Z}^0 \to \mathrm{e}^+\mathrm{e}^-$ *and* $\mathrm{W}^\pm \to \mathrm{e}^\pm\nu$ *cross sections[11].*

in the literature and with the theoretical predictions from Stirling *et.al.*.

9.2 W Cross section estimation

The cross section $\sigma(\bar{\mathrm{p}}\mathrm{p} \to W^\pm)$ times the branching ratio $\mathrm{Br}(\mathrm{W}^\pm \to \mathrm{e}^\pm\nu)$ is calculated using the expression given in section 2.4

$$\sigma_{\mathrm{W}} \cdot Br(\mathrm{W}^\pm \to \mathrm{e}^\pm\nu) = \frac{\mathrm{N}_{\mathrm{W}}^{candidates} - \mathrm{N}_{\mathrm{W}}^{background}}{A_{\mathrm{W}} \cdot \epsilon^e_{trig} \cdot \epsilon_{zvertex} \cdot \epsilon_{\mathrm{W}} \cdot \int Ldt}$$

where

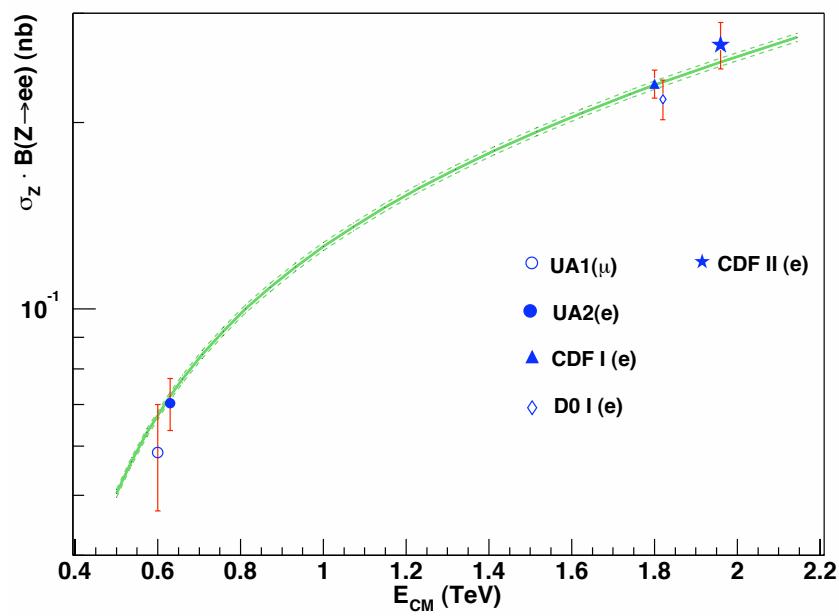

Figure 9.1: $Z \to \ell^+\ell^-$ *cross section measurements as a function of the centre of mass energy* $\sqrt{s}$ *for this measurement (indicated with the star) compared with other measurements in literature. The solid line corresponds to the standard model calculation from [5].*

- $N_W^{candidates} = 38628 \pm 197(stat.)$;
- $N_W^{background} = 2456 \pm 678$;
- $A_W = (24.62 \pm 0.69)\%$;
- $\langle \epsilon^e_{trig} \rangle = (96.6 \pm 0.1)\%$;
- $\epsilon_{zvertex} = (95.1 \pm 0.5)\%$;
- $\epsilon_W = (84.2 \pm 0.7)\%$;
- $\int \mathcal{L} dt = (72.0 \pm 4.3)\ \mathrm{pb}^{-1}$;

Substituting these values

$$\begin{aligned} \sigma_W \cdot Br(\mathrm{W}^\pm \to \mathrm{e}^\pm \nu) &= 2.64 \pm 0.01(stat.) \pm 0.09(syst.) \pm 0.16(lum.)\ \mathrm{nb} \\ &= (2.64 \pm 0.18)\ \mathrm{nb}. \end{aligned}$$

The theoretical value[5] at $\sqrt{s} = 1.96$ TeV with NNLO corrections is (2.687 ± 0.040) pb, where the considerations stated for the Z apply. This value agrees

well with the measurement reported here and with the recent theoretical calculation [83] of (2.688 ± 0.094) pb. Table 9.4 shows the recent calculations of

Corrections	$\sqrt{s}$ (TeV)	$\sigma_W \cdot Br(W^{\pm} \to e^{\pm}\nu)$(nb)
LO	1.80	1.736 ± 0.026
NLO	1.80	2.369 ± 0.036
NNLO	1.80	2.501 ± 0.038
LO	1.96	1.909 ± 0.029
NLO	1.96	2.594 ± 0.039
NNLO	1.96	2.687 ± 0.040

Table 9.4: *Improved calculation of* $W^{\pm} \to e^{\pm}\nu$ *cross-section by W.James Stirling et al. for both* $\sqrt{s}$ *= 1.8 and* $\sqrt{s}$ *= 1.96 TeV [11]. The uncertainties reflect the 1.5% uncertainty on the calculation of the PDFs [12].*

Stirling *et al.* [11] for $\sqrt{s} = 1.8$ TeV compared to $\sqrt{s} = 1.96$ TeV. The higher energy increases the $W^{\pm}$ cross section by $\sim 9\%$. The uncertainties reflect the 1.5% uncertainty on the calculation of the PDFs [12]. The parameters used in the calculation are as in Table 9.3. The Run Ia measurement[9] reported the following value

$$\sigma_W \cdot Br(W^{\pm} \to e^{\pm}\nu) = (2.49 \pm 0.12)\,\text{nb};$$

scaling this value up by 9%, it yields to

$$\sigma_W \cdot Br(W^{\pm} \to e^{\pm}\nu) = (2.76 \pm 0.13)\,\text{nb};$$

which is consistent with the measurement reported here. Figure 9.2 shows this measurement compared with the other measurements in literature and with the theoretical predictions from Stirling *et.al.*.

9.3 Calculation of R = σ_W/σ_Z

As already stated in section 2.2, the ratio of the W and Z cross sections can be expressed as

$$R = (\sigma_W \cdot B(W \to e\nu))/(\sigma_Z \cdot B(Z^0 \to e^+e^-)) =$$

$$= \frac{I_1}{I_2} \cdot \frac{N_W^{candidates} - N_W^{background}}{N_Z^{candidates} - N_Z^{background}} \cdot \frac{A_Z}{A_W} \cdot \frac{\epsilon_Z^{trig}}{\epsilon_W^{trig}} \cdot \frac{\epsilon_Z^{ID}}{\epsilon_W^{ID}} \tag{9.1}$$

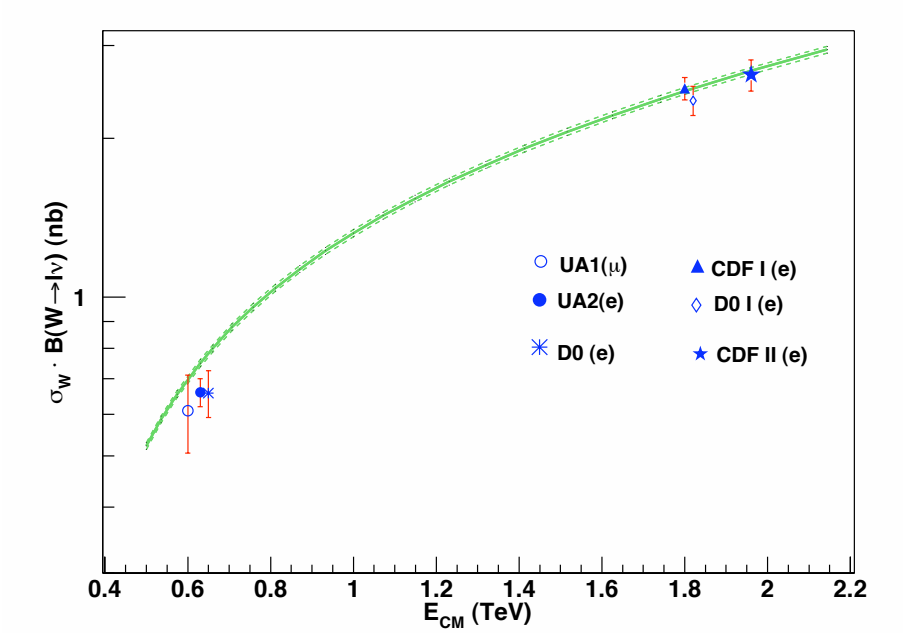

Figure 9.2: $W^{\pm} \to \ell^{\pm}\nu$ *Cross section measurements as a function of the centre of mass energy* $\sqrt{s}$ *for this measurement (indicated with the star) compared with other measurements in literature. The solid line corresponds to the standard model calculation from [5].*

where all the symbols have the same meaning as in sections 9.1 and 9.2. Table 9.5 is a summary of their values. The quantities presented in this table, and summarised in sections 9.1 and 9.2, are used to extract the ratio of cross sections. The systematic uncertainty on R is dominated by the systematic uncertainties on the acceptances, A_W and A_Z. The effects of the various systematic effects on the ratio A_Z/A_W have been analysed, following the same procedure as in section 8.1.1 and 8.2.1. The results are reported in Table 9.6.

Systematic	δA_W	δA_Z	$\delta(A_Z/A_W)$
Energy Scale	0.15	0.03	0.0016
Energy Resolution	0.01	0.02	0.00006
Electron p_T Resolution	0.02	0.02	0.00003
p_T Boson	0.04	0.01	0.0004
W Recoil Energy	0.17	-	0.0032
PDF's	0.58	0.34	0.0029
Material	0.29	0.54	0.0166
Total	$\mathbf{A_W = 24.62 \pm 0.69\%}$	$\mathbf{A_Z = 11.49 \pm 0.64\%}$	$\mathbf{A_Z/A_W = 0.4667 \pm 0.0172}$

Table 9.6: Systematic uncertainties in W, Z acceptances and on the ratio of acceptances.

As already anticipated, many of the systematic uncertainties in the acceptances cancel in the ratio. The dominant source comes from the variation in the amount of material in the detector used in the simulation, which is currently under investigation.

Using the numbers in Table 9.5 and substituting in the expression 9.1

$$R = 9.88 \pm 0.24(stat.) \pm 0.47(syst.) = 9.88 \pm 0.53.$$

This quantity can be compared with the value obtained with CDF Run II data in the muon channel, $10.69 \pm 0.27(stat.) \pm 0.33(syst.)$[91].
The value published in Run I for the electron channel is 10.90 ± 0.43 [10].
The NNLO calculation at $\sqrt{s} = 1.96$[1] TeV, $R = 10.66 \pm 0.05$ [83] agrees with the value measured here within 1.5σ. In this calculation, the largest theoretical uncertainty on the W and Z cross sections comes from the choice of the PDFs; for CTEQ6 it is assigned to be 3.5%, which results in a 0.5 % fractional error on the ratio. This number can be compared with the value 10.92 obtained by Stirling [5], using the cross sections given in Table 9.4 and 9.2. In Figure 9.3 the measurement obtained here is compared with other measurements in the literature.

[1]The measurement is compared to the calculation in [83] since the propagation of the theoretical uncertainties on the ratio of the cross sections is unknown for the calculation in [5].

9.4 Extraction of Br($W^{\pm} \to e^{\pm}\nu$)

From the formula

$$R = \frac{\sigma(p\bar{p} \to W)}{\sigma(p\bar{p} \to Z)} \frac{\Gamma(W \to e\nu)}{\Gamma(Z \to e^+e^-)} \frac{\Gamma(Z)}{\Gamma(W)}. \tag{9.2}$$

the branching ratio of the W boson into electron and neutrino, Br($W^{\pm} \to e^{\pm}\nu$) can be extracted. Using:

- the theoretical value of $\frac{\sigma(p\bar{p}\to W)}{\sigma(p\bar{p}\to Z)} = 3.361 \pm 0.024$, where the central value comes from the ratio of the cross sections

  $$\sigma(p\bar{p} \to W + X) = 25.173\,\text{nb [83]}$$

  and

  $$\sigma(p\bar{p} \to Z + X) = 7.4891\,\text{nb [83]},$$

  The error is calculated adding in quadrature the PDFs error of 0.5% with the error due to the Electroweak coupling parameters (CKM matrix and $\sin^2\theta_W$), estimated to be 0.5%;

- the measurement of $\Gamma(Z \to e^+e^-)/\Gamma(Z) = 3.3658 \pm 0.0023$ % [6, 92].

The value of Br($W^{\pm} \to e^{\pm}\nu$) is measured to be:

$$\begin{aligned} Br(W^{\pm} \to e^{\pm}\nu) &= \frac{\Gamma(W^{\pm} \to e^{\pm}\nu)}{\Gamma(W)} \\ &= (9.89 \pm 0.24(stat.) \pm 0.42(syst.) \pm 0.07(ext.syst.))\% \\ &= (9.89 \pm 0.49)\%. \end{aligned}$$

where the systematic uncertainty includes the systematic uncertainty on R, and the external systematic uncertainty includes the uncertainties on the $\Gamma(Z \to e^+e^-)/\Gamma(Z)$ measurement and on the ratio of cross sections.
This value is within 1σ from the PDG value of 10.72±0.16 GeV [6] and the theoretical prediction of 10.82±0.18 GeV [6].

9.5 Extraction of $\Gamma(W)$

Proceeding as in the previous section, from the formula 9.2 the total width of the W boson Γ(W) can be extracted. Using the values quoted in section 9.4

and the theoretical value of $\Gamma(W \to e\nu) = 226.4 \pm 0.3$ MeV [2], the value of Γ(W) is measured to be:

$$\begin{aligned}\Gamma(\mathrm{W}) &= 2.29 \pm 0.06(stat.) \pm 0.10(syst.) \pm 0.02(ext.syst.)\mathrm{GeV} \\ &= 2.29 \pm 0.12\mathrm{GeV},\end{aligned}$$

where the systematic uncertainty includes the systematic uncertainty on R, and the external systematic uncertainty includes the uncertainties on the $\Gamma(\mathrm{Z} \to \mathrm{e}^+\mathrm{e}^-)/\Gamma(\mathrm{Z})$ measurement, on the theoretical value of $\Gamma(\mathrm{W} \to \mathrm{e}\nu)$ and on the ratio of cross sections.
This value agrees with the PDG fit of 2.118 ± 0.042 GeV [6] and the theoretical prediction of 2.0921 ± 0.0025 GeV [6]. In Figure 9.4 this measurement of Γ(W) is compared with other measurements in the literature [6].

9.6 Extraction of V_{cs}

Using the formula 2.13, the $\mathrm{Br}(\mathrm{W}^\pm \to \mathrm{e}^\pm\nu)$ can be expressed as[36]

$$\frac{1}{Br(\mathrm{W}^\pm \to \mathrm{e}^\pm\nu)} = 3 + f_{QCD}\sum_{ij}|V_{ij}|^2;$$

V_{ij} is the CKM matrix element, with $i, j =$ u,d,c,s,b, and f_{QCD} is a QCD form factor equal to

$$\begin{aligned}f_{QCD} &= 3 \cdot (1 + \alpha_s(M_W)/\pi + 1.409(\alpha_s(M_W)/\pi)^2 + ...) = \\ &\simeq 3.122,\end{aligned}$$

where the value of $\alpha_s(M_W) = 0.121 \pm 0.002$ has been used. From this expression, using the value of the $\mathrm{Br}(\mathrm{W}^\pm \to \mathrm{e}^\pm\nu)$ as measured in the previous section, the sum of the squares of the elements of the CKM matrix can be extracted. This is found to be

$$\sum_{ij}|V_{ij}|^2 = 2.28 \pm 0.16.$$

Using the experimental value for the sum of all elements except $|V_{cs}|^2$, namely 1.0477 ± 0.0074[6], the value

$$|V_{cs}| = 1.11 \pm 0.07$$

[2]See [6], page 010001-103,formula 10.47a.

can be extracted. In this, the input CKM uncertainty is $\pm$ 0.004, and that from $\alpha_s(M_W)$ is negligible. This value is more precise than the direct measurement at LEP, $|V_{cs}| = 0.97 \pm 0.11$[6], but not as precise as the combined value from LEP and Run I at the Tevatron, $|V_{cs}| = 0.998 \pm 0.013$[36].

9.7 Conclusions

The cross-sections of the Z boson decaying into electron-positron pairs and the W boson decaying into electron and neutrino are measured using high p_T electrons. The data were taken from March 2002 through January 2003, with a total integrated luminosity of 72.0 pb^{-1}. These measurements yielded values of

$$\begin{aligned} \sigma_Z \cdot Br(\mathrm{Z}^0 \to \mathrm{e}^+\mathrm{e}^-) &= (267.0 \pm 6.3(stat.) \pm 15.2(syst.) \pm 16.0(lum.))\ \mathrm{pb} \\ &= (267.0 \pm 23.0)\ \mathrm{pb} \end{aligned}$$

and

$$\begin{aligned} \sigma_W \cdot Br(\mathrm{W}^\pm \to \mathrm{e}^\pm\nu) &= (2.64 \pm 0.01(stat.) \pm 0.09(syst.) \pm 0.16(lum.))\ \mathrm{nb} \\ &= (2.64 \pm 0.18)\ \mathrm{nb} \end{aligned}$$

which agree well with both the theoretical prediction at $\sqrt{s} = 1.96$ TeV and the Run Ia measurements when the correction due to the change in the centre-of-mass energy is made. From the ratio of these cross sections,

$$\begin{aligned} \mathrm{R} &= \frac{\sigma_W \cdot Br(\mathrm{W}^\pm \to \mathrm{e}^\pm\nu)}{\sigma_Z \cdot Br(\mathrm{Z}^0 \to \mathrm{e}^+\mathrm{e}^-)} \\ &= 9.88 \pm 0.24(stat.) \pm 0.47(syst.) = 9.88 \pm 0.53, \end{aligned}$$

the branching ratio of W in electron and neutrino and the total width of the W boson are extracted, giving

$$\begin{aligned} Br(\mathrm{W}^\pm \to \mathrm{e}^\pm\nu) &= \frac{\Gamma(\mathrm{W}^\pm \to \mathrm{e}^\pm\nu)}{\Gamma(W)} \\ &= (9.89 \pm 0.49)\%, \text{ and} \\ \Gamma(W) &= (2.29 \pm 0.12)\ \mathrm{GeV}. \end{aligned}$$

The latter value agrees within 2σ of the Standard Model value, as shown in Figure 9.4. In addition, the CKM matrix element $|V_{cs}|$ has been extracted, giving

$$|V_{cs}| = 1.11 \pm 0.07.$$

This value is consistent with the other measurements in the literature.

9.8 Future Prospects

Improvements on the R measurement can be made with higher statistics and a better understanding of the systematic effects.
With 1 fb^{-1} of data expected by the end of 2004, the statistical error can be reduced by roughly a factor four. A further improvement will come from the inclusion of events in the EM plug calorimeter, which will essentially double the sample and reduce the uncertainty on the acceptance. The main systematic uncertainty on the measurement of R comes from the 20% uncertainty on the amount of material in the detector simulation. Several studies are currently underway, involving comparison of photon conversion events in data and Monte Carlo, to precisely quantify this effect. To reduce this uncertainty to the same order of the statistical one, the amount of material needs to be known to a 3% level, which seems achievable. The second largest error comes from the uncertainty on the calculation of the QCD background in the W sample. Several different methods are being explored at present to confirm the number obtained with the method described in section 6.2.1; they include studies of QCD events in data and Monte Carlo. This will allow to reduce the conservative estimate associated with this method from 50% to better than 15%, resulting in a 1% uncertainty on R. As other sources of uncertainties (as the choice of PDFs) can be reduced with the collection of more data and the inclusion of events in the Plug EM calorimeter, it seems reasonable to expect an overall precision of about 1% on the measurement of R in Run II.

	W's	**Z's**
Candidates	38628	1830
Background :		
QCD	1344 ± 677	8.7 ± 4.7
$Z^0/\gamma^* \to \tau^+\tau^-$	–	1.0 ± 0.2
$Z^0 \to e^-e^-$	344 ± 17	
$W \to \tau\nu$	768 ± 22	–
Total Background	2456 ± 678	9.7 ± 5.3
Signal	$36172 \pm 197_{stat} \pm 678_{syst}$	$1820.3 \pm 42.8_{stat} \pm 5.3_{syst}$
Acceptance :		
$A_{W,Z}$	$24.62 \pm 0.04_{stat} \pm 0.69_{syst}$ %	$11.49 \pm 0.07_{stat} \pm 0.54_{syst}$ %
A_Z/A_W	0.467 ± 0.020	
ID Efficiencies :		
ϵ_T	$84.2 \pm 0.7\%$	$84.2 \pm 0.7\%$
ϵ_L		$93.9 \pm 0.5\%$
$c_{CES fiducia}$		$99.92 \pm 0.01\%$
$\epsilon_{W,Z}$	$84.2 \pm 0.7\%$	$87.1 \pm 0.9\%$
ϵ_Z/ϵ_W	1.034 ± 0.013	
Trigger Efficiencies :		
$c_{W,Z}$	96.6 ± 0.1 %	$99.9\ ^{+0.1}_{-0.7}$ %
Drell-Yan correction(I_1/I_2)		1.004 ± 0.001
Luminosity	72.0 ± 4.2 pb^{-1}	
Vertex cut efficiency	95.1 ± 0.5 %	
$\sigma \cdot B$(no lum error)	$2.64 \pm 0.01_{stat} \pm 0.09_{syst}$	$0.267 \pm 0.006_{stat} \pm 0.015_{syst}$
$\sigma(p\bar{p} \to W \to e\nu)/\sigma(p\bar{p} \to Z^0 \to ee)$	$\mathbf{9.88 \pm 0.24_{stat} \pm 0.47_{syst}}$	

Table 9.5: *Summary of the results from the W and Z cross section results.*

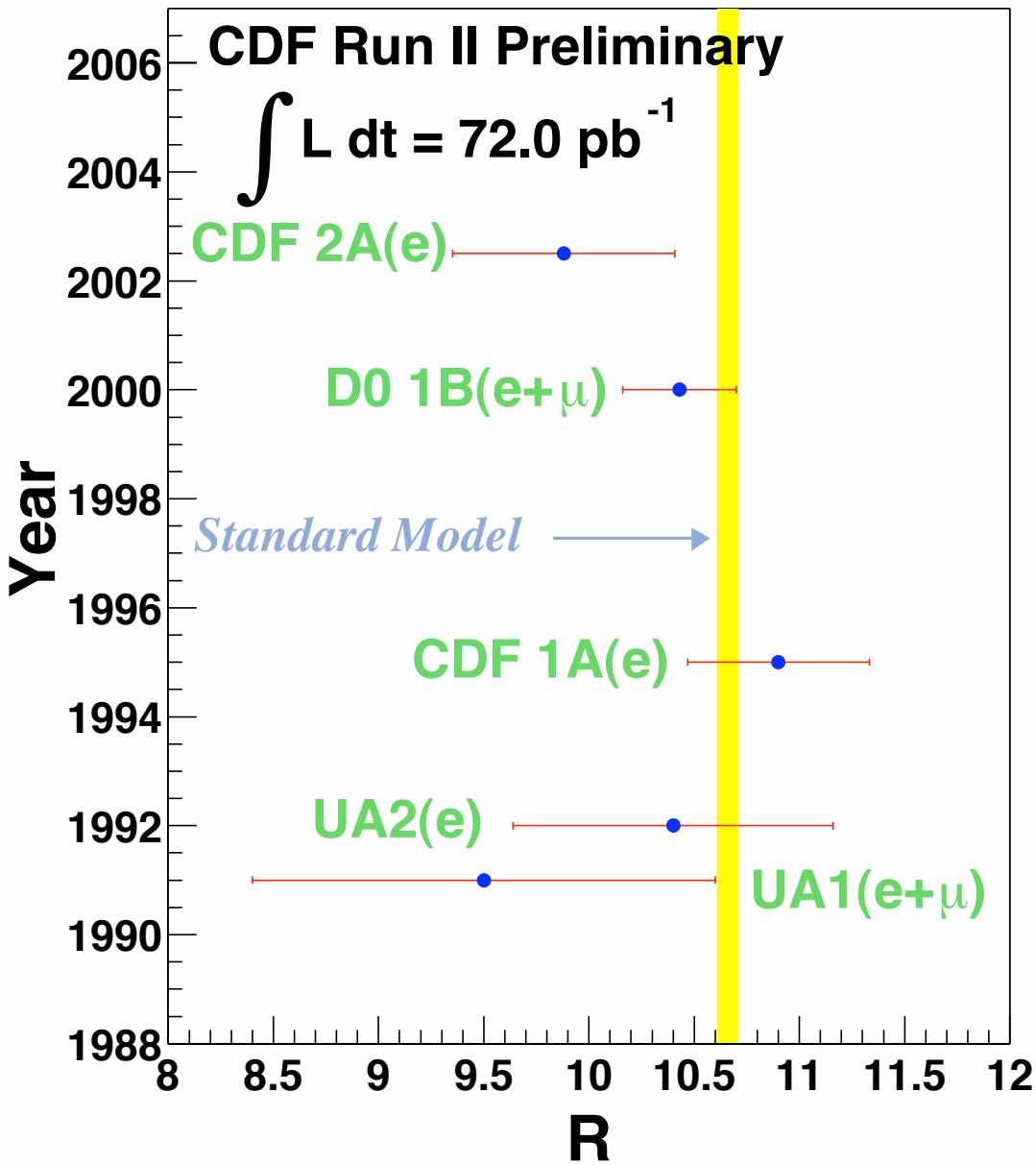

Figure 9.3: *Measurements of* $R = \frac{\sigma_W}{\sigma_Z}$ *performed in the years between 1991 and 2000 are compared with this measurement. The World Average is the value reported in the PDG [6], while the Standard Model prediction is taken from [6].*

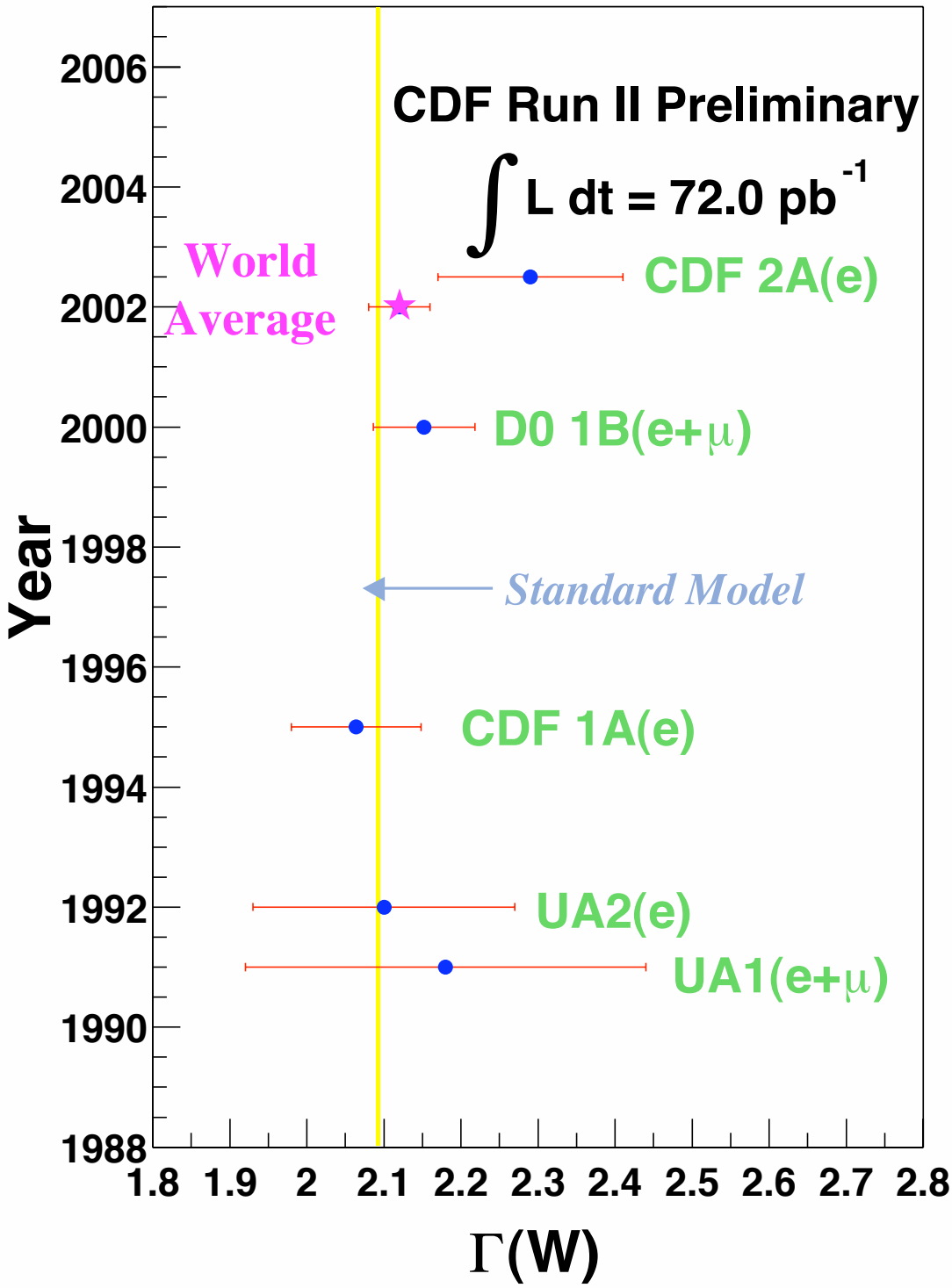

Figure 9.4: *Measurements of $\Gamma(W)$ performed in the years between 1991 and 2000 are compared with this measurement. The World Average is the value reported in the PDG [6], while the Standard Model prediction is taken from [6].*

Appendix A

Baseline Selection Criteria for Tight Central Isolated Electrons

In this appendix the selection criteria described in chapter 5 are discussed[7]. The values chosen for each variable shown in Table 5.3 are motivated, and more details are given on the procedures used in choosing them.

A.1 Method

The decision on the values of the different variables to cut on is based on studies of the efficiency versus the background rejection of the single variables.

The **efficiency** of each quantity is estimated using a subset of the tight central isolated electron sample described in chapter 5, collected between March and October 2002. This is a sample of $Z^0/\gamma^* \rightarrow e^+e^-$ events, selected in a slightly different way than in the analysis (described in section 5.2.5), in order to obtain an unbiased sample. For each event, an electron candidate passing the kinematic selection criteria[1] is selected "at random"[2] and subsequently tested through the central tight isolated electron criteria (as defined in Table 5.3). If it satisfies the criteria, the second electron in the event is

[1]They are those based on the E_T,p_T and the fiduciality selection.

[2]Meaning without requiring it to be the highest energy cluster or any other prerequisite.

taken as unbiased with respect to the identification variables. If it fails the central tight electron criteria, the event is discarded.
The **rejection of the background** is found using the W electron sample, collected in the same period as the $Z^0/\gamma^* \rightarrow e^+e^-$ sample with the same trigger. The W sample is taken as a representative sample with non-negligible background contamination. Hence the background fraction in the W sample is taken as the figure of merit for the background rejection.

For each variable the distribution for the $Z^0/\gamma^* \rightarrow e^+e^-$ sample is reported, for which the background is assumed to be negligible. The number of events for which the considered variable has a value that is higher than the chosen value are counted (N_{higher}). The ratio of N_{higher} divided by the total number of events (N_{total}) is defined as the efficiency for electrons; that is,

$$\epsilon = \frac{N_{higher}}{N_{total}}. \tag{A.1}$$

The background for the W sample is calculated once the selection criteria have been applied to see the effect on the background fraction[3]. The values of the variables are chosen such that they reject the most background whilst maintaining intact a high fraction of the signal.

A.2 Variables

The variables used in the selection of the tight central isolated electron samples are described in chapter 4 and summarised in Table 5.3. Both the Z^0 and W samples are subsamples of this sample. All the corrections described in chapter 4 are applied here. All the variables will be described in turn, and the choice of the proposed value assigned to them will be discussed and motivated.

- **Electron Energy** E_T.
  The proposed cut for this variable is 25 GeV. Both the values of 20 and 25 GeV have been studied using the W electron sample. Moving from 25 to 20 the QCD background, which is the main source of background,

[3]See section 6 for details on the background calculation in the W sample.

grows from 3%[4] to 6%; as the systematic uncertainty on this number is about 50% (see section 6.2.1), an error of 6% would reflect in a 3% systematic error on the cross-section measurement, which means that it would be the dominant systematic uncertainty. As moving the cut to 25 GeV reduces the signal by about 14%, but significantly improves the background rejection, the value of 25 GeV is adopted.

- **Electron Track** p_T.
  The proposed cut for this variable is 10 GeV. As the cut at the trigger level is 9 GeV, cutting at 10 GeV gives a safety margin above the trigger value. Because, at trigger level no Beam Constrained tracking is used, cutting at the same p_T might bias the calculation of acceptances and efficiencies.

- **Calorimeter Isolation** $E_T^{iso}/E_T^{cluster}$.
  The proposed cut for this variable is 0.1; as it can be seen in Figure A.1, placing the cut at this value has the advantage of having high efficiency.

- **E/p**.
  The application of an upper cut on the ratio of E/p is made in order to keep the events where electrons have undergone bremsstrahlung (which appear in the tail at 1< E/p <2), and still reject the background which will contaminate the region $E/p > 2$. Thus, the cut chosen for E/p is $E/p < 2$.
  This choice is supported from the distributions of efficiency and background in Figure A.2. In addition to an upper cut on E/p, some other CDF analyses have imposed a lower cut, such as $E/p > 0.5$. This hasn't been done in the inclusive tight isolated selection for two reasons. Firstly, the cut becomes unreliable for very large values of p_T. A second reason for not imposing the cut is more philosophical; the rate for good electrons with $E/p < 0.5$ should be zero, and so the cut should not remove any significant number of events. However, tracking errors, including alignment problems and database mistakes, will move events around in E/p, with some showing up in this region where no events are expected. Consequently, this region can be used as a sensitive measure of one class of tracking problems and a measure of non-Gaussian tails on the tracking resolution due to them. Cutting out

[4]See section 6.2.1 for the estimate of the QCD background in the W sample.

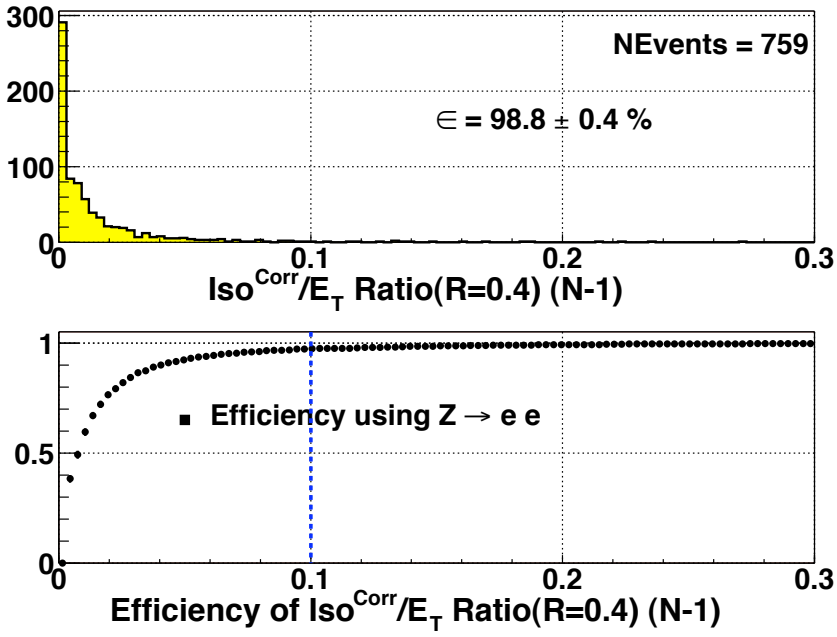

Figure A.1: *In the upper plot, the distribution of the isolation variable in the sample of* $Z^0/\gamma^* \rightarrow e^+e^-$ *events is plotted. The events are selected applying all the cuts as in the text apart from the cut on the variable which is plotted ("N-1"). In the bottom plot, the efficiency of the chosen cut is shown as a function of the variable itself, when all the selection criteria except the one including the variable itself are applied ("N-1"). The background for this variable is not shown for two reasons; Firstly, the isolation is used to calculate the background and thus changing the cut will change the background itself; secondly, the background considered depends on the kind of physics processes analysed. The value of the efficiency for the chosen value is given[7].*

a very small number of events doesn't have much effect, and only can hide such problems.

- **Had/EM.**
  The leakage of electromagnetic showers into the hadron compartment was measured in a test beam of electrons during Run I. Beam energies ranged from 10 to 150 GeV. A fit to the points up to Had/EM (cut) = A + B * E(GeV)/100 describes the data reasonably well, although due to pedestal noise the 10 and 15 GeV data fit less well. A logarithmic dependence seems to give much worse agreement. The parameters are as shown in Table A.1. Thus, the chosen cut is Had/EM $< 0.055 +$

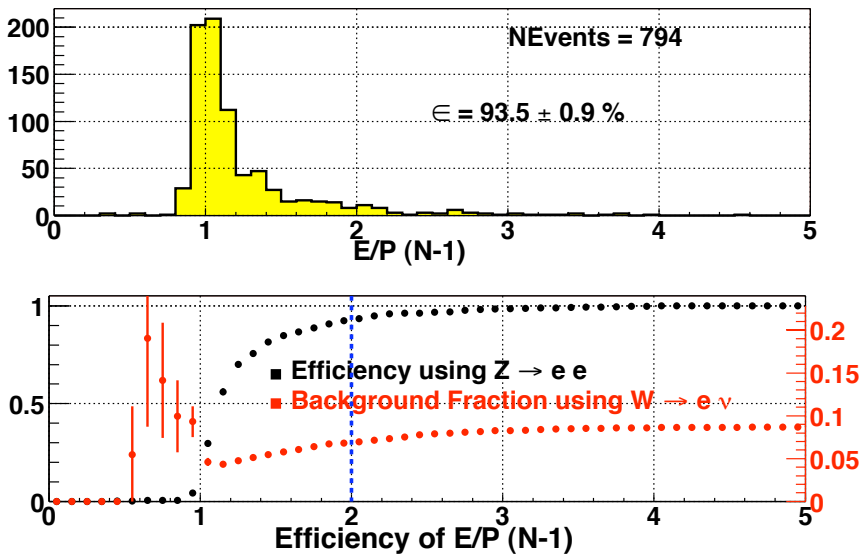

Figure A.2: *In the upper plot, the distribution of the E/p variable in the sample of $Z^0/\gamma^* \rightarrow e^+e^-$ events, selected as in the text, is plotted. In the bottom plot, the efficiency of the chosen cut is shown as a function of the variable itself, together with the background contamination from the W sample, as explained in the text. Both plots are made when all the selection criteria,except the one including the variable itself, are applied("N-1"). The value of the efficiency for the chosen value is given[7].*

Electron Eff.	A	B
0.98	.053	.043
0.95	.039	.029
0.90	.030	.021
0.85	.025	.018

Table A.1: *The parameters in the linear fit to the cut in Had/EM to maintain the efficiency in column 1[7].*

0.045 E (GeV)/100. Figure A.3 shows the *inefficiency* of a fixed cut of Had/EM = 0.05 for electrons from a W sample selected with the running cut of Had/EM = 0.055 + .045 E (GeV)/100. The inefficiency grows with E_T, as expected from the test beam data.

- **Lshr.**
  Based on the plot in Figure A.4, which shows the efficiency and background rejection of the cut, the chosen cut is Lshr < 0.2.

- **CES-Track Matching**.
  The proposed cut on ΔZ is $|\Delta Z| < 3.0$ cm, while that on $Q \cdot \Delta X$ is -3.0 cm $< Q \cdot \Delta X <$ 1.5 cm. These choices are justified by the plots in Figure A.5 and Figure A.6.

- χ^2_{strips}
  The chosen value of $\chi^2_{strip} < 10$ keeps most of the signal and rejects a large fraction of the background, as shown in Figure A.7.

- The choice on the two remaining variables, Fiduciality and Track Quality Cuts, is explained in more detail in [7].

Distributions of the variables described in this appendix are shown in Chapter 5 using the all set of data available for this analysis.

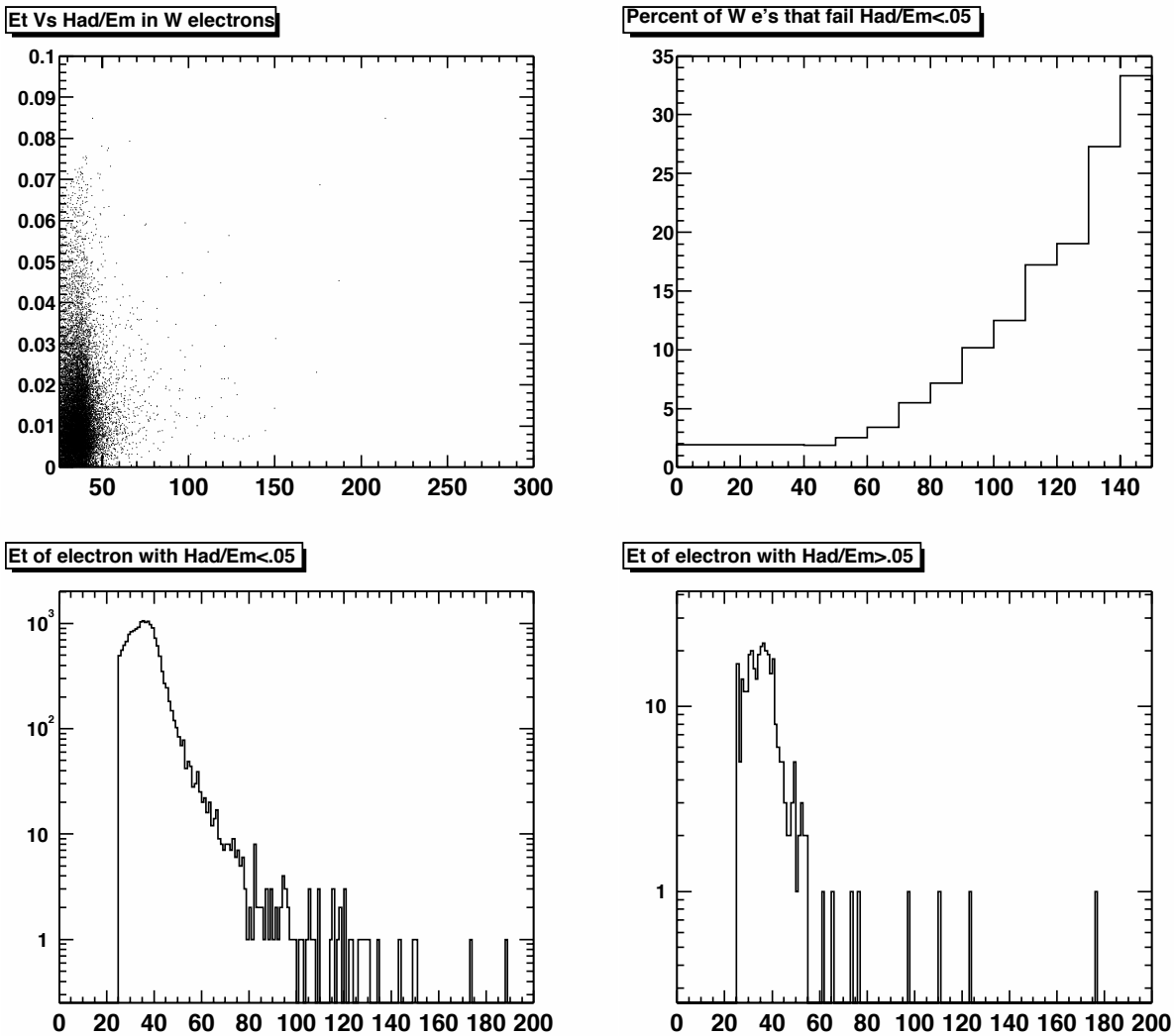

Figure A.3: *Top Left: Had/Em vs.* E_T *for tight electrons with* $E_T > 25$ *GeV in events with* $\not{E}_{\mathrm{T}} > 25$ *GeV. Top Right: the fraction of events that pass the running Had/EM cut that fail the fixed cut of Had/EM <0.05 as a function of the value of the cut on* E_T *. Bottom Left: the* E_T *spectrum of events with Had/EM <0.05. Bottom Right: the* E_T *spectrum of events with Had/EM >0.05[7].*

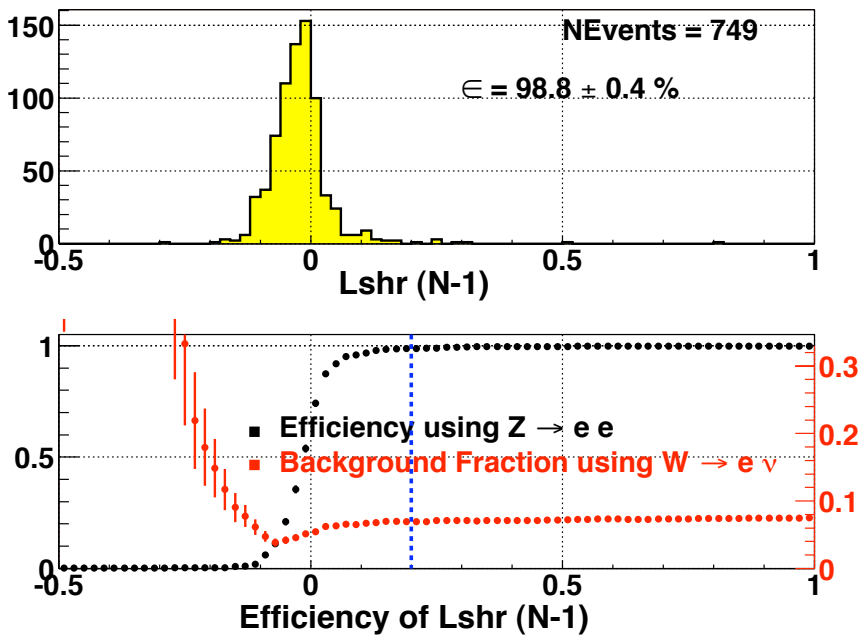

Figure A.4: *In the upper plot, the distribution of the Lshr variable in the sample of* $Z^0/\gamma^* \rightarrow e^+e^-$ *events, selected as in the text, is plotted. In the bottom plot, the efficiency of the chosen cut (left-hand scale) is shown as a function of the variable itself, together with the background contamination from the W sample (right-hand scale), as explained in the text. Both plots are made when all the selection criteria, except the one including the variable itself, are applied ("N-1"). The value of the efficiency for the chosen value is given[7].*

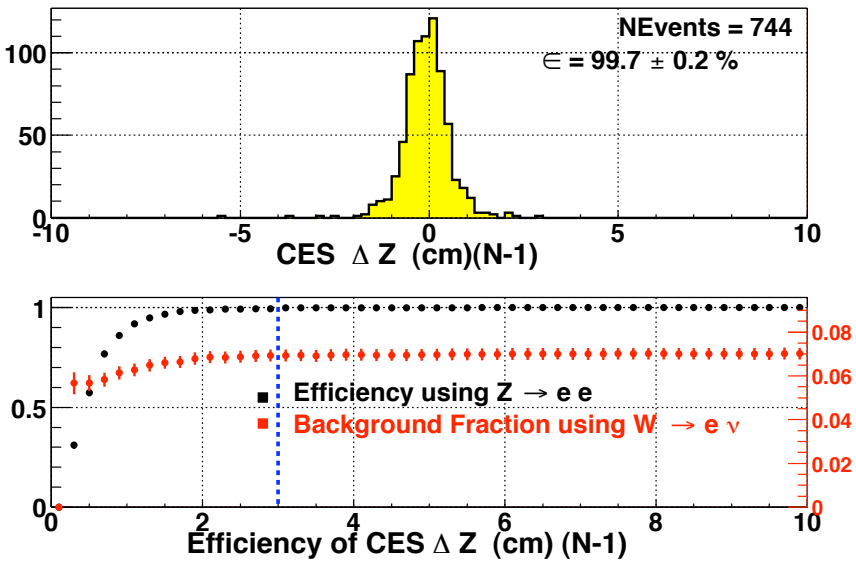

Figure A.5: *In the upper plot, the distribution of the ΔZ variable in the sample of $Z^0/\gamma^* \rightarrow e^+e^-$ events, selected as in the text, is plotted. In the bottom plot, the efficiency of the chosen cut (left-hand scale) is shown as a function of the variable itself, together with the background contamination from the W sample (right-hand scale), as explained in the text. Both plots are made when all the selection criteria, but the one including the variable itself, are applied ("N-1"). The value of the efficiency for the chosen value is given[7].*

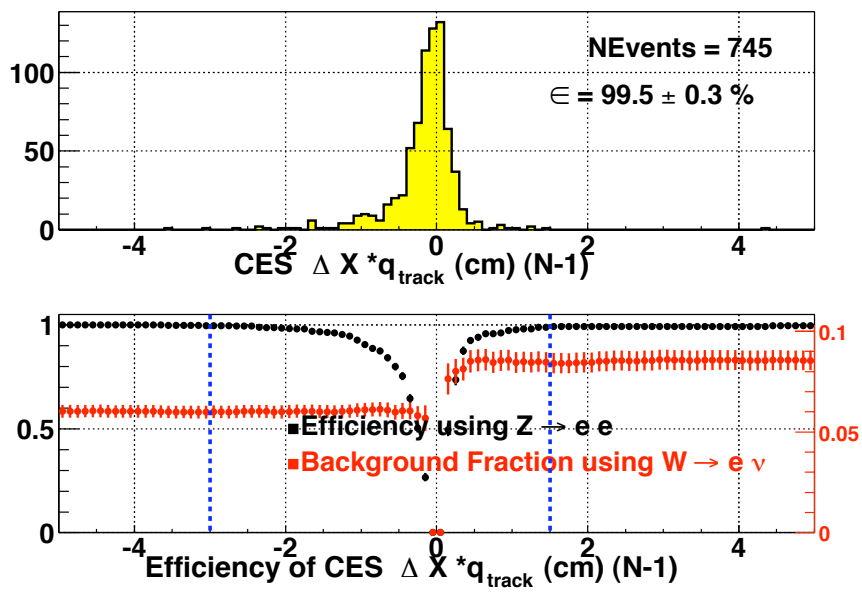

Figure A.6: *In the upper plot, the distribution of the ΔX variable in the sample of $Z^0/\gamma^* \rightarrow e^+e^-$ events, selected as in the text, is plotted. In the bottom plot, the efficiency of the chosen cut (left-hand scale) is shown as a function of the variable itself, together with the background contamination from the W sample (right-hand scale), as explained in the text. Both plots are made when all the selection criteria, but the one including the variable itself, are applied ("N-1"). The value of the efficiency for the chosen value is given[7].*

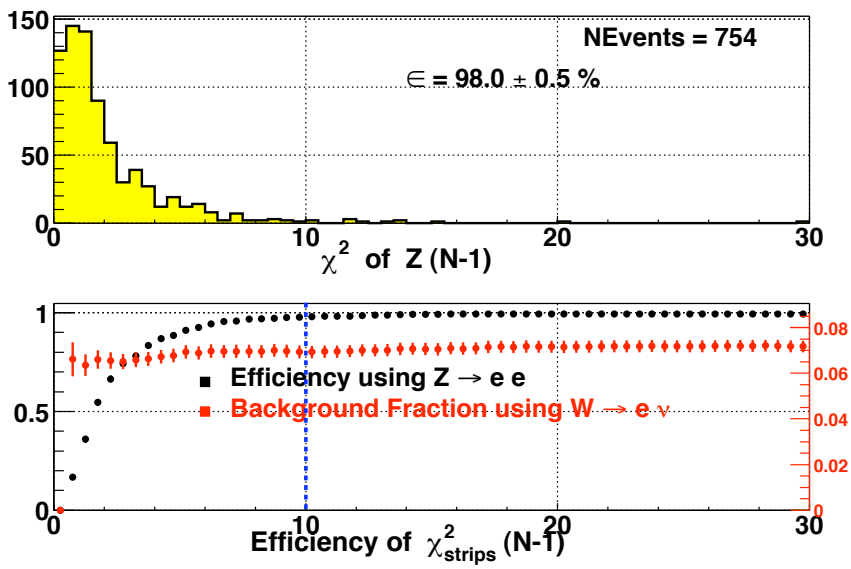

Figure A.7: *In the upper plot, the distribution of the χ^2 variable in the sample of $Z^0/\gamma^* \to e^+e^-$ events, selected as in the text, is plotted. In the bottom plot, the efficiency of the chosen cut is shown as a function of the variable itself, together with the background contamination from the W sample, as explained in the text. Both plots are made when all the selection criteria but the one including the variable itself are applied. The value of the efficiency for the chosen value is given[7].*

Appendix B

Electron Efficiencies using $Z^0 \to e^+e^-$ data

In this appendix the formulae used to calculate the efficiencies in section 7.3.2 are derived. $Z^0 \to e^+e^-$ data are used in this calculation, since they have a very clean signature and thus are ideal for this kind of study.

B.1 Method

Starting with a sample of events with at least one tight central isolated electron[1], the following variables are defined:
ϵ_T = the efficiency of one leg passing the tight central electron requirements;
ϵ_L = the efficiency of one leg passing the loose central electron requirements;
P_T = the probability that one electron passes the tight central electron cuts;
P_L = the probability that one electron passes the loose central electron cuts but not the tight requirements;
The quantities P_T and P_L can be written as

$$P_T = \epsilon_T, \tag{B.1}$$

$$P_L = (\epsilon_L - \epsilon_T) \tag{B.2}$$

[1]See section 5.2.4 for the definition of the tight central isolated electron sample.

Using the expressions B.1 and B.2, the probability for a Z to pass the central tight-central loose selection can be written as

$$\begin{aligned}
\epsilon_Z &= P_T \cdot P_T + P_T \cdot P_L + P_L \cdot P_T \\
&= P_T \cdot P_T + 2P_T \cdot P_L \\
&= \epsilon_T^2 + 2\left[\epsilon_T\left(\epsilon_L - \epsilon_T\right)\right] \\
&= 2\epsilon_T\epsilon_L - \epsilon_T \\
&= \epsilon_T \cdot \left(2\epsilon_L - \epsilon_T\right), \qquad \text{(B.3)}
\end{aligned}$$

as already stated in section 7.3.2.
The numbers of events introduced in section 7.3.2 can be written as

$$\begin{aligned}
N_{CC} &= \left[2\epsilon_T \cdot (1-\epsilon_L) + \epsilon_T^2\right] \cdot N \\
&= \epsilon_T \cdot (2-\epsilon_T) \cdot N; \qquad \text{(B.4)} \\
N_{TT} &= \epsilon_T^2 \cdot N; \qquad \text{(B.5)} \\
N_{TL} &= \epsilon_T \cdot (2\epsilon_L - \epsilon_T) \cdot N, \qquad \text{(B.6)}
\end{aligned}$$

with:
N = the total number of events in the data;
N_{TT} = the number of events with both legs passing the tight central electron cuts in Table 7.3;
N_{TL} = the number of events with one leg passing the tight and the other passing the loose central electron cuts;
N_{CC} = the number of events with only one leg passing the tight selection criteria and the other leg passing the cuts in the rightmost column of Table 7.3.
Solving for ϵ_T and ϵ_L,

$$\epsilon_T = \frac{2N_{TT}}{N_{CC} + N_{TT}},$$
$$\epsilon_L = \frac{N_{TL} + N_{TT}}{N_{CC} + N_{TT}},$$

while the efficiencies of the single cuts are

$$\epsilon^i = \frac{N_{Ti} + N_{TT}}{N_{CC} + N_{TT}},$$

as stated in section 7.3.2.

Bibliography

CDF notes which are not publically available can be obtained from the author on request.

[1] Eva Halkiadakis, Andy Hocker, Young-Kim Kee, Giulia Manca, Willis Sakumoto & Greg Veramendi. "$W^{\pm} \rightarrow e^{\pm}\nu$ Cross Section Analysis with Run II data". CDF Note 6300.

[2] Young-Kee Kim, Jason Nielsen, Lauren Tompkins & Greg Veramendi. "Trigger Efficiencies for High P_T Electrons". CDF Note 6234.

[3] W. Sakumoto. " Event |Zvtx| < 60 cm Cut Efficiency for Run II". CDF Note 6331.

[4] "Plots kindly provided by Eva Halkiadakis".

[5] A.D.Martin *et al.* *Phys.Lett.B*, **531** (2002) 216.

[6] K. Hagiwara *et al.* *Phys.Rev.*, **D66** (2002) 010001.

[7] M. Coca *et al.* "Baseline Analysis Cuts for Central High-p_T Isolated Electrons". CDF Note 6454.

[8] A. Denner & T. Sack. *Zeit.Phys.*, **C46** (1990) 653.

[9] F. Abe *et al.*, (CDF collaboration). "Measurement of $\sigma \cdot B(W \rightarrow e\nu)$ and $\sigma \cdot B(Z\ 0 \rightarrow e\ +e\ -)$ in $p\overline{p}$ collisions at $\sqrt{s} = 1.8$ TeV". *Phys. Rev. Lett.*, **76** (1996) 3070–3075. hep-ex/9509010.

[10] F. Abe *et al.* *Phys.Rev.Lett.*, **64** (1990) 157.

[11] W.J. Stirling. *private communication.*

[12] A.D. Martin, R.G. Roberts, W.J. Stirling & R.S. Thorne. "Uncertainties of predictions from parton distributions I: Experimental errors, hep-ph/0211080".

[13] P.B. Renton. *Electroweak Interactions,*Cambridge University Press,*1990*.

[14] K. Nakamura, (Super-Kamiokande Collaboration). "Atmospheric neutrino results from Super-Kamiokande". *Nucl. Phys. Proc. Suppl.*, **66** (1998) 282–289.

[15] Q.R. Ahmad *et al.*, (SNO collaboration). "Direct evidence for neutrino flavor transformation from neutral-current interactions in the Sudbury Neutrino Observatory". *Phys. Rev. Lett.*, **89** (2002) 011301. Nucl-ex/0204008.

[16] Q.R. Ahmad *et al.*, (SNO collaboration). "Measurement of the charged current interactions produced by B-8 solar neutrinos at the Sudbury Neutrino Observatory". *Phys. Rev. Lett.*, **87** (2001) 071301. Nucl-ex/0106015.

[17] Lee Smolin. "How far are we from the quantum theory of gravity?" hep-th/0303185.

[18] A.G. Holzner, (LEP Higgs working group 2002-01). "Search for the standard model Higgs boson at LEP". hep-ex/0208045.

[19] R.K. Ellis, W.J. Stirling & B.R. Webber. "QCD and Collider Physics". Cambridge University Press (1996).

[20] P. W. Higgs. "Broken symmetries, massless particles and gauge fields". *Phys. Lett.*, **12** (1964) 132–133.

[21] P. W. Higgs. "Spontaneous symmetry breakdown without massless bosons". *Phys. Rev.*, **145** (1966) 1156–1163.

[22] P. W. Higgs. "Broken symmetries and the masses of gauge bosons". *Phys. Rev. Lett.*, **13** (1964) 508–509.

[23] Gerard 't Hooft. "Renormalization of massless Yang-Mills fields". *Nucl. Phys.*, **B33** (1971) 173–199.

[24] Gerard 't Hooft. "Renormalizable lagrangians for massive Yang-Mills fields". *Nucl. Phys.*, **B35** (1971) 167–188.

[25] M. J. G. Veltman. "Perturbation theory of massive Yang-Mills fields". *Nucl. Phys.*, **B7** (1968) 637 650.

[26] The LEP collaborations:ALEPH,DELPHI,L3 & OPAL. "Combination procedure for the precise detrmination of Z boson parameters from results of the LEP experiments". hep-ex/0101027.

[27] T. Affolder *et al.*, (CDF collaboration). *Phys. Rev.*, **D64** (2001) 032002.

[28] S. Abachi *et al.*, (D0 collaboration). "Measurement of the top quark pair production cross section in p anti-p collisions". *Phys. Rev. Lett.*, **79** (1997) 1203 1208. hep-ex/9704015.

[29] G.P. Zeller *et al.*, (NuTeV Collaboration). *Phys. Rev. Lett.*, **88** (2002) 091802. hep-ex/0110059.

[30] Nima Arkani-Hamed, Savas Dimopoulos & G. R. Dvali. "The hierarchy problem and new dimensions at a millimeter". *Phys. Lett.*, **B429** (1998) 263–272. Hep-ph/9803315.

[31] Lisa Randall & Raman Sundrum. "A large mass hierarchy from a small extra dimension". *Phys. Rev. Lett.*, **83** (1999) 3370 3373. Hep-ph/9905221.

[32] Simona Rolli, (CDF Collaboration). "Searches for New Particles in CDF". Moriond, Les Arcs,France, 15-22 March 2003. `http://moriond.in2p3.fr/EW/2003/`

[33] Alexei Safonov, (CDF and D0 Collaborations). "SUSY Searches at the Tevatron". Moriond, Les Arcs,France, 15-22 March 2003. `http://moriond.in2p3.fr/QCD/2003/`

[34] Luca Scodellaro, (CDF Collaboration). "Searches for New Phenomena in CDF". XVII Rencontres de Physique de la Vallee d'Aoste, La Thuile,Valle d'Aoste,Italy, 9-15 March,2003. `http://www.pi.infn.it/lathuile/lathuile_2003.html`

[35] APS/DPF Meeting, Philadelphia. "http://www.aps.org/meet/APR03/" (April 2003).

[36] P.B. Renton. "Precision Electroweak Test of the Standard Model". *Rep.Prog.Phys.*, **65** (2002) 1271–1330. hep-ph/0206231.

[37] E. Fermi. *Ric.Sci.*, **4** (1933) 491.

[38] E. Fermi. *Z.Phys.*, **88** (1934) 161.

[39] O. Klein. "Les Nouvelles Théories de la Physique". *Proceedings of a symposium held in Warsaw*. 30 May-3 June 1938 (Institut International de Cooperation Intellectuelle, Paris,1938) p.6.

[40] S. Weinberg. *Phys.Rev.Lett.*, **19** (1967) 1264.

[41] A. Salam. "Elementary Particle Theory". ed. N.Svartholm (Stockholm:Almqvist,1968), page 367.

[42] S.L. Glashow. *Nucl.Phys.*, **22** (1961) 579.

[43] S.D. Drell & T.-M. Yan. *Phys.Rev.Lett.*, **25** (1970) 316.

[44] T. Affolder *et al.*, (CDF collaboration). "Measurement of the W boson mass with the Collider Detector at Fermilab". *Phys. Rev.*, **D64** (2001) 052001. hep-ex/0007044.

[45] V.M. Abazov *et al.*, (D0 collaboration). *Phys. Rev.*, **D66** (2002) 012001.

[46] D. Acosta *et al.*, (CDF and D0 collaborations). "Combination of CDF and DO Results on W Boson Mass and Width". CDF Note 6371.

[47] A. Sirlin. *Phys.Rev.*, **D22** (1980) 971.

[48] W. Hollik. *Fortschr.Phys.*, **38** (1990) 165.

[49] F. Abe *et al.* *Phys.Rev.Lett.*, **80** (1998) 2773.

[50] N. Cabibbo. *III Topical Conference on Proton-Antiproton Collider Physics,Rome,*Jan 1983.

[51] C. Albajar *et al.* "Measurement of the ratio R=$\sigma_W Br(\mathrm{W} \to \mu\nu)/\sigma_Z Br(\mathrm{Z}^0 \to \mu\mu)$ and $\Gamma_{\mathrm{W}}^{tot}$ at the CERN proton-antiproton collider". *Phys.Lett.*, **B 253** (1991) 503.

[52] J. Alitti *et al.* "Measurement of the W and Z production cross-sections at the CERN $\mathrm{p\bar{p}}$ collider". *Z.Phys.C.*, **47** (1990) 11–22.

[53] S. Abachi *et al.* *Phys.Rev.Lett.*, **75** (1995) 1456.

[54] B. Abbott *et al.* *Phys.Rev.*, **D61** (2000) 072001.

[55] The LEP Electroweak Working Group & the SLD Heavy Flavour Working Group. "A combination of preliminary electroweak measurements and constraints on the standard model". hep-ex/0212036.

[56] `http://www.fnal.gov//pub/inquiring/physics/accelerators/chainaccel.html`

[57] "Tevatron Run II handbook". `http://www-bd.fnal.gov/lug/runII_handbook/RunII_index.html`.

[58] "Talk given by S.Holmes at the *Particle Physics Project Prioritization Panel (P5)*, 26th March 2003". `http://www.fnal.gov/directorate/program_planning/P5_Holmes.pdf`

[59] F. Abe *et al.* *FERMILAB-Pub-96/390-E,(1996).*

[60] A. Mukherjee & R. Wagner, (COT group). "COT Central Outer Tracker (public version)". CDF Note 6267.

[61] T. Pratt. "New Physics Searches in High Mass Dimuons at CDF". *D.Phil thesis,(2002).*

[62] Chris Green, Jim Kowalkowsi & Marc Paterno. "CDF Simulation Framework Developer's Guide". CDF Note 5369.

[63] Robert G. Wagner. "Electron Identification for Run II: Algorithms". CDF Note 5456.

[64] M. Brozovic, A.T. Goshaw & W.J. Robertson. "Jet Vertex Resolution in a Run I Z Event Sample". CDF Note 5698.

[65] M.Coca *et al.* "A First Look at Run 2 High p_T Electrons". CDF Note 5803.

[66] "Nodulman,Larry". *private communication.*(CDF Note 5803).

[67] K.Yasuoka *et al.* *Nuclear Instruments and Methods*, **A267** (1988) 315.

[68] Beate Heinemann Angela Wyatt. "*Correction for Leakage Energy in the Central and Plug Calorimeters in Run II*". CDF Note 6167.

[69] P. Tamburello. "http://www-cdf.fnal.gov/internal/physics/top/r2leptons/etf/agenda/10_15_01.html".

[70] F. Abe *et al.* *Phys.Rev.Lett.*, **74** (1995) 2900.

[71] E.J. Thomson *et al.* *IEEE Trans.Nucl.Sci.*, **49** (2002) 1063.

[72] Torbjorn Sjöstrand, Leif Lonnblad & Stephen Mrenna. "PYTHIA 6.203: Physics and manual *and* http://www.thep.lu.se/ torbjorn/Pythia.html". hep-ph/0108264.

[73] "http://www.phys.psu.edu/ cteq/".

[74] J. Elias *et al.* "Luminosity monitor based on Cherenkov counters for p$\bar{p}$ colliders". *Nuclear Instruments and Methods*, **441(3)** (Mar 2000) 366 373.

[75] D. Acosta *et al.* "Estimation of CLC acceptance to inelastic p-pbar interactions". CDF Note 6054.

[76] S. Klimenko, J. Konigsberg & T. Liss. "Averaging of the inelastic cross-section measured by the CDF and the E811 experiments". CDF Note 6314.

[77] D. Perkins. *Introduction to High Energy Physics (Addison Wesley Publishing Company).*

[78] F. Abe *et al.*, (CDF collaboration). "Measurement of the Ratio sigma(W $\rightarrow$ e neutrino)/ sigma(Z $\rightarrow$ e e) in anti-p p collisions at $\sqrt{s} = 1.8$ TeV". *Phys. Rev. Lett.*, **64** (1990) 152–156.

[79] B.Winer R.Hughes, E.Thomson. "Performance study of the eXtremely Fast Tracker in High Luminosity". CDF Note 5986.

[80] D. Glenziski, M. Herndon, C.-J. Lin, J. Thom & A. Yagil. "Determination of the Run IIa COT Tracking Efficiency Using the W-No-Track Sample". CDF Note 5973, version 5.0.

[81] Giulia Manca & Young-Kee Kim. "$Z^0 \rightarrow e^+e^-$ Cross Section Measurement with Run II Data". CDF Note 6202.

[82] J. Wahl. " W and Z Boson Acceptances in the R analysis ". CDF Note 4599.

[83] W. Sakumoto. " W/Z Cross Section Predictions for $\sqrt{s} = 1.96$ TeV,". CDF Note 6341.

[84] T. Affolder *et al.*, (CDF collaboration). "Measurement of d(sigma)/dy for high mass Drell-Yan e+ e- pairs from p anti-p collisions at $\sqrt{s} = 1.8$ TeV". *Phys. Rev.*, **D63** (2001) 011101. Hep-ex/0006025.

[85] W.Badgett *et al.* "Event Z vertex efficiency as a luminosity correction for Run Ia". CDF Note 2703.

[86] D. Cronin-Hennessy, A. Beretvas & P. F. Derwent. "Luminosity Monitoring and Measurement at CDF". *Nuclear Instruments and Methods in Physics Research*, **A 443/1** (2000) 37–50.

[87] R. Hamberg, W.L. van Neerven & T. Matsuura. "". *Nucl.Phys.*, **B359**.

[88] R.V. Harlander & W.B. Kilgore. "". *Phys.Rev.Lett.*, **88**.

[89] J. Pumplin *et al.* "New Generation of Parton Distributions with Uncertainties from Global QCD Analysis ". Hep-ph/0201195.

[90] A.D. Martin *et al.* "Uncertainties of predictions from parton distributions. I: experimental errors. ". Hep-ph/0211080.

[91] K.Bloom*et al.* "Measurement of $\sigma(\mathrm{p\bar{p}} \to \mathrm{W} \to \mu\nu)/\sigma(\mathrm{p\bar{p}} \to \mathrm{Z}^0 \to \mu\mu)$ with Data from CDF II". CDF Note 6025.

[92] Alan D. Martin, R. G. Roberts, W. James Stirling & R. S. Thorne. "Parton distributions and the LHC: W and Z production". *Eur. Phys. J.*, **C14** (2000) 133–145. hep-ph/9907231.